Colloid (Nano- and Micro-Particle) Transport and Surface Interaction in Groundwater

William P. Johnson and Eddy F. Pazmiño

THE GROUNDWATER PROJECT

Colloid (Nano- and Micro-Particle) Transport and Surface Interaction in Groundwater

The Groundwater Project

William P. Johnson

Professor, Department of Geology & Geophysics,
University of Utah
Salt Lake City, Utah, United States

Eddy F. Pazmiño

Assistant Professor at Escuela Politécnica Nacional,
Quito, Pichincha, Ecuador

Colloid (Nano- and Micro-Particle) Transport and Surface Interaction in Groundwater

The Groundwater Project
Guelph, Ontario, Canada

ii

Please consider signing up for the GW-Project mailing list to stay informed about new book releases, events, and ways to participate in the GW-Project. When you sign up for our email list it helps us build a global groundwater community. Sign up↗.

Cover Image: Happel unit cell: metallic sphere represents a porous media grain; discrete nanoscale surface heterogeneity (green) allows colloid filtration under unfavorable conditions; flow is from top to bottom, concurrent with gravity; colloids on red trajectories attach to the grain while those on cyan pass without attachment; white is the Happel fluid shell which is proportional to porosity (Eddy Pazmiño, 2022).

Dedication

We dedicate this text to the many colleagues and students from whom we have learned across lifetimes and generations including Charlie O'Melia, Chi Tien, Bruce Logan, and many others.

Table of Contents

The Groundwater Project Foreword

At the United Nations (UN) Water Summit held on December 2022, delegates agreed that statements from all major groundwater-related events will be unified in 2023 into one comprehensive groundwater message. This message was released at the UN 2023 Water Conference, a landmark event that brought attention at the highest international level to the importance of groundwater for the future of humanity and ecosystems. This message clarified groundwater issues to advance understanding globally of the challenges faced and actions needed to resolve the world's groundwater problems. Groundwater education is key.

The 2023 World Water Day theme *Accelerating Change* is in sync with the goal of the Groundwater Project (GW-Project). The GW-Project is a registered Canadian charity founded in 2018 and committed to the advancement of groundwater education as a means to accelerate action related to our essential groundwater resources. To this end, we create and disseminate knowledge through a unique approach: the democratization of groundwater knowledge. We act on this principle through our website gw-project.org/↗, a global platform, based on the following principle:

"Knowledge should be free, and the best knowledge should be free knowledge." Anonymous

The mission of the GW-Project is to promote groundwater learning across the globe. This is accomplished by providing accessible, engaging, and high-quality educational materials—free-of-charge online and in many languages—to all who want to learn about groundwater. In short, the GW-Project provides essential knowledge and tools needed to develop groundwater sustainably for the future of humanity and ecosystems. This new type of global educational endeavor is made possible through the contributions of a dedicated international group of volunteer professionals from a range of disciplines. Academics, consultants, and retirees contribute by writing and/or reviewing the books aimed at diverse levels of readers from children to high school, undergraduate and graduate students, or professionals in the groundwater field. More than 1,000 dedicated volunteers from 127 countries and six continents are involved—and participation is growing.

Hundreds of books will be published online over the coming years: first in English and then in other languages. An important tenet of GW-Project books is a strong emphasis on visualization, with clear illustrations to stimulate spatial and critical thinking. As with this book, future publications will include videos and other dynamic learning tools.

Revised editions of the books are published from time to time. Users are invited to propose revisions. We thank you for being part of the GW-Project Community. We hope to hear from you about your experience with the project materials, and welcome ideas and volunteers!

The Groundwater Project Board of Directors, January 2023

Foreword

This book is an introduction to the processes in groundwater that govern small particles known as colloids. These particles are important because they are often mobile. They are larger than the chemical molecules referred to as solutes for which the conventional theory of groundwater transport and fate is well known. The behavior of colloids in groundwater is more complex than that of solutes because more processes are involved. The modern industrial economy produces many colloidal-size substances that enter groundwater, some harmful and some not.

Colloid mobility science is at the intersection of physics and chemistry. Understanding the mobility of colloids is important because they include several types of harmful and potentially harmful entities such as viruses, plastics, large organic molecules, and mineral matter—some are natural, and some are produced by humans. Some colloids are not harmful on their own, but in some circumstances, they carry harmful solutes that associate with them by electrical and other surface interactions. In addition, the movement of colloidal particles is important when they cause changes in the properties of the permeable media, which in turn influences fluid flow.

Although colloids can be important in diverse ways, in a water quality and flow context they are little recognized as important in groundwater beyond the small expert community engaged in their study. This lack of recognition is likely due to the exclusion of colloids from water quality sampling in the water filtering process; so, their harmful effects are difficult to discern. I expect that colloids in groundwater will soon be recognized as a substantial threat to human health. The groundwater science community needs to bring this to attention. This book is a starting point for becoming informed about colloids in groundwater.

The co-authors of this book are well established as pioneers in the field of groundwater colloids based on their research that ranges from laboratory experiments to field studies and modeling: Bill Johnson, a professor of earth sciences at the University of Utah, and Eddy Pazmiño, an assistant professor at Escuela Politécnica Nacional in Quito, Pichincha, Ecuador. Although this book serves as an introduction to the behavior of colloids in groundwater, the authors are rigorous in presenting explanations based on physics and chemistry—at times, beyond what most readers will have sufficient background to completely understand. However, for these readers, the story is also conveyed by many conceptual figures and inserted videos. Moreover, Parti-Suite freeware is provided for readers so they can undertake simulations that will clarify their understanding of the processes discussed by the authors.

John Cherry, The Groundwater Project Leader

Guelph, Ontario, Canada, August, 2023

Preface

The field-scale transport and spatial distribution of colloids (e.g., pathogens, clays, nanomaterials, nanoplastics, microplastics) in groundwater is impacted by nanoscale interactions with surfaces and pore-scale forces such as fluid drag, diffusion, and gravity. In this text, we provide basic and advanced information about these interactions and forces and how they can be addressed and simulated at nano- to field-scales. Exercises that use numerical modeling freeware are incorporated to allow those new to the field as well as advanced researchers to explore the concepts presented herein.

Acknowledgments

We deeply appreciate the thorough and useful reviews of and contributions to this book by the following individuals:

❖ Dr. Diogo Bolster of the Department of Civil and Environmental Engineering and Earth Sciences at the University of Notre Dame, South Bend, Indiana, USA, who was superbly kind and rigorous in his input, which greatly improved our presentation. His doctoral candidate Sabrina Volponi improved the clarity of our text by identifying several areas needing clearer explanation for readers who are relatively early in their exploration of the subject.

❖ Dr. Veronica Morales of the Department of Civil and Environmental Engineering at the University of California, Davis, California, USA, who clearly understood our intent and suggested additions that greatly improved how we approached the subject.

❖ Dr. Xitiong Liu of the School of Engineering and Applied Sciences, George Washington University, Washington, DC, USA, who corrected important problems in equations and figures, thereby improving their accuracy and clarity.

❖ Connie Bryson, Science Editor, The Groundwater Project, Ontario, Canada.

1   Scope of this Book

This book is meant to serve as an introduction to colloids in groundwater, focusing on their transport, since their transport largely governs their significance in groundwater. In writing this text, we also aspire to provide a resource for colloid transport researchers and practitioners to explore the concepts we describe using computational freeware (Parti-Suite website↗) that is introduced in videos linked throughout this text (e.g., Figure 1).
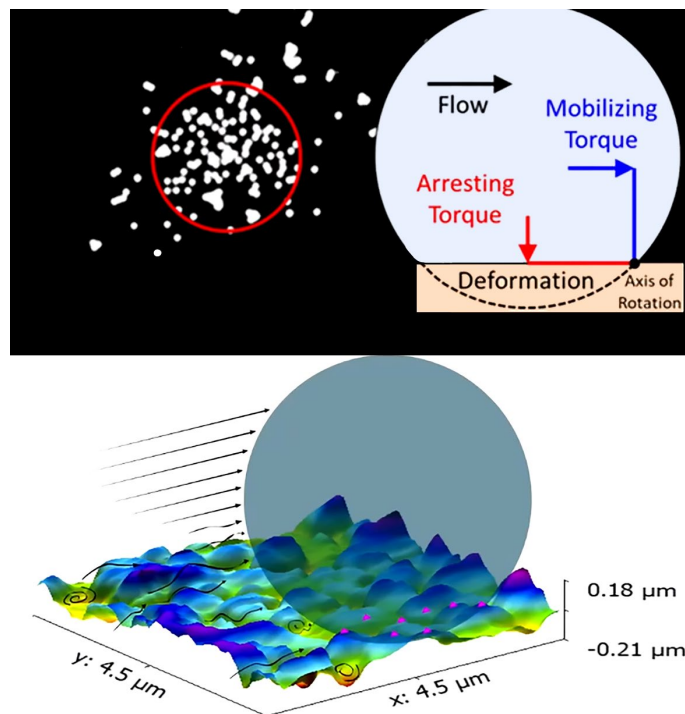
Figure 1 – An introduction to Parti-Suite freeware is provided in a video that can be watched by clicking on the white arrow in the middle of the figure and the subsequent video symbol "▶", or clicking here YouTube▶.

Section 8 includes nine sets of exercises and their solutions, that are linked to their corresponding figures. For example, Exercise 1 corresponds with Figure 1. After viewing the video by clicking on the white arrow in the figure, then on "▶" in the next screen that appears, the reader can go directly to the exercise in Section 8. Alternatively, readers can link to the exercise from the body of the text as shown here for Exercise 1↓. A link to the solution for each exercise is provided at the end of the exercise. The solutions are presented in Section 11. Links at the end of each solution provide access back to the exercise and back to the location in the text where the exercise is first mentioned.

1.1 The Need for Multiple Scales

The transport of colloids in the field is influenced by processes operating not only at field scale but also by smaller pore-scale processes—particularly by processes operating

1

at the nanoscale between colloids and grain surfaces (Figure 2). Our primary goals in writing this textbook are to

1. give readers a coherent understanding of the processes operating at each of these scales and
2. delineate our current capacity to predict corresponding colloid transport behaviors.

As explained in more detail in Section 6, colloid transport in granular porous media at the laboratory to field *continuum scale* (Figure 2d)—was originally expected to show compounded loss among the colloid population for each grain passed. This leads to a relatively predictable reduction in the population as a function of distance transported.
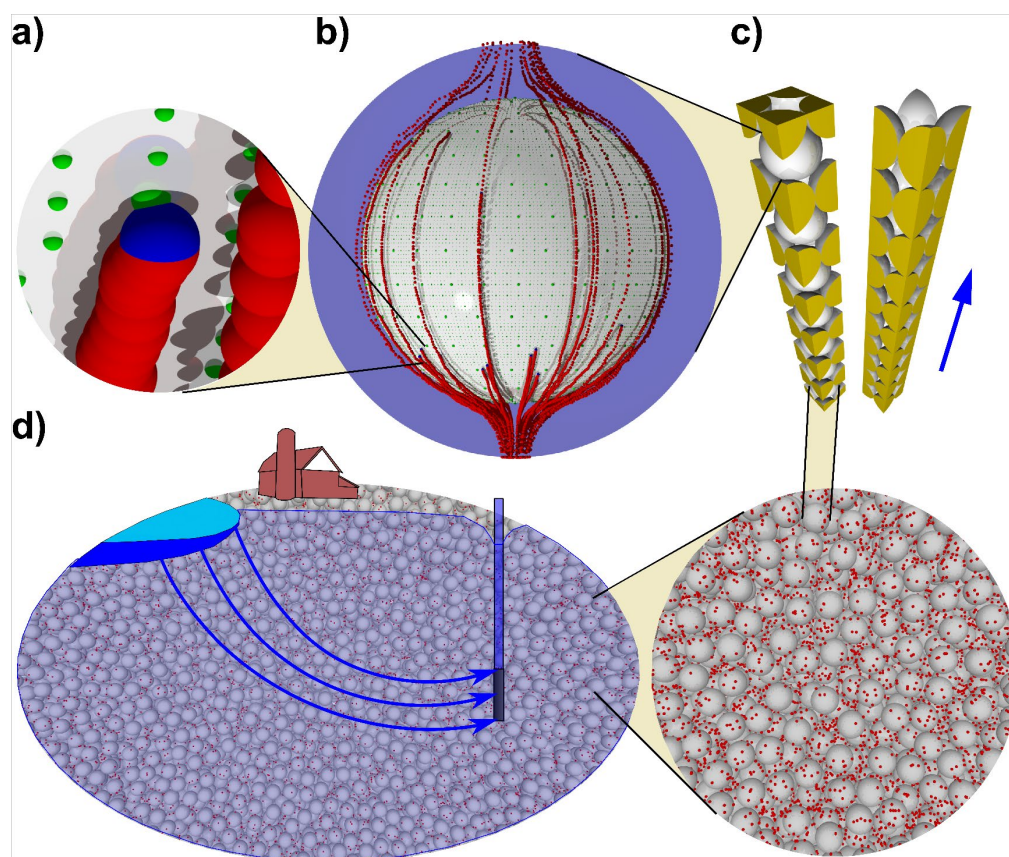
Figure 2 - Schematic of the range of scales involved in colloid transport in groundwater. Scales range from a) nanoscale where colloids (transitioning from red for mobile to blue for attached) interact with charged heterogeneities (green) on grain surfaces (white), as simulated at b) the pore scale in representative collectors (grain plus fluid shell) that in series represent c) a granular media. The transport characteristics determined via simulation in representative collectors are upscaled to continuum-scale rate coefficients to represent d) transport in granular media at the laboratory column and field scales.

This expectation turns out to be met only under a certain condition, which is that colloids and surfaces carry opposite charge (e.g., grain surfaces negative, colloid surfaces positive). Predicting the loss per grain passed requires understanding of the underlying processes and mechanisms operating at the pore scale (Figure 2c) including colloid

2

filtration theory (Figure 2b), which arose from leveraged pore-scale experiments and numerical simulations as described in Section 5.

Unfortunately, in the environment, both surfaces tend to be negatively charged as explained in Section 6. As such, environmental colloid transport typically defies original expectations and confounds simple prediction. Accordingly, development of useful predictive capability under environmental conditions has required us to further our understanding of nanoscale interactions between colloids and surfaces arising from surface charge as well as other colloid and surface properties (Figure 2a). This is described in Section 4. For example, improved transport prediction under environmental conditions has required us to understand how these nanoscale interactions impact pore-scale transport as described in Section 5. It has also required us to understand how impacts on pore-scale transport propagate to continuum-scale outcomes as described in Section 6.

Sections 2 and 3 provide conceptual introductions to colloids, scale, and forces/energies. These sections are included to help the reader who is new to these concepts. In contrast, Sections 4 through 6 provide formidably dense information regarding processes and mechanisms operating at the nano-, pore-, and continuum scales. Sections 4 to 6 are designed to be useful to both beginners and experts. They are not solely introductory. It is our sincere hope that beginners will become experts through their study of these sections, associated videos, software, and many of the cited references.

1.2 Knowledge and Misperceptions

The complexity of colloid transport research has allowed misperceptions to accumulate in the research literature. For example, inferences made but unproven in preceding publications are occasionally invoked as fact in subsequent reports even when such inferences were proven incorrect in the meantime.

One of the goals of this textbook is to correct ongoing misperceptions about mechanisms governing colloid transport, attachment, and retention. We realize that by assuming this responsibility we risk arrogance, and so we invite readers to challenge any mistakes we may have inadvertently made in order to improve the science of colloid transport in groundwater.

1.3 Our Approach

We should emphasize that this textbook is not intended to be a comprehensive review of contributions to the literature; rather, it is a straightforward summary of our current knowledge of colloid transport in groundwater. As such, we rely primarily on readily-accessible citations to support our statements on the topics covered; some of these were produced by us and our associates. The citations are neither exhaustive nor intended to indicate a primary or seminal contribution. We offer our sincere apologies to the

hundreds of authors whose work would do just as well to substantiate the statements made in this text but were not utilized due concerns for space and readability.

Similarly, the various expressions we provide in subsequent sections to explain the mechanisms operating at nano-, pore, and continuum scales are not intended to reflect all options. Instead, we present them to show what is currently implemented in freeware (i.e., software that is free to use while remaining proprietary and closed source) available to describe and predict colloid transport. Parti-Suite is an example of such freeware.

1.4 Our Objectives for this Book

We intend this text to serve as an introduction to and guide for interested persons from readers new to colloid transport to advanced researchers exploring the genuinely fascinating and complex subject of colloid transport in groundwater. We strove to make each section of the text, and Parti-Suite freeware, independent such that readers can focus attention on whatever scale (nano, pore, or continuum scale) is of most interest at any given time.

We realize that this book might deter new readers of this subject due to the long lists of references and many equations with many parameters. We request new readers to ignore the references and the equations and focus solely on the text, figures, videos, and exercises to allow absorption of concepts. Intermediate and expert readers can explore the references and equations to whatever extent their interest warrants. We apologize to beginners for cluttering their view with extensive references and equations, but as these readers advance, we expect it will be advantageous to have the literature and mathematical/modeling resources available within their conceptual context.

We emphasize that we want to help readers grow the number of modules and videos to address new capabilities and contexts with the intent of producing a community-based freeware resource for the science of colloid transport in groundwater.

2 Introduction to Groundwater Colloids

2.1 Colloids Defined (The What)

As formally defined by the International Union of Pure and Applied Chemistry (IUPAC), colloids are molecules or polymolecular particles dispersed in a medium and having—in one direction at least—a dimension roughly between 1 nm and 1 μm (McNaught & Wilkinson, 1997; Ritschel et al., 2021). We extend this definition to include suspended microparticles with dimensions up to 10 or so μm (e.g., protozoa, micro-activated carbon); otherwise, an important contingent of suspended colloids in groundwater would not be addressed, and the range of behaviors that emerge as a function of colloid size would be incompletely described.

2.2 Colloid Significance (The Why and Where)

Colloids in groundwater can be contaminants themselves (Figure 3) that drive, for example, pathogen exposure (e.g., pathogenic proteins, viruses, bacteria, and protozoa) in private drinking water wells (Borchardt et al., 2003; Conboy & Goss, 2000; Embrey & Runkle, 2006; Kelly et al., 2009; Lindsey et al., 2002; Swistock et al., 2013; Wallender et al., 2013) and public water supplies (Bradbury et al., 2013; Hrudey & Hrudey, 2004; O'Connor, 2002; Worthington & Smart, 2017).
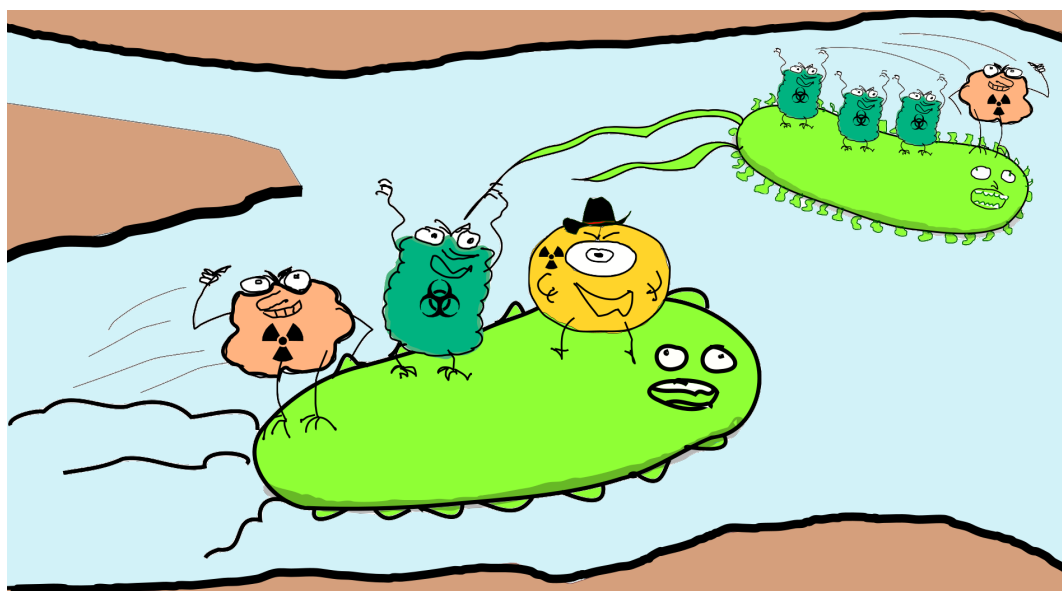
Figure 3 - Schematic of facilitated transport of hazardous solutes via solute-colloid association (heavily inspired by McCarthy & Zachara, 1989).

Colloids can also act as carriers of contaminants and nutrients. Colloidal organic matter, clays, or nano- and micro-plastics sorb contaminants and facilitate their transport, as reported for radionuclide contaminants and hydrophobic organic contaminants (Kersting et al., 1999; McCarthy & Zachara, 1989; Ryan et al., 1998; Saiers & Hornberger,

1996; Johnson & Amy, 1995; MacKay & Gschwend, 2001). As carriers of nutrients (Yang et al., 2021) and precious metals such as gold (Johnson et al., 2020a), they may serve as groundwater remediation agents such as nano zero-valent iron (Bianco et al., 2017; Busch et al., 2015) or activated carbon and black carbon (Gomez-Eyles et al., 2013; Jahan et al., 2019; Rakowska et al., 2012; Yang et al., 2020; Yang et al., 2019).

Colloids also act as clogging agents (e.g., mobilized clays and other fines), for example, during oil recovery (Yang et al., 2016). As such, the subsurface depths across which colloids are of interest range from kilometers (e.g., enhanced oil recovery) to the hyporheic zone immediately below and adjacent to rivers and streams (Johnson et al., 2020b; Packman & MacKay, 2003).

2.3 Colloid Transport (The How…and the Rest of this Book)

This text focuses on the mechanisms underlying colloid transport and colloid interaction with surfaces in groundwater across nano-, pore-, and continuum (laboratory and field) scales. An aspect of colloid transport we will not explicitly address is their interaction with other colloids of the same type (homo-aggregation) or different types (hetero-aggregation). While this text does not directly address colloid aggregation, the description we provide regarding mechanisms of interaction with, and attachment to, granular surfaces will help the reader understand the mechanisms underlying colloid aggregation.

3 Sizes, Scales, Forces, and Energies

3.1 Sizes and Scales

A primary governor of colloid transport in groundwater is colloid size, thus it is useful to review the scales involved in the range between granular media grains, colloids, and solutes. We define solutes as having sizes < 1 nm following the IUPAC definition (McNaught & Wilkinson, 1997; Ritschel et al., 2021). Notably, in field groundwater sampling, the distinction between *dissolved* and *particulate* is operationally defined according to the cut-off size of the filter used for separation, which is typically either 450 nm or 220 nm (Johnson et al., 2020b). This operational separation classifies nano-colloids in the range between 1 nm and several hundred nm as dissolved. We aim for this text to help the reader understand the significance of this operational lumping of nanoparticles and solutes in the size range below 450 nm, at least in so far as it impacts anticipated transport of entities in that size range in groundwater.

The range of sizes from solutes to the largest colloids (micro-particles) is vast (Figure 4), spanning approximately five orders of magnitude from 0.1 nm for the smallest molecules to 10 or so *μ*m for the largest colloids. Our text explains the significance of this range for the contrasting transport behaviors of solutes relative to colloids, as well as to nano- versus micro-particles.
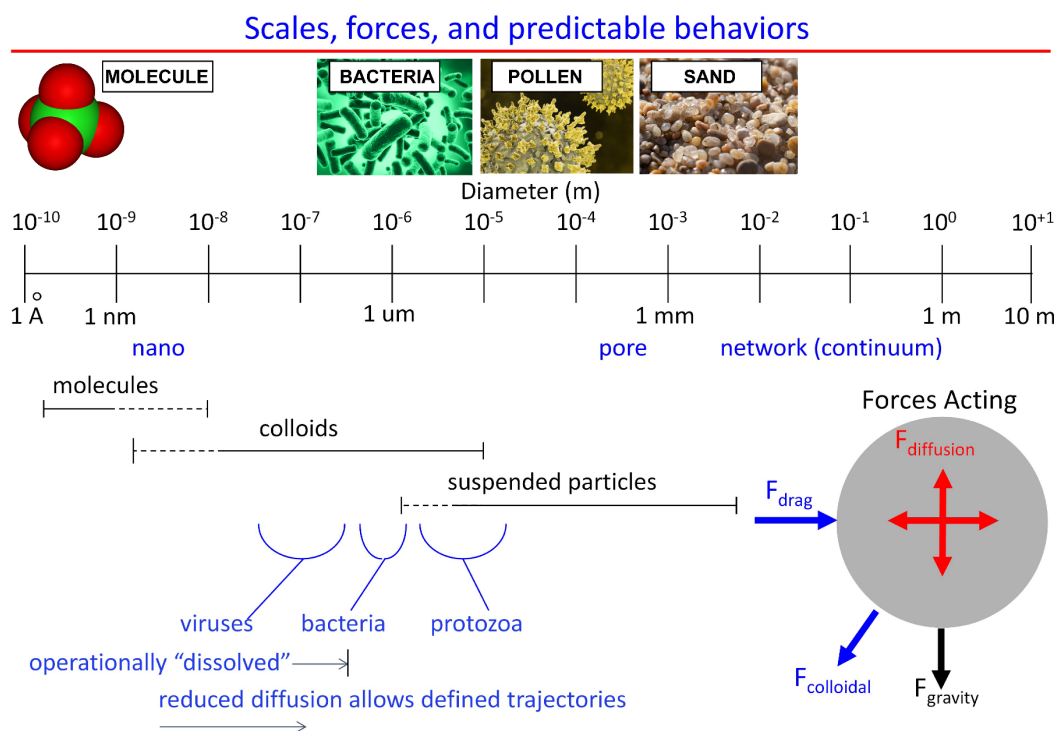
Figure 4 - Colloidal particle size range encompasses many orders of magnitude. Particle size has a great influence on the forces acting on the particle. Smaller colloids tend to behave as molecules (with increased diffusion) while larger ones tend to settle. Both processes are less influential on intermediate-size colloids, which are generally the most mobile.

To put this within a readily accessible human perspective, this span across solute to colloid sizes is comparable to that between a fine sand grain (0.1 mm) and massive boulder (10 m) (Figure 4), where one can easily anticipate a vast range of transport behaviors due to gravitational effects alone. As discussed in the subsequent text, other forces in addition to gravity such as diffusion and colloid-surface interaction further distinguish transport behavior across the range from the smallest solutes to the largest colloids.

At the smallest scale, colloid-surface interactions operate across approximately three orders of magnitude in scale (Figure 4), from atomic 0.1 nm (angstrom) to approximately 100 nm for the longest-range colloid–surface interactions—van der Waals. These nanoscale colloid-surface interactions act along with other forces such as fluid drag (advection) and other hydrodynamic interactions, as well as diffusion and gravitational settling that act at the pore-scale across sizes of approximately 100 μm to 100 mm (another three order-of-magnitude span; Figure 4). Both nano- and pore-scale processes impact transport behaviors observed across multiple pores (a pore network) at what we refer to as the continuum scale. Herein the continuum scale ranges from approximately 100 mm to 100 m or larger (another three order-of-magnitude span; Figure 4). At the continuum scale the impacts of fluid mixing and physical heterogeneity are superimposed onto smaller scale interactions to produce macroscale dispersion.

Given this nine-order-of-magnitude span from nano to field scale, we organized this text according to nano-, pore-, and continuum-scale observations, processes, and mechanisms. Furthermore, given the profound influence on colloid transport of repulsion between colloids and grain surfaces, each of these sections is sub-organized according to the absence versus presence of a repulsive barrier in the colloid-surface interaction profile.

3.2 Forces and Energies

Before discussing nanoscale interactions, we review the distinction between forces and energies, since colloid-surface and associated interactions are often cast in either form. In simulating colloid transport at the pore scale, we typically utilize a force (F) and torque (T) balance according to Newton's 2nd Law where $F = ma$, and where m is the colloid mass, a is its acceleration, and $T = Fl$, where l is a lever arm. Whereas forces and torques impact colloids both in fluid and in contact with surfaces, force balance predominantly governs colloid transport in fluid (Section 5.2.1). In contrast, a torque balance predominantly governs colloid mobilization versus arrest once in contact with a surface (Section 5.2.2).

A simple example of force balance may consider an airborne particle released at a given height on a wind-free day (Figure 5). As the particle begins to fall downward, the gravitational force will accelerate the particle from an initial particle velocity of zero ($u = 0$) to some maximum value of (u = terminal velocity). There will be no further acceleration at terminal velocity ($du/dt = 0$) because the gravitational force will be balanced by the frictional

force of air (with its viscosity) against the surface of the falling particle as shown in Equation (1) and Figure 5.

$$\frac{du}{dt} = mg - 6\pi\mu a_p u \tag{1}$$

where:

u = terminal velocity (LT^{-1})

t = time (T)

m = mass (M)

g = acceleration of gravity (LT^{-2})

μ = viscosity (ML^{-1}T^{-1})

a_p = particle radius (L)
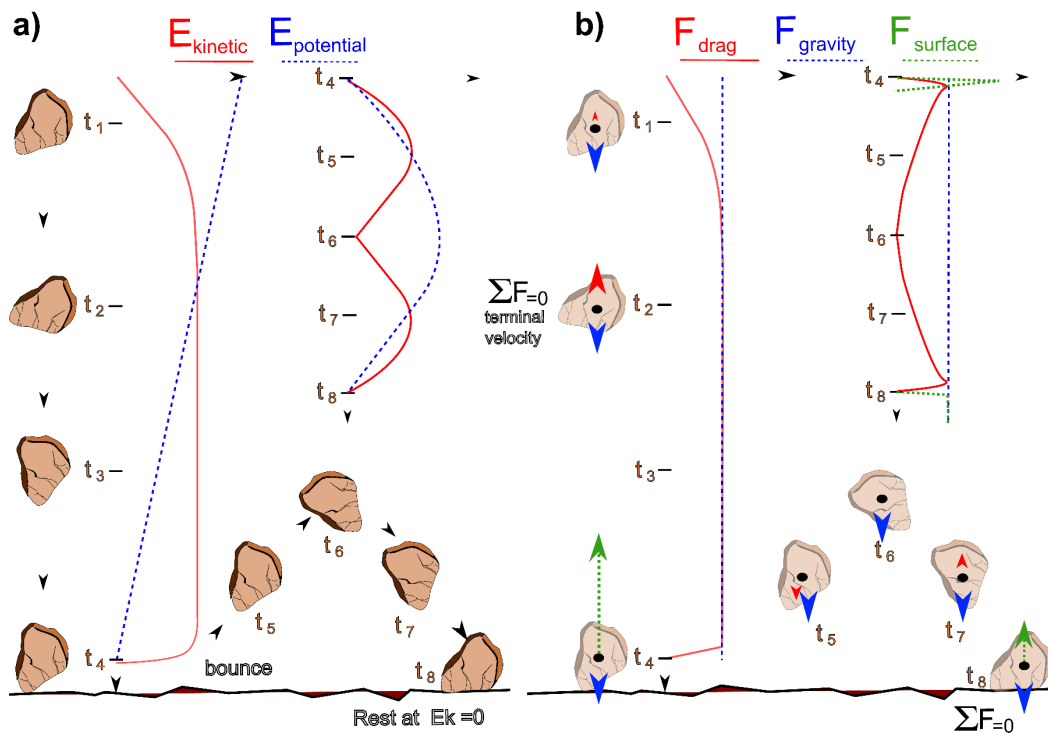
Figure 5 - a) Potential and kinetic energy of a falling particle. b) Forces acting on falling particle. At time t_1, the particle starts to fall in response to gravity with potential energy below its starting value and relatively small kinetic energy corresponding to relatively low velocity. Friction with air yields a drag force that opposes motion. As the particle accelerates, potential energy is converted to kinetic energy, and the drag force increases with velocity. Maximum (terminal) velocity is reached once the drag force equals the gravitational force ($t \geq t_2$) m after which its kinetic energy remains constant and the drag force equals the gravitational force. At impact ($t = t_4$), potential energy is minimum (local reference level) and kinetic energy is transferred to the surface. The surface force (a combination of elastic and action-reaction forces) lifts the particle, converting kinetic to potential energy, and the drag force opposes upward motion ($t - t_5$). Once lift and drag forces equal zero ($t = t_6$), the overall process repeats until the particle comes to rest in a stable equilibrium (t_8) with net force zero and overall energy minimized.

Re-arranging the Equation (1) with $du/dt = 0$ and solving for u yields the terminal velocity as expressed in Equation (2).

$$u = \frac{mg}{6\pi\mu a_p} \tag{2}$$

In Equation (2), the terminal velocity (u) increases with particle mass and decreases with increasing particle radius for a given mass (decreased particle density). Eventually the particle will strike ground surface at terminal velocity, meeting an equal and opposite force (neglecting elastic and plastic deformation of the particle and ground surface) as well as equal and opposite torque produced by offset of the particle center of mass relative to the initial point of contact. Elastic deformation and torque in turn produce upward forces (lift) that drive particle rebound from the surface to a point where upward forces balance the downward gravitational force; the above force balance progression is repeated until the particle comes to rest (Figure 5).

Section 5 demonstrates integration of the forces and torques acting on colloids during transport in groundwater to calculate their trajectories (movement across space and time). Ultimately, this is used to estimate their transport distance prior to attachment to a grain surface, as well as their concentration in groundwater at a given distance from their source (Section 6).

We now discuss energy balance in contrast to force balance since, for example, colloid–surface interactions (Section 4) are often cast both as forces and energies. The falling particle trajectory analysis described earlier can also be expressed as an energy balance, where potential energy (corresponding to an initial height of release) is converted to kinetic energy as the particle loses height (starting from height H) and gains speed (increased u). The kinetic energy ($1/2\ mu^2$, with dimension ML^2T^{-2}) reaches a maximum value when the terminal velocity is reached (Figure 5); however, the particle will fall until it strikes ground (or another surface), at which time its bounce upward will temporarily convert kinetic energy back to potential energy, followed by the opposite, and this will repeat until the rock comes to rest. This entire process can be repeated if the work is done (energy expended) to raise the rock back to its original height H, with stored potential energy being the distance (height) across which the gravitational force was opposed (mgH, with units ML^2T^{-2}; Figure 5).

4 Nanoscale Interactions

Colloid transport science sits at the intersection of physics and chemistry as applied to colloid transport and interaction with surfaces in groundwater. Nanoscale interactions also include solute association with colloid surfaces (sorption), and so we briefly mention these interactions in Section 4.1 before addressing colloid interaction with grain surfaces in Section 4.2.

4.1 Nanoscale: Solute Interaction with Colloids

Sorption of solutes to colloid surfaces can alter the surface properties of colloids, therefore their interaction with grain surfaces and, by extension, their transport. These interactions can alter the transport of both the sorbing solute and the colloid (Figure 6). Some of these interactions are mentioned briefly here and their impacts on colloid and solute transport are discussed in the continuum-scale section (Section 6).
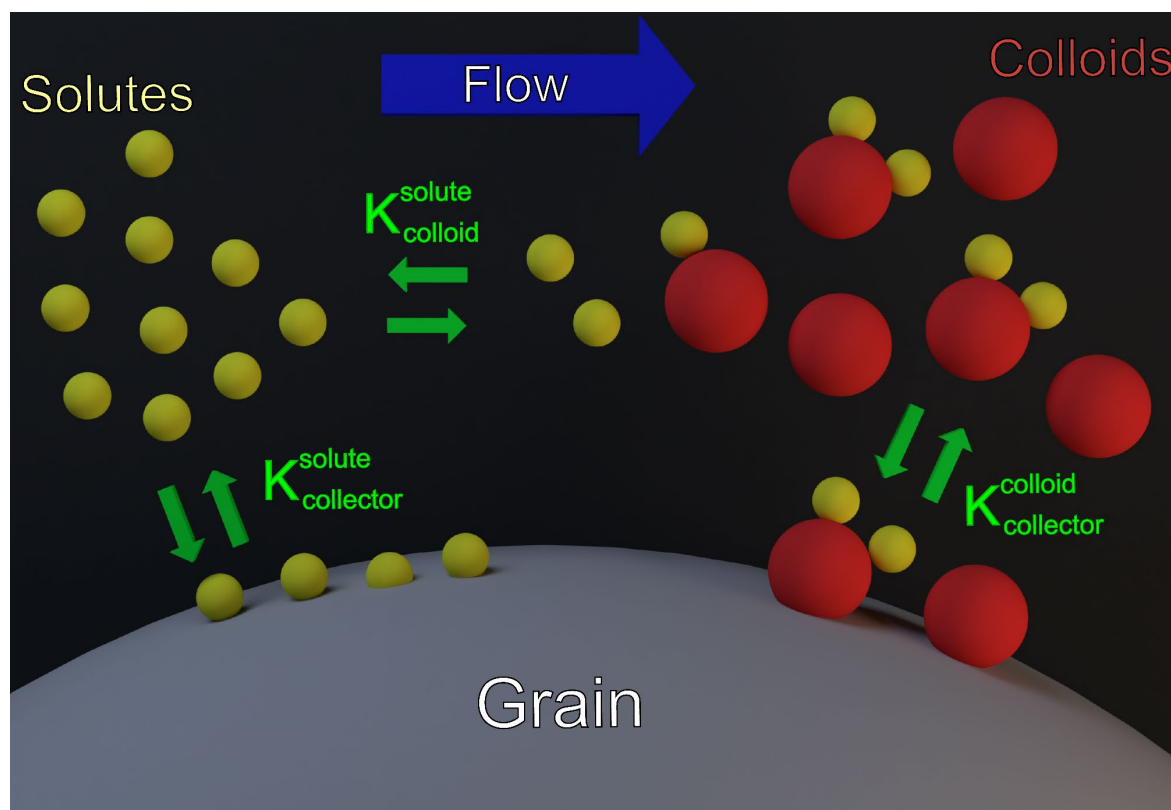
Figure 6 - Multiple interactions between dissolved solutes and suspended colloids, and each of them with grain surfaces. Constants for equilibrium partitioning of solutes and colloids with the grain surface and with each other are denoted with K_j^i where i and j are the interacting moieties.

Solute sorption to colloids may occur by multiple mechanisms depending on the nature of the solute and colloid. Some sorption processes yield a linear (or near-linear) relationship between the aqueous and sorbed solute concentrations. An example process involving linear sorption (or approximately linear sorption) is the partitioning of

11

hydrophobic solutes (such as polycyclic aromatic hydrocarbons) to natural organic matter (Chiou et al., 1986).

In contrast, other sorption processes yield strongly non-linear relationships between sorbed and aqueous concentrations. An example of non-linear sorption is ionic exchange where, for example, multiple cations (e.g., Na^+ and Ca^+) may compete for a limited number of sites to shield the negative charge on a surface such that the sorbed concentration reaches an asymptote as the dissolved solute concentration increases (Ashraf et al., 2014; Saiers & Hornberger, 1996). Dissolved organic matter (DOM) can undergo sorption to surfaces via a process called ligand exchange. This DOM sorption on clays and other mineral colloids typically imparts or increases negative charge on the surfaces of these colloids (Cheng & Saiers, 2015; Davis, 1982; Jardine et al., 1989; Johnson & Logan, 1996; Tipping & Cooke, 1982). The impact of increasing negative charge on surfaces is discussed in the subsequent section; however, in groundwater it typically increases the transport of colloids.

4.2　Nanoscale Colloid Interactions with Surfaces

The interactions of colloids (and solutes) with surfaces are well described in the famous text by Israelachvili (2011), which provides a more in-depth description of the mechanisms and processes. Critical aspects of these interactions as they relate to colloid transport in groundwater and their implementation in Parti-Suite freeware are briefly reviewed in Section 4.2.1.

The primary interactions between colloids and surfaces, in order of longest to shortest range, are van der Waals (VDW), electric double layer (EDL), and Born, which extend to colloid-surface separation distances up to approximately 200 nm, 50 nm, and 0.167 nm, respectively (Figure 7). These distances are approximate since solution and surface chemistries impact the distance over which the interactions occur, as will be described subsequently. DLVO theory (Derjaguin & Landau, 1941; Verwey & Overbeek, 1947)—named for the surnames of the four physicists by whom it was developed—superimposes VDW, EDL, and Born interactions to produce the profile of combined interactions as a function of separation distance between colloids and surfaces (Figure 7).
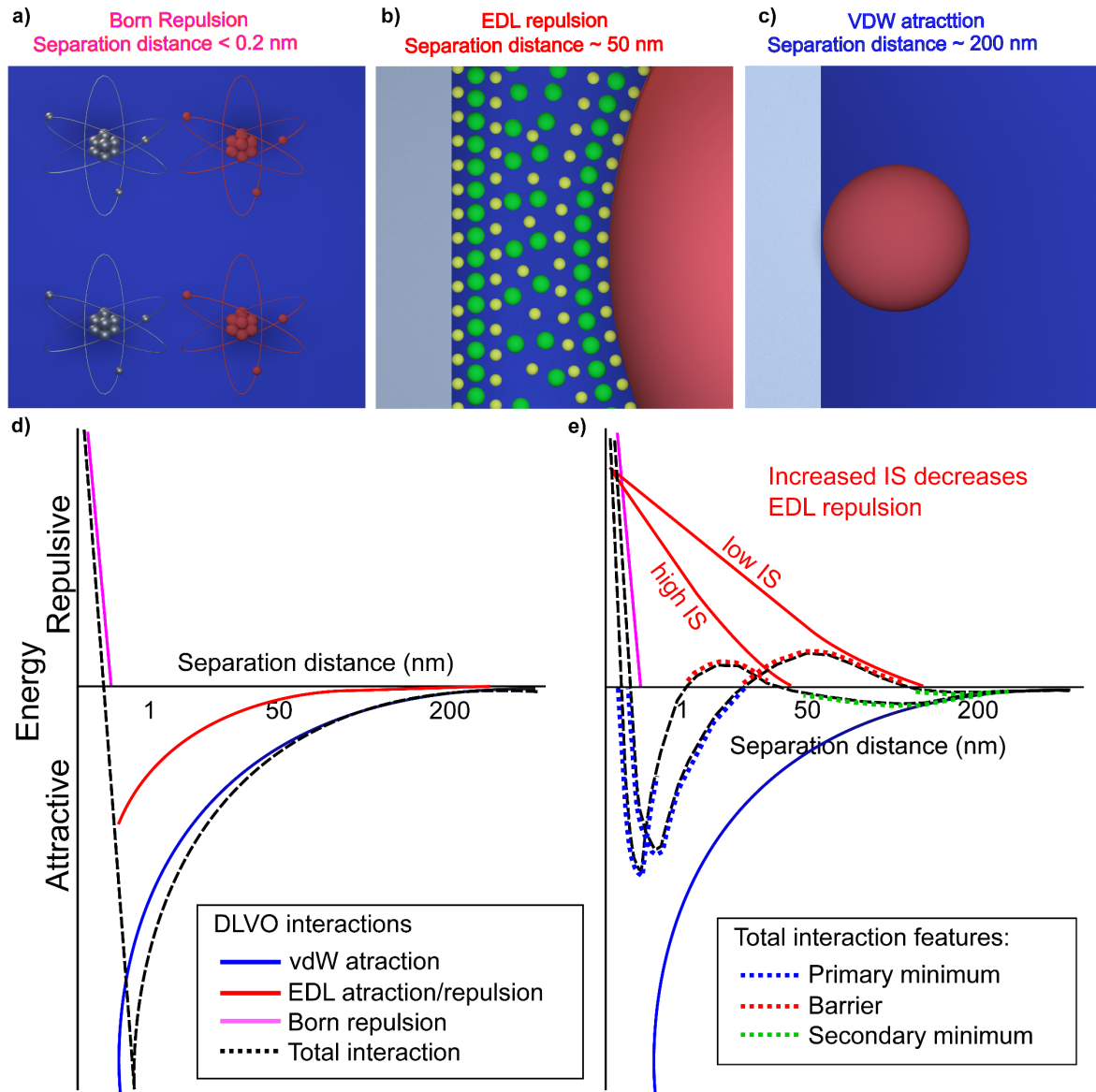
Figure 7 - Colloid-surface (DLVO) interactions. Schematized Born, EDL, and VDW interactions between colloid (red) and grain (gray) surfaces (IS is ionic strength): a) electron orbital overlap, b) counterion-counterion interaction, and c) instantaneous bond dipole interaction. Schematics are scaled according to maximum reach of the interaction. Graphs show DLVO interaction profiles arising from superposition of Born, EDL, and VDW, interactions: d) DLVO profile with attractive EDL interactions (from oppositely charged surfaces) show an attractive primary minimum and absence of a repulsive barrier, e) DLVO profiles show repulsive EDL interactions (from like-charged surfaces) with a relatively shallow primary minimum and a repulsive barrier. The depth of the primary minimum increases, and the height of the repulsive barrier decreases, with increased ionic strength.

VDW interactions originate from electrodynamic and dipole interactions across the two surfaces, which arise from instantaneous (for electrodynamic) or permanent (for dipole) skewing of electron clouds in the bonds between elements that constitute each surface (Israelachvili, 2011). EDL interactions originate from interactions among ions in solution between the two surfaces, the concentrations of which exceed their bulk concentration for *counterions* that shield (are opposite in charge to) the intrinsic charge on each surface. The intrinsic surface charge is therefore shielded by counterions to an extent directly dependent on *ionic strength* (IS).

The shielded surface charge is measured directly using techniques that examine the motion of colloids in response to an applied electric field (electrophoresis and related techniques), and is called the ζ-*potential* (zeta-potential), which has units of volts (V) as described in Section 4.2.4. The magnitude of the excess counterion concentration is proportional to the charge—that is, the ζ-potential—on each surface. The counterion concentrations associated with each surface decay exponentially with distance from the surface, according to the Poisson-Boltzmann distribution, over an effective distance characterized by the *Deby length* that depends inversely on solution IS.

The excess counterion concentrations associated with two like-charged surfaces (e.g., both negatively charged) set up repulsive electroosmotic (EDL) interactions between those counterions occupying the solution between the surfaces. These electroosmotic interactions are repulsive or attractive depending on whether the surfaces are like- versus opposite-charged, respectively. EDL interactions are defined by surfaces, as opposed to VDW interactions that penetrate some distance into the interiors of the interacting bodies.

Born interactions are the shortest range (and steepest) of the colloid–surface interactions since they represent physical contact (i.e., overlap of electron orbitals of elements across the surfaces in contact). Additional, more-recently characterized interactions such as Lewis acid-base (LAB) and steric/hydration interactions (to be described subsequently) extend over relatively short distances (several nm); they are included in so-called extended DLVO (xDLVO) theory (Israelachvili, 2011).

These nanoscale interactions are considered to act independently, and so are superimposed such that their different decay lengths (persistence as a function of colloid-surface separation) produces contrasting colloid-surface interaction profiles depending on whether surfaces are oppositely charged (Section 4.2.1) versus like-charged (Section 4.2.2). We describe how the relatively short decay lengths of colloid-surface interactions produce a finite zone across which colloids interact with grain surfaces (Section 4.2.3*)*. We provide a detailed description of the colloid–surface interactions for interested readers (Section 4.2.4).

4.2.1 Nanoscale Colloid-Surface Interaction Under Favorable Conditions

Under conditions where the colloid and grain surfaces are oppositely charged—so-called favorable attachment conditions—the profile of superimposed interactions (VDW, EDL, Born) produce what is referred to as a primary minimum (Figure 7) where attractive VDW and EDL interactions increase with decreasing separation distance until Born repulsion dictates an equilibrium separation distance of approximately 0.16 nm$W$ (in a vacuum, neglecting hydration and other steric interactions). At this separation distance, the stiff increase in Born repulsion defines a finite magnitude (depth) of attractive interactions (Figure 7). It is worthwhile to emphasize that while we colloquially refer to the colloid as being *in* the primary minimum, that terminology can be inadvertently misleading, since for a 1 μm colloid (for example), its "rear end" protrudes far beyond the primary minimum

into the bulk water and is subject to other forces such as fluid drag as described in the pore-scale interactions section (Section 5).

4.2.2 Nanoscale Colloid-Surface Interaction Under Unfavorable Conditions

Under conditions where the colloid and grain surfaces are like-charged (both positive or both negative; so-called unfavorable attachment conditions), the profile of superimposed interactions (VDW, EDL, Born) produces a repulsive barrier between the primary minimum and another weakly attractive zone referred to as a secondary minimum at separation distances beyond the repulsive barrier (Figure 7). Depths of primary and secondary minima and heights of repulsive barriers are governed by the surface properties in the expressions for VDW and EDL interactions (Section 4.2.4). Among them, the colloid and grain ζ-potentials play critical roles; their magnitudes are governed by intrinsic properties of the surfaces as well as solution pH and IS (Israelachvili, 2011).

For silicate minerals, which are intrinsically negatively charged in the range of groundwater pH (Schwarzenbach et al., 1993; Trauscht et al., 2015), increasing pH increases the magnitude of negative charge on their surfaces. For a given pH, increasing IS decreases the magnitude of the charge due to shielding by counterions and consequent contraction of the EDL interactions. Hence, between negatively charged surfaces, the magnitude of the repulsive barrier decreases and the magnitude of the attractive secondary minimum increases as pH decreases and IS increases (Figure 7).

The relatively short distances across which steric and Lewis acid-base (LAB) interactions reach limit their impacts essentially to the depth of the primary minimum (Figure 8). As repulsive steric or LAB interactions increase, the equilibrium separation distance increases and the magnitude of the attractive primary minimum decreases, thereby reducing the adhesion force holding the colloid in contact with the surface.
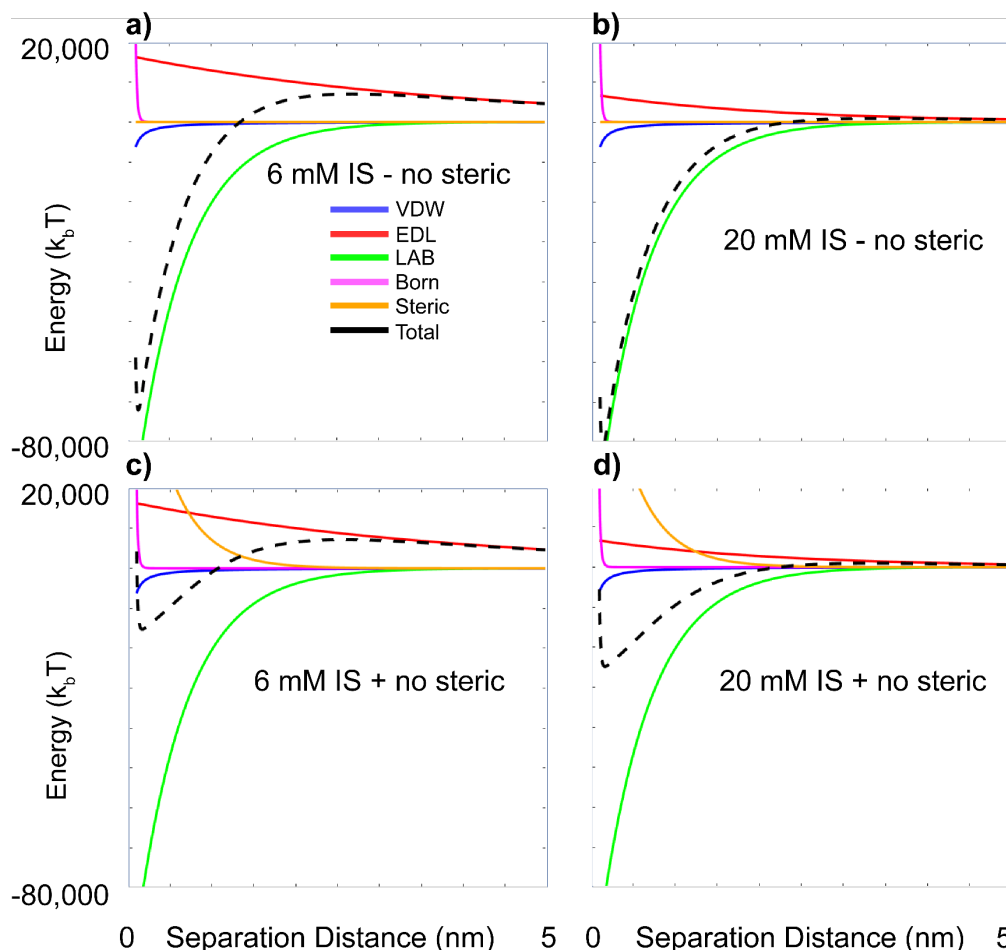
Figure 8 - Influence of xDLVO interactions in the primary energy minima: a) and b) show negligible fluence of IS increase in the primary minima depth, c) and d) show the effect of steric interactions. Energy minima depth is reduced by a factor of approximately 4 due to the increased repulsion. The IS influence is more noticeable. In all cases Lewis AB interactions are the most important contributions to the minima depth. For this reason, there is not a clear shift of the primary minimum location in response to steric repulsion.

4.2.3 Zone of Colloid-Surface Interaction (ZOI)

Because the distances over which xDLVO interactions act are relatively short (< 200 nm) and the separation distances increase away from the point of closest colloid-surface separation due to curvature of the surfaces, xDLVO interactions act over a finite zone of interaction (ZOI). The radii of the ZOI for EDL and LAB interactions are determined accordingly (Bendersky & Davis, 2011; Rasmuson et al., 2019a) as shown in Equations (3) and (4) and Figure 9.

$$a_{ZOI-EDL} = 2\sqrt{\kappa^{-1}a_p} \tag{3}$$

where:

κ = inverse Debye length (L^{-1})

a_p = colloid radius (L)

16

$$a_{ZOI-LAB} = 2\sqrt{\lambda_{AB} a_p} \qquad (4)$$

where:

λ_{AB} = Lewis acid-base decay distance (L)
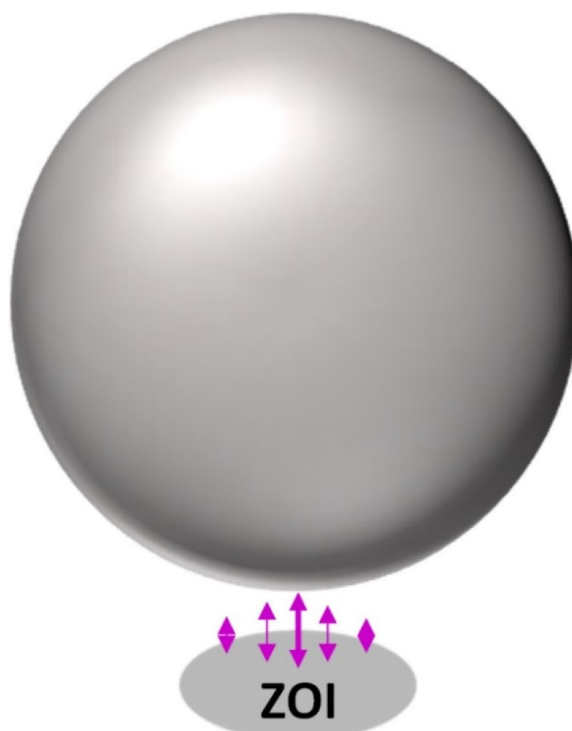
Figure 9 - Zone of colloid-surface interaction (ZOI) between a colloid (denoted by sphere) and an implied flat surface on which the ZOI (shaded circular area) is shown. xDLVO interactions are integrated across this zone. Only normal interactions are considered. The magnitudes of the interactions are denoted by the lengths of the magenta double-headed arrows, which are largest at the location of smallest separation distance between the surfaces.

This finite zone of interaction between colloids and surfaces is an important aspect of colloid-surface interactions under unfavorable conditions, where the ZOI may move (with the colloid) over a nanoscale zone of charge that is attractive to the colloid (*heterodomain*), thereby reducing repulsion or even flipping repulsion to attraction depending on the degree of overlap of the heterodomain with the ZOI (Pazmiño et al., 2014a; Ron and Johnson, 2020) as shown in Figure 10. Nanoscale charge heterogeneity may arise from ion substitution, impurities, defects, localized sorbates and precipitants, localized oxidation or reduction, and other variations in mineral and other surfaces. Because the ZOI decreases with decreasing colloid size, a given-sized heterodomain occupies an increasing fraction of the ZOI as colloid size decreases such that interactions with a given-sized heterodomain may be net repulsive for a larger colloid and net attractive for a smaller colloid (Figure 10). In other words, the heterogeneous grain surface that the

17

The GROUNDWATER PROJECT   ©The Author(s)   Free download from gw-project.org

Anyone may use and share gw-project.org links. Direct distribution of the book is strictly prohibited.

colloid "sees" depends on the size of the colloid. It also depends on solution IS, as described in Figure 10.
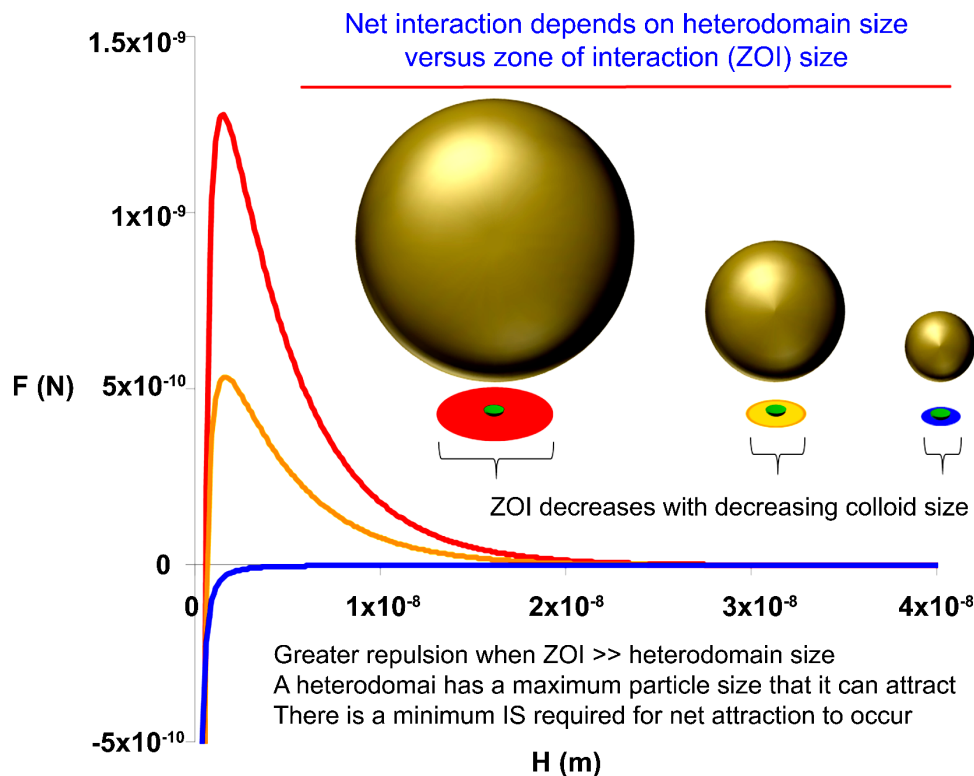
Figure 10 - Colloid-heterodomain interactions as a function of colloid size. Colloids are depicted as gold spheres interacting with an implied surface below the sphere across a zone of interaction (ZOI) depicted by red, yellow, and blue disks that, for a given solution ionic strength (IS), are proportional in size to the colloid. An area of charge heterogeneity on the surface is depicted as green disks. The greater the fraction of ZOI occupied by heterodomain, the lesser the repulsive barrier as depicted force profiles (F) versus colloid-surface separation distance (H) using colors (red, yellow, and blue) for the ZOI of the three colloid sizes. Positive values of F are repulsive, while negative values are attractive.

The radius of the ZOI (aZOI) expands and contracts with decreasing and increasing IS, respectively as discussed in Section 4.2.4.4; for a given sized colloid and heterodomain, the interaction may flip from net repulsive to net attractive as the ZOI contracts with increased IS (Figure 11). This expansion and contraction of ZOI has important implications for the impact of IS on colloid attachment and detachment under unfavorable conditions, as described in the pore-scale section of this book (Section 5). The impact of nanoscale heterogeneity (attractive heterodomains) is demonstrated in the xDLVO module of Parti-Suite, as described in the next section (Section 4.2.4).
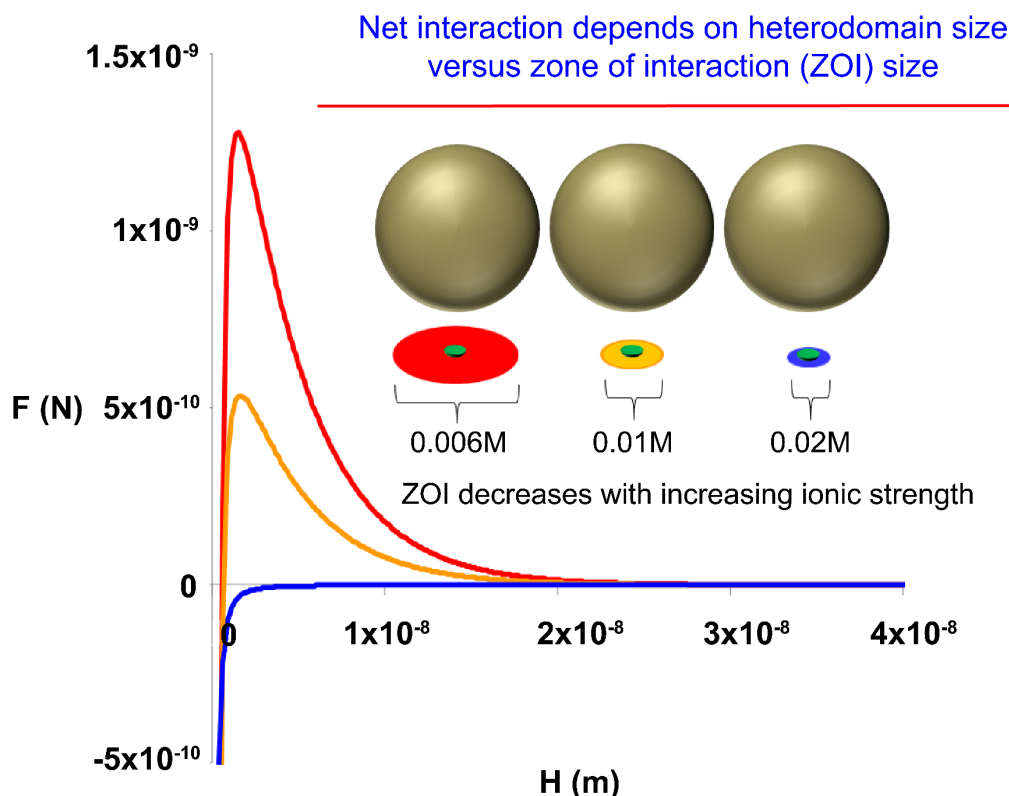
Figure 11 - Colloid–heterodomain interactions as a function of ionic strength. Colloids are depicted as gold spheres interacting with an underlying implied surface across a zone of interaction (ZOI) depicted by red, yellow, and blue disks. For a given size colloid ZOI is inversely proportional in size to solution ionic strength (IS). The area of charge heterogeneity on the surface is depicted as a green disk. The greater the fraction of ZOI occupied by heterodomain, the lesser the repulsive barrier as depicted by force profiles (F) versus colloid-surface separation distance (H) using colors (red, yellow, and blue) for the ZOI of the three colloid sizes. Positive values of F are repulsive, while negative values are attractive.

4.2.4 DLVO and xDLVO Interactions in Detail

For interested readers, we provide detailed descriptions of DLVO and xDLVO interactions in the forms in which they are incorporated into the xDLVO and trajectory modules of Parti-Suite. Subsequent sections describe VDW, EDL, Born, LAB, and steric interactions in detail. The impacts of nanoscale surface roughness on these interactions are outlined in an additional section (Section 4.2.4.6). The dimensions and specific values of the parameters used in these calculations are provided in the Parti-Suite freeware.

Calculation of the interactions requires an assumption about the geometry between colloids and surfaces in the vicinity of the interaction. This is called the *Derjaguin approximation* (Israelachvili, 2011). This approximation is applicable only when $H \ll a_p$. For example, calculated interactions beyond 200 nm separation distances violate the limit of the Derjaguin approximation for colloids with 200 nm radius. Colloid–surface interactions exist beyond the *Derjaguin limit*, but they are not accurately quantified by the Derjaguin approximation. Parti-Suite allows this Derjaguin limit to be violated for colloids < 200 nm radius; but adheres to the Derjaguin limit for rough surfaces such that their

interactions are not included when separation distance exceeds the asperity radius (Section 4.2.4.6).

4.2.4.1. Van der Waals (VDW) Interactions

VDW interactions originate from electrodynamic and permanent dipole interactions across the two surfaces. These interactions arise from instantaneous or permanent skewing of electron clouds (dipoles) in the bonds between elements that constitute each surface (Israelachvili, 2011). In groundwater, these interactions are mediated by the electrodynamic characteristics of the two surfaces (e.g., 1 and 2) interacting across water (3), such that the so-called combined Hamaker energy is denoted A_{132}. The xDLVO module in Parti-Suite implements the expression of Gregory (1981) to calculate the change in free energy (ΔG) and force of retarded *VDW* interactions for sphere–sphere geometry as shown in Equations (5), (6), and (7).

$$\Delta G_{VDW}(H) = \frac{A_{132} a_{eff}}{6H}\left[1 - \frac{5.32H}{\lambda_{VDW}} ln\left(1 + \frac{\lambda_{VDW}}{5.32H}\right)\right] \tag{5}$$

$$\overrightarrow{F_{VDW}}(H) = -\frac{A_{132} a_{eff}}{6H^2}\left(\frac{\lambda_{vdW}}{\lambda_{vdW} + 5.32H}\right) \tag{6}$$

where:

H = colloid–surface separation distance (L)

A_{132} = Hamaker constant (ML^{2}T^{-2})

λ_{vdW} = characteristic VDW wavelength (L)

a_{eff} = ratio of the product over the sum of the colloid (a_p) and grain (a_g) radii (L)

$$a_{eff} = \frac{a_p a_g}{a_p + a_g} \tag{7}$$

VDW interactions extend over distances of hundreds of nm and as such have the longest range among colloid–surface interactions. As shown in Equation (7), VDW interactions increase with colloid size.

The xDLVO module in Parti-Suite provides the option to calculate Hamaker constants for the individual phases from their permittivity values (ε) and refractive indices (n) (Israelachvili, 2011), as shown in Equations (8) and (9). The user may choose to use these values instead of the values from the expression of Gregory (1981).

$$A_{ij} = \sqrt{A_{ii}A_{jj}} \tag{8}$$

$$A_{ii} = \frac{3}{4}k_B T\left(\frac{\varepsilon_i - \varepsilon_{vacuum}}{\varepsilon_i + \varepsilon_{vacuum}}\right)^2 + \frac{3h\nu_e\left(n_i^2 - n_{vacuum}^2\right)^2}{16\sqrt{2}\left(n_i^2 + n_{vacuum}^2\right)^{3/2}} \tag{9}$$

where:

k_B = Boltzmann constant, typically J/K ($ML^2T^{-2}\Theta^{-1}$)

T = temperature (Θ)

ε = permittivity ($ML^{-3}T^4I^2$) where I is charge

h = Planck's constant (ML^2T^{-1})

ν_e = main electronic absorption frequency (T^{-1})

n = refractive index (dimensionless)

Parti-Suite also provides the option to calculate *VDW* interactions for layered systems such as core-shell colloids or coated grains. The specific expressions for coated (layered) surfaces are provided by Ron and others (2019b).

4.2.4.2 Electric Double Layer (EDL) Interactions

EDL interactions originate from electroosmotic interactions among ions in solution between two surfaces where excess concentrations of counterions shield the intrinsic charge on each surface. The magnitude of the excess counterion concentration is proportional to the charge on each surface. This charge is approximated by the experimentally measured ζ-potential (*V*) of each surface.

The counterion concentrations on each surface decay exponentially with distance from the surface according to the Poisson-Boltzmann distribution. This decay takes place over an effective distance characterized by a Debye length, which depends inversely on solution IS. EDL interactions are defined by surfaces, in contrast to VDW interactions that penetrate some distance into the interiors of the interacting bodies. The xDLVO module of Parti-Suite implements the expression of Lin and Wiesner (2012) for change in free energy and the force as shown in Equations (10), (11), (12), and (13).

$$\Delta G_{EDL}(H) = 64\pi\varepsilon a_{eff}\left(\frac{k_BT}{zq}\right)^2 \tanh\left(\frac{zq\zeta_1}{4k_BT}\right)\tanh\left(\frac{zq\zeta_2}{4k_BT}\right)e^{-\kappa H} \tag{10}$$

$$\overrightarrow{F_{EDL}}(H) = 64\pi\varepsilon\kappa a_{eff}\left(\frac{k_BT}{zq}\right)^2 \tanh\left(\frac{zq\varsigma_1}{4k_BT}\right)\tanh\left(\frac{zq\varsigma_2}{4k_BT}\right)e^{-\kappa H} \tag{11}$$

where:

ε = permittivity of water, typically in C^2/Jm ($I^2T^2M^{-1}L^{-3}$)

k_B = Boltzmann constant, typically in J/K ($ML^2T^{-2}\Theta^{-1}$)

T = temperature Θ

z = valence of the electrolyte (dimensionless)

q = elementary charge (I)

ζ_1 and ζ_2 = colloid and collector ζ-potential, respectively, typically in volts ($ML^2T^3I^{-1}$)

κ = inverse Debye length, typically in 1/m (L^{-1})

$$\kappa^{-1} = \sqrt{\frac{\varepsilon k_B T}{2N_A z^2 q^2 N_{IO}}} \tag{12}$$

where:

N_A = Avogadro's number = $6.02 \times 10^{+23}$/mol, a mole is a unit amount of substance containing Avogadro's number of elementary entities (e.g., electrons, atoms, molecules)

N_{IO} = solution ionic strength (IS), typically mol/m^3 (amount-of-substance L^{-3})

$$IS = \frac{1}{2}\sum z_i^2 c_i \tag{13}$$

where:

c_i = concentration of ion i in solution, typically in mol/m^3 (ML^{-3})

EDL interactions extend to intermediate separation distances (from several nm to several tens of nm) as moderated by solution IS and surface ζ-potentials. As shown in Equations (10) through (13), EDL interactions increase with colloid size or, more specifically, radius of curvature as shown in these equations. The radius of curvature becomes an important distinction from colloid size in the event that roughness (asperities of small radii of curvature) exists on the surface, as described further in Section 4.2.4.6.

4.2.4.3 Born Interactions

Born interactions are the shortest range (and steepest) of the colloid-surface interactions since they represent physical contact (overlap of electron orbitals of elements across the surfaces in contact). The expression for Born interaction (as energy and force) that is implemented in Parti-Suite was obtained from Ruckenstein and Prieve (1976) and is shown in Equations (14) and (15).

$$\Delta G_{Born}(H) = \frac{A_{132}\sigma_c^6}{7560}\left(\frac{6a_p - H}{H^7} + \frac{8a_p + H}{(2a_p + H)^7}\right) \tag{14}$$

$$\overrightarrow{F_{BORN}}(H) = \frac{A_{132}\sigma_c^6}{1260}\left(\frac{7a_p - H}{H^8} + \frac{9a_p + H}{(2a_p + H)^8}\right) \tag{15}$$

where:

σ_c = Born collision diameter in the range of 0.5 nm (Hahn et al., 2004), with the default value in the *xDLVO* module of Parti-Suite being 0.3 nm (L)

4.2.4.4 Lewis Acid-Base (LAB) Interactions

LAB interactions arise from electron donor and electron acceptor pair characteristics of the surfaces in contact (van Oss, 1994), and are significant up to several *nm* separation distance. LAB forces can be attractive or repulsive depending on the relative hydrophilic versus hydrophobic natures of the interacting surfaces. LAB forces are significant in systems with strong hydrogen bonding or where other polar interactions are present (common in biological and environmental systems; van Oss, 1994). The expressions for energy and the force of LAB interactions implemented in Parti-Suite were obtained from Wood and Rehmann (2014) as shown in Equations (16) and (17).

$$\Delta G_{AB}(H) = (Correction)\pi a_{eff}\lambda_{AB}\gamma_0^{AB}e^{-\left(\frac{H-h_0}{\lambda_{AB}}\right)} \tag{16}$$

$$\overrightarrow{F_{AB}}(H) = (Correction)\pi a_{eff}\gamma_o^{AB}e^{-\left(\frac{H-h_o}{\lambda_{AB}}\right)} \tag{17}$$

where:

λ_{AB} = LAB decay distance, typically in m (L)

h_0 = minimum separation distance in contact (L)

The minimum separation is generally set to 0.158 *nm* when contact is defined by Born interaction in a vacuum (Israelachvili, 2011) and the dimensionless geometric *correction* depends on the ratio of the colloid to grain radii within limits ranging from unity (sphere-sphere geometric correction, F_{SS}) to zero (sphere-plate geometric correction, F_{SP}) (Wood and Rehmann, 2014) as shown in Equations (18), (19), and (20).

$$(Correction) = \left(\frac{a_p}{a_g}\right)F_{SS} + \left(1 - \frac{a_p}{a_g}\right)F_{SP} \tag{18}$$

$$F_{SS} = 1 - \frac{\lambda_{AB}}{a_{eff}} + \frac{\lambda_{AB}^2}{2a_{eff}^2} - \frac{4a_{eff}}{3\lambda_{AB}}e^{-\left(\frac{2a_{eff}}{\lambda_{AB}}\right)} - \left(1 + \frac{\lambda_{AB}}{a_{eff}} + \frac{\lambda_{AB}^2}{2a_{eff}^2}\right)e^{-\left(\frac{4a_{eff}}{\lambda_{AB}}\right)} \tag{19}$$

$$F_{SP} = 1 - \frac{\lambda_{AB}}{a_{eff}} + (1 + \frac{\lambda_{AB}}{a_{eff}})e^{-\left(\frac{2a_{eff}}{\lambda_{AB}}\right)} \tag{20}$$

where:

γ_0^{AB} = LAB energy at minimum separation distance is calculated from (van Oss, 1994) as shown in Equation (21), typically in J (ML^2T^{-2})

$$\gamma_0^{AB} = 2\left[\sqrt{\gamma_3^+}\left(\sqrt{\gamma_1^-} + \sqrt{\gamma_2^-} - \sqrt{\gamma_3^-}\right) + \sqrt{\gamma_3^-}\left(\sqrt{\gamma_1^+} + \sqrt{\gamma_2^+} - \sqrt{\gamma_3^+}\right) - \sqrt{\gamma_1^+\gamma_2^-} - \sqrt{\gamma_1^-\gamma_2^+}\right] \tag{21}$$

Here, the surface energies have superscripts +/- that indicate electron acceptor/donor properties, and subscripts 1, 2, and 3 that indicate the colloid, grain, and fluid, respectively. The values for the polystyrene latex-silica-water system are provided as defaults in Parti-Suite.

4.2.4.5 Steric/Hydration Repulsion

Hydration repulsion interactions refer to steric repulsion arising from the Hydrogen-bonded structure of water molecules hydrating the respective surfaces. Because ions are also hydrated by water molecules, hydration interactions are moderated by solution IS (Israelachvili, 2011). They are significant over several nm of separation distance. More generally, steric repulsion can arise from surface molecular structures on either or both surfaces. Surface molecules that also carry ionic functionality (e.g., carboxyl groups in acidic polysaccharides and natural organic matter) produce a combined electrosteric interaction. Sources cited in Israelachvili (2011) provide more information regarding steric and electrosteric interactions. Steric interactions in Parti-Suite are implemented using the simple expressions for change in free energy and for force as provided by Butt and others (2005) as shown in Equations (22), (23), and (24).

$$\Delta G_{STE} = \gamma_0^{STE} \pi a_{STE}^2 e^{-\left(\frac{H}{\lambda_{STE}}\right)} \tag{22}$$

$$\overrightarrow{F_{STE}}(H) = \frac{\gamma_o^{STE}}{\lambda_{STE}} \pi a_{STE}^2 e^{-\left(\frac{H}{\lambda_{STE}}\right)} \tag{23}$$

$$a_{STE} = \sqrt{a_{cont}^2 + 2\lambda_{STE}\left(a_p + \sqrt{a_p^2 + a_{cont}^2}\right)} \tag{24}$$

where:

λ_{STE} = steric decay distance, typically in m (L)

γ_0^{STE} = steric energy at minimum separation distance, typically in J (ML^2T^{-2})

a_{STE} = steric hydration contact radius, typically in m (L)

The xDLVO module of Parti-Suite calculates xDLVO interactions for multiple geometries (sphere-sphere and sphere-plate) in terms of both force and energy as a function of separation distance. To assist users, default values in xDLVO modules of Parti-Suite are provided for polystyrene latex colloids interacting with silica across water.

4.2.4.6 Roughness Impacts

We turn now to the impacts of roughness on colloid-surface interactions as they are implemented in the xDLVO module of Parti-Suite. Further discussion of the impacts of nanoscale roughness in pore-scale transport is provided in Section 5 to address the impacts of roughness on hydrodynamic interactions.

Because asperities (protrusions) locally reduce the radius of curvature of the surface on which they occur, roughness reduces the magnitude of non-contact colloid-surface interactions (VDW and EDL) as noted by Bargozin and others (2015), Bhattacharjee and others (1998), Hoek and Agarwal (2006), and Hoek and others (2003). Effectively, two layers of interaction occur between two surfaces when one or both of them has nanoscale roughness according to separation distances for the asperities (*H*) and for the more separated equivalent smooth surface(s) (*H'*) as discussed in Huang and others (2010) and Jin and others (2015).

These two layers of interaction between asperities and equivalent smooth surfaces set up a non-monotonic trend in the magnitude of colloid-surface interaction as a function of asperity size, where the magnitude decreases dramatically in the transition from smooth to rough surfaces with asperities on the order of 10 to 20 nm, and then rebounds as asperities increase thereafter (Jin et al., 2015). This is shown by the non-monotonic trend in the width (and height) of the repulsive barrier (and depth of the secondary minimum) as roughness increases across this range (Figure 12).
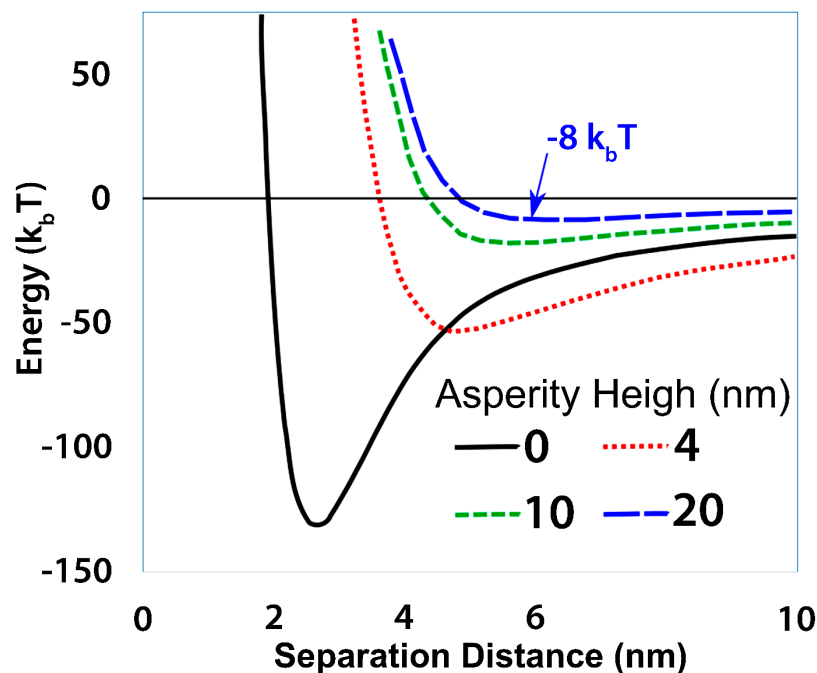
Figure 12 - Interaction energy profiles for 2 μm colloids under favorable conditions. Interactions for a smooth surface (i.e., no asperities present) are shown as a black line and interactions with 4 nm, 10 nm, and 20 nm asperities are shown with stippled red, dash-dot green, and dashed blue lines, respectively. Favorable conditions (pH 2, 50 mM) were calculated using $\zeta_{colloid}$= -5.1 mV and $\zeta_{collector}$= 10.0 mV.

The GROUNDWATER PROJECT   ©The Author(s)   Free download from gw-project.org

Anyone may use and share gw-project.org links. Direct distribution of the book is strictly prohibited.

While others have treated asperities as protruding pillars occupying a specified fraction of the surface (e.g., Shen et al., 2018), Parti-Suite treats them as hemispheres protruding contiguously across the surface (Rasmuson et al., 2019a). For either option, the equivalent smooth surface separation distance (H') determined by the asperities protruding from only one of the surfaces is shown in Equation (25).

$$H' = H + a_{asp} \tag{25}$$

where:

H' = equivalent smooth colloid-surface separation distance (L)

H = colloid-surface separation distance (L)

a_{asp} = radius of asperities (L)

When asperities are present on both surfaces, we assume them to be equivalently sized (as an approximation), since roughness is fractal, such that smaller asperities are superimposed on larger asperities (Rasmuson et al., 2019a). Equivalently sized hemispherical asperities on the two surfaces may not interact head-on (e.g., according to simple cubic packing) but are more likely offset (e.g., according to dense cubic packing) (Figure 13).
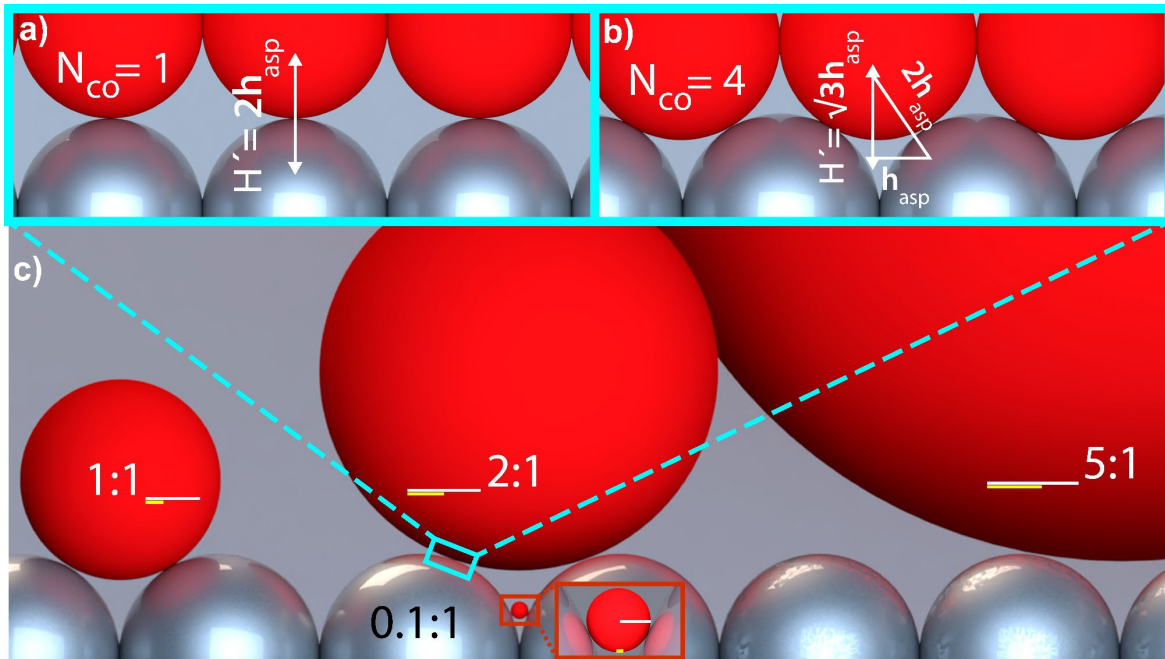
Figure 13 - Schematic showing geometries for hemispheres representing roughness asperities on colloid (red) and grain (metallic silver) surfaces in a) opposed (simple cubic packed, N_{co} = 1) and b) complimentary (dense packed, N_{co} = 4) configurations. c) Colloids (red) achieving a contact area (radius shown by bold horizontal yellow line) with asperities on grain surface (metallic silver) relative to a lever arm defined by multiple contacts established as a function of the colloid:asperity ratio (white horizontal line). Colloid asperity ratios are shown in the white text. Contact radii for the CML glass system were approximately 10 percent of the colloid radius. Calculations for the separation distance (H') between the equivalent smooth surfaces located at asperity minima are shown in (a) and (b). The inset and its magnified view are shown for a 0.1:1 colloid:asperity ratio (modified from Rasmuson et al., 2019a).

As such, the equivalent smooth surface separation distance is (Rasmuson et al., 2019a) shown in Equation (26).

$$H' = H + \frac{(2a_{asp} + \sqrt{3}a_{asp})}{2} \tag{26}$$

The reader should note this treatment assumes multiple asperities may exist within the ZOI (Rasmuson et al., 2019a) such that the correction for the non-contact colloid-surface interactions (ΔG_{NC}) is as shown in Equations (27) and (28).

$$\Delta G_{NC}(H) = \Delta G_{VDW}(H') + N_{asp}\Delta G_{VDW}(H) + \Delta G_{EDL}(H') + N_{ASP}\Delta G_{EDL}(H) \tag{27}$$

where:

N_{asp} = number of asperities in the ZOI (dimensionless)

$$N_{asp} = \frac{A_{ZOI}}{A_{asperity}}J \tag{28}$$

where:

J = jamming limit for hemispheric asperities in the circular ZOI (dimensionless)

J equals the ratio of the areas of the projected circle versus circumscribed square of the base of the hemispheric asperity shown by Equation (29).

$$J = \frac{\pi a_{asp}{}^2}{4a_{asp}{}^2} = \frac{\pi}{4} \tag{29}$$

Roughness reduces both repulsive and attractive interactions (Figure 12), which means that roughness alone cannot explain attachment of colloids under unfavorable conditions (Rasmuson et al., 2019a) as is further examined in Section 5 regarding simulating pore-scale colloid transport. As described in this section, the Derjaguin approximation limits colloid-surface interactions to separation distances less than the colloid radius ($H \ll a_p$). In the xDLVO and atomic force microscopy (AFM) modules of Parti-Suite (as well as the trajectory modules described in Section 5.2), the xDLVO interactions involving roughness asperities are not included for $H \gg a_{asp}$.

Links to videos explaining the xDLVO module of Parti-Suite are provided in the caption of Figure 14. Readers who would like to follow along with a version of xDLVO on their computer while watching the video and perhaps try their own simulation experiments can download it at this link: The Parti-Suite xDLVO module↗. There are two download options, one for those who already have access to MATLAB Runtime and another much larger file that includes MATLAB Runtime for academic use only. To use either exe file, double click on it and, if the integrity of the installation is questioned, click the button to "learn more" then scroll to the right and click the button to allow the installation to run on the computer. Continue to answer the questions that appear on the screen followed by

27

"next" until the installation is complete. When completed the code named *Parti_Suite_xDLVO_GUI.exe* will be in the folder the user chose for installation. The default folder is *"C:\Program Files\W.P. Johnson Research Group\Parti_Suite_xDLVO_GUI0.25\application"*. To use the program, find the file on the computer then right-click on the file and choose to run as administrator. A power shell window will appear, followed shortly by the graphical user interface (GUI) for Parti_Suite_xDLVO. A more in-depth discussion about downloading and using the software is provided in Section 5.2.
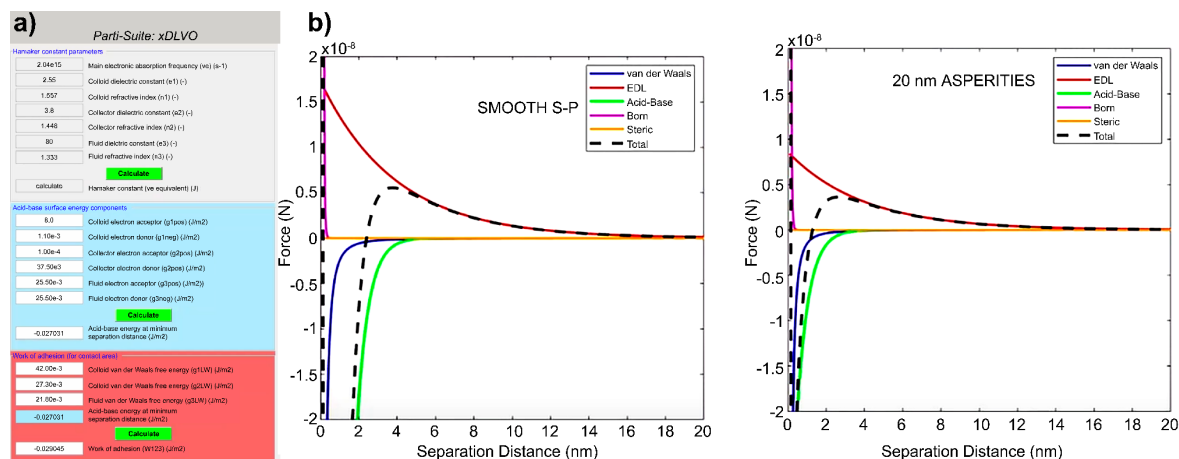
Figure 14 – The xDLVO module of Parti-Suite© with inputs shown in a) can be watched at this link YouTube▶ and comparison of b) smooth surface behavior with behavior near a rough surface can be viewed here YouTube▶. The default inputs in the xDLVO graphical user interface (GUI) correspond to carboxylate-modified polystyrene latex microspheres interacting with glass slides across water and provide a specific example of the units used for these inputs.

The video of Figure 14 provides information needed to complete the second exercise at the link provided here: Exercise 2⤓.

5 Pore-Scale Colloid Transport Processes

Pore-scale colloid transport concerns the delivery of colloids to grain surfaces, their subsequent interaction with surfaces following delivery (with or without attachment) (Figure 15), and their potential detachment following attachment. Because colloid-surface interactions extend no longer than approximately 200 nm separation distance from the grain surface, we can categorize pore-scale colloid transport according to two fluid zones (i.e., two ranges in separation distance):

1. the bulk fluid domain that lies outside the approximately 200 nm separation distance beyond which colloid-surface interactions are negligible, and

2. the near-surface fluid domain that lies within that 200 nm separation distance where colloid-surface interactions are significant.
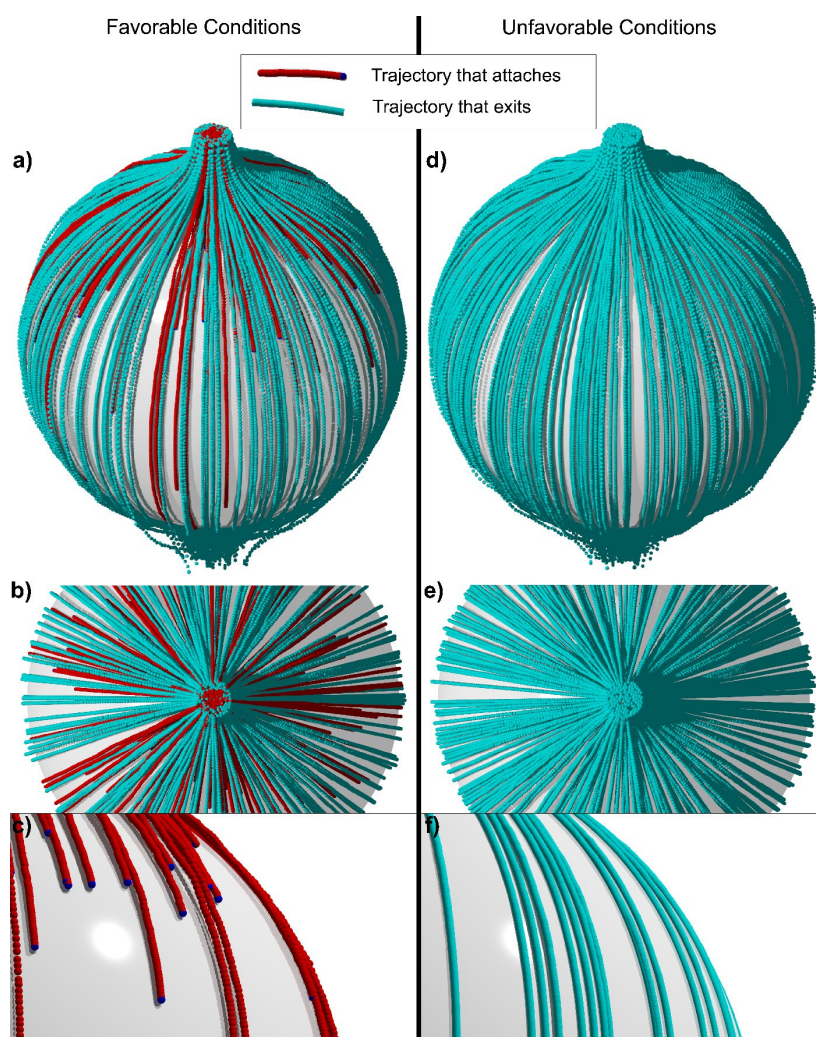
Figure 15 - Simulated colloid trajectories in a Happel sphere-in-cell collector lacking nanoscale charge heterogeneity with flow from top to bottom for favorable conditions (a, b, and c) and unfavorable conditions (d, e, and f). Trajectories are red for colloids that attach and cyan for colloids that exit without attachment. Three views are provided: distant side view (a and d), top downward view (b and e), and close side view 0f trajectories that attach under favorable conditions (c and f).

In the bulk fluid domain, colloid-surface interactions are negligible and the force/torque balance is dominated by fluid drag, diffusion, and gravitational settling. In contrast, in the near-surface fluid domain, colloid-surface interactions are significant and typically dominate the force/torque balance. As such, we can consider transport in the bulk fluid as governing the likelihood of colloid delivery to the near-surface fluid surrounding the grains; additionally, we can consider transport in the near-surface fluid domain as governing the likelihood of colloid retention, either with attachment (via arrest in primary minima) or without attachment (via secondary minimum association with grain surfaces in zones of low fluid drag) as shown in Figure 15.

Colloid transport in the bulk fluid domain (colloid delivery to the near-surface fluid) is negligibly affected by the existence of a repulsive barrier to attachment in the colloid-surface interaction profile (favorable versus unfavorable conditions). In contrast, the processes governing colloid transport in the near-surface fluid domain (retention with or without attachment, and re-entrainment back to the bulk fluid domain) are highly dependent on the existence of a repulsive barrier to attachment and an attractive secondary minimum in the colloid-surface interaction profile. Even under favorable conditions, a large fraction of the colloid trajectories exit the collector without interacting with the grain surface; this is explained in detail in Section 5.2. These processes are explored in the following sections:

- first, these processes are examined in terms of experimental observations (Section 5.1),
- then in terms of simulating these processes using force and torque balance in mechanistic pore-scale transport simulations (Section 5.2),
- after which long-established short-cuts to mechanistic simulation of these processes are considered (Section 5.3),
- and finally, Section 5.4 examines transition to continuum-scale transport by considering equilibrium versus kinetic pore-scale processes as applied solute versus colloid transport.

5.1 Experimentally Observed Pore-Scale Transport Processes

A critically important and ubiquitous phenomenon observed during colloid transport in granular media is the profound contrast in transport behaviors under conditions where a repulsive barrier is absent (favorable conditions for attachment) versus present (unfavorable conditions for attachment). The most common circumstance for generating unfavorable attachment conditions is the existence of like charges (e.g., both negative) among colloids and grain surfaces that, under environmental conditions, typically involves negative measured ζ- potentials for both surfaces. First, we examine the experimentally observed influence of favorable versus unfavorable conditions on pore-scale colloid motion in near-surface fluid (Section 5.1.1), then we explore colloid

attachment (Section 5.1.2) and colloid detachment (Section 5.1.3). Finally, we review the experimentally observed impacts of roughness on colloid attachment and adhesion (Section 5.1.4).

5.1.1   Colloid Motion in Near-Surface Fluid Domain in Pore-Scale Experiments

In pore-scale transport experiments (i.e., where colloid motion is directly observed in micromodels), a primary contrast is the absence versus presence of colloid motion in the near-surface fluid domain under favorable versus unfavorable conditions, respectively (Figure 16). Under favorable conditions, colloid advection, dispersion, and attachment in pore water is revealed in time-lapse images that record colloid trajectories. Among these trajectories, a fraction terminate at the grain surface where the corresponding colloids entered the near-surface fluid domain, contacted the surface, and arrested (attached) as shown in Figure 16. Notably, the portion of the trajectory between the point of intercepting the near-surface fluid and the point of arrest, was minimal under favorable conditions, and typically less than the resolution of optical microscopy (Figure 16). In contrast, under unfavorable conditions where a repulsive barrier exists in the colloid-surface interaction profile, the near-surface portion of colloid trajectories show a large range of distances (and residence times) between the point of surface interception (of the near surface fluid) and arrest (Figure 16). Some of these near-surface colloid trajectories culminate with colloid re-entrainment back into the bulk fluid rather than arrest (Figure 16). This pore-scale contrast in near surface fluid transport behaviors under favorable versus unfavorable conditions feeds several larger scale (continuum-scale) phenomena that are examined in Section 6 where we discuss continuum-scale transport.
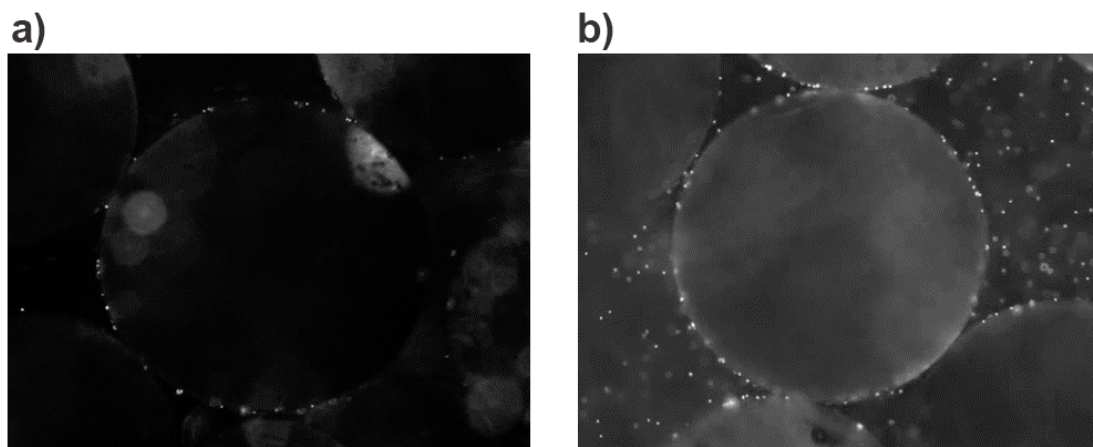
Figure 16 - Direct observation of colloid (fluorescent carboxylate-modified polystyrene latex microspheres of 2 μm diameter) transport in a microscopic granular media domain (glass beads of approximately 1 mm diameter). The main flow direction is from bottom left to top right. Colloids show as bright white dots. For favorable conditions shown in video a)▶, attachment occurs immediately once the colloid enters the near-surface fluid domain; there is no action at the grain surface other than the sudden appearance of the attached colloid. In contrast, for unfavorable conditions shown in video b)▶, colloids spend a significant time in the near-surface fluid domain prior to attachment or re-entrainment back to bulk fluid; there is frequent slow colloid motion along the grain surface, with a subset of the colloids becoming attached.

5.1.2 Collector Efficiencies in Pore-Scale Experiments

The contrasting near-surface transport under unfavorable relative to favorable conditions also manifests in the ratio of retained versus *entered* colloids, where entered refers to the total number of colloids that entered the *collector* (a volume defined by a grain plus its fluid shell) representing the granular media. The ratio of retained to entered colloids is referred to as the *collector efficiency* (η). Collector efficiencies (η) are lower (sometimes orders of magnitude lower, but not zero!) under unfavorable relative to favorable conditions. The magnitude of this difference increases with the degree of unfavorable-ness, that is, the increased magnitude of the repulsive barrier.

The repulsive barrier magnitude increases with increasing pH and reduced IS under like-charged (both surfaces negative) unfavorable conditions. This impact of pH and *IS* on colloid transport is shown in impinging jet micromodel experiments (Ron et al., 2019a) as shown in Figure 7. Collector efficiencies (η) for 1 μm carboxylate-modified polystyrene latex microspheres (CML) interacting with silica across water show a gap between favorable conditions (blue lines in Figure 17) and unfavorable conditions (red lines in Figure 17). This gap varies with colloid size, with the maximum gap corresponding to colloids in the size range corresponding to the transition from *nm* to *μ*m scales—what Ron and others (2019a, 2020) call the *n-μ transition* (Figure 17). The mechanisms behind this observation are described in the following sections that discuss simulated pore-scale transport as well as in Ron and others (2019a) and Ron and Johnson (2020). Values of η observed at the pore-scale under unfavorable conditions approach those for favorable conditions for colloid sizes exceeding several *μ*m in diameter (Figure 17). This attribute of microscale colloids appears to be general, as explored by Ron and others (2019b). The gap between favorable and unfavorable η increases greatly with increasing unfavorable conditions (i.e., with increased pH and decreased IS for these negatively charged surfaces) as shown in Figure 17a versus Figure 17d.
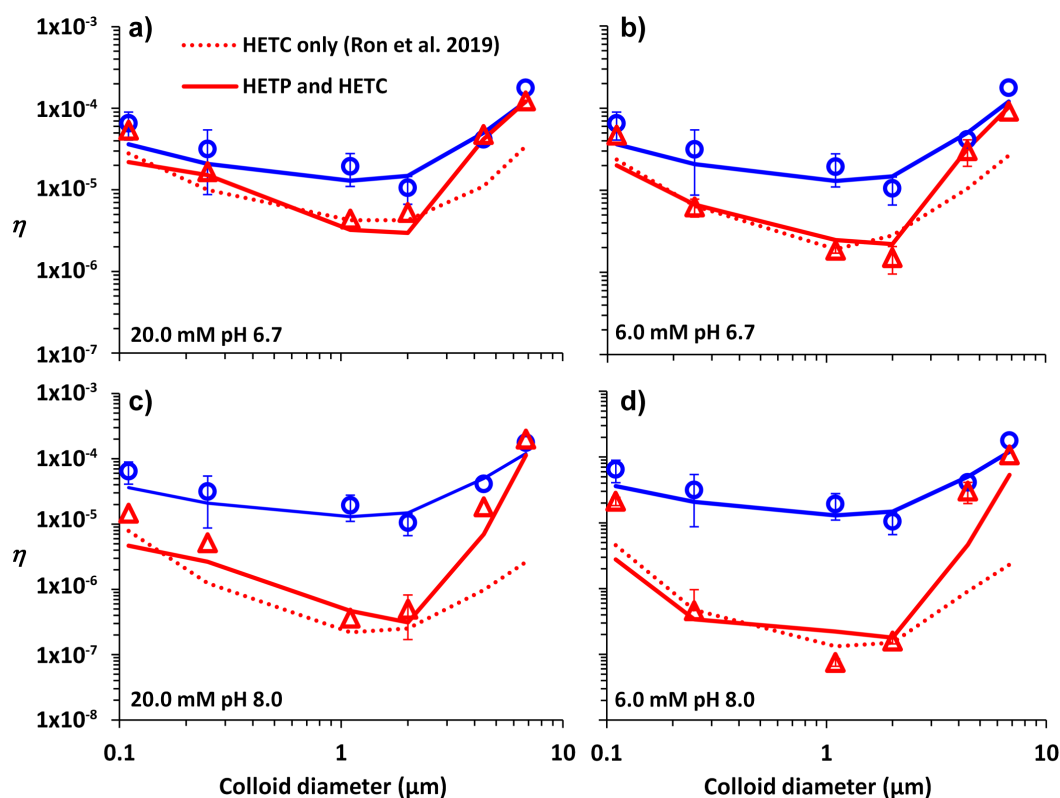
Figure 17 - Experimental (symbols) versus simulated (lines) trends of collector efficiency as a function of colloid diameter under favorable (blue) versus unfavorable conditions (red). Efficiency varies depending on ionic strength and pH: a) IS 20 mM and pH 6.7, b) IS 6 mM and pH 6.7, c) IS 20 mM and pH 8, and d) IS 6 mM and pH 8. The surface is silica and the colloids are carboxylate-modified polystyrene latex microspheres. For colloids between the 1 to 2 μm diameter size, the gap between favorable and unfavorable collector efficiencies (η) is greatest. This gap decreases for smaller and larger colloid sizes outside the n-μ transition. Repulsion (and the gap between favorable and unfavorable (η) increases with increased pH and the associated decreased IS in this system. Simulations were performed for nanoscale heterogeneity on the collector only (HETC) and for nanoscale heterogeneity on both the collector and the colloid (HETP) (from Pazmiño et al., 2014; Ron et al., 2020).

5.1.3 Detachment in Pore-Scale Experiments

Arrested (attached) colloids are not easily detached with increased flow, except at flows much higher relative to those under which they were attached (Johnson et al., 2010). This is true regardless of whether colloid arrest occurred under favorable versus unfavorable conditions (Pazmiño et al., 2014b; Rasmuson et al., 2019a; VanNess et al., 2019). However, pore-scale experiments also demonstrate that a fraction of colloids arrested (or retained without attachment) under unfavorable conditions are re-entrained in response to IS reduction (Pazmiño et al., 2014b; Rasmuson et al., 2017, Rasmuson et al., 2019a).

The significance of these observations is explored under the simulated pore-scale transport section (Section 5.2). Many continuum scale experiments (e.g., packed columns) report detachment in response to perturbation in flow or IS. However, it is not possible to distinguish (at the continuum scale) between actual detachment of previously attached colloids versus re-entrainment of colloids that were retained without attachment via secondary minimum interactions.

5.1.4 Roughness Impacts in Pore-Scale Experiments

The presence of surface roughness closes the gap on collector efficiencies (η) of pore-scale colloid transport observed under favorable versus unfavorable conditions, (Rasmuson et al., 2017). Closing of this gap in response to increased surface roughness is demonstrated in Figure 18. The difference in values of η for carboxylate-modified polystyrene latex microspheres (CML) interacting with a glass surface were previously shown to be much larger under favorable relative to unfavorable conditions (Figure 17), at least for CML sizes in the *n-μ transition*. This gap between favorable and unfavorable values of η was nearly eliminated by introducing 38 nm root mean square (RMS) roughness to the glass surface (Figure 18; Rasmuson et al., 2017).
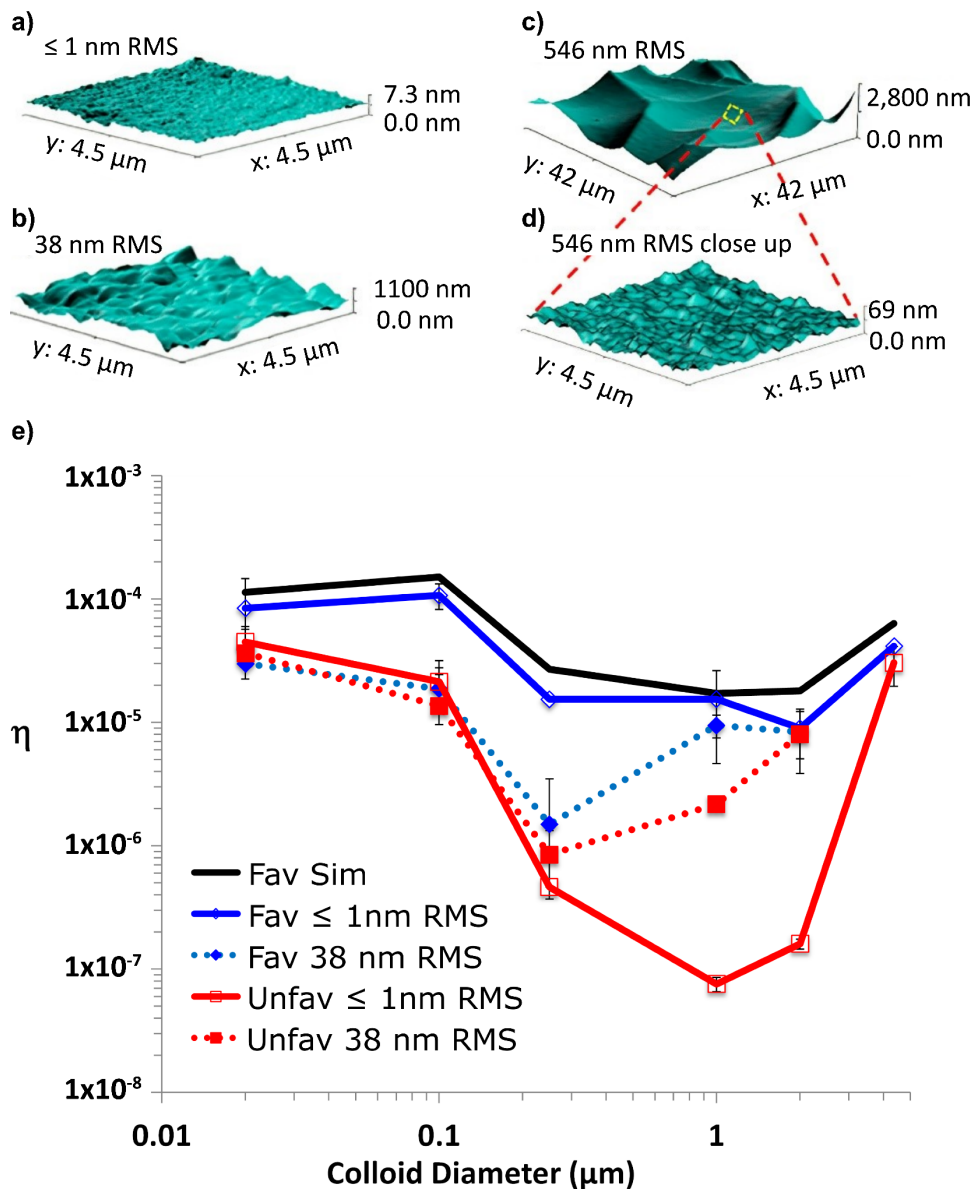
Figure 18 - Atomic force microscopy (AFM) nano topography of samples with increasing root mean squared (RMS) roughness: a) < 1 nm, b) 38 nm, and c) 546 nm, with d) showing a close-up of (c). e) Collector efficiency as a function of colloid size for different values of RMS roughness under favorable and unfavorable conditions, as well as simulated under favorable conditions (Fav Sim; from Rasmuson et al., 2017).

This trend is consistent with decreased repulsion accompanying increased roughness, in qualitative agreement with the impact of roughness described in the nanoscale interactions section. However, pore-scale experimental observations also show that roughness increases adhesion because detachment from rough surfaces requires stronger perturbations in flow or IS (Rasmuson et al., 2017). But the trend of increased adhesion with increased roughness is *not* in agreement with the expected impact of roughness on colloid-surface attraction (Section 4.2.4.6) since both attractive and repulsive interactions decrease with decreased radius of curvature. Explaining increased adhesion with increased roughness requires additional mechanisms such as the creation of nanoscale charge heterogeneity to generate local zones of attraction. This is explored further in the next section on simulated pore-scale transport. The multiple points of contact that may be established on rough surfaces likely also plays a role in adhesion (Section 5.2.2.2). The impact of roughness on adhesion presents an opportunity for further research (Li et al., 2022).

5.2 Simulating Pore-Scale Colloid Transport

This section describes the process of simulating pore-scale colloid transport in five subsections.

1. First, by using a mechanistic force and torque balance in representative collectors where colloid delivery to surfaces occurs (Section 5.2.1).
2. Then by considering colloid attachment (Section 5.2.2).
3. Next colloid detachment is included (Section 5.2.3).
4. That is followed by taking up the subject of mechanistic simulation under unfavorable conditions, which requires incorporation of representative nanoscale charge heterogeneity into the mechanistic trajectory simulations (Section 5.2.4).
5. Finally, the impact of colloid shape is included (Section 5.2.5).

5.2.1 Simulating Pore-Scale Colloid Delivery to Surfaces via Mechanistic Force and Torque Balance

The mechanistic force/torque balance at separation distances beyond contact (beyond the reach of Born, LAB, and steric forces, in the range of several nm) is provided in the Langevin equation in Figure 19.

$$\frac{\left[\vec{F}_{Drag} + \vec{F}_{Brownian} + \vec{F}_{Gravity} + \vec{F}_{Colloidal}\right]}{m_p}\Delta t + \vec{u}^{t-1} = \vec{u}^t$$
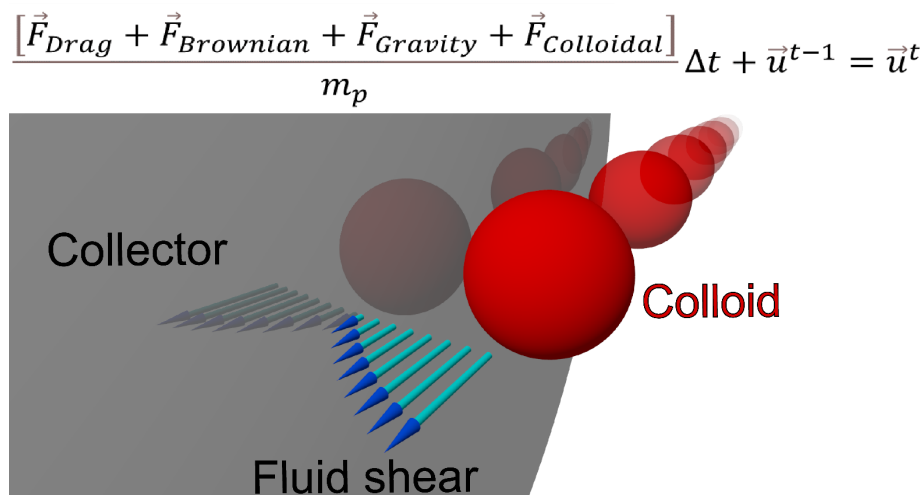
Figure 19 - Representation of colloid trajectory simulation obtained from a force balance. At relatively longer separation distances (> 200 nm) where colloidal forces are negligible. Once the colloid is near the surface (< 200 nm), colloidal forces play a critical role in colloid attachment (immobilization in contact), retention (weak association in the secondary energy minimum in zones of small fluid shear), and re-entrainment back to the bulk fluid.

The Langevin equation applies Newton's 2nd Law to determine the change in colloid velocities based on forces acting in the normal and tangential directions (superscripts [n] and [t], respectively) relative to the surface at any given location in the fluid surrounding the grain as shown in Equation (30).

$$\left(m_p + m^*\right) \cdot \frac{du_n}{dt} = F_{COLL}^n + F_G^n + F_D^n + F_B^n + F_L^n \tag{30}$$

where:

m_p = colloid mass (M)

m^* = colloid virtual mass (M)

F_G^n = normal components of gravity (MLT^{-2})

F_D^n = fluid drag (MLT^{-2})

F_B^n = diffusion (MLT^{-2})

F_L^n = lift (MLT^{-2})

Colloid virtual mass impacts colloid acceleration and deceleration at high colloid velocities by accounting for the inertia added to a system because an accelerating or decelerating body must deflect some volume of surrounding fluid as it moves through it. The virtual mass of a sphere is equal to one-half the displaced volume of fluid. It is derived from consideration of the total kinetic energy of a system of a particle moving through fluid (Gondret et al., 2002). F_{COLL} is the sum of the colloid-surface interaction forces illustrated in Figure 19 and shown by Equation (31).

$$F_{COLL}^n = F_{VDW} + F_{EDL} + F_{Born} + F_{AB} + F_{STE} \tag{31}$$

Colloid-surface interactions act on the normal between the grain and colloid surfaces (on the pole connecting the colloid and grain centers). Additional pore-scale forces acting on the normal between the colloid and grain include the normal components of gravity (F_G^n), fluid drag (F_{GD}^n), diffusion (F_B^n), and lift (F_L^n), which are described in detail in Section 5.2.1.3.

Applying the Langevin equation to the tangential force balance results in Equation (32).

$$(m_p + m^*) \cdot \frac{du_t}{dt} = F_B^t + F_G^t + F_D^t \tag{32}$$

Equations (30), (31), and (32) dictate the force balance acting on colloids in groundwater. Solving these equations for colloid velocities to perform trajectory simulations is shown in Section 5.2.1.3, *Pore-Scale Forces in Detail: Gravity, Fluid Drag, and Diffusion*.

It should be noted that the fluid shear-driven torque spins colloids according to the differential fluid velocities impinging on the nearest versus farthest points of the colloid (from the grain surface). This rotation in the fluid is currently implicit (i.e., not explicitly calculated) in Parti-Suite, although it is explicitly calculated for non-spherical colloids in an extension of the Parti-Suite Happel trajectory source code (Li & Ma, 2019).

Substituting the colloidal force expression in Equation (31) and the fluid drag forces discussed in Section 5.2.1 into Equations (30) and (32), then substituting a discrete time step (Δt) between times τ and τ-1, and finally re-arranging, yields the non-contact colloid velocities normal and tangential to the grain surface—u_n and u_t, respectively—for time (τ) based on a previous time (τ-1) as modified by the forces and torques acting at the location corresponding to τ (VanNess et al., 2019) as shown by Equations (33) and (34). This simple forward difference is implemented in Parti-Suite's trajectory simulation modules.

$$u_n^\tau = \frac{(m_p + m^*)u_n^{\tau-1} + F_B^n \Delta t + F_G^n \Delta t + F_{COLL}^n \Delta t + F_L^n \Delta t + f_2 6\pi\mu a_p v_t^\tau \Delta t}{(m_p + m^*) + \frac{1}{f_1} 6\pi\mu a_p \Delta t} \tag{33}$$

$$u_t^\tau = \frac{(m_p + m^*)u_t^{\tau-1} + F_B^t \Delta t + F_G^t \Delta t + \frac{f_3}{f_4} 6\pi\mu a_p v_t^\tau \Delta t}{(m_p + m^*) + \frac{1}{f_4} 6\pi\mu a_p \cdot \Delta t} \tag{34}$$

More complex numerical integration algorithms have not (yet) been implemented in Parti-Suite because the nanoscale surface interactions change dramatically over extremely small separation distances in the near-surface fluid domain that, along with the random diffusion force, challenge more sophisticated numerical integration approaches. As performed in Parti-Suite trajectory modules, the colloid is introduced to the collector at

37

the upstream outer-most boundary of the fluid envelope where the force and torque balance is performed to update the colloid velocity. This process is repeated many (e.g., trillions) times to develop the Lagrangian trajectory of the colloid in the collector where the trajectory may do any of the following:

- associate with the surface via secondary minimum interactions and move slowly downgradient, or
- attach via primary minimum interactions, or
- exit the collector as described in Section 5.2.1.1.

The simulation framework described briefly here is explored in greater detail with respect to the different grain and fluid flow geometries that are used to represent granular media in Section 5.2.1.1 and the collector efficiencies obtained using such representative collectors is explored in Section 5.2.1.2. Detailed description of the forces acting at the pore scale are also provided in Section 5.2.1.3.

5.2.1.1 Simulating Pore-Scale Colloid Delivery to Surfaces in Representative Collectors

Discussion of colloid delivery to surfaces requires introduction of the term *collector*. A collector encompasses a grain plus its surrounding fluid domain *watershed* that together represent a *unit cell* of a given porous media (Figure 20). Parti-Suite provides colloid trajectory modules for all four of the representative collectors shown in Figure 20, albeit only the Happel collector trajectory module is available in MATLAB with a user-friendly graphical user interface (GUI). Once a user becomes familiar with the GUI, they will be able to navigate the more cryptic (but very fast running and parallelizable) input files needed to run the versions of Parti-Suite that exist in Fortran for the other collector geometries.
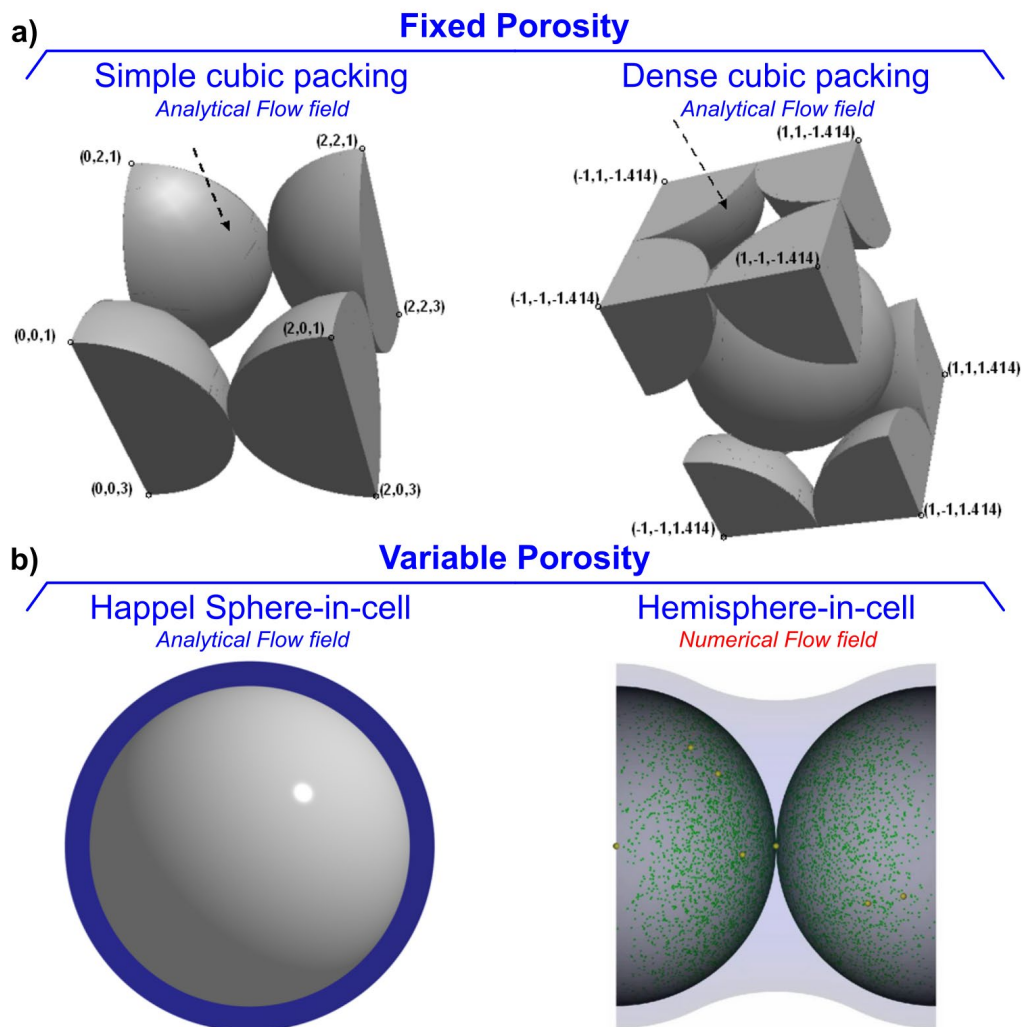
Figure 20 - Most common unit cells used in pore-scale colloid transport simulations: a) variations of fixed packing, and b) variable porosity.

The first unit cell proposed by Yao and others (1971) considered colloids approaching a single, isolated collector that was perfectly spherical and surrounded by an infinite fluid. This approach, as noted by Yao and others (1971), produced velocity distributions that were likely poor representations of actual porous media. This isolated-sphere approach was subsequently modified to employ a Happel sphere-in-cell geometry (Happel, 1958) that represented porosity via the thickness of the fluid shell associated with the grain (Figure 21). Alternatively, a constricted tube collector was explored (Burganos et al., 1992; Burganos et al., 1994; Paraskeva et al. 1991; Payatakes et al., 1974a; Payatakes et al., 1974b).
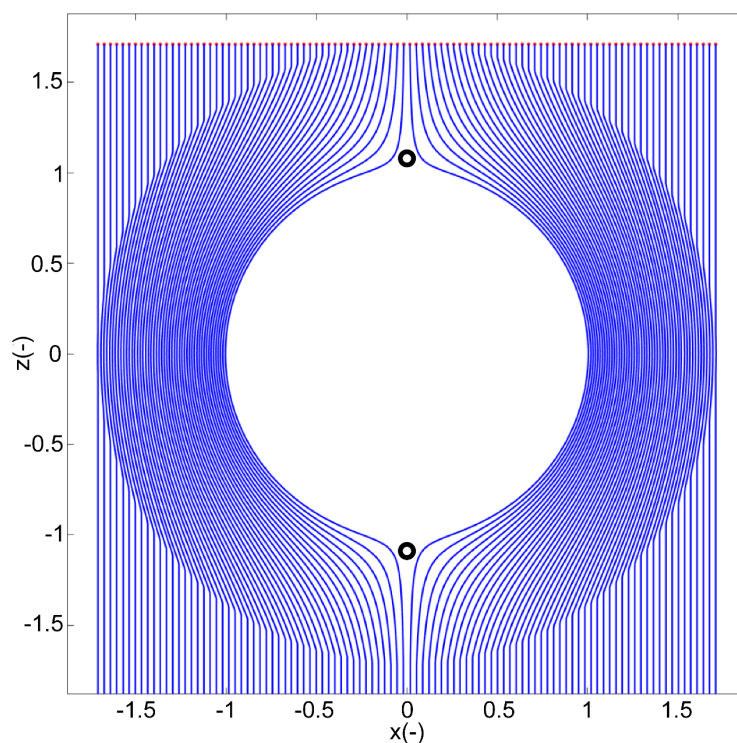
Figure 21 - Two-dimensional representation of Happel sphere-in-cell collector flow field streamlines. A uniform flow field (downward) exists outside the Happel fluid shell (shown for porosity = 0.85 for clarity). Streamlines diverge around the upstream hemisphere and converge around the downstream hemisphere, forming forward and rear flow stagnation zones indicated by small black circles in the upstream and downstream hemispheres, respectively.

The Happel cell was first employed by Rajagopalan and Tien (1976) and has been used in more recent colloid filtration theory models (Nelson & Ginn, 2011; Tufenkji & Elimelech, 2004). The flow field around the grain is assumed to be equivalent to Stokes (i.e., creeping) flow where advective inertial forces are small compared with viscous forces, a type of laminar flow.

Because an actual porous medium includes grain-to-grain contacts, it may yield flow phenomena around a Happel collector inconsistent with Stokes flow including recirculation/vortex zones (Cardenas, 2008; Dykaar & Kitanidis, 1996; Li et al., 2010a; Torkzaban et al., 2008) and low flow zones (Li et al., 2010a, 2010b). To represent these and other impacts of grain-to-grain contacts in a Happel-like model, Ma and others (2009) developed a hemispheres-in-cell model with grain-to-grain contact with the line connecting grain centers oriented perpendicular to flow (Figure 19). Others developed dense (Cushing & Lawler, 1998) or simple (Johnson et al., 2007a) cubic packing collectors as well as collectors composed of randomly packed porous media (Long & Hilpert, 2009), with the limitation that they have fixed porosities (Figure 20).

A description of collector geometries is provided in Molnar and others (2015). Each collector has a specified fluid flow field where v_n and v_t are specified at all locations in the collector fluid. However, the hemisphere-in-cell (Ma et al., 2009) and random-packed (Long

& Hilpert, 2009) collectors are described by numerical (rather than analytical) flow fields. This requires data input/output that may slow simulations in those collectors relative to collectors for which an analytical flow field exists.

The Happel sphere-in-cell collector flow field (Figure 21) is described by a stream function (ψ, with dimensions of L^3/T) around a spherical collector (Happel & Brenner, 1983) as expressed in Equation (35).

$$\psi = \frac{V_{sup}a_g^2}{2}\sin^2(\omega)\left[K_1\left(\frac{1}{r^*}\right) + K_2(r^*) + K_3(r^*)^2 + K_4(r^*)^4\right] \tag{35}$$

where:

θ = volume of water per volume of representative elementary volume (dimensionless)

a_g = collector radius (L)

r = radial coordinate (L)

r^* = normalized radial coordinate $\frac{r}{a_g}$ (dimensionless)

ω = tangential coordinate (radians)

w = $2 - 3\gamma + 3\gamma^5 - 2\gamma^6$ (dimensionless)

K_1 = $\frac{1}{w}$ (dimensionless)

K_2 = $-\frac{3+2\gamma^5}{w}$ (dimensionless)

K_3 = $\frac{2+3\gamma^5}{w}$ (dimensionless)

K_4 = $-\frac{\gamma^5}{w}$ (dimensionless)

The fluid velocity vector (LT^{-1}) is obtained from the partial derivative of the stream functions (Nelson & Ginn, 2001). It depends on the radial (r) and tangential (ω) locations in the domain bound by the collector surface and the fluid shell ($a_g < r < r_B$, with r_B the Happel fluid shell radius). The tangential location is defined by the angle from the positive vertical axis (z axis) shown in Equation (36).

$$\vec{V}(r,\omega) = -\frac{1}{r^2\sin\omega}\frac{\partial\psi}{\partial\omega}\hat{e}_r + \frac{1}{r\sin\omega}\frac{\partial\psi}{\partial r}\widehat{e_\omega} \tag{36}$$

where:

$\hat{e}_r$ = radial unit vector (dimensionless)

$\widehat{e_\omega}$ = tangential unit vector (dimensionless)

The radial and tangential velocities obtained are described by Equations (37) and (38).

$$v_r = -V_{sup}\left(\frac{K_1}{r^{*3}} + \frac{K_2}{r^*} + K_3 + K_4 \cdot r^{*2}\right)\cos\omega \tag{37}$$

$$v_\omega = V_{sup} \left(-\frac{K_1}{2r^{*3}} + \frac{K_2}{2r^*} + K_3 + 2K_4 r^{*2} \right) \cos\omega \tag{38}$$

It is convenient to define radial and tangential functions as shown in Equations (39) and (40).

$$f_r = \frac{K_1}{r^{*3}} + \frac{K_2}{r^*} + K_3 + K_4 \cdot r^{*2} \tag{39}$$

$$f_\omega = -\frac{K_1}{2r^{*3}} + \frac{K_2}{2r^*} + K_3 + 2K_4 r^{*2} \tag{40}$$

The radial and tangential unit vectors can be expressed in terms of cartesian coordinates as shown in Equations (41) and (42).

$$\widehat{e_r} = (\sin\omega)\,\hat{\jmath} + (\cos\omega)\,\widehat{k} \tag{41}$$

$$\widehat{e_\theta} = (\cos\omega)\,\hat{\jmath} - (\sin\omega)\,\widehat{k} \tag{42}$$

where:

$\hat{\jmath}$ = x- direction

$\widehat{k}$ = y- direction

Combining the last six equations produces a solution for the components of the fluid velocity as a function of cartesian coordinates as shown in Equations (43), (44), and (45).

$$v_x = -V_{sup}\left(\frac{xz}{r^2}\right)(f_r - f_\omega) \tag{43}$$

$$v_y = -V_{sup}\left(\frac{yz}{r^2}\right)(f_r - f_\omega) \tag{44}$$

$$v_z = -V_{sup}\left(\frac{z^2}{r^2}\right)\left[f_r + f_\omega\left(\frac{x^2 + y^2}{r^2}\right)\right] \tag{45}$$

Misconception: The Happel sphere-in-cell collector is too non-physical to be useful.

Five concepts relevant to this misconception are listed here as a through e.

a. The trend in collector geometries has been toward more realism, using x-ray microtomography to produce more realistic pore spaces, and conducting intensive transport simulations in these realistic pore domains (e.g., Molnar et al., 2015). Certainly, insights arise with increased realism. However, insights are also gained from mechanistic simulations in representative systems.

b. The Happel sphere-in-cell collector captures the following essential features:

  i. zones of flow impingement on grains where colloid delivery to surfaces occurs (the forward flow stagnation zone),

    ii.   zones of low fluid velocity where colloids may remain associated with the surface via secondary minimum interactions without attachment (rear flow stagnation zone), and

    iii.   zones of high fluid shear where the force/torque balance may prevent attachment (equatorial region).

c.   The Happel sphere-in-cell has the following drawbacks:

    i.   Grain-to-grain contacts are absent; these zones collect colloids, particularly larger colloids in the multi-micron size range (Johnson et al., 2007a; Li et al., 2006a; Li et al., 2006b).

    ii.   It is non-physical (non-stackable), so persistence of behaviors during transport from cell to cell cannot be explored. Related to its non-stackable nature is the assumed complete fluid mixing at the inlet of the Happel collector where the uniform flow field is interfaced with the fluid shell via a non-tangential stress condition imposed at the intersection of the uniform flow field and the outer boundary of the fluid shell (Happel, 1958). The significance of this condition is that incomplete fluid mixing would not be reflected in the flow field of a series of Happel cells even if they were stackable.

d.   The drawbacks of item (c) are addressed in dense and simple cubic packing unit cells as well as random-packed unit cells. These cells can be represented with an analytical flow field; however, they have a fixed porosity. Fortran codes for mechanistic transport simulations in dense and simple cubic unit cells are available in Parti-Suite. Stacked cells are available for dense cubic packing.

e.   Such idealized collectors can obscure the impact of gravity on filtration. Since gravity is unidirectional, its impact may become dependent on collector geometry for some of the collectors. For example, in single grain collectors like the Happel sphere-in-cell collector or in single-pore collectors like the simple cubic packed collector, colloids may be located in entry positions from which gravity will not deliver them to grains no matter the magnitude of the gravitational force (i.e., for colloids located at the periphery of the Happel cell or the center of the simple cubic packed cell). These collector geometries will therefore predict an asymptotic sub-unity value of the collector efficiency as gravitational force increases (e.g., by virtue of increased colloid density). In contrast, for colloids within a granular media, the collector efficiency should approach unity above some threshold colloid density due to the certainty of collision with grain surfaces.

      A link to a video introducing the mechanistic trajectory simulators for various representative collectors in Parti-Suite is given in Figure 22, which can be accessed via the white arrow in the middle of the figure, followed by clicking on "▶" in the next screen. The video provides information to assist readers in completing the corresponding Exercise 3↳.

2 μm CML on 510 μm glass beads
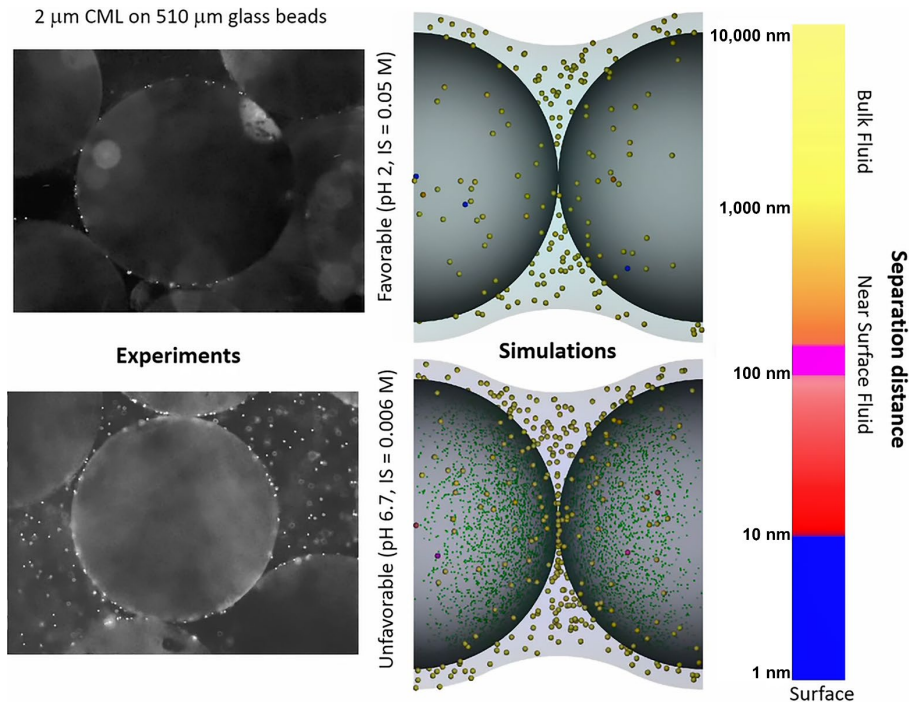
Figure 22 - A video introducing the colloid trajectory simulation module in Parti-Suite can be watched by clicking on the white arrow in the middle of the figure and the subsequent video symbol "▶", or clicking here YouTube ▶.

A link to a video describing simulation of colloid trajectories in a representative collector in Parti-Suite is given in Figure 23. It can be accessed by clicking on the white arrow in the middle of the figure, then on "▶" in the next screen. The video provides information for undertaking the corresponding Exercise 4 ⤵.
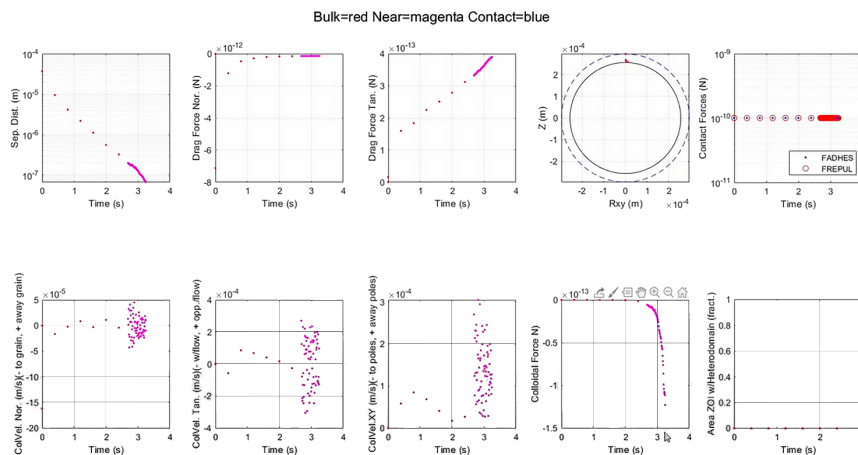
Figure 23 - A video introducing colloid trajectory simulations under favorable conditions in Parti-Suite can be watched by clicking on the figure and the subsequent video symbol "▶",or clicking here YouTube ▶.

5.2.1.2 Collector Efficiencies (η) From Mechanistic Trajectory Simulations

For a given colloid size, grain size, fluid velocity, colloid density, and media porosity, the essential question is whether the colloid will intercept the surface and attach. This question boils down to whether colloids lie on a fluid streamline that will deliver them

44

to a surface. If this seems strangely specific, a useful analogy is to envision that you have fallen out of a raft into a raging, boulder-strewn river (Figure 24). Assuming your goal is to get onto one of the boulders before drowning, even at a subconscious level, you will likely dog-paddle toward streamlines that will carry you into collision with a boulder (softly, we hope).
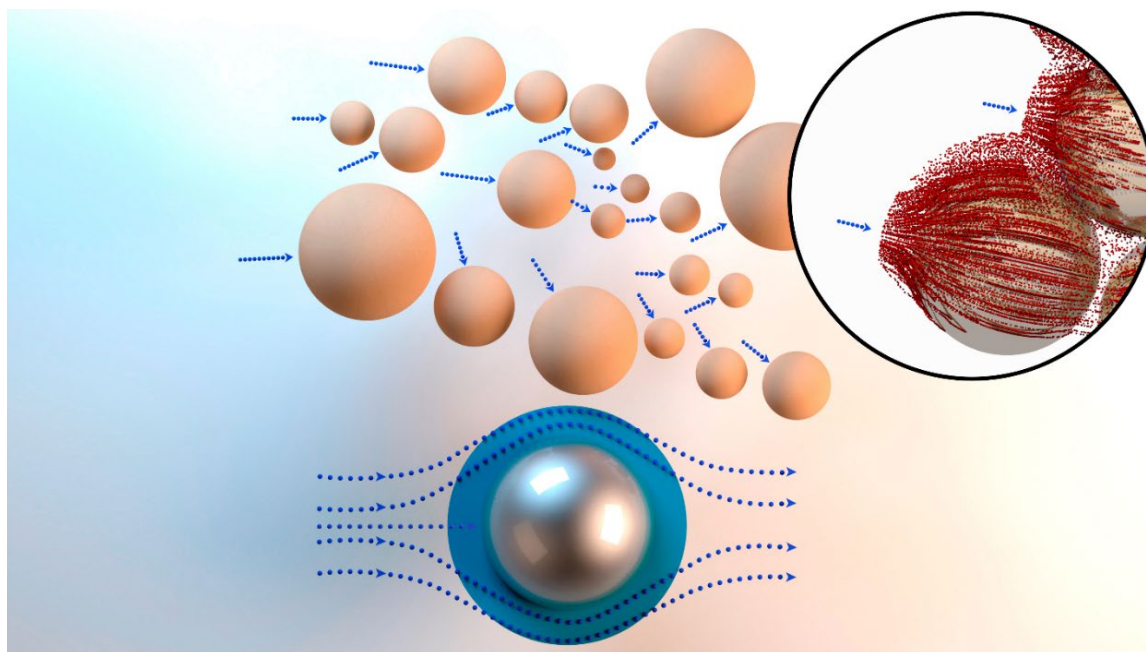
Figure 24 - Schematic of a porous medium at the top of this figure shows (solid blue arrows) the main zones of colloid delivery to each grain surface, which are the forward flow stagnation zones (FFSZ). The Happel unit cell shown below the porous medium has an FFSZ in its flow field highlighting its utility as a colloid transport model. The inset shows colloid trajectories (in red) associated with the FFSZ.

In fluid flow terms, those streamlines correspond to forward flow stagnation zones (FFSZ). Your likelihood of intercepting a boulder despite being slightly off the FFSZ axis increases with your size. The likelihood also increases the more you can dog-paddle randomly across streamlines (to mimic diffusion) or swim single-mindedly across streamlines toward the shore (to mimic settling). The same is true for colloids in granular media. Colloids delivered to surfaces are those with the highest combined motion across streamlines via either diffusion (for the smallest colloids) or settling (for large and/or dense colloids).

For colloids in granular media (and castaways in a boulder-strewn river), those with the lowest combined diffusion and settling will have the least likelihood of intercepting a boulder or grain; those that are too far from an FFSZ will be swept past the boulder even with the help of diffusion and settling, demonstrating that the physics of delivery dictates the observed minimum collector efficiency (η) observed for n-μ transition colloids under favorable conditions (Figure 18).

It also demonstrates the limiting distance (radius) from the FFSZ—beyond which there is no chance of getting to (intercepting) the boulder. The fraction of fluid flow field

streamlines that intercept FFSZ or otherwise impinge on the surface (η) depends on the collector geometry, the porosity, and the flow rate. In this way, colloid filtration theory boils down the complex tortuous flow field in granular media to an array of FFSZs as shown in Figure 24 (Rajagopalan & Tien, 1976; Yao et al., 1971).

Misconception: Smaller colloids undergo less filtration.

In fact, for colloids with equivalent surface properties, the least filtration occurs for the size with the least combined diffusion and sedimentation. For near-neutrally buoyant colloids at typical groundwater velocities, the minimum falls in the size range corresponding to the *n-μ* transition.

Based on mechanistic simulation of colloid trajectories in representative collectors, this colloid filtration framework allows us to predict the likelihood that colloids will intercept the grain surface as quantified by the collector efficiency (η): the number of colloids that intercept relative to the number introduced to the collector. The continuum-scale transport section of this book (Section 6) shows how η is upscaled to predict the transport distances that colloids may achieve prior to their concentration being reduced below some threshold that, for example, protects human health. The trajectory simulations are the foundation of colloid filtration theory since they allow quantitative prediction of η, which is upscaled to produce quantitative prediction of colloid transport distances as described in Section 6.

Misconception: Attaining equilibrium in batch mixing experiments indicates that filtration does not apply (this misconception is used to argue that nanoparticles partition rather than undergo filtration).

Two concepts relevant to this misconception are presented here as a and b.

a. Filtration involves the two-step process of 1) delivery to surfaces and 2) attachment upon delivery. If step (1) does not occur, step (2) is moot. According to colloid filtration theory, the rate of colloid delivery to grain surfaces from surrounding pore water is governed by the processes of fluid drag, diffusion, and settling in a laminar flow field within a pore network. To state filtration situationally: If the colloid is not positioned on a streamline that will deliver it to the grain surface, then the question becomes whether diffusion and settling will be sufficient to drive the colloid to a grain surface even if it starts on a streamline lateral to the FFSZ. In contrast, when a container is shaken in a batch experiment, the pore network and laminar flow streamlines are destroyed, thus grains and colloids are mixed throughout a turbulent fluid, guaranteeing delivery of colloids to grain surfaces. This mixing obviates the roles of fluid streamlines, settling, and diffusion in the delivery of colloids to surfaces. In short, batch experiments by-pass the physics of colloid delivery to surfaces during flow in porous media; they address only the issue of attachment following colloid delivery to the surface under the highly turbulent air-water mixing conditions of batch experiments.

b. By-passing the limited mass transfer to the surface via streamlines, diffusion, and settling allows batch experiments to measure attachment efficiency upon delivery to surfaces under conditions that may or may not match those of flow in porous media. Accordingly, batch experiments can—potentially—explore the attachment part of filtration, but batch experiments cannot assess the delivery to grain surfaces (collector efficiency) part of filtration.

A video describing the process of determining collector efficiencies in representative collectors in Parti-Suite is provided via the white arrow in the middle of Figure 25. The video provides information for undertaking the corresponding <u>Exercise 5</u>⬐.
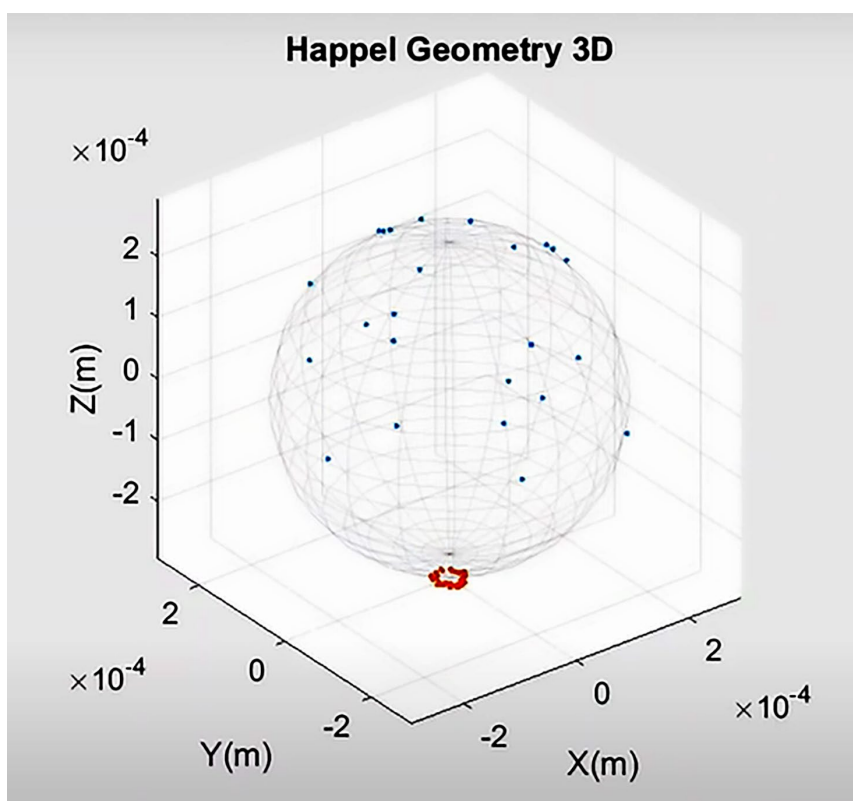
Figure 25 - A video introducing determination of collector efficiencies in Parti-Suite can be watched by clicking the white arrow in the middle of the figure and the subsequent video symbol "▶", or clicking here <u>YouTube</u>▶.

5.2.1.3 Pore-Scale Forces in Detail: Gravity, Fluid Drag, and Diffusion

Forces acting in addition to the nanoscale interactions include gravity, fluid drag, and diffusion Figure 19. The corresponding equations for each of these forces are presented in the following sub-sections. Other excellent texts also cover this subject including, for example, Elimelech and others (1998).

Gravity

The gravitational force that drives colloid settling arises from the colloid-fluid density differential acted upon by the gravitational field (Prieve & Ruckenstein, 1974) as expressed in Equation (46).

$$\overrightarrow{F_G} = \frac{4}{3}\pi a_p^3 (\rho_p - \rho_f)g \tag{46}$$

where:

ρ_p and ρ_f = densities (typically kg/m³, ML⁻³) of the colloid and fluid, respectively

g = gravitational constant (9.81 m/s², LT⁻²)

The normal and tangential components of F_G relative to the surface are tracked in Parti-Suite trajectory simulations for the different grain geometries described earlier.

Fluid drag and lift

The fluid drag force (F_D) advects colloids downstream with a force proportional to the velocity of the fluid (v) and the fluid viscosity (μ) (Goren & O'Neill, 1971) such that for a spherical colloid of radius (a_p), the fluid drag force in the normal and tangential directions (to the surface) are as shown in Equations (47) and (48).

$$F_D^n = -\frac{6\pi\mu a_p u_n}{f_1} + 6\pi\mu a_p v_n f_2 \tag{47}$$

$$F_D^t = -\frac{6\pi\mu a_p u_t}{f_4} + 6\pi\mu a_p v_t \frac{f_3}{f_4} \tag{48}$$

where:

f_1 through f_4 = hydrodynamic correction factors (dimensionless)

Hydrodynamic correction factors account for the impacts of fluid expulsion between colloids and stationary surfaces when colloids are within several tens of radii of the stationary surface (Brenner, 1961; Goldman et al., 1967a, 1967b; Gondret et al., 2002; Goren et al., 1971; Masliyah & Bhattacharjee, 2005). The expressions that follow in Equations (49), (50), (51), and (52) are heuristic fits to mathematical manipulations of physical relationships for which the derivation is described in detail in Box 1⤓.

$$f_1 = 1 - 0.3990 e^{-0.1487\frac{H}{a_p}} - 0.601 e^{-1.202\left(\frac{H}{a_p}\right)^{0.9267}} \tag{49}$$

$$f_2 = 1 + 1.355 e^{-1.36\frac{H}{a_p}} + 0.875 e^{-0.525\left(\frac{H}{a_p}\right)^{0.5695}} \tag{50}$$

$$f_3 = 1 - 0.1430 e^{-1.472\frac{H}{a_p}} - 0.6772 e^{-2.765\left(\frac{H}{a_p}\right)^{0.2803}} \tag{51}$$

$$f_4 = 1 - 0.2942 e^{-0.9041\frac{H}{a_p}} - 0.6054 e^{-1.291\left(\frac{H}{a_p}\right)^{0.2653}} \tag{52}$$

Dispersion arises predominantly from variation in pore-scale v around its mean value in flowing systems, from near zero at the stationary grain surface to a maximum at the pore center. As such, FD forces vary along a given fluid streamline, and vary among

streamlines depending on their proximity to the stationary surfaces or pore centers; this velocity variance yields dispersion. At the pore network scale (continuum), additional dispersion occurs because fluid velocities vary due to varying pore size resulting from variations in grain size, grain shape, and packing structure, as well as larger-scale heterogeneities as described in the continuum-scale transport section (Section 6).

Lift ($\overrightarrow{F_L}$) and virtual mass forces also emanate from fluid shear and fluid displacement, respectively. The virtual mass force manifests as an additional mass term in the force integration (Gondret et al., 2002) as shown in Equation (53).

$$m^* = -\frac{4}{3}\pi a_p^3 \frac{1}{2}\rho_f \tag{53}$$

Because the lift force is insignificant at typical groundwater velocities, we do not discuss it here. Other literature provides further description of this force (Goldman et al., 1967a, 1967b; VanNess et al., 2019; Yahiaoui & Feuillebois, 2010).

Roughness impacts fluid drag at the grain surface where the tops of asperities create an effective contact surface at which v_t is non-zero, whereas v_n, the normal component of velocity, (vertical in Figure 26) is effectively zero (Rasmuson et al., 2019a; Vinogradova & Belyaev, 2011). The no-slip surface (where $v_t = 0$) occurs at some depth below the effective contact surface (asperity tops) such that a *slip layer* of thickness b exists below the effective contact plane (asperity tops) (Rasmuson et al., 2019a) as shown in Figure 26. The impact on the force torque balance is to introduce a non-zero tangential velocity (v_t) at the plane of contact. Hydrodynamic retardation functions for tangential fluid drag as shown in Equations (35) and (36) are shifted such that $f_i(H)$ becomes $f_i(H+b)$ for $i = 3$ and 4 (i.e., the tangential hydrodynamic correction factors).
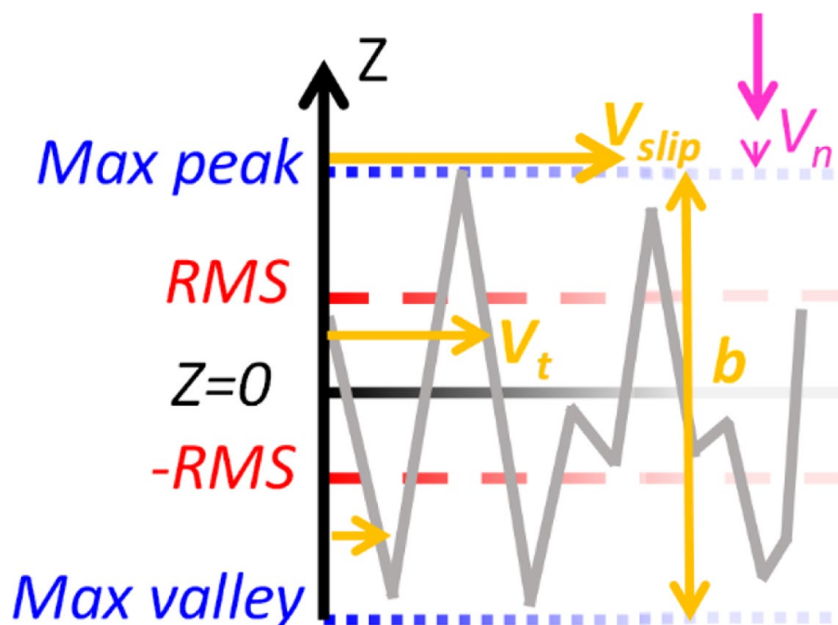
Figure 26 - Schematic of parameters modified in the impinging jet model to account for slip, with the explicit rough surface represented by the jagged gray line. The continuum expressions for v_t are a function of $z + b$, with $b = 0$ for smooth surfaces. For rough surfaces, the no-slip condition for the normal component v_n occurs at the effective contact plane and the no-slip condition for the tangential component v_t occurs at distance b below the effective contact plane. The slip velocity (v_{slip}) is the finite tangential fluid velocity at the effective contact plane (a plane lying on the highest asperity tops, i.e., labeled Max peak in the image).

Diffusion (Brownian motion)

Translations associated with Brownian (random) motion of colloids in water scale inversely with colloid size and fluid viscosity and directly with *T*, according to the Stokes-Einstein diffusion coefficient that governs Fick's Law of diffusion shown in Equation (54).

$$D = \frac{k_B T}{6\pi\mu a_p} \tag{54}$$

In simulations, diffusion is often implemented as a random displacement (e.g., Nelson & Ginn, 2011) but can be incorporated into simulations as a force (Kim & Zydney, 2004) to apply the hydrodynamic retardation functions as in Equation (55). The normal and tangential components of F_B relative to the surface are tracked in Parti-Suite trajectory simulations.

$$\overrightarrow{F_B} = 1.35\left(\Re \cdot \sqrt{\frac{12\pi a_p \mu k_B T}{\Delta t}}\right) \tag{55}$$

where:

$\Re$ = a Gaussian-distributed random number (dimensionless), the algorithm in Parti-Suite was adopted from a Fortran code developed by researchers Nelson and Ginn (2005) and described in Pazmiño and others (2014a)

50

Δt = time step used for numerical integration of the force balance as subsequently described (T)

Notably, the challenge in typical numerical integration is to minimize Δt to the extent that allows one to achieve a tractable simulation time. However, in the case of Brownian motion, the lower limit for Δt is scaled to the momentum relaxation time (*MRT*), which is the time associated with individual segments of correlated motion within the random movement observed at larger time scales as described by Nelson and Ginn (2005) and in Equation (56).

$$MRT = \frac{m_p}{6\pi\mu a_p} \tag{56}$$

where:

m_p　=　colloid mass (M)

Values of Δt should significantly exceed *MRT* to honor random Brownian motion (Chandrasekhar, 1943; Ermak & McCammon, 1978; Uhlenbeck & Ornstein, 1930). In Parti-Suite, the numerical integration time steps are set by time step multipliers, which should exceed at least 2 in the near-surface and bulk fluid to honor Brownian motion. The time step multiplier should be smaller in the near-surface fluid than that in the bulk fluid to avoid numerical colloid crashing into the grain surface.

5.2.2　Simulating Pore-Scale Colloid Attachment (Arrest) via In-Contact Torque Balance

The process of colloid attachment following delivery to the near-surface fluid domain involves first closing the separation distance to the point where contact forces (steric, LAB, and Born) may arrest the colloid according to a torque balance (Section 5.2.2.1). The in-contact torque balance is governed by contact mechanics (Section 5.2.2.2) that may reduce the colloid tangential (rolling) velocity to zero, constituting arrest (Section 5.2.2.3), which may be influenced by nanoscale roughness (Section 5.2.2.4). The shear induced by the non-uniform fluid velocity field generates torque on the colloid which in turn spins in the fluid. Spin yields the lift force mentioned above, but it is insignificant at typical groundwater velocities for spheroidal colloids (Goldman et al., 1967a, 1967b; VanNess et al., 2019; Yahiaoui & Feuillebois, 2010). More information about the impact of torque from fluid shear is provided in <u>Box 1</u>⤵ and in Section 5.2.5.

5.2.2.1 In-Contact Torque Balance

Upon delivery of colloids to the near-surface fluid domain, arrest is predicted only when contact with the surface is made, meaning that colloids must approach the surface to within several *nm* where steric/hydration, LAB, or Born surface interactions define contact between the surfaces. Once in contact, the surface friction between the colloid and the surface converts the non-contact fluid friction-driven colloid rotation into in-contact colloid

rolling across the surface with an axis of rotation assumed perpendicular to the tangential fluid velocity. Upon colloid contact and rolling, an explicit torque balance determines whether colloid arrest will occur.

The arresting torque is the product of the net adhesive force (F_{adh}) and a lever arm (a_{cont}) defined by deformation upon contact as shown in Figure 27 and Equation (57).
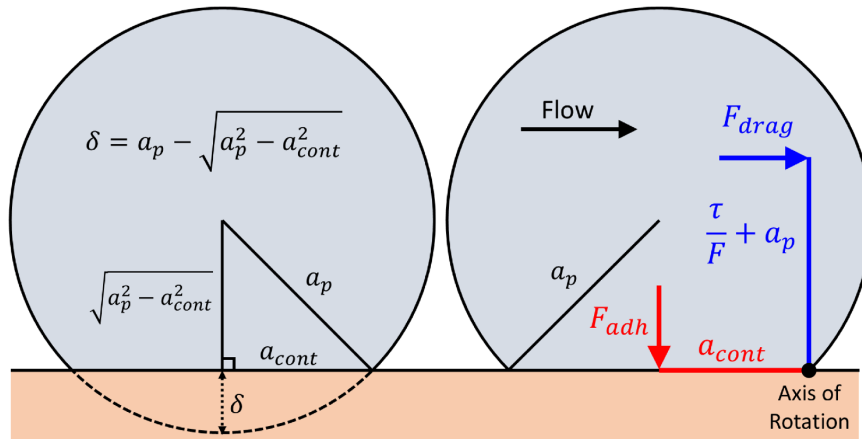
Figure 27 - Conceptual figure showing the deformation (left) and torque balance (right) applied to the colloid in contact with the collector surface.

$$\text{Arresting Torque} = F_{adh} a_{cont} \tag{57}$$

where:

a_{cont} = lever arm defined by deformation upon contact (L)

F_{adh} = net adhesive force (MLT^{-2})

The mobilizing torque is composed of the tangential hydrodynamic drag force (F^t_D) that acts on an effective lever arm created by the ratio of the torque to force acting at a distance greater than the colloid radius (Goldman et al., 1967b; Hubbe, 1984; Figure 27) as expressed by Equation (58). As separation distance (H) approaches 0, the mobilizing torque lever arm approaches 1.37 (Hubbe, 1984).

$$\text{Mobilizing torque} = F^t_D \left(a_p + \frac{\tau_i}{F_i} \right) \tag{58}$$

where:

τ_i = fluid torque (ML^2T^{-2})

F_i = fluid drag force (MLT^{-2})

subscript i = indicates fluid forces and torques due to colloid translation, or rotation, or fluid shear (VanNess et al., 2019) (dimensionless)

5.2.2.2 Contact Mechanics

Colloid and grain surface deformation occur upon contact in response to the net adhesive force (F_{adh}), that arises from F_{VDW}, F_{EDL}, F_D^n, F_G^n, and attractive F_{AB}. While some of the acting forces can be repulsive (e.g., F_{EDL}, F_L), they are all included in the net adhesive force so long as they are non-contact (VanNess et al., 2019). Forces not included in the net adhesive force are F_B, F_{STE}, and repulsive F_{AB} because these are repulsive contact forces. These forces create the repulsive force that is equal and opposite to the adhesive force, thereby setting the equilibrium colloid-collector separation distance (VanNess et al., 2019).

The contact area produced by deformation has a radius (a_{cont}) governed by the work of adhesion (W) and the combined elastic modulus of the colloid and collector (K) as discussed by Johnson and others (1971), where the radius is expressed as shown in Equation (59). Values of γ for the polystyrene latex, silica, water system are given as defaults in the Parti-Suite xDLVO and trajectory modules.

$$a_{cont} = \left(\frac{6\pi W a_p^2}{K}\right)^{1/3} \tag{59}$$

where:

W is calculated using Lifshitz-VDW and LAB interaction theory (van Oss, 1994; van Oss, 2008) as shown in Equation (60).

$$W_{132} = 2\left[\sqrt{\gamma_1^{LW}\gamma_3^{LW}} + \sqrt{\gamma_2^{LW}\gamma_3^{LW}} - \sqrt{\gamma_1^{LW}\gamma_2^{LW}} - \gamma_3^{LW}\right.$$
$$+ \sqrt{\gamma_3^+}\left(\sqrt{\gamma_1^-} + \sqrt{\gamma_2^-} - \sqrt{\gamma_3^-}\right) + \sqrt{\gamma_3^-}\left(\sqrt{\gamma_1^+} + \sqrt{\gamma_2^+} - \sqrt{\gamma_3^+}\right) \tag{60}$$
$$\left. - \sqrt{\gamma_1^+\gamma_2^-} - \sqrt{\gamma_1^-\gamma_2^+}\right]$$

where:

superscripts LW = surface energy superscripts LW indicate Lifshitz-VDW properties

superscripts +/- = indicate electron acceptor/donor properties

subscripts *1, 2,* and *3* = indicate the colloid, grain, and fluid, respectively

K = combined elastic modulus of the colloid and collector ($ML^{-1}T^{-2}$)

K is the combined elastic modulus of the colloid and collector calculated as shown in Equation (61). In Equation (61), E_i and v_i are the Young's modulus and Poisson's ratio for material *i*, respectively. The deformation is considered to increase linearly with respect to normal deformation (δ) from no deformation at the colloid-collector separation distance where contact first occurs to the maximum contact radius at the minimum separation distance.

$$K = \frac{4}{3\left(\dfrac{1-v_1^2}{E_1} + \dfrac{1-v_2^2}{E_2}\right)} \tag{61}$$

where:

v_i = Poisson's ratio for material i (dimensionless)

E_i = Young's modulus for material i (ML⁻¹T⁻²)

subscripts 1 and 2 = indicate the colloid and grain respectively

Deformation affects not only the arresting torque but also (slightly) the adhesive force because the periphery of the non-contact ZOI moves closer to the surface upon deformation (by the normal distance δ, Figure 27), thereby increasing the ZOI radius. This alters the fraction of ZOI occupied by heterodomains by an extent and direction that depends on the location of the ZOI relative to the heterodomain(s) as described by VanNess and others (2019). This slight enhancement of F_{adh} is incorporated into the contact mechanics calculations in Parti-Suite.

5.2.2.3 Tangential Velocity from Rolling in Contact

The translational velocity of a colloid rolling in contact with the surface that results from equating the arresting and mobilizing torques is described by VanNess and others (2019) as shown in Equation (62).

$$u_t^\tau = \frac{1.4(m_p + VM)u_t^{\tau-1} + 6\pi\mu(a_p - \delta)v_t\Delta t\left(F_t^{s*} + \frac{2}{3}\cdot\frac{a_p}{h+a_p}\cdot T_t^{s*}\right) - F_{adh}\dfrac{a_{cont}(a_p - \delta)}{a_p^2}\Delta t}{1.4(m_p + VM) - 6\pi\mu(a_p - \delta)\Delta t\left(F_t^{tr*} + F_t^{r*} + \frac{4}{3}(T_t^{tr*} + T_t^{r*})\right)} \tag{62}$$

where:

$F_t^{s*}\ F_t^{tr*}\ F_t^{r*}$ = shear, translational, and rotational components of tangential fluid drag force (MLT⁻²)

$T_t^{s*}\ T_t^{tr*}\ T_t^{r*}$ = shear, translational, and rotational components of torque (ML²T⁻²)

Expressions for the shear, translational, and rotational components of the tangential fluid drag force (F_t^{s*}, F_t^{tr*}, and F_t^{r*}, respectively) and torque (T_t^{s*}, T_t^{tr*}, and T_t^{r*}, respectively) are provided in <u>Box 2</u>⤓ along with the derivation of Equation (62).

In contact, the torque balance would be interrupted by inclusion of the random force associated with colloid diffusion. As such, the contact torque balance in Parti-Suite neglects diffusion while in contact, and absent the need to honor diffusion, the in-contact time step multiplier can be < 1 such that $\Delta t < MRT$. A potential enhancement to Parti-Suite trajectory simulations would be to account for the in-contact intrinsic colloid energy (diffusion or vibration energy) appropriately in the force/torque balance governing contact.

5.2.2.4 Roughness Impacts on Contact Mechanics

It was experimentally observed (Section 5.1.4) that roughness on surfaces decreases the reversibility of attachment (Rasmuson et al., 2017). However, roughness is expected to decrease both repulsive and attractive interactions, and thereby decrease adhesion and increase reversibility of detachment (Section 4.2.4.6). We therefore infer that multiple areas of contact are established on rough surfaces to produce the increased adhesion that decreases reversibility of attachment on rough surfaces (Rasmuson et al., 2019a). This phenomenon is also referred to as attachment in *concavities* (Li et al., 2022).

To account for this impact of roughness, the xDLVO and trajectory simulation modules in Parti-Suite invoke a simple rule that substitutes a roughness-based lever arm (r_{lever}) in place of a_{cont} in the arresting torque when $r_{lever} > a_{cont}$ (Rasmuson et al., 2019a) as is shown in Figure 28.
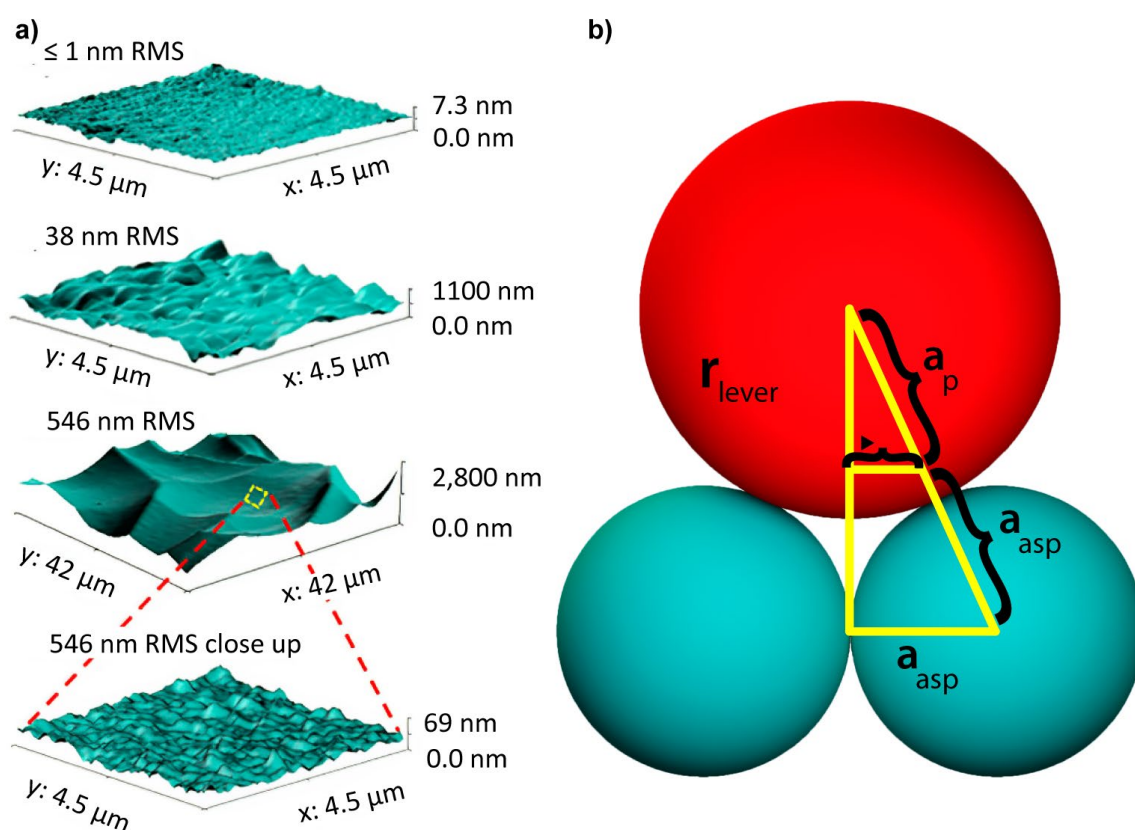
Figure 28 - Geometry of roughness a) surface topography revealed by atomic force microscopy for surfaces of three different root mean square (RMS) roughness. The fourth surface is a close-up of the 546 nm RMS roughness showing the fractal nature of roughness wherein smaller scale asperities occur on larger-scale asperities. b) Schematic of the geometric relationship used to determine the arresting lever arm (r_{lever}) resulting from contact with multiple asperities based on colloid and asperity radii of curvature (a_p and a_{asp}, respectively).

Equation (63) provides a relationship between r_{lever} and a_{cont} based on geometric relationships between a_p and the radius of asperities (a_{asp}) and Equation (64) yields a solution for r_{lever}.

$$\frac{a_p}{r_{lever}} = \frac{a_p + a_{asp}}{a_{asp}} \tag{63}$$

$$r_{lever} = \frac{a_p a_{asp}}{a_p + a_{asp}} \tag{64}$$

At the time of writing this textbook, the authors were developing a Parti-Suite module to simulate AFM colloidal probe force volume imaging. A beta version of this module is available on the Parti-Suite website. AFM colloidal force volume imaging typically assays a surface with a colloidal probe at regular intervals across the surface, advancing the colloidal probe toward and away from the surface along a line of action approximately normal to the surface. As such, the incorporation of explicit roughness and the colloidal probe location relative to roughness asperities is easily implemented in the AFM Force-Volume module (relative to the trajectory modules) of Parti-Suite. We expect observed variance in measured via AFM force-volume experiments will be reflected in force simulations that incorporate explicit roughness.

5.2.3 Simulating Pore-Scale Colloid Detachment

For an attached colloid, initiation of rolling and detachment may occur when the arresting torque is decreased (e.g., reduction of the adhesion force, F_{adh}) or when the mobilizing torque is increased (e.g., increase in tangential fluid drag, F^t_D). Notably, colloids attached to a surface experience solely the fluid shear component in Equation (57) (VanNess et al., 2019), whereas a number of studies examining colloid detachment have included all components: translation, rotation, and shear (Pazmiño et al., 2014b; Ryan & Elimelech, 1996; Sharma et al., 1992). We note that while steric and repulsive LAB do not typically reach out to sufficient separation distances to produce a repulsive barrier, they can shift the primary minimum to sufficiently greater separation distances such that the adhesive torque is decreased while the mobilizing torque is increased, thereby facilitating detachment (VanNess et al., 2019).

In Parti-Suite, a hysteresis factor < 1 (e.g., 0.5) is used to reduce the arresting torque lever arm (a_{cont}) to recognize that colloid deformation is kinetic under arresting conditions, where the colloid rolls to arrest (VanNess et al., 2019). Under mobilization conditions, the hysteresis factor is set to unity since, upon arrest, colloids are assumed to have sufficient time to relax fully into the estimated deformation. Derivation of the expression governing the rolling velocity of the colloid is provided in the *Supporting Information* section of VanNess and others (2019). This supporting information is also available as Box 2⤵. The white arrow in the middle of Figure 29 provides a link to a video demonstrating simulation of detachment in response to flow or solution IS perturbations in Parti-Suite. The video provides information for undertaking the corresponding Exercise 6⤵.
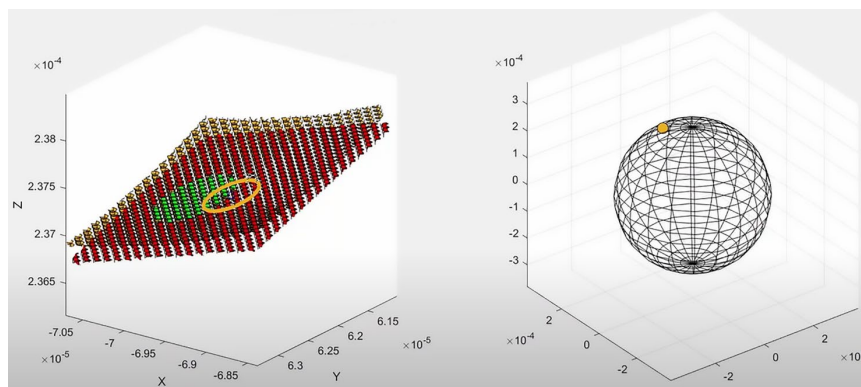
Figure 29 – A video introducing colloid detachment trajectory simulations using the Traj-Hap module's perturbation mode can be watched by clicking on the white arrow in the figure and the subsequent video symbol "▶" or clicking here: YouTube ▶.

The dynamic deformation of the colloid as it achieves contact with the surface (contact mechanics) is accounted for in the trajectory simulation and AFM modules of Parti-Suite, whereas the dynamics of contact mechanics is not accounted for in the xDLVO module—instead, a fixed contact area is assumed. As such, steric and other repulsive forces in contact differ between the xDLVO and the other modules, and it is useful to recognize that this difference exists.

5.2.4 Simulating Pore-Scale Colloid Transport Under Unfavorable Conditions

The challenge in developing functional simulations of colloid attachment under unfavorable conditions is to allow colloids to achieve sufficiently small separation distances to achieve contact, that is, distance within approximately several nm depending on steric interactions. Under unfavorable conditions, this is prevented by the formidable repulsive barriers calculated on the basis of measured ζ-potentials. This discrepancy led to the inference that nanoscale charge heterogeneity exists on surfaces, and locally reduces or eliminates the colloid-surface repulsive barrier (Elimelech & O'Melia, 1990).

Whereas nanoscale roughness can reduce colloid-surface repulsion and allow contact, mechanistic simulations indicate that the coincident reduction in both attractive and repulsive interactions prevents attachment (Rasmuson et al., 2019a). This indicates that surface charge heterogeneity is required to explain observed colloid attachment on rough surfaces. Since surface charge heterogeneity is also required to explain colloid attachment on unfavorable smooth surfaces, it seems reasonable to conclude that surface charge heterogeneity is operative on both rough and smooth surfaces (Ron et al., 2019a; Rasmuson et al., 2019a).

In terms of quantitative prediction under unfavorable conditions, xDLVO calculations assuming homogenous surfaces (mean-field xDLVO) fail dramatically. The magnitudes of calculated barriers typically far exceed the 1.5 (or 3.5) kbT energy associated with colloid diffusion such that calculated repulsive barriers rarely allow the colloid attachment that is observed experimentally (Elimelech & O'Melia, 1990).

The same failure to explain colloid attachment under unfavorable conditions having significant repulsion applies to mechanistic force/torque balance trajectory simulations (Pazmiño et al., 2014a), shown in Figure 30. In these simulations, as colloids encounter the near-surface fluid domain (e.g., within 200 nm separation distance), their trajectories become biased toward the surface due to slight but far-reaching attractive VDW interactions, the magnitude of which depends directly on colloid size and the combined Hamaker constants for the system, as described in the nanoscale interactions presented in Section 4. Once the colloid moves sufficiently close to the surface that repulsive EDL forces become significant relative to the attractive VDW forces, a steady-state separation distance is achieved corresponding to the secondary minimum. The colloid will translate downgradient with the near-surface fluid and with diffusion-driven excursions from the steady-state separation distance in the secondary minimum (Figure 30). Under unfavorable conditions (absent nanoscale heterogeneity), the colloid will translate downgradient in the near-surface fluid domain until it is either expelled to bulk fluid or remains indefinitely (depending on colloid diffusion) without attachment in flow recirculation zones (vortices) that may occur even under low Reynolds' number flow conditions in, for example, the zones lateral to the flow impingement zone of the impinging jet collector (VanNess et al., 2019). However, experimental (direct) observation of significant colloid retention in flow recirculation zones is sparse to nonexistent.
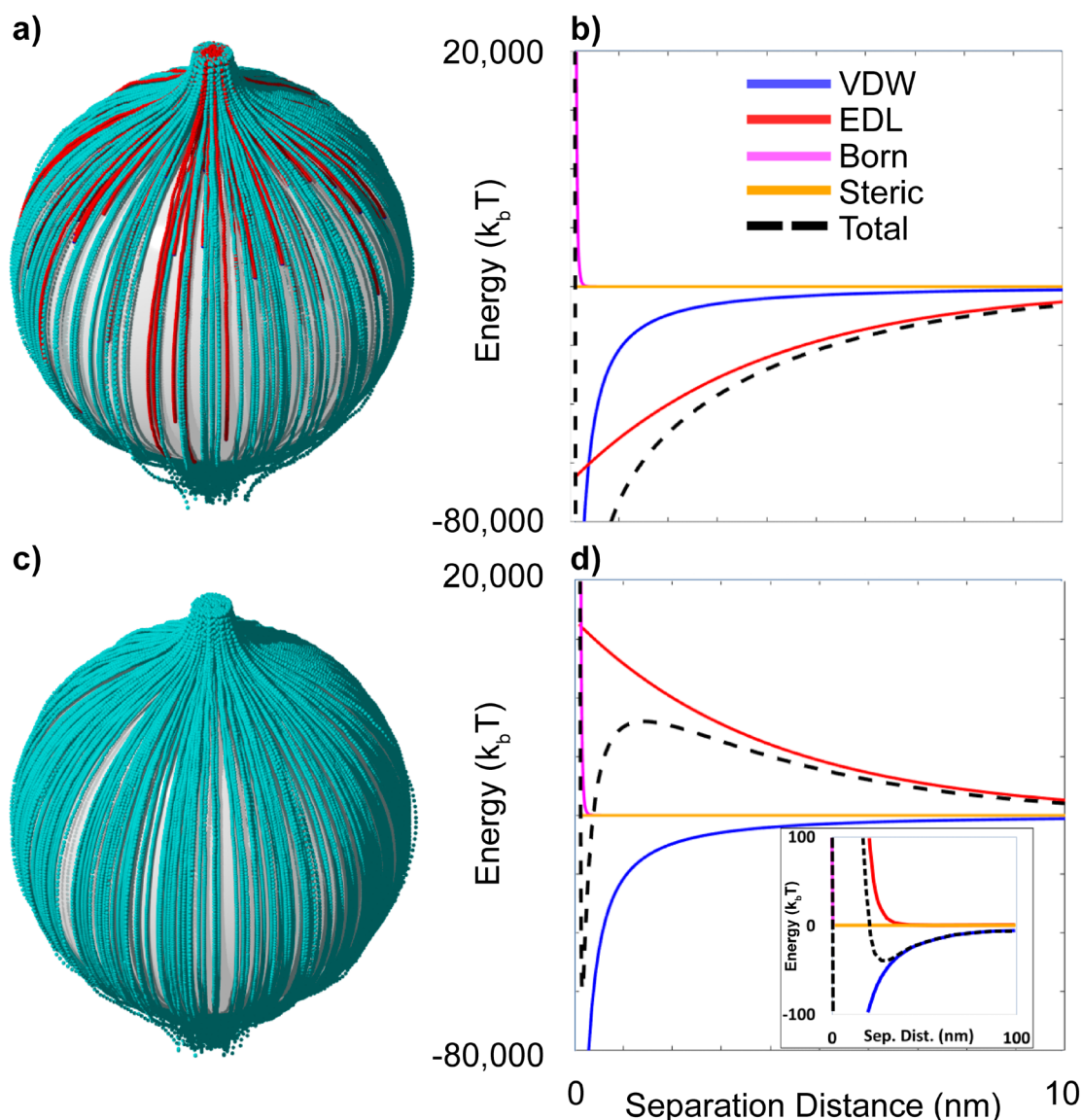
Figure 30 - a) Trajectory simulation with attachment trajectories in red and exit trajectories in cyan in the Happel unit cell and b) DLVO energy profiles for favorable conditions in contrast to c) and d) for unfavorable conditions. Under favorable conditions, there is no repulsive barrier to prevent attachment, and so colloid trajectories that are in near-surface fluid result in attachment. In contrast, under unfavorable conditions lacking nanoscale charge heterogeneity, a significant repulsive barrier ($\approx 8000\ k_bT$) prevents attachment, whereas secondary minimum attraction (inset of (d)) associates near-surface colloids with the grain surface such that they translate slowly downgradient in the near-surface domain (without contact).

The failure of theory to explain observed colloid retention under unfavorable conditions (having a significant repulsive barrier) has long led to the inference that while surfaces may appear homogeneously repulsive according to readily available measurements, nanoscale charge heterogeneity is present to locally reduce or eliminate the repulsive barrier and allow colloid attachment under unfavorable conditions.

The direct detection of nanoscale charge heterogeneity via spectrometric or spectroscopic means remains elusive, as further described in Section 5.2.4.1. The elusiveness of direct characterization of nanoscale charge heterogeneity arises because the significance of detected heterogeneity to colloid transport is not straightforward, which

59

The GROUNDWATER PROJECT   ©The Author(s)   Free download from gw-project.org

Anyone may use and share gw-project.org links. Direct distribution of the book is strictly prohibited.

motivates incorporation of simulated nanoscale charge heterogeneity into transport simulations to understand its potential influence as discussed in Section 5.2.4.2.

5.2.4.1 Detection of Nanoscale Heterogeneity

Detection of nanoscale heterogeneity on surfaces is possible using current analytical capabilities (e.g., electrophoresis, x-ray photoelectron spectroscopy, AFM force volume, or other techniques) as described by Shellenberger and Logan (2002), Taboada-Serrano and others (2005), and Drelich and Wang (2011). However, the detected heterogeneity depends on the resolution of the analysis: only beyond certain scales and spatial densities of attractive and repulsive domains will heterogeneity actually influence colloid transport (Elimelech et al., 2000; Wang & Keller, 2009) because the footprint of the heterogeneity has to be sufficiently large and spatially frequent to allow colloids to experience attraction (and thereby biased diffusion) to make contact (Pazmiño et al., 2014a). Various surface-sensitive techniques among microscopic, spectrometric, potentiometric, physicochemical adsorption, and others can identify spatial variation in topography (Rasmuson et al., 2017), chemical composition (Metwalli et al., 2006), surface charge (Charmas et al., 2004), and propensity to sorb (Prélot et al., 2003).

As explained in the nanoscale interactions section of this book (Section 4), the significance of detected nanoscale heterogeneity differs with the scale of interacting moieties: Sparse molecular-scale charge heterogeneity may be significant to adsorption of molecules but may not be significant to attachment of microscale colloids. The measurement most relevant to colloid transport is colloidal probe AFM at high spatial density across surfaces that show spatial variation (Shellenberger & Logan, 2002; Taboada-Serrano et al., 2005). However, to date, even these most relevant measurements lack the requisite resolution to define the scales and spatial densities of nanoscale heterogeneity relevant to colloid transport. Elucidating the relationship between atomic to molecular scale surface heterogeneity and nanoscale heterogeneity relevant to colloids is challenging.

5.2.4.2 Representative Nanoscale Charge Heterogeneity

A number of numerical approaches have been employed to represent nanoscale charge heterogeneity on surfaces (Bendersky et al., 2011; Duffadar & Davis, 2007; Duffadar & Davis, 2008; Duffadar et al., 2008; Ma et al., 2011; Ron et al., 2019a; Ron & Johnson, 2020; Shen et al., 2013). Common to these approaches is designation of heterodomains, discrete nanoscale zones of opposite charge to the mean surface, on either the grain or the colloid. The radius of the ZOI is far larger than molecular scales, and scales with Debye length and colloid size ranging from ≈15 nm to ≈115 nm for 0.1 µm and 6.8 µm diameter, respectively (Duffadar et al., 2008), for CML in MOPS-buffered water at 6 mM IS (NaCl) and pH 6.72 (Rasmuson et al., 2019a).

The point is that as colloids move into proximity with heterodomains, colloid-collector interactions will be net repulsive or net attractive depending on the fraction of the ZOI occupied by heterodomain(s). To allow attachment, a heterodomain (nanoscale attractive zone) must occupy a sufficient fraction of the ZOI to yield net attraction (Figure 10 and Figure 11). Because the ZOI increases with colloid size (Figure 10) and contracts with increased IS (Figure 11), colloid-collector interactions depend on colloid size and solution IS. This is in addition to whether colloid rotation or translation places sufficient heterodomain(s) within the ZOI to cause net attraction.

Because nanoscale heterogeneity is assumed to arise from random substitutions or other defects in mineral structure/chemistry—or from other randomly-distributed sorption, precipitation, or other processes—we expect a natural clustering of randomly located primary (smallest) heterodomain such that the spatial frequency of larger (clustered) heterodomains decreases according to a power law as discussed by Pazmiño and others (2014a), Ron and others (2019a), and Ron and Johnson (2020) and is illustrated in Figure 31.
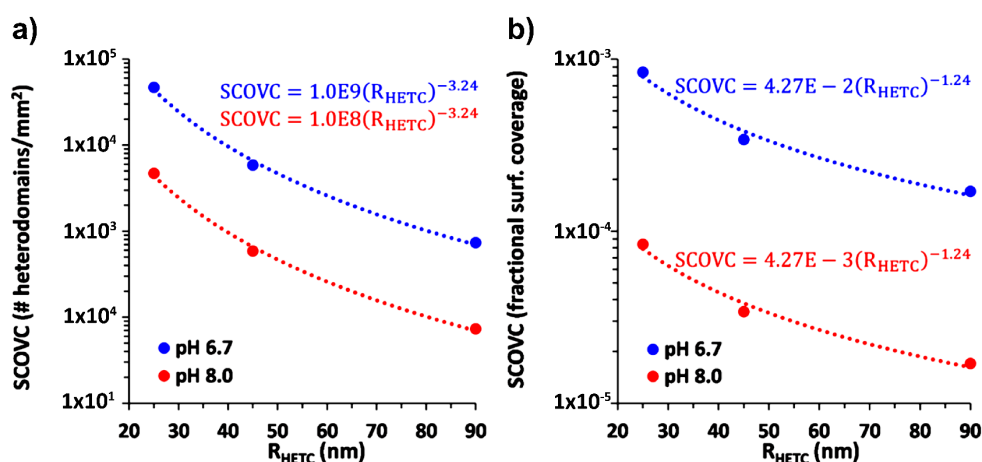
Figure 31 - Discrete representative nanoscale heterogeneity (DRNH) distributions utilized in colloid trajectory simulations with surface coverage (SCOVC) as a function of radius of heterodomains on a) the collector (R_{HETC}) expressed as number per area and b) fraction of total surface area. Heterodomain size distribution follows a power law (dotted lines) with decreasing abundance for increasing heterodomain size (from Ron & Johnson, 2020).

Random placement of primary (e.g., several nm scale) heterodomains on surfaces, with data file-tracking of their locations, has been performed to examine the kinetics of colloid attachment to surfaces with randomly located nanoscale heterogeneity (Shave et al., 2018), and to reproduce the variety of pore-scale colloid transport behaviors observed under unfavorable conditions (i.e., attachment, slow motion of near-surface colloids, re-entrainment and attachment of different fractions of the near-surface colloid population) as noted by Ma and others (2011). Two drawbacks of random placement to produce natural clustering are that

1. data file look-up increases numerical intensity, and
2. it becomes difficult to define the quantity of different cluster sizes.

61

To ease numerical intensity and explicitly represent heterodomain cluster sizes, an alternative approach is to implement discrete representative nanoscale heterogeneity (DRNH) in which a power law-distributed range of heterodomain sizes (cluster sizes) are represented at regularly spaced locations on the surface (Figure 32). Because colloid-surface interactions and the ZOI each depend on colloid size and solution IS, DRNH can be backed out via comparison of colloid trajectory simulations to experiments performed under varied colloid size, fluid velocities, IS, and pH values (Pazmiño et al., 2014a; Ron et al., 2019a; Ron et al., 2020; Trauscht et al., 2015).
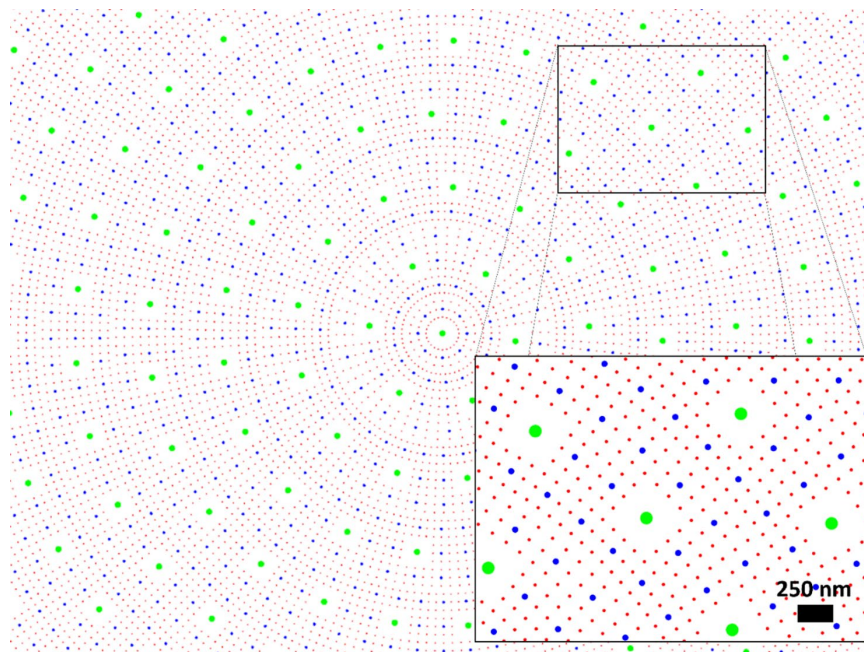
Figure 32 - Representation of DRNH (discrete representative nanoscale heterogeneity) on the collector surface. HETC (heterogeneity on the collector surface only) were represented by three R_{HETC}: 90 (green), 45 (blue), and 25 (red) nm with spatial frequency ratios of 1, 8, and 64, respectively. All three HETC were present on the simulated collector surface. In this representation, SCOVC (surface coverage colloid) was increased for visualization purposes.

It is worth noting that while a power law distribution of heterodomain sizes may sound complex, it is actually quite simple in that it effectively comes down to determining the heterodomain size capable of arresting a given size colloid under a given condition (e.g., a given IS). Once that relevant heterodomain size has been determined, heterodomains of significantly smaller size are irrelevant to the arrest of that colloid. These heterodomains presumably exist but do not impact the outcome in terms of attachment. Furthermore, while larger heterodomains can also arrest the colloid, they are far less plentiful—so they also do not significantly impact the outcome. Hence, the attachment behavior of a given colloid under a given condition is largely explained by a single size of heterodomain. The purpose of the power law distribution is therefore to explain attachment outcomes beyond a single size of colloid under a given condition, that is, for a range of colloid sizes across a

range of conditions, as explained by Bendersky and Davis (2011) and Ron and Johnson (2020).

The standing hypothesis that DRNH meaningfully represents nanoscale heterogeneity and can serve as a guide for efforts to directly detect nanoscale heterogeneity is supported by its ability to explain some experimentally observed colloid transport behaviors. Among them is the ability to produce a self-consistent explanation of both sides of the colloid attachment-detachment process under unfavorable conditions, wherein translation of the ZOI over a heterodomain of sufficient size produces net attraction that explains attachment (Pazmiño et al., 2014a); subsequent expansion of the ZOI upon IS reduction produces net repulsion thereby explaining detachment (Pazmiño et al., 2014b; Rasmuson et al., 2019a; VanNess et al., 2019).

The range of fractions of ZOI attained upon attachment may also explain the fact that only a fraction of colloids are detached in response to IS or flow perturbations (Pazmiño et al., 2014b; Rasmuson et al., 2019a; VanNess et al., 2019). Another transport behavior explained by mechanistic trajectory simulations implementing DRNH is the minimum collector efficiency observed for n-μ transition colloids under unfavorable conditions (Figure 17). This is explained in simulations as being due to these colloids having the lowest combined diffusion and hydrodynamic drag, which slows their kinetics of encountering nanoscale heterogeneity (Ron et al., 2019a).

The simulations also reveal that the smallest (nanoscale) colloids would produce the highest collector efficiencies under unfavorable conditions based on their physics of delivery (high diffusion), but their surface properties thwart attachment via repulsion (Ron et al., 2019a, 2019b). Explaining the near-favorable collector efficiencies of micro-particles under unfavorable conditions (Figure 17) required DRNH to be implemented on both the colloid and grain surfaces (Ron et al., 2020). Whether direct detection of heterogeneity on surfaces will support this expectation remains to be determined.

Mechanistic pore-scale trajectory simulations incorporating DRNH also reproduce the experimentally observed contrasts in pore-scale colloid transport behaviors (Figure 17), wherein colloid transport distances (and residence times) in the near-surface fluid domain prior to attachment is much greater under unfavorable relative to favorable conditions. Consistent with this, n-μ transition colloids have relatively low α values due their having the least combined fluid drag and diffusion, which together impede their encounter of heterodomains. Since fluid drag is driven by fluid velocity, the impacts of colloid size and velocity are interrelated, suggesting the possibility of development of a regression or correlation equation for α based on such simulations—a potential opportunity for continued research.

In summary, the process of colloid delivery to the grain surface (near-surface fluid domain) is equivalent under favorable and unfavorable conditions. What is distinguished under favorable versus unfavorable conditions is their transport in the near-surface fluid

63

domain, where under either condition they may attach; however, attachment occurs only under the unfavorable condition if they remain without attachment, or re-entrain back to the bulk fluid domain, as shown in pore-scale simulations (Figure 33) and experiments (Figure 16). Links to videos are provided in Figure 34, which can be viewed by clicking on the arrows in the caption.
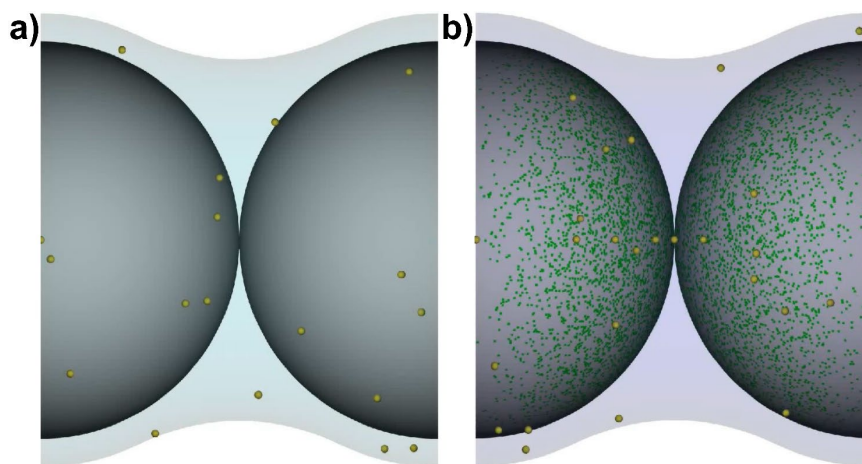
Figure 33 - Example simulations of colloid transport under a) favorable versus b) unfavorable conditions with discrete nanoscale heterogeneity (tiny green specs). Colloids in these mechanistic simulations are colored gold in the bulk fluid domain, magenta in the near-surface fluid domain, and blue when in contact with the grain surface. A major distinction between favorable and unfavorable conditions is the much less attachment and much longer residence times in the near-surface fluid domain under unfavorable relative to favorable conditions. To view the video contrasting favorable and unfavorable conditions, click here YouTube ▶.
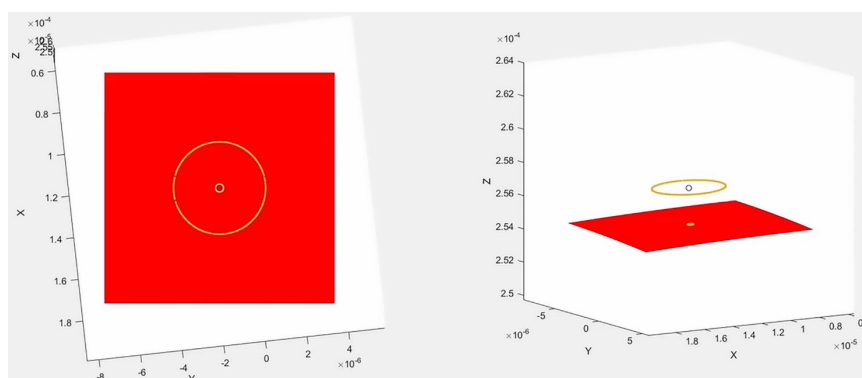
Figure 34 - A video demonstrating colloid trajectory simulations under unfavorable conditions in Parti-Suite can be viewed by clicking on the white arrow in the middle of the figure, then on "▶" in the next screen, or on YouTube ▶.

It is also highly useful to keep in mind that colloid attachment to nanoscale heterogeneity on surfaces under unfavorable conditions is effectively a three-step process.

1. The colloid is delivered to the near-surface fluid domain.
2. The colloid makes contact with heterodomains ("finds the landing pad" as simulated via diffusion and advection).
3. Finally, the colloid arrests on heterodomains once in contact ("sticks the landing" as simulated via torque balance).

64

Any of these three steps can be limiting for attachment depending on the physicochemical conditions involved (colloid size, fluid velocity, heterodomain size, surface chemistry, solution chemistry). The link demonstrating colloid trajectory simulation under unfavorable conditions in Parti-Suite associated with Figure 34 provides the information needed to undertake the corresponding Exercise 7⤵.

Consensus across the colloid transport literature is that nanoscale heterogeneity is responsible for colloid attachment under unfavorable conditions; however, the specific nature of heterogeneity remains unclear since direct detection has yet to be convincingly achieved. The method to account for the impacts of nanoscale heterogeneity described above (and incorporated into Parti-Suite) is one of many methods that we encourage readers to explore in the cited literature.

The treatment of charge heterogeneity discussed in this section is explicit, such that the degree of ZOI overlap with heterodomains varies among the attached colloid population, thereby leading to variations in residence times prior to attachment as well as propensity to detach, as described further in the continuum-scale simulations section. This explicit treatment of charge heterogeneity in Parti-Suite is in contrast to the implicit treatment of roughness. Because roughness asperities are currently implicit (i.e., they are not explicitly represented) in Parti-Suite, only the average impacts on hydrodynamic and colloid-surface interactions are represented. As such, the possibility is not accounted for in the AFM or trajectory modules of Parti-Suite that colloids may interact with, for example, low spots (e.g., concavities) or high spots (e.g., asperity tops) on the rough collector surface. An important future improvement to Parti-Suite will be the explicit representation of roughness to thereby predict the range of behaviors that can emerge from interaction with rough surfaces.

5.2.5 Impacts of Colloid Shape (and Type)

Up to this point, colloids have been assumed to be spherical. However, among colloids, pathogen shapes range from spheres to rods, while clays and red blood cells are shaped like platelets, and carbon nanotubes have the shape of filaments. Three primary impacts of colloid shape are:

1. radius of curvature governing colloid-surface interaction, since that radius depends on orientation relative to the surface for non-spherical colloids;
2. fluid drag impacts on translation and rotation; and
3. contact area attained upon attachment, which will be much greater for a flat face versus an edge (e.g., edge-on versus face-on attachment for clay platelets, and facet-scale ZOIs for crystalline magnetite nanoparticles, as described by Lecoanet et al., 2004).

Colloid structures such as pilli+, fimbriae, or flagella that can be associated with bacteria are not considered in this book.

Transport simulations that account for the impacts of aspect ratio across the range between spheres and rods demonstrate the minimum η associated with the n-μ size transition for spherical colloids is overprinted with (i.e., dampened or eliminated by) a local maximum in the center of that range for rod-shaped colloids. This is due to the impact of additional translation imparted by uneven rotation of rods near surfaces (Jeffery, 1922; Li & Ma, 2019; Liu et al., 2010; Ma et al., 2020; Salerno et al., 2006; Zhao & van Wachem, 2013) Such impacts of shape are only recently being parameterized and simulated. As such, this is an important opportunity for further research in colloid transport science.

5.3 Short-cuts to Pore-Scale Colloid Transport Simulation

Prior to the computational capacity we now enjoy, we were able to develop a number of approximate approaches to simulate pore-scale colloid transport, with varying degrees of usefulness. We describe these in the sections that follow and address misconceptions about their use:

1. the use of correlation equations based on mechanistic simulations as a shortcut to collector efficiencies (Section 5.3.1):
2. incorporation of a perfect sink boundary condition as a shortcut to the in-contact torque balance for attachment (Section 5.3.2);
3. comparison of arresting versus mobilizing energies as a shortcut to mechanistic pore-scale simulations (Section 5.3.3);
4. further examination of the impact of secondary minima (Section 5.3.4);
5. the common invocation of straining as a colloid retention mechanism (Section 5.3.5); and
6. the utility of the so-called attachment efficiency (α) as a shortcut to collector efficiencies under unfavorable conditions (Section 5.3.6).

5.3.1 Correlation Equations as a Shortcut to Collector Efficiency (η)

Mechanistic models underlying colloid filtration theory are time consuming to develop. Whereas mechanistic models are now readily accessed through freeware like Parti-Suite, easy prediction was previously provided through heuristic expressions fit to mechanistic simulations run under a range of conditions. These heuristic expressions are called *correlation equations* composed of dimensionless groups of relevant physicochemical parameters that are fit to produce results (values of η) approximating those from the mechanistic simulations.

Such correlation equations currently exist only for favorable attachment scenarios (repulsive barrier absent) since the underlying mechanistic models incorporating mean-field xDLVO interactions (nanoscale heterogeneity absent) predict no attachment under unfavorable attachment scenarios (as described subsequently). Three (or more) distinct dimensionless numbers are used in the correlation equations to represent interrelated mechanisms for intercepting the surface:

66

1. interception via fluid drag alone;
2. diffusion-enhanced interception; and
3. sedimentation-enhanced interception.

Separate contributions to the overall η are determined for each dimensionless number: η_I, η_D, and η_G, respectively (Table 1, Table 2, Table 3). Further details regarding dimensionless parameters and correlation equations are provided in Molnar and others (2015).

Table 1 - Correlation equations for η. Dimensionless parameters used in correlation equations are provided in Table 2 (from RT 1976, Rajagopalan & Tien, 1976; TE 2004, Tufenkji & Elimelech, 2004; LH 2009, Long & Hilpert, 2009; NG 2011, Nelson & Ginn, 2011; MHJ 2013, Ma, Hradisky & Johnson, 2013a, 2013b).

Source	Definition
RT 1976	$\eta = \gamma^2 \left[A_s N_{Lo}^{1/8} N_R^{15/8} + 0.00338 A_s N_G^{1.2} N_R^{-0.4} + 4 A_s^{1/3} N_{PE}^{-2/3} \right]$
TE 2004	$\eta = 2.4 A_s^{1/3} N_R^{-0.081} N_{Pe}^{-0.715} N_{vdw}^{0.052} + 0.55 A_S\, N_R^{1.675} N_A^{0.125} + 0.22 N_R^{-0.24} N_G^{1.11} N_{vdw}^{0.053}$
LH 2009	$\eta = (15.56 \pm 0.21) \dfrac{(1-\epsilon)^3}{\epsilon^3} N_{Pe}^{-0.65 \pm 0.023} N_R^{0.19 \pm 0.03} + 0.55 A\ \ N_R^{1.675} N_A^{0.125} + 0.22 N_R^{-0.24} N_G^{1.11} N_{vdw}^{0.053}$
NG 2011	$\eta = \gamma^2 \left[2.4 A_s^{1/3} \left(\dfrac{N_{PE}}{N_{PE}+16} \right)^{0.75} N_{Pe}^{-0.68} N_{Lo}^{0.015} N_G^{0.8} + A_s N_{Lo}^{1/8} N_R^{15/8} + 0.7 \left(\dfrac{N_G}{N_G+0.9} \right) N_R^{-0.05} N_G^{1.1} \right]$
MHJ 2013	$\eta = \gamma^2 \left[\dfrac{8 + 4(1-\gamma) A_s^{1/3} N_{Pe}^{1/3}}{8 + (1-\gamma) N_{Pe}^{0.97}} N_{Lo}^{0.015} N_{Gi}^{0.8} N_R^{0.028} + A_s N_R^{15/8} N_{Lo}^{1/8} + 0.7 N_R^{-0.05} N_G \dfrac{N_{Gi}}{N_{Gi}+0.9} \right]$

Table 2 - Dimensionless Numbers in Correlation Equations (parameters in dimensionless numbers are provided in Table 3).

Parameter	Definition	Description
N_{Lo}	$\dfrac{A_{132}}{9\pi\mu a_p^2 V_{sup}}$	London number, attractive versus mobilizing interactions
N_R	$\dfrac{a_p}{a_g}$	aspect ratio of fluid shell radius to grain radius in the Happel unit cell
N_G	$\dfrac{2 a_p^2 (\rho_p - \rho_f) g}{9 \mu V_{sup}}$	Gravity number, settling versus mobilizing interactions
N_{Gi}	$\dfrac{1}{N_G + 1}$	Inverse gravity number
N_{Pe}	$\dfrac{2 V_{sup} a_g}{D_{BM}}$	Ratio of advective to diffusive transport
N_A	$\dfrac{A_{132}}{12\pi\mu a_p^2 V_{sup}}$	Attraction number, attractive versus mobilizing interactions
N_{vdw}	$\dfrac{A_{132}}{k_B T}$	VDW number, attractive versus thermal interactions

Table 3 - Parameters in Dimensionless Numbers

Parameter	Definition	Units	Dimensions
a_p	Particle radius	m	L
a_g	Collector radius	m	L
V_{sup}	Superficial (approach) velocity	ms^{-1}	LT^{-1}
A_{132}	Hamaker constant	J	ML^2T^{-2}
D_{BM}	Stokes-Einstein bulk diffusion coefficient	m^2s^{-1}	L^2T^{-1}
k_B	Boltzmann constant: 1.3806×10^{-23}	JK^{-1}	$ML^2T^{-2}\theta^{-1}$
g	Gravitational acceleration: 9.8067	ms^{-2}	LT^{-2}
ρ_p	Particle density	kgm^{-3}	ML^{-3}
ρ_f	Fluid density	kgm^{-3}	ML^{-3}
μ	Fluid viscosity	$kgm^{-1}s^{-1}$	$ML^{-1}T^{-1}$

Users of correlation equations should examine the corresponding publications to be aware of the range of conditions considered in their development, since use of these equations will be invalid beyond the specified ranges of grain size, colloid size, fluid velocity, colloid density, orientation of flow relative to gravity, porosity, and other characteristics. Notably, the vast majority (if not all) correlation equations were developed for mechanistic simulations under the condition where flow was aligned concurrent with gravity (downward flow), whereas the majority of reported column-scale experiments align flow counter-current to gravity (upward flow). Hence, for upward flow experiments with microscale or non-neutrally buoyant colloids, correlation equations may significantly mis-predict η due to mis-prediction of η_G since they were developed from mechanistic simulations with opposite orientation of flow relative to gravity.

It is far more preferable to use mechanistic simulations to predict η for the many experimental conditions that do not happen to match the conditions used to develop existing approximating correlation equations. This mechanistic simulation capability is provided in the trajectory modules of Parti-Suite. However, for easy, rapid, and qualitative prediction with the caveat described above, a correlation equation module is provided in Parti-Suite (CorrEqn) to examine the impacts of different parameters on η.

Misconception: Correlation equations are colloid filtration theory and correlation equations are empirical.

a. The truth is that correlation equations are a derivative of filtration theory for those who do not wish to perform numerical simulations. They are approximate functions used to describe the results of mechanistic numerical simulations under a given set of conditions. They serve as quick estimations without having to perform numerical simulation. However, as such, they represent only a given range of input parameter values used in the numerical simulations. They are also limited to whatever orientations of gravity relative to flow were set in the original numerical simulations. So, they reflect the specific range of colloid sizes, grain sizes, and fluid velocities input into the simulations.

Nelson and Ginn (2011) highlighted the fact that preceding correlation equations gave non-physical collector efficiencies (exceeding unity) under low fluid velocity conditions. The issue was not a limitation in the underlying numerical models, but instead in the range of parameter values that had been input to those models that produced the results from which the correlations were developed. That is, low velocities were not included in the range of input parameters, and so the fits (correlations) were unable to predict physically meaningful values (collector efficiencies) when lower velocities were plugged into them.

b. One should use correlation equations only after understanding the range of parameter values used for the underlying numerical results (e.g., velocities, colloid sizes, grain size, porosity). For quick exploration of the influence of physical parameters, Parti-Suite includes a module (CorrEqn) that utilizes correlation equations to approximately predict η under favorable conditions.

c. With dramatically increased computational capacity over the past two or so decades, one does not need to rely on correlation equations. Particle trajectory simulation freeware such as Parti-Suite provides the ability to directly perform mechanistic trajectory simulations. Physicochemical parameters can be changed as desired without having to rely on conditions approximated in the correlation equations.

5.3.2 Perfect Sink Boundary Condition as a Shortcut to In-Contact Torque Balance

In the preceding literature, an in-contact torque balance was often not performed at the grain surface because of computational intensity. Instead, attachment was assumed once the colloid reached within a specified separation distance from the surface (e.g., 1 nm). This approximation is reasonable under favorable conditions with the modest fluid drag forces typical of groundwater. A good exploration of failure of this perfect sink approximation under high fluid velocities is provided by VanNess and others (2019).

Of course, the perfect sink condition is likely to fail under unfavorable conditions—even under groundwater velocity conditions—due to the reduced adhesion force associated with unfavorable conditions. We also note that the *sink* part of this phrase refers to the fact that attached colloids are assumed to not impact the attachment of colloids that subsequently intercept that location on the grain. This *sink* assumption can apply to both the *perfect sink* and *in-contact torque balance* approaches, since in both approaches the arrest Oof colloids on the grain surface is often assumed to not impact the subsequent arrest of colloids on that portion of the surface. As described in Section 6.2.3.5, an opportunity for further development of colloid transport simulations is to implement colloid-colloid interaction at the surface, which in Lagrangian trajectory simulations requires interprocessor communication to allow mobile colloids to "be aware" of attached colloids.

Colloid delivery and attachment are easily examined in trajectory simulations in different collectors in Parti-Suite trajectory codes under both contact torque balance or perfect sink attachment conditions. The Matlab-based Happel collector simulator

69

(Traj-Hap) is the best module for training new users, who—if they wish—can then proceed to perform simulations in other collectors using the Fortan executables.

5.3.3 Comparison of Arresting and Mobilizing Energies as a Shortcut to Mechanistic Pore-Scale Simulations

The decrease in colloid-surface repulsion with increased IS under unfavorable conditions (Figure 7) indicates that experimentally observed pore-scale colloid attachment efficiencies (η) should increase with increased IS. This expected qualitative agreement between DLVO or xDLVO theory and experiment has been long established for both pore-scale (Ron et al., 2019a; Ron & Johnson, 2020) as demonstrated in Figure 17 and continuum-scale colloid transport experiments (Li et al., 2004; Li & Johnson, 2005; Tong & Johnson, 2006a). Such agreement also qualitatively explains colloidal phenomena in broader contexts beyond groundwater such as the aggregation and settling of clays in river mouths upon discharge to estuaries and coasts where mixing with seawater raises solution salinity (IS).

Quantitative agreement between theory and experiment is more difficult to attain. In one simplified approach to quantitative comparison that neglects the impacts of fluid drag and gravity, the intrinsic energy of colloids driving Brownian diffusion is compared to DLVO or xDLVO energies to draw conclusions regarding the possibility of (Figure 35)

1. overcoming an energy barrier to attach in a primary minimum,
2. overcoming an energy barrier to detach from a primary minimum, and
3. overcoming an energy barrier to re-entrain from a secondary minimum.

According to the equipartition theorem of classical physics, molecular intrinsic energy is on average 1.5 k_bT in three dimensions and 0.5 k_bT in any given dimension. This has been adopted by colloid transport researchers to compare colloid diffusive energies to colloid-surface interaction energies. Since the 1.5 k_bT in three dimensions represents an average intrinsic energy, the possibility of overcoming the barrier to attachment in primary minima—outcome (a)—is not fully prevented until the energy barrier exceeds approximately (20 k_bT), as determined by simulating colloid trajectories using mechanistic force/torque balance including representation of diffusion (Johnson et al., 2007a). However, calculated repulsive energy barriers based on measured ζ-potentials typically exceed this 20 k_bT threshold by orders of magnitude, preventing outcome (a) shown in Figure 35 in the vast majority of experimental systems despite direct observation of colloid arrest and attachment in those systems (Elimelech & O'Melia, 1990; Pazmiño et al., 2014a; Ron & Johnson, 2020).
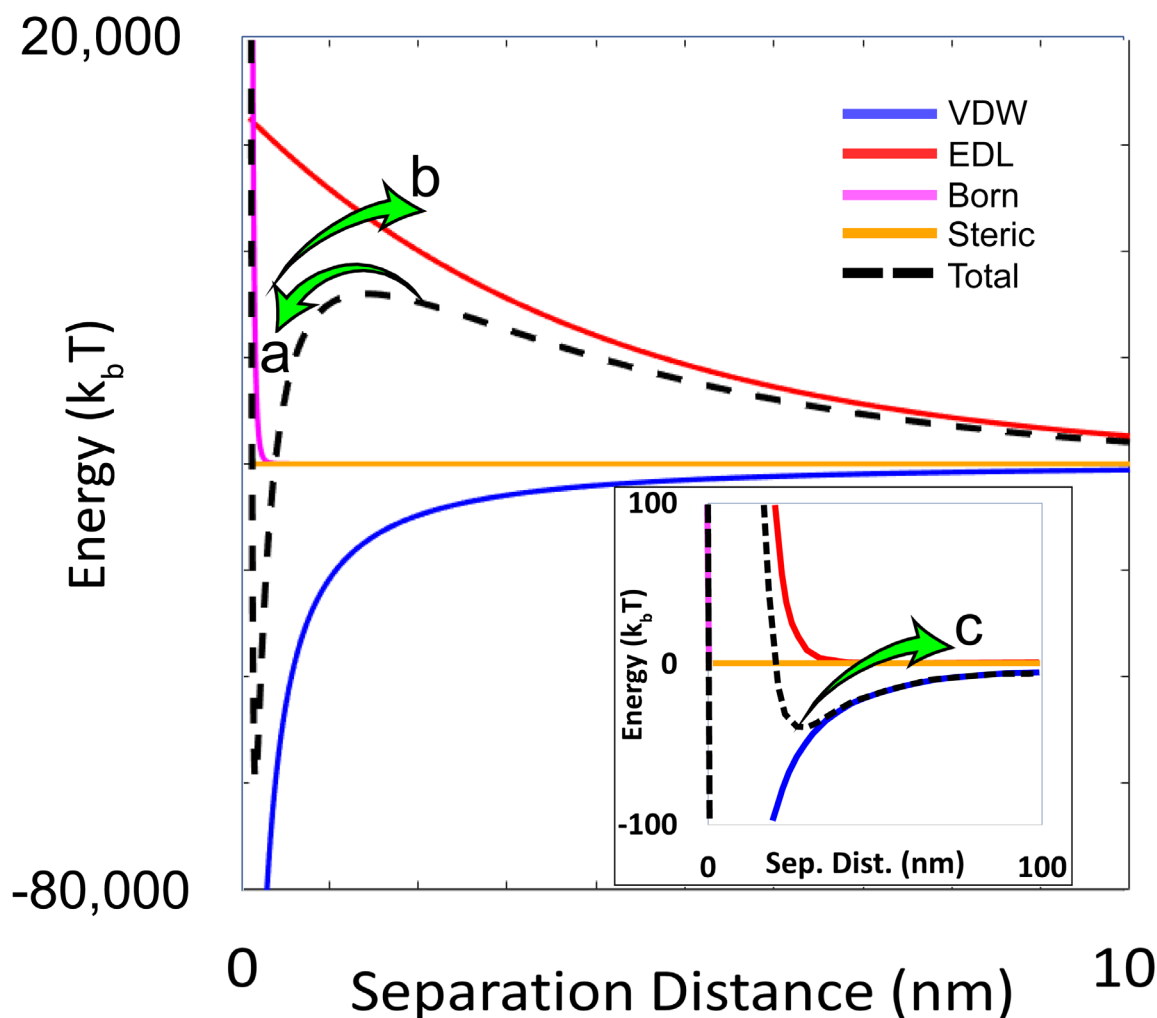
Figure 35 - Interpreting xDLVO profiles in terms of "label a" overcoming an energy barrier to attach in a primary minimum, and "label b" overcoming an energy barrier to detach from a primary minimum, and "label c" overcoming an energy barrier to re-entrain from secondary minimum. The VDW interaction increases via power law with decreasing separation distance such that it steepens similarly despite the vastly different y-scales in the inset and main figures.

With respect to outcome (b) of Figure 35, a primary objective is to explain observed release of colloids in response to IS reduction. However, the barrier to detachment from the primary minimum is little changed in response to IS reduction (Pazmiño et al., 2014b) since the difference between primary minimum and repulsive barrier maximum hardly decreases with decreased IS (Figure 7). Some researchers invoke increased repulsive contact forces (steric or repulsive LAB) to decrease the primary minimum depth (Figure 8), and thereby decrease the barrier to colloid detachment (VanNess et al., 2019). However, addition of repulsive contact forces to explain observed detachment has limited utility if the repulsive barrier is too large to explain attachment in the first place (VanNess et al., 2019). To be convincing, simulations should be capable of self-consistent explanation of both sides of the process (attachment and detachment) as noted by VanNess and others (2019). This possibility is further explored in Section 5.2.4.

With respect to outcome (c), we cannot over-stress the fact that the term *re-entrainment* is used for escape from a secondary minimum. Release from secondary minima is re-entrainment rather than *detachment* because retention in secondary minima is by definition non-contact and far outside the reach of contact forces such as Born, LAB, and steric that define contact and drive colloid arrest, as discussed in Section 5.2.2. We provide a further discussion about secondary minimum interactions and the distinction between attachment and retention in Section 5.3.4.

Misconception: A shallow primary minimum and low energy barrier means that equilibrium partitioning will occur, and that filtration theory does not apply.

A low energy barrier to detachment (i.e., low barrier to attachment plus a shallow primary minimum) relative to the often-assumed intrinsic energy of colloids adopted from the equipartition theorem ($1.5\,k_bT$ in three dimensions) does indeed indicate that colloids can enter and leave primary minimum contact by diffusion. However, this circumstance speaks to the reversibility of attachment that follows colloid delivery to the near-surface fluid domain. It does not speak to the rate of delivery to the near-surface fluid domain, which is not an equilibrium process due to relatively low colloid diffusion.

Misconception: The qualitative agreement with xDLVO calculations explains colloid attachment under unfavorable conditions.

Many studies show that barrier height is reduced by three factors:

1. increased IS,
2. roughness, and
3. decreased pH.

These studies also show decreased barrier height corresponds to increased attachment. However, the barrier heights remain insurmountable according to force and torque balance, which requires consideration of other explanations for observed colloid attachment under unfavorable conditions. One possible explanation is that the expressions for the various colloid-surface interactions are not quantitatively correct, and that a more correct expression would quantitatively reflect experimental observations. However, as reviewed in Section 5.2, incorporation of nanoscale heterogeneity explains not only observed colloid attachment under a given set of unfavorable conditions, but also explains such attachment as a function of colloid size (Figure 17). Although it is doubtful that changes in one or more expressions quantifying colloid-surface interaction will succeed in quantitatively explaining attachment under unfavorable conditions as a function of colloid size, the possibility cannot be ruled out.

5.3.4 Retention in and Re-entrainment from Secondary Minima

The inability to mechanistically predict colloid attachment (let alone detachment) under unfavorable conditions led many researchers to interpret colloid retention and re-entrainment solely in terms of association with secondary minima. This attribution is

partly correct since pore-scale experiments under unfavorable conditions show both arrested colloids as well as the existence of slow-moving near-surface non-arrested colloids that are not present under favorable conditions (Figure 16). This demonstrates colloid association with both primary and secondary minima under unfavorable conditions (Johnson et al., 2010; Johnson et al., 2018; Pazmiño et al., 2014a, b; Ron et al., 2019a; Tong & Johnson, 2006a).

Secondary minimum-associated colloids are, in fact, re-entrained in response to reduced IS in experiments (Franchi & O'Melia, 2003; Hahn et al., 2004); this process is corroborated by mechanistic trajectory simulations and in energy comparisons since the depth of the secondary minimum decreases with decreased IS (Figure 7). Hence, at the pore network level (continuum-scale), it is reasonable to expect that at least some of the experimentally observed re-entrainment in response to IS reduction represents secondary minimum-associated colloids. However, in pore-scale experiments under unfavorable conditions, attached (immobilized) colloids can detach in response to decreased IS (Brow et al., 2005; Johnson et al., 2010; Pazmiño et al., 2014a; Tong & Johnson, 2006a). Neither their attachment nor detachment are explained by simple energy comparisons.

Misconception: Attachment Occurs in Secondary Minima (It does not!).

An unfortunate misconception that has arisen and taken hold in colloid transport science is the notion that attachment (arrest) of colloids can be mechanistically explained on the basis of non-contact secondary minimum association (Johnson et al., 2009; Torkzaban et al., 2008). This notion, which we refer to as *secondary minimum surface friction*, is incorrect for the following reasons:

1) Attachment involves contact. Secondary minimum association is by definition non-contact (Israelachvili, 2011). As described in Section 5.2.2, arrest (attachment) requires primary minimum interaction (contact), which involves one or more among repulsive Born, repulsive LAB, and repulsive steric interactions in the primary minimum (e.g., VanNess et al., 2019), as described in Section 4. These interactions extend to separation distances up to several *nm*, far lower than the reach of the repulsive barrier. The repulsive barrier occupies intermediate separation distances—separating contact interactions from non-contact interactions and defining the boundaries of the secondary minimum that occupy separation distances ranging from several tens of *nm* to hundreds of *nm*. It is therefore self-contradictory to invoke surface friction (contact) at separation distances corresponding to secondary minimum.

2) As such—since there is no contact area from which to define the lever arm for the adhesive torque—one cannot perform a meaningful torque balance to examine attachment in secondary minima. The repulsive forces that define contact (Born, LAB, steric) do not reach beyond several nm; thus, the deformation (contact area) defined by contact mechanics (Section 4.2.2.2)

73

cannot be assumed to apply to secondary minimum interactions. The approach using contact mechanics in secondary minima is an unfortunate mash-up of contact mechanics and non-contact interactions, that researchers should not perpetuate.

The Maxwell approach (Hahn et al., 2004) examines outcome (c) in Figure 35 by comparing the kinetic energy distribution (derived from velocity distribution of colloids according to diffusion) to the depth of the secondary minimum (e.g., k_bT). Colloids in the Maxwell-Boltzmann-informed kinetic energy distribution having kinetic energies that exceed the secondary minimum are assumed to re-entrain from the secondary minimum. The Maxwell approach has been used by many authors as a shortcut for predicting re-entrainment of colloids that are associated with (but which are not arrested in) secondary minima. This process is more completely represented in mechanistic force/torque simulations where the range of diffusive forces is also represented in addition to fluid drag, gravity, and other forces as is performed in the mechanistic trajectory simulation modules in Parti-Suite.

Misconception: The Maxwell velocity (kinetic energy) distribution can be applied to attached colloids.

Some authors have attempted to apply the Maxwell approach to examine the potential detachment of attached colloids. This is incorrect—not only because colloids do not attach in secondary minima (as described above) but also for the following reasons:

> *The Maxwell distribution applies to colloids unbounded by surfaces! Authors who attempt to apply the Maxwell distribution to attached colloids must first answer the question: What is the velocity distribution of an arrested (primary minimum) colloid? Whereas attached colloids must certainly still hold intrinsic energy, the fact that they are immobile must certainly mean their velocity distribution (their kinetic energy distribution) must be greatly reduced relative to that determined by Maxwell for fully mobile unbounded colloids.*

To summarize, the secondary minimum plays a role in colloid retention, but it must be stressed that this non-contact force does not by itself cause colloid arrest (attachment). Retention of secondary minimum-associated colloids (slowly mobile) is therefore defined by the temporal and spatial scales of observation, as is further explored in Section 6.

5.3.5 Straining as a Shortcut Pore-Scale Mechanism for Colloid Retention

Straining has often been invoked to explain the retention of colloids in granular media that are assumed (typically without substantiation) to contain no heterogeneity (Johnson et al., 2011). Straining is the capture of colloids in pore throats too small to pass such as rinsing seeds in a strainer (McDowell-Boyer, et al., 1986). If straining were the removal mechanism in filtration, our natural and engineered sand filters would rapidly clog, rendering them useless. Instead, to be effective, sand filtration in both engineered and

natural systems must allow colloids to penetrate into the porous media and attach on grain surfaces even though the colloids are much smaller than the pore throats (Figure 36).
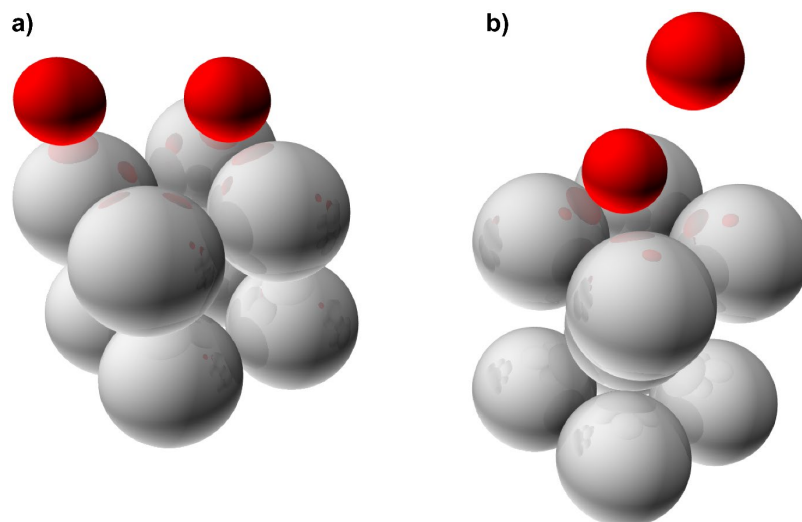
Figure 36 - Unit cells for a) simple cubic packing and b) dense cubic packing (grains are metallic gray) into which enter colloids (red spheres larger than pore throats). Will the red colloids be strained? Yes!

The issue is not presence versus absence of clogging, but rather the timescale of effective filtration prior to clogging. Once retention passes the "clean-bed" threshold, colloid accumulation will eventually begin to clog the pore space, which is why we periodically reverse flow and fluidize slow sand filters used in water treatment.

While many studies have inferred straining as the primary process of colloid retention in packed columns, weakness in these inferences have been reviewed (Johnson et al., 2011). This is not to say straining does not occur, since it does (e.g., Auset & Keller, 2006). Rather, for mechanistic purposes, it simply means that straining is uninteresting. Beyond a given threshold colloid size, there is no dependence of attachment on colloid size, fluid velocity, and the colloid-grain interactions described earlier (e.g., Figure 30). Straining is governed simply by the pore throat size distribution of the granular media (a continuum-scale characteristic). Yet, strangely, colloid transport studies rarely provide or utilize size distribution information when they invoke straining as the mechanism of retention.

Another process related to straining is *hydrodynamic bridging*, which is defined as the simultaneous arrival of multiple colloids at the pore throat wherein they together are strained (Lin et al., 2021). Given the difficulty and unclear significance of distinguishing processes such as hydrodynamic bridging from *funneling*—and subsequent colloid-colloid attachment at pore throats (Tong et al., 2008)—we do not further distinguish hydrodynamic bridging, funneling, and colloid aggregation in solution, since the end result for all three processes is straining, where aggregates form, wherever and whenever they are, in pore throats too small to pass.

Three misconceptions regarding straining:

1) Increasing retention with decreasing grain size reflects straining.

    Mechanistic simulations (and even correlation equations) show that as grain size decreases, filtration increases. This is not simply a matter of increasing surface area to volume ratio as grain size decreases since—as described earlier—the low diffusion coefficients of colloids do not guarantee their interception of surfaces. For a given porosity, the fluid envelope thickness decreases with decreasing grain size. This drives increased filtration with decreasing grain size. Increased retention with decreased grain size does not prove straining as a mechanism of retention; one can quantitatively and mechanistically examine this via Parti-Suite trajectory modules.

2) Straining does not involve attachment.

    A period or state of inactivity or equilibrium—a stasis—of being trapped in a pore throat but not in contact with grain surfaces is highly unlikely. The fluid flow upstream of (behind) the colloid will force it into contact with the surfaces in which it is trapped. One can prove this using Parti-Suite mechanistic simulations in the simple or dense cubic packing collectors (Fortran executables only). One will find that beyond a certain colloid size, colloids entering the collector will be forced into primary minimum contact (attachment) with the grains that form the pore throat (straining).

3) Straining is complex.

    Straining as a pore-scale process is simple since colloids can either pass or not pass beyond a given pore throat. However, complexity may arise from the distribution of pore throat sizes or the distribution of colloid sizes via aggregation. Defining colloid size can also be complicated if surface molecules extend into solution to lengths that are significant relative to the colloid size. However, these complexities affect both filtration and straining. In the absence of these complications, straining of a mono-disperse colloid suspension in porous media of a uniform grain size is a binary function of the ratio of colloid and pore throat sizes (pass/no pass). In contrast, filtration of a mono-disperse colloid suspension in porous media of a uniform grain size is a function of colloid size (diffusion, settling, fluid drag), grain size, fluid velocity, porosity, and colloid-surface interaction as one can explore using the trajectory modules in Parti-Suite.

5.3.6 Attachment Efficiency (α) as a Shortcut to Unfavorable Collector Efficiencies

The gap between unfavorable and favorable η values is often expressed as a ratio called the *attachment efficiency* ($\alpha = {}^{\eta_{un}}\!/_{\eta_{fav}}$). This concept follows from the hypothesis that a correlation equation can be developed to predict α from parameters ranging across relevant colloid sizes, colloid and collector surface properties (including ζ-potential), and fluid velocities (Bai & Tien, 1996; Chang et al., 2009; Elimelech, 1992; Trauscht et al., 2015; Vaidyanathan & Tien, 1989). These studies attempted to develop regression equations to predict α by regression of experimentally determined α values to experimental parameters.

The regressions developed for α represent a far less robust predictive approach relative to the correlation equations previously developed to predict collector efficiencies (η) under favorable conditions. The correlation equations for η under favorable conditions are approximations of predictive mechanistic simulations; as such, they are not merely empirical, although they are limited in that they were developed for a limited range of parameter values. In contrast, the regression equations for α currently lack grounding in predictive mechanistic simulations because, as described earlier, the calculated repulsive barriers are too large to predict attachment. For this reason, users of regression equations to predict α should be highly suspicious of their accuracy.

Major challenges in developing predictive regression equations for α include the fact that α varies dramatically with colloid size as indicated by the gap between favorable and unfavorable η values (Figure 17). Furthermore, α also varies with fluid velocity (Johnson et al., 2011). Quantifying attachment under unfavorable conditions, whether it is cast as η or α, requires functional mechanistic simulations that explain observed colloid attachment under unfavorable conditions. Nanoscale charge heterogeneity is discussed in Section 4.

Misconception: The attachment efficiency (α) under unfavorable conditions reflects only the chemistry, and so is a single value across physical parameters such as colloid size or fluid velocity.

Attachment efficiency (α) varies with colloid size under a given condition (Ron et al., 2019a) as shown in Figure 17. Whereas collector efficiency (η) can be considered to reflect physical processes, attachment efficiency (α) reflects a combination of chemical and physical processes as demonstrated by the impact of colloid size on α. Furthermore, explaining breakthrough-elution curves and profiles of retained colloids requires recognition of multiple efficiencies for retention and attachment (even for a single colloid size), as explored in Johnson and others (2018) and Johnson (2020). This is discussed further in Section 6.2.

5.4 Solute Versus Colloid Transport at the Pore Scale

The range and magnitude of solute-surface interactions are orders of magnitude lower than those for colloid-surface interactions (Israelachvili, 2011), whereas solute diffusion is much greater than that of colloids. Both of these differences are driven by the fact that solutes are tens to hundreds of times smaller than the smallest colloids (e.g., nanoparticles). Solutes can be generalized as moving like mosquitos whereas, in contrast, colloids move like blimps (Figure 37). Under the slow velocities (e.g., m/day) associated with typical groundwaters, solutes can be expected to reach surfaces surrounding a pore, but the ratio of mobilizing versus arresting energies (diffusive to adhesive energies) is far greater for solutes relative to colloids. This makes delivery to surfaces—and reversibility of attachment to surfaces—far greater for solutes relative to colloids (Hunt & Johnson, 2016).
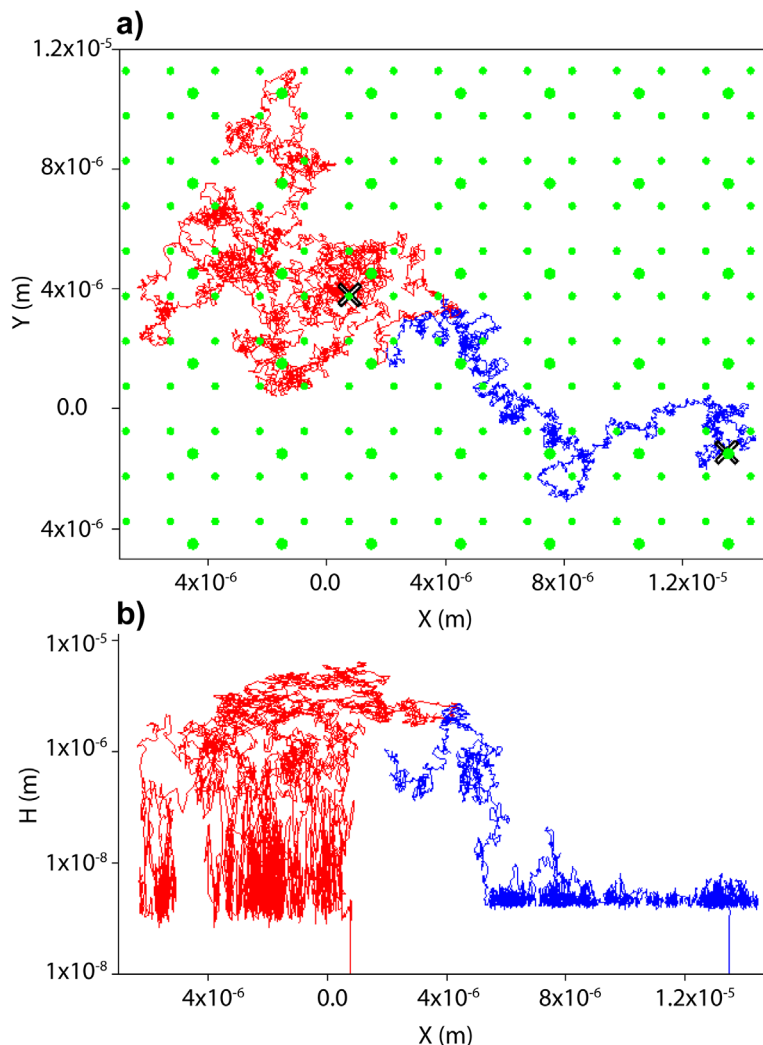
Figure 37 - a) Plan view and b) cross view of two representative colloid trajectories under unfavorable conditions over a collector surface (located at H=0 in b). The 0.25 μm colloid (red) is more mobile due to increased diffusion and its behavior resembles a mosquito. In contrast, the 1.95 μm colloid (blue) has reduced diffusion and a deeper secondary energy minimum, which results in less vertical mobility and slow lateral movement while near the surface, resembling the tracking behavior of a bloodhound.

Solutes therefore move more readily than colloids to and from grain surfaces. As such, a local equilibrium may be achieved for solutes between solution and surface concentrations under typical groundwater velocities (*the local equilibrium assumption*). The equilibrium that can be attained by solutes between solution and surface concentrations is described by a sorption isotherm, which provides the equilibrium relationship between solute on sediment (C_{sed}: e.g., mg_{solute}/mg_{sed}) and solute in water (C: e.g., mg_{solute}/ml_{soln}) at a given temperature, as shown in Equation (65) for a linear isotherm.

$$C_{sed} = K_d C \quad \rightarrow \quad \frac{dC}{dt} = \frac{\left(\frac{1}{K_d}\right) dC_{sed}}{dt} \tag{65}$$

where:

K_d = equilibrium constant for distribution of solute between sediment and solution (L^3M^{-1})

The equation states that the sediment concentration changes inversely (and in this case linearly) to the aqueous concentration to maintain the proportion between the two concentrations according to K_d. In other words, what leaves the water goes to the sediment and vice versa. This relationship can also be non-linear, although we will leave that unaddressed here.

Colloids, in contrast to solutes, have relatively low diffusion such that colloids being advected and dispersed in a pore do not necessarily reach a surface (as described in detail in Section 5.2). However, when colloids do reach a surface and attach, their relatively strong adhesion force and relatively low diffusion keeps them on the surface until some perturbation drives detachment (e.g., capillary forces from drainage or imbibition of water). Their intrinsic energy is typically too weak to provide the kinetic energy to break them free of primary minimum surface attraction. Hence, the rate of colloid loss from solution is described largely by an irreversible kinetic rate coefficient described in Equation (66).

$$\frac{dC}{dt} = -k_f C \tag{66}$$

where:

k_f = irreversible filtration rate coefficient (T^{-1})

Equation (66) says that colloids leave the water at a characteristic rate (k_f) and never return. Since the net transfer of colloids to the sediment is irreversible, colloids simply accumulate on the sediment unless some perturbation in flow or solution chemistry forces their detachment. Of course, degrading solutes also leave the water irreversibly, so the contrast highlighted here is between non-degrading solutes and colloids.

The impacts of reversible (equilibrium) and irreversible (fully kinetic) pore-scale interactions with surfaces on transport behavior at the continuum scale and the upscaling process that relates η (collector efficiency) to the kinetic colloid filtration rate coefficient (k_f) are reviewed in Section 6.

6 Continuum-Scale (Pore Network) Colloid Transport

This final section describes continuum-scale colloid transport for which the term *continuum* as used here refers to the continuum of pores (networks of pores) at scales greater than those at which pore-scale colloid transport behaviors can be resolved. The term continuum is also used in other contexts (e.g., molecular dynamics simulations) to describe properties beyond atomic and molecular scales that obey continuum laws such as those described in Section 4. As used herein, the term continuum for pore networks refers to pore networks at the laboratory column scale (e.g., tens of cm) and beyond. Continuum-scale colloid transport is first described in terms of experimentally observed continuum-scale transport (Section 6.1) and then in simulated continuum-scale transport (Section 6.2).

6.1 Experimentally Observed Continuum-Scale Colloid Transport

This section briefly describes a massive area of scientific literature concerned with experimental observations of colloid transport at the continuum scale. This is accomplished by generalizing transport behaviors to efficiently orient newly interested researchers toward areas that we view (admittedly, subjectively) as deserving priority in future research. We intend that our, likely incomplete, rendering of existing literature allows researchers to more readily navigate the trove of publications that exist on this subject.

We briefly address inferring mechanisms from the continuum scale in Section 6.1.1, then tip our hats to the subject of macroscale physical and chemical heterogeneity that lies beyond the scope of this text in Section 6.1.2, before settling into our comfort zone regarding experimentally observed impacts of favorable versus unfavorable conditions at the continuum scale in Section 6.1.3. We end this section with discussion of potential implications of these generalized experimental observations in Section 6.1.4.

6.1.1 Inferring Operating Mechanisms

Continuum-scale colloid transport behaviors are typically observed through experiments performed in packed sediment columns, laboratory flumes, and field settings, such that pore-scale mechanisms at play are inferred rather than observed directly. As such, one must treat with caution any conclusions drawn about pore-scale mechanisms inferred solely from continuum-scale data such as packed-column or larger scale experiments.

Colloid transport science is plagued by conclusions regarding pore-scale mechanisms that are inferred from continuum-scale observations, for example, the role of straining (Johnson et al., 2011), and the roles of attachment versus retention without attachment in secondary minima. These processes are described in some detail in Section 5 but are mentioned again here because inference of pore-scale mechanisms from continuum column-scale experiments is a major driver of misperceptions.

6.1.2 Macroscale Physical and Chemical Heterogeneity

Relative to pore-scale experiments, column- and larger-scale experiments introduce the possibility of preferential flow paths arising from variation in grain packing structure, grain size (Pazmiño et al., 2011), and grain shape. This is also possible with variation in retention arising from variation in surface chemistry for sediments composed of multi-mineral grains (Johnson et al., 1996; Loveland et al., 2003; Song & Elimelech, 1994; Song et al., 1994; Trauscht et al., 2015). At the flume and field scales, additional physical and chemical heterogeneities arise from biological activities (e.g., rootholes, burrows, exudates), fractures, and stratigraphy.

The subject of macroscale porous media heterogeneity lies beyond the scope of this textbook The topic is covered in other books published by the Groundwater Project including: Hydrogeologic Properties of Earth Materials and Principles of Groundwater Flow↗ (Woessner & Poeter, 2020), Introduction to Karst Aquifers↗ (Kuniansky et al., 2022), and Electrical Imaging for Hydrogeology↗ (Singha et al., 2022). This textbook focuses on phenomena that propagate from nanoscale interactions to pore-scale transport and that, in turn, impact continuum-scale transport by their superposition on the impacts of physical and chemical heterogeneity that increase as scale increases to field settings.

A seminal example of the importance of macroscale physical heterogeneity to colloid transport is the work of McKay and others (1993) that demonstrated the rapid breakthrough of viruses in fractured till, where colloid (virus) breakthrough times were far shorter than those of the co-injected solute. It was inferred that diffusion of the solute into the matrix porosity greatly exceeded that of the far larger viruses that are far less diffusive relative to the solute (Figure 4 and Figure 37). This *size exclusion* of viruses effectively focused their transport into the highly advective fracture domain and thereby facilitated their transport relative to solutes in systems with preferential flow paths (Figure 38). Such differential advection is well reported (Zhang et al., 2001a). Unfortunately, some more recent publications have unnecessarily conflated the term size exclusion with straining, whereas these terms originally had distinct meanings as described in this book.
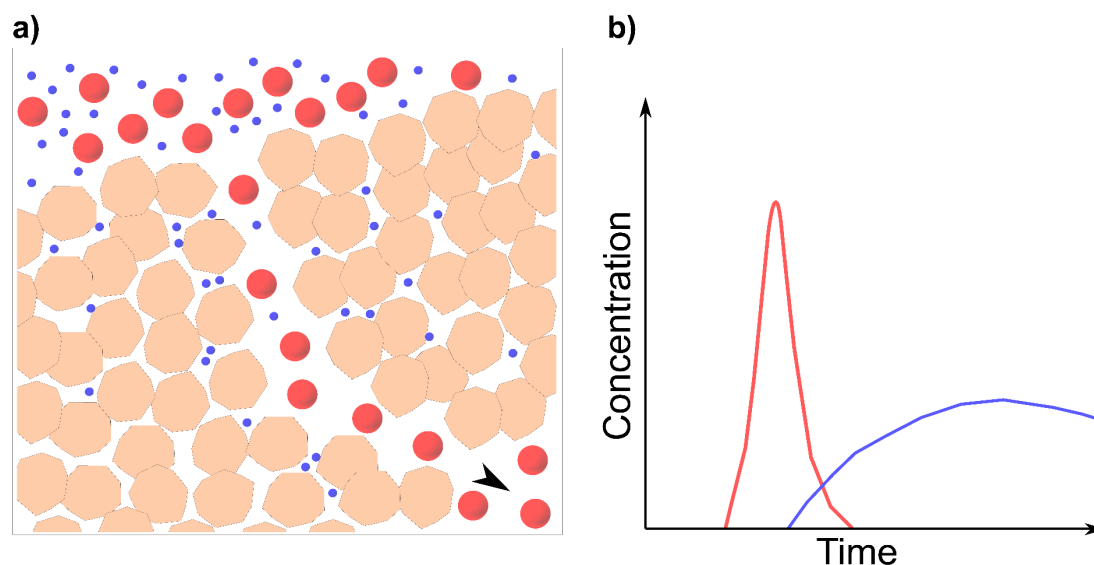
Figure 38 - Schematic of size exclusion of colloids relative to solutes in media with preferential flow. a) A preferential flow path through the host matrix. Larger colloids (red) are far less likely to enter the matrix porosity due to their relatively low diffusion (even when their physical size allows entry), thereby remaining in the higher velocity pore space. Smaller colloids (blue) have sufficiently high diffusion to enter the matrix porosity and experience slower fluid velocities. b) The resulting breakthrough-elution concentration histories demonstrate the resulting greater advection (arriving at earlier times) and lesser dispersion (the higher peak concentration) for colloids (red) relative to solutes (blue).

6.1.3 Experimentally Observed Impacts of Favorable Versus Unfavorable Conditions at the Continuum Scale

The nanoscale interactions and pore-scale transport sections discussed the profound impacts of charge repulsion between colloids and surfaces (unfavorable conditions) such as much greater colloid residence times in the near surface fluid domain under unfavorable relative to favorable conditions. These impacts manifest at the continuum scale breakthrough-elution concentration (BTC) histories and retained colloid concentration profiles (RCP) (Figure 39) as described in a large body of accumulated literature that tends to have evolved from biological, to non-biological polystyrene microspheres, to engineered nanoparticles (e.g., Harvey et al., 1991; Scholl & Harvey, 1992; McCaulou et al., 1995; Harvey, 1997; Ryan et al., 1999; Schijven et al., 1999; Harter et al., 2000; Jin et al., 2002; Tufenkji et al., 2004; Dunphy Guzman et al., 2006; Shen et al., 2007; Jaisi et al., 2009; Berge & Ramsburg, 2009; Scheibe et al., 2011; May et al., 2012; Russell et al., 2012; Raychoudhury et al., 2012; Johnson et al., 2013; Neukum et al., 2014; Tosco et al., 2014), and which is now moving into nano- and microplastic transport. This section summarizes the predominant features of continuum-scale colloid transport from this literature.
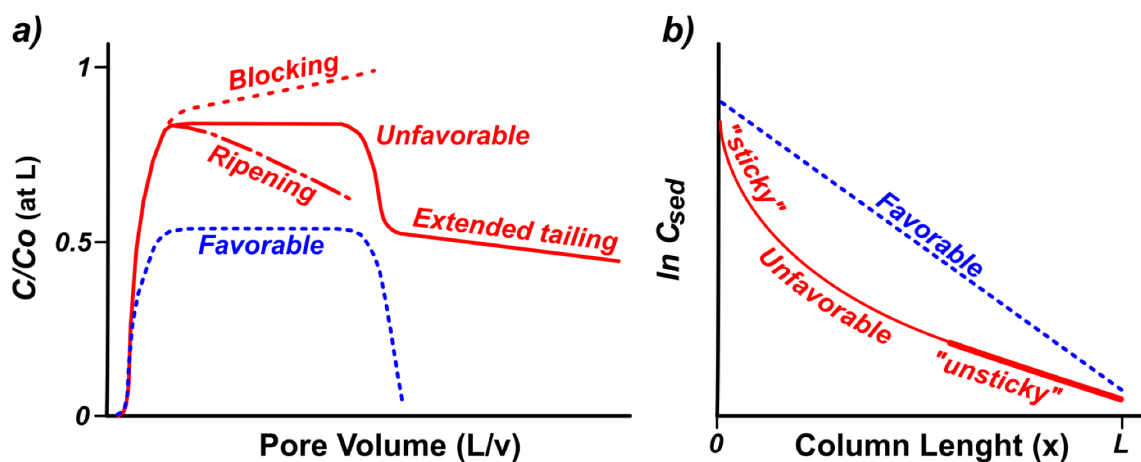
Figure 39 - a) BTC and b) RCP for step injection experiments for favorable (blue) and unfavorable (red) conditions. The behaviors labeled as blocking, ripening, extended tailing, sticky, and unsticky are explained in Section 6.2.

The BTCs and RCPs in Figure 39 represent experiments performed with step injection of colloids where the duration of colloid injection exceeded one pore volume. The pore volume is the volume of pore space in the sediment-packed column. The representation shown reflects a three-pore volume injection of colloid suspension followed by seven pore volumes of elution with equivalent colloid-free solution (Li & Johnson, 2005; Li et al., 2004; Tong et al., 2006a). The rationale for a step injection as opposed to a pulse injection (duration less than on pore volume) is that in the BTCs, the impacts of dispersion are readily distinguished from the impacts of colloid-surface interaction. Dispersion manifests in the initial s-shaped breakthrough portion of the BTC between first detection (first occurrence of $C/C_0 > 0$) and the steady-state breakthrough plateau ($C/C_0 > 0$ and relatively constant with time), where C_0 is the injected concentration, and C is the concentration measured at some distance downgradient (e.g., the outlet of 20 cm long sediment-packed columns) as shown in Figure 39). Dispersion again manifests upon cessation of injection (following three pore volumes of injection in Figure 39) as the advective front between colloid-free versus colloidal suspension advances through the packed column (Figure 39).

Whereas the mean breakthrough defined by advection occurs at one pore volume (i.e., $C/C_0 = 0.5$ in homogenous media), dispersion around the mean velocity causes portions of the colloid population to break through earlier, or later, than the mean, and so produces s-shaped curvature in the initial breakthrough and initial elution portions of the BTC (Figure 39). Dispersion arises from combined mechanical dispersion (pore- and continuum-scale variations around the mean velocity value) and molecular diffusion (Brownian motion from intrinsic energy of the colloid or solute).

An important contrast in transport behaviors under unfavorable versus favorable conditions follows initial elution, which is the *extended tailing* of low colloid concentrations under unfavorable (but not favorable) conditions shown in Figure 39. Following the first elution pore volume, colloid concentrations typically decrease below detection under

83

The GROUNDWATER PROJECT   ©The Author(s)   Free download from gw-project.org

Anyone may use and share gw-project.org links. Direct distribution of the book is strictly prohibited.

favorable conditions but decrease to some low but detectable value (typically orders of magnitude lower than steady-state breakthrough) under unfavorable conditions (Figure 39). This distinction typically requires a log scale on the y-axis (Johnson et al., 1995).

The extended tailing of low colloid concentrations following initial elution has been attributed to detachment in previous studies (Johnson et al., 1995; Tong et al., 2005). This interpretation has more recently been broadened to recognize the possibility (likelihood) of the phenomenon reflecting re-entrainment of non-attached retained colloids (Hilpert et al., 2017; Johnson, 2020; Johnson & Hilpert, 2013; Johnson et al., 2018).

Between initial breakthrough and initial elution, the steady-state breakthrough plateau (Figure 39) is defined by the rate of colloid loss by filtration, as we describe in section 6.2.3. The steady-state breakthrough concentration is typically lower (indicating greater retention) with favorable conditions, whereas it is higher (indicating lesser retention) with unfavorable conditions (Li et al., 2004; Li & Johnson 2005). Furthermore, under unfavorable conditions, the steady-state breakthrough concentration increases (retention decreases) with increasingly unfavorable conditions, that is, under conditions that produce a higher repulsive barrier calculated according to xDLVO interactions, thereby showing qualitative agreement between experiment and theory.

RCPs also show a profound contrast under unfavorable relative to favorable conditions. Under favorable conditions, retained colloid concentrations decrease exponentially with increasing distance from the source, producing a log-linear RCP (Figure 39). In contrast, under unfavorable conditions, colloid concentrations decrease non-exponentially with increasing distance from source (Figure 39); colloids show less retention under unfavorable relative to favorable conditions (under otherwise equivalent conditions). The number of colloids retained (integrated area under the RCP) typically decreases with increasing height of the repulsive barrier calculated from xDLVO theory, demonstrating qualitative agreement between experiments and theory. Two forms of non-exponential (non-log-linear) RCPs are typically reported under unfavorable conditions:

1. *multi-exponential*, formerly referred to as *hyper-exponential*; and
2. *non-monotonic*, where the maximum retained colloid concentrations occurs at some distance downgradient of the source.

The potential mechanisms driving these observed deviations from log-linear RCPs are described in Section 6.2.

Colloids of different shapes/types show the above continuum-scale transport behaviors such as the occurrence of steady-state breakthrough plateaus for step injection BTCs; an inverse relationship between the steady-state breakthrough concentration and solution IS as shown for clays (Won et al., 2021) as well as nano- and microplastics (Wu et al., 2020). Furthermore, extended tailing in BTCs and non-exponential RCPs under unfavorable conditions are reported for

- biological colloids such as bacteria, viruses, and protozoa (Albinger et al., 1994; Baygents et al., 1998; Bolster et al., 1999, 2000; DeBorde et al., 1999; Elimelech, 2005a; Foppen et al., 2007s; Harvey et al., 1995; Hendry et al., 1997; Johnson et al., 2006; Martin et al., 1996; Schijven & Hassanizadeh, 2000; Schijven & Šimůnek, 2002; Simoni et al., 1998; Tufenkji; Zhang et al., 2001b; & Pang et al., 2005),
- polymeric (non-biological) colloids (Johnson et al., 2007b; Li et al., 2004; Li et al., 2005; Tufenkji & Elimelech, 2004; Tufenkji & Elimelech, 2005b; Tong et al., 2006a; Tong et al., 2006b), and
- engineered nanomaterials (Liang et al., 2013; Wang et al., 2014).

6.1.4 Practical Implications of Continuum-Scale Experimental Observations

A practical implication of the contrasting continuum-scale colloid transport behaviors under favorable versus unfavorable conditions discussed in the previous section is that in groundwater—where surfaces are predominantly negatively charged either intrinsically or due to overprinting by natural organic matter (Tipping & Cooke, 1982; Davis, 1982; Jardine et al., 1989)—colloid transport is enhanced and unpredictable relative to favorable conditions. Whereas a steady-state breakthrough plateau is often observed under both favorable and unfavorable conditions (Li et al., 2004; Li et al., 2005; Johnson et al., 2020a), the temporal constancy of the breakthrough plateau in the absence of blocking or ripening (Figure 39 - a) BTC and b) RCP for step injection experiments for favorable (blue) and unfavorable (red) conditions. The behaviors labeled as blocking, ripening, extended tailing, sticky, and unsticky are explained in Section 6.2.) does not reveal the various possible non-exponential shapes of the RCP that occur under unfavorable conditions (Figure 39b) ranging from multi-exponential to non-monotonic.

These non-log-linear RCPs observed under unfavorable conditions demonstrate an effective spatial variation in the stickiness of the colloid population under unfavorable conditions (Li et al., 2004; Johnson et al., 2020a), often producing decreased k_f with increasing distance of transport (Johnson et al., 2020) as shown in Figure 40 As a result, one option to colloquially explain the multi-exponential RCPs is as retention of sticky colloids upgradient of unsticky colloids (Figure 39). Regardless of how one explains these features, predicting colloid transport distances under unfavorable conditions is extremely difficult.
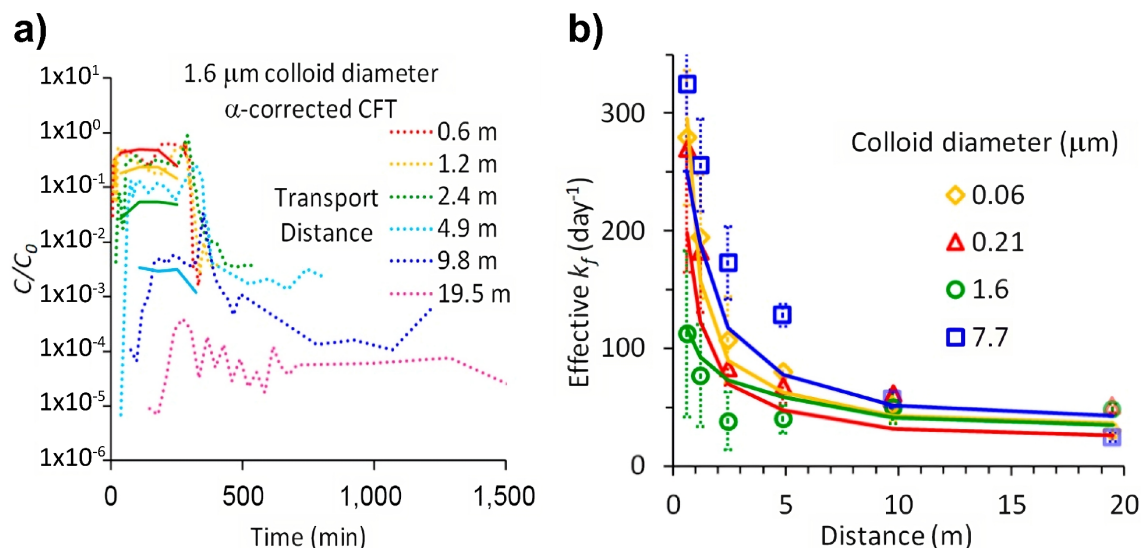
Figure 40 - Breakthrough-elution concentration histories in pea gravel for carboxylate-modified polystyrene latex colloids (1.6 μm diameter) with experimental results shown by dotted lines colored according to transport distance. a) Steady-state breakthrough according to α-corrected colloid filtration theory is shown by solid-colored lines, with α determined from the 0.6 m transport distance. b) Values of effective k_f as a function of transport distance determined from experimentally observed steady-state breakthrough (shown by symbols) with error bars representing error propagation as described in Johnson and others (2020). Solid colored lines in (b) show values of k_f from upscaling of mechanistic pore-scale trajectory simulations incorporating representative nanoscale heterogeneity, which is described in Section 6.2 (modified from Johnson et al., 2020a).

The slow motion of near-surface colloids observed in pore-scale experiments under unfavorable (but not favorable) conditions are expected to contribute to the experimentally observed extended tailing and non-log-linear RCPs observed under unfavorable (but not favorable) conditions in continuum-scale packed column experiments (Li et al., 2004) and field experiments (Johnson et al., 2020a). Continuum-scale experiments demonstrate that IS reduction during elution produces an increased concentration pulse during extended tailing, reflecting the release of colloids from sediment grain surfaces or from the near-surface fluid. The concentration pulse likely reflects a combination of colloids reentrained via elimination of secondary minima (Hahn et al., 2004) plus colloids detached from primary minima due to expansion of ZOI to include a greater fraction occupied by non-attractive surface (Pazmiño et al., 2014b). Both processes are described in detail in Section 5.2.

These impacts of IS reduction may drive, at least in part, the observed association of disease outbreaks with heavy rainfall (Curriero et al., 2001; Auld et al., 2004) and observed pulses of pathogen concentrations in response to rainfall and snowmelt (Bradbury et al., 2013), both of which involve the propagation of a low IS pulse into the subsurface. However, other impacts in addition to IS are at play during storm water infiltration (Zhuang et al., 2009).

We can expect that environmental surfaces are predominantly negatively charged. This negative charge is due to overprinting of an intrinsic positive charge initially associated with—for example—metal oxyhydroxide coatings by subsequently sorbed

86

natural organic acids (Tipping & Cooke, 1982; Davis, 1982; Jardine et al., 1989). However, the extent to which sorption-desorption and dissolution-precipitation equilibria regenerate granular media surfaces to expose their intrinsic charge in groundwater is uncharacterized, at least in the colloid transport literature. Silicate versus carbonate grains typically carry intrinsic negative versus positive charge, respectively, in the typical range of groundwater pH values (Trauscht et al., 2015; Schwarzenbach et al., 1993). This potential impact on observed colloid transport distances as a function of geologic terrane has not been systematically examined and presents an opportunity for larger-scale inquiry.

6.2　Simulating Continuum-Scale Colloid Transport

In this section, we describe simulation of continuum-scale colloid transport using the advection-dispersion equation with reaction rate coefficients and explore approaches for predicting (or at least linking) the rate coefficients from (to) more fundamental parameters. As such, this section is organized according to the level at which empirical information is fed into the simulations. We do not review literature regarding continuous time random walk (CTRW), multi-rate mass transfer (MRMT), and related methods to simulate continuum-scale colloid transport behaviors (Haggerty et al., 2000; Dentz & Berkowitz; Cortis et al., 2006; Ginn, 2009). While there exist various such *anomalous transport* models capable of capturing several of the behaviors described previously, their application in a mechanistic predictive manner is still elusive. Further understanding of the mechanisms that we discuss here will ultimately improve this capability, but we will not delve deep into this arena in this book. A review of anomalous transport is provided by Sund and others (2019).

As described subsequently, rate coefficients may be used to represent colloid interaction with grain surfaces in terms of, for example, retention and re-entrainment. Rate coefficients are typically backed out (toggled) to achieve a best fit to experimental data, as performed (quite well) by the transport software Hydrus (Šimůnek et al., 2016). However, researchers surprisingly often assume a mechanistic role for a given rate coefficient even when no such mechanism has been proved. For example, Johnson and others (1995) and Ginn (2000) simulated experimentally observed extended tailing of bacterial concentrations observed in column transport experiments using multiple rate coefficients to represent time-dependent detachment. The adequate fit to the observed data in no way proved that detachment was the actual mechanism by which extended tailing occurred, that is, by which bacteria were re-entrained into bulk flow to exit the column long after initial tailing (Figure 39).

In fact, based on pore-scale observations described in Section 5, the likely mechanism did not involve attachment or detachment; rather, it likely involved the re-entrainment of slow-moving near-surface secondary minimum-associated bacteria that were retained (without attachment) in the packed column across the timescale of

observation, a process of detachment described in Section 5.2. Likewise, others have utilized a depth-dependent attachment rate coefficient in simulations to describe the experimentally observed multi-exponential RCPs from column transport experiments (Johnson et al., 2011).

The ability to simulate the experimental data using a depth-dependent rate coefficient (called a *straining coefficient*) in no way proved the possibility that straining was the mechanism of retention (Johnson et al., 2011). In fact, other potential mechanisms can describe such data equally well. For example, variable collector efficiencies (heterogeneity in stickiness among the colloid population) also quite convincingly simulates experimentally observed multi-exponential RCPs from column transport experiments under unfavorable conditions (Li et al., 2004). Success in simulating experimental observations using rate coefficients does not prove any particular mechanism that may underly the rate coefficients. Therefore, simulation of continuum-scale transport is addressed in terms of three aspects:

1. simulating continuum-scale hydrodynamic processes (advection and dispersion; Section 6.2.1);
2. simulating continuum-scale reactive transport using rate coefficients (Section 6.2.2); and
3. getting "under the hood" of the rate coefficients by mechanistically linking them to pore- and nano-scale transport processes, thereby incorporating empirical information at a deeper level in the simulations (Section 6.2.3).

6.2.1 Simulated Continuum-Scale Hydrodynamic Processes

The continuum-scale hydrodynamic processes governing colloid transport in porous media are advection and dispersion, where the advective flux through an area of a Cartesian REV (Figure 41) accounts for displacement arising from the average pore fluid velocity as shown in Equation (67).
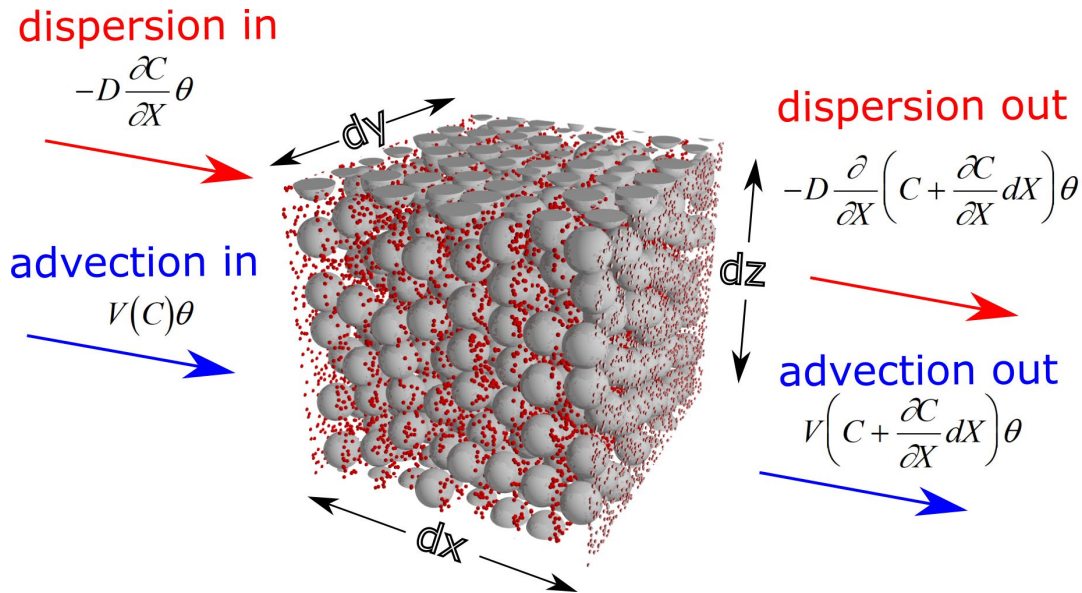
Figure 41 - Control volume to perform mass balance in derivation of the advection-dispersion equation. Gray spheres represent grains; red spheres represent solute.

$$J_A = v\theta C \tag{67}$$

where:

J_A = advective flux, $\left[\dfrac{L_{REV}}{T} \dfrac{L_w^3}{L_{REV}^3} \dfrac{M_c}{L_w^3} = \dfrac{M_c}{L_{REV}^2 t} \right]$, i.e., (ML^{-2} T^{-1})

v = average pore fluid velocity (LT^{-1})

θ = volumetric water content (dimensionless)

C = average concentration in water (ML^3)

In Equation (67), the units of v, θ, and C cancel to produce the mass flux (solute or colloid) per time through a given area of the *REV*.

Whereas the advective flux describes the average behavior driven by the average pore water velocity, a dispersive flux (J_D) arises from velocity variations around the average pore water velocity. This hydrodynamic dispersion is composed of fluid velocity variations around the mean value (mechanical dispersion) and molecular scale random motion (diffusion). This is driven by intrinsic energy of atomic, molecular, colloidal constituents. Because this hydrodynamic dispersive flux is represented by Gaussian variance around a mean value—similar to the variance around a mean position produced by molecular diffusion—it is represented according to a flux-gradient law adopted from Fick's First Law of diffusion as shown in Equation (68).

$$J_D = -D_h \theta \frac{\partial C}{\partial x} \tag{68}$$

where:

D_h = hydrodynamic dispersion coefficient that relates the flux to the spatial gradient of the concentration (L^2T^{-1})

Because the hydrodynamic dispersion coefficient arises from velocity variations rather than solely intrinsic molecular energy, it is generally not constant for a given moiety size (as opposed to molecular diffusion) and is a tensorial quantity when expressed in multiple dimensions.

A mass balance in the x-direction (Figure 41) accounting for the advective and dispersive fluxes through the *Δy∆z* faces of a three-dimensional *REV* can be performed by representing the change in these fluxes across the length of the REV as shown in Equations (69) and (70).

$$J_{A,x} = v\theta C \Delta y \Delta z, J_{A,x+\Delta x} = v\theta \left(C + \frac{\partial C}{\partial x} \Delta x \right) \Delta y \Delta z \tag{69}$$

$$J_{D,x} = -D\theta \frac{\partial C}{\partial x} \Delta y \Delta z, J_{D,x+\Delta x} = -D\theta \frac{\partial}{\partial x} \left(C + \frac{\partial C}{\partial x} \Delta x \right) \Delta y \Delta z \tag{70}$$

where solute or colloid accumulation/depletion in the REV (M_c/T) is shown in Equation (71).

$$\theta \frac{\partial C}{\partial t} \Delta x \Delta y \Delta z \tag{71}$$

and which results from the difference between the combined fluxes exiting versus entering the Δy∆z faces—subtracting the fluxes at $x + \Delta x$ from those at x—as shown in Equation (72).

$$\theta \frac{\partial C}{\partial t} \Delta x \Delta y \Delta z = -v\theta \frac{\partial C}{\partial x} \Delta x \Delta y \Delta z + D\theta \frac{\partial}{\partial x} \left(\frac{\partial C}{\partial x} \Delta x \right) \Delta y \Delta z \tag{72}$$

Taking derivatives and simplifying yields the advection-dispersion Equation (73) (with dimensions ML^{-3}T^{-1}).

$$\frac{\partial C}{\partial t} = -v \frac{\partial C}{\partial x} + D \frac{\partial^2 C}{\partial x^2} \tag{73}$$

where the term on the left-hand side of Equation (73) reflects accumulation/depletion (transience) of solute in the water and the terms on the right-hand side reflect advection and dispersion.

The average breakthrough time at distance *L* is obtained by neglecting dispersion and occurs at the time equal to *L/v* (Figure 39). The complete concentration history (Figure 39) that includes dispersion is given by integration of the advection-dispersion equation under different boundary conditions. This produces an analytical solution for *C(x,t)*, e.g., with initial, inlet boundary, and outlet boundary solute concentrations specified as 0, C_0, and 0, respectively; Ogata & Banks, 1961).

6.2.2 Simulated Continuum-Scale Reactive Transport Using Rate Coefficients

The amount of literature concerning simulated continuum-scale colloid transport behavior rivals that for experimental observations. To provide a framework for new (and possibly advanced) colloid transport researchers to navigate this complex body of literature, this section is organized into three parts:

1. the contrasting impacts of equilibrium constants versus rate coefficients in simulations (Section 6.2.2.1);
2. simulating continuum-scale solute-colloid co-transport using equilibrium constants (Section 6.2.2.2); and
3. simulating continuum-scale BTCs and RCPs under favorable versus unfavorable conditions using rate coefficients (Section 6.2.2.3).

6.2.2.1 Contrasting Impacts of Equilibrium Constants Versus Rate Coefficients

Reactive transport of solutes and colloids is represented by the reversible and irreversible rate coefficients described in Section 5.4, which discusses contrasting pore-scale transport behaviors and surface interactions of solutes versus colloids.

For reversible interactions with grain surfaces (e.g., solute reversible linear partitioning, or ion exchange, or any other readily reversible phase change of the solute), the mathematical statement (*in the absence of advection and diffusion*) is that the change in contaminant concentration with time in water is opposite to that in sediment as shown in Equation (74).

$$\frac{\partial C}{\partial t}\theta = -\frac{\partial C_{sed}}{\partial t}\rho_b \tag{74}$$

where:

C = solute concentration in water (ML^{-3})

C_{sed} = solute concentration on sediment, mass of solute per mass of sediment (MM^{-3})

ρ_b = dry bulk density (ML^{-3})

θ = volumetric water content (dimensionless, L^3 L^{-3})

and ρ_b and θ serve to relate the solute concentrations in water and sediment back to the overall REV such that mass is traded in apples versus apples, as they say. The dimensions and their connection with phases in Equation (74) are shown as Equation (75) in which both sides represent change in solute mass in the REV, $M_c^*/(L_{REV}^3 TM_{REV}^3)$: the left hand side is change in solute mass in water, the right hand side is change in solute mass on the sediment.

$$\frac{M_c^*}{TL_w^3}\frac{L_w^3}{L_{REV}^3} = -\frac{M_c^*}{TM_{sed}}\frac{M_{sed}}{L_{REV}^3} \tag{75}$$

where the subscripted dimensions are associated with phases as follows:

L_w^3 = volume of water in REV

L_{REV}^3 = volume of REV

M_c^* = solute mass in the REV associated with the phase by which it is normalized to produce either C in water or C_{sed} on sediment

M_{sed} = sediment mass in the REV

Inserting this reversible sorption or partitioning relationship (or precipitation-dissolution, or any reversible trade relationship with another phase/state) into the advection-dispersion equation yields Equation (76).

$$\frac{\partial C}{\partial t}\theta = -v\frac{\partial C}{\partial x}\theta + D\frac{\partial^2 C}{\partial x^2}\theta - \frac{\partial C_{sed}}{\partial t}\rho_b \qquad (76)$$

Where linear and non-linear reversible processes occur, we examine reversible linear partitioning, which is represented by a direct proportionality of solute concentrations between water and sediment as described in Section 5.4 regarding contrasting solute and colloid pore-scale transport behaviors and is shown in Equation (77).

$$C_{sed} = K_d C \qquad (77)$$

where:

K_d = distribution coefficient, quotient of C_{sed} to C, at equilibrium, $K_d =$

$\frac{C_{sed}}{C} = \frac{\frac{M_c^*}{M_{sed}}}{\frac{M_c^*}{L_w^3}}$.

Considering the case where the solute mass M_c^* is equivalent in the water and sediment phases, the value of K_d (L_w^3, M_{sed}^{-1}) gives the relative volumes of water and sediment that would produce equivalent solute masses in water and sediment, thus reflecting the affinity of the solute for one phase relative to the other. The two phases are linked back to the REV though θ and ρb, which themselves have units that can be linked to their phases (L³w/L³REV and Msed/L³REV, respectively). Thus, the solute mass distributed among water and sediment at equilibrium is determined from the combination of K_d, θ, and ρb, as developed immediately below.

The dimensions with connection to phases for Equation (77) are given in Equation (78).

$$\frac{M_c^*}{M_{sed}} = \frac{L_w^3}{M_{sed}}\frac{M_c^*}{L_w^3} \qquad (78)$$

Differentiating Equation (77) with respect to time yields Equation (79).

$$\frac{\partial C_{sed}}{\partial t} = K_d \frac{\partial C}{\partial t} \qquad (79)$$

92

This can be substituted into the advection-dispersion-reversible loss described in Equation (76) to yield Equation (80).

$$\frac{\partial C}{\partial t}\theta = -v\frac{\partial C}{\partial x}\theta + D\frac{\partial^2 C}{\partial x^2}\theta - K_d\frac{\partial C}{\partial t}\rho_b \tag{80}$$

where all terms have units $ML^{-3}T^{-1}$ (or $ML^{-3}_wT^{-1}$ when linked back to phase), and the sole dependent variable is C. Combining like terms yields Equation (81).

$$\left(1 + \frac{\rho_b}{\theta}K_d\right)\frac{\partial C}{\partial t} = -v\frac{\partial C}{\partial x} + D\frac{\partial^2 C}{\partial x^2} \tag{81}$$

The right-hand side represents solely advection and dispersion, whereas the bracketed term on the left-hand side is called the retardation factor (R), which is dimensionless even when the units are linked to phases (it is worthwhile to prove that to yourself). R captures the solute partitioning between water and sediment, and represents a factor by which the average velocity of the solute is reduced relative to the average velocity of groundwater, such that if groundwater takes one year to travel a given distance, a solute undergoing partitioning will require R years to attain $C/C_0 = 0.5$ at that same distance (Figure 42).
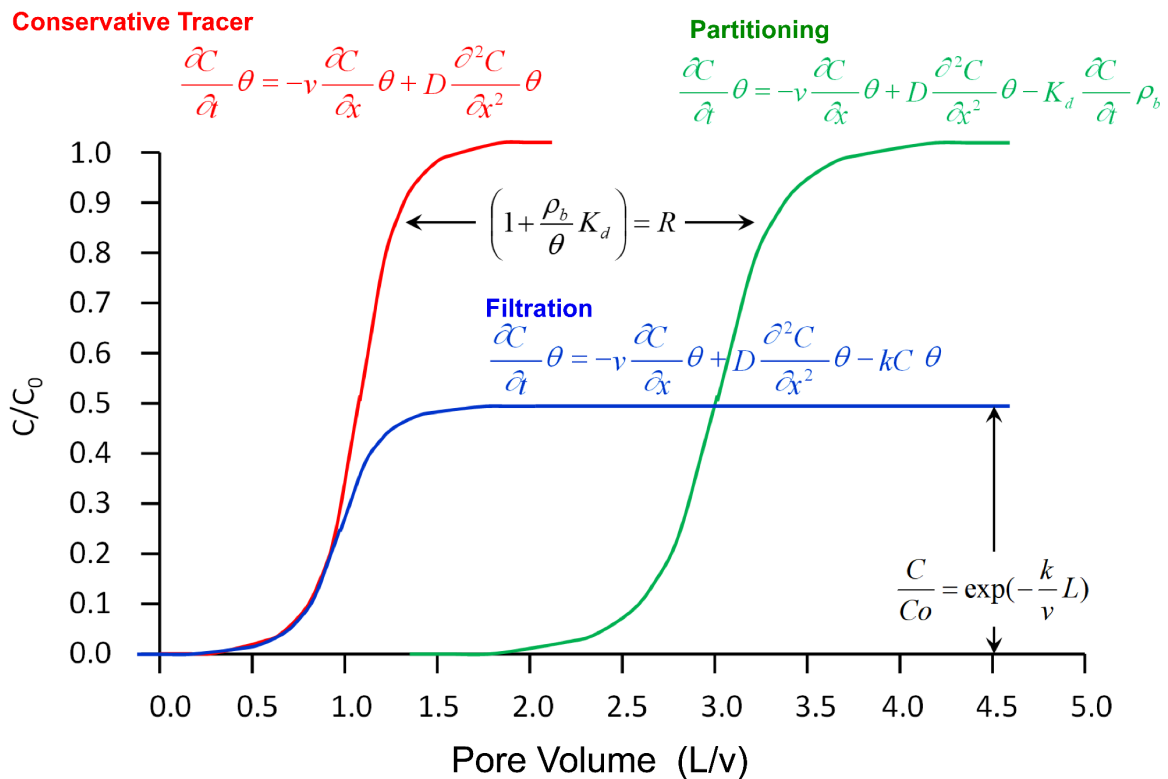
Figure 42 - BTCs for a conservative tracer (red), partitioning solute (green), and irreversibly lost solute or colloid (e.g., filtration; blue) (after Hunt & Johnson, 2016).

For irreversible solute loss from water (e.g., degradation), the modification to the advection-dispersion equation is quite simple, since no solute is returned (no talk-back) from the other phase (e.g., sediment), yielding Equation (82).

$$\frac{\partial C}{\partial t}\theta = -v\frac{\partial C}{\partial x}\theta + D\frac{\partial^2 C}{\partial x^2}\theta - k_f C\theta \tag{82}$$

where:

k_f = first-order rate coefficient (T^{-1})

that may, for example, represent colloid filtration, which is largely irreversible in the absence of perturbations in solution IS and fluid velocity (e.g., VanNess et al., 2019; Rasmuson et al., 2019a), as well as other irreversible processes for both solutes and colloids (e.g., degradation, and precipitation followed by removal from contact with aqueous phase).

Insight into the behavior of this governing equation is provided under the condition of steady-state breakthrough, where the impacts of dispersion that manifest during initial breakthrough and initial elution in the BTC (Figure 39) are negligible due to continuous solute input (step injection), and so the transient and dispersion terms can be neglected to produce Equation (83).

$$v\frac{\partial C}{\partial x} = -k_f C \tag{83}$$

Rearranging terms for integration produces Equation (84).

$$\frac{\partial C}{C} = -\frac{k_f}{v}\partial x \tag{84}$$

Integrating across the solute concentration range from C_0 to C across the distance from the source ($x = 0$) to a downgradient distance ($x = L$) demonstrates that the log relative concentration decreases linearly with distance as shown in Equation (85).

$$ln\frac{C}{C_0} = -\frac{k_f}{v}L \tag{85}$$

Taking the exponent demonstrates that the relative concentration decreases exponentially with distance (Equation (86).

$$\frac{C}{C_0} = e^{-\frac{k_f}{v}L} \tag{86}$$

The exponential RCPs observed under favorable conditions are indicated by Equation (86) to represent a spatially invariant retention rate coefficient (k_f). That is, k_f does not change with transport distance under favorable conditions. The corollary is that k_f does effectively change with transport distance under unfavorable conditions, which makes transport prediction difficult under unfavorable conditions.

The retained concentrations can also be examined. In the case of irreversible filtration, colloid mass accumulates unidirectionally on sediment (no return to fluid). Under this condition, accumulation during step injection is expressed as Equation (87).

$$\frac{\partial C_{sed}}{\partial t}\rho_b = k_f C\theta \tag{87}$$

Rearranging Equation (87) yields Equation (88).

$$\partial C_{sed} = k_f \frac{\theta}{\rho_b} C \partial t \tag{88}$$

Integrating time from 0 to t_0 (total injection time) and substituting the steady state C at distance L yields Equation (89).

$$C_{sed(x=L)} = k_f \frac{\theta}{\rho_b} C(x = L) t_0 \tag{89}$$

Substituting the expression for steady state C as delineated in Equation (86) into Equation (89) yields Equation (90).

$$C_{sed} = k_f \frac{\theta}{\rho_b} t_0 C_0 e^{-\frac{k_f}{v}L} \tag{90}$$

The two relationships shown in Equations (86) and (90) provide C and C_{sed} as a function of transport distance (exponentially decreasing with distance from source; Figure 39). Under clean-bed conditions (in the absence of temporal changes in retention rates via blocking or ripening as described in Section 6.2.2.3), C is temporally constant during steady-state breakthrough at any given distance; C_{sed} increases linearly with time until some indefinite time where blocking, ripening, or pore clogging occurs.

Misconception: Steady-state breakthrough reflects an equilibrium between colloid attachment and detachment.

1. Equilibrium interaction with sediment yields retarded transport (e.g., Figure 41), not a reduced steady-state plateau, which is produced by irreversible interactions.

2. Instead, the steady-state plateau reflects irreversible loss of colloids from solution. Observed colloid attachment tends to be irreversible in the absence of perturbations (e.g., increased flow or decreased IS). There are always exceptions, but these prove the rule of generally irreversible colloid attachment (in the absence of perturbations in flow or solution chemistry) that arises because colloids have low diffusion relative to solutes, and strong VDW attraction relative to solutes.

6.2.2.2 Simulating Continuum-Scale Solute-Colloid Co-transport with Equilibrium Constants

Facilitated or retarded transport of solutes by colloids (or vice versa) is well reported in the literature for solutes and colloids that interact with each other (deJong et al., 1998; Johnson & Amy, 1994; Novikov et al., 2006; Ouyang et al., 1996; Saiers & Hornberger, 1996; Sen & Khilar, 2006; Sprague et al., 2000). Their modified co-transport may be described using a modified retardation factor (R^*) that accounts for equilibrium (and in this case linear) interactions between: a) solute-sediment ($K_{sol-col}$) (same as K_d) b) colloid-sediment ($K_{sol-sed}$), and c) solute-colloid ($K_{sol-col}$) (Johnson et al., 1995) as shown in Equation (91).

$$R^* = \frac{1 + \frac{\rho_b}{\theta} K_{sol-sed} + K_{sol-col} C_{coll} + \frac{\rho_b}{\theta} K_{sol-col} K_{col-sed} C_{coll}}{1 + K_{sol-col} C_{coll}} \qquad (91)$$

where:

C_{coll} = colloid concentration (ML^{-3})

The value of R^* may be smaller (facilitated transport) or greater (retarded transport) than R (colloids and solutes may facilitate or retard one another's transport) depending on the relative values of $K_{sol-sed}$ (K_d), $K_{col-sed}$, and $K_{sol-col}$. Example colloids such as DOM (which falls into the size range between solutes and colloids), engineered nanomaterials, clays, and nano- and microplastics each have their own surface properties that yield different interactions with solutes and surfaces. As such, the outcomes regarding facilitated or retarded transport differ among these materials.

Non-linear interactions and pore size exclusion are incorporated into the expression for R^* in Johnson and others (1998). A significant body of literature exists on this subject (Corapcioglu & Jiang, 1993; Magee et al., 1991; Saiers & Hornberger, 1996). Representing colloid-sediment interaction with a linear equilibrium constant is not accurate for irreversible filtration, for which case the fraction of contaminant removed with colloids would never emerge in the BTC. The fraction of contaminant associated with non-filtered colloids would not be retarded and would emerge in the BTC corresponding to one pore volume (one *L/v*; Figure 39). The contrast between equilibrium and kinetic processes provides useful bounding expectations, although the reality is sometimes not so well defined.

6.2.2.3 Simulating Continuum-Scale BTCs and RCPs Under Favorable Versus Unfavorable Conditions Using Rate Coefficients

A good description of BTCs and RCPs observed under favorable conditions is generated by using a single retention rate coefficient (k_f) in the advection-dispersion-filtration equation (Figure 39). The steady-state breakthrough between initial breakthrough and initial elution is described by k_f under conditions where colloid accumulation is

sufficiently low to avoid temporal impacts of blocking and ripening. Upon elution, the rapid decay to undetectable colloid concentrations following initial elution is described by advection and dispersion (Figure 39 and Figure 42). The k_f that describes the steady-state breakthrough concentration also provides a good description of the RCP that is experimentally observed under favorable conditions. In short, under favorable conditions the advection-dispersion-filtration equation with an irreversible retention rate coefficient (k_f) is sufficient to describe experimentally observed continuum-scale data, at least in homogenous porous media with mono-disperse spheroidal colloids.

In contrast, under unfavorable conditions the experimentally observed BTCs and RCPs require the addition of more parameters to the advection-dispersion-filtration equation. For example, a re-entrainment rate coefficient (k_f) is needed to capture the observed extended tailing of low colloid concentrations following initial elution (Johnson et al., 1995; and Figure 39). Re-entrainment in response to perturbations (e.g., increased flow and decreased IS) can be described using k_f but with additional modifiers to accurately describe the observed temporal spike in relative concentration. This is because only a fraction of the retained concentration is typically released (Hahn et al., 2004).

The non-exponential RCPs observed under unfavorable conditions signal that the filtration rate coefficient effectively changes with transport distance—decreasing with increasing transport distance for multi-exponential RCPs (Li et al., 2004). Processes that produce this effect include:

a) multiple filtration rate coefficients (heterogeneity) among the colloid population such that more-sticky colloids are retained upgradient of less-sticky colloids, and

b) changes in physical or chemical characteristics of the granular media with increased transport distance.

Possibility (a) has been invoked in many studies (Albinger et al., 1994, Simoni et al., 1998; Chatterjee et al., 2011; Tong & Johnson, 2006b) as shown in Figure 39. While there are contexts where heterogeneity in the colloid population exists to justify multiple rate coefficients within a population such as size variability (Babakhani et al., 2019; Bedrikovetsky et al., 2019; Taghavi et al., 2015; Yang & Balhoff, 2017), in many contexts where multi-exponential RCPs are observed no detectable heterogeneity exists in the population (Li et al., 2004; Tufenkji & Elimelech, 2005a; among many others).

Possibility (b) is potentially explained by additional constituents that may impact granular media surfaces proximal to the source including films from microbial exudates of bacteria (Liu et al., 2007) or surfactant stabilizers from stock micro- or nano-particle suspensions. This possibility may also be explained by the occurrence of dead-end pores (straining) that enhance retention near the granular media surface (Bradford et al., 2003).

The ubiquity of non-exponential RCPs in many cases where no heterogeneity is apparent among the colloid population—and where straining and conditioning films either

97

The GROUNDWATER PROJECT   ©The Author(s)   Free download from gw-project.org

Anyone may use and share gw-project.org links. Direct distribution of the book is strictly prohibited.

seem to be absent or are present under both favorable and unfavorable conditions—suggests that a deeper mechanism drives the ubiquity of non-exponential RCPs under unfavorable (but not favorable) conditions, as described in Section 6.2.3.

The governing equations for descriptive simulation of BTCs and RCPs correspond to so-called clean-bed conditions where colloid accumulation on surfaces does not impact colloid retention rates. As colloids accumulate beyond clean-bed conditions, temporal changes in relative concentration may occur during injection in what would otherwise be the steady-state portion of the BTC. These temporal changes include decreased retention with increased injection time (temporally increasing breakthrough concentration) driven by colloid repulsion with attached colloids and blocking of subsequent retention (Figure 39a). This is described using a blocking term that sets maximum retention (e.g., S_{max}) to reflect blocking of subsequent retention by retained colloids (Camesano et al., 1999).

Alternatively, if colloid-colloid repulsion is relatively low or absent, then attached colloids may enhance subsequent attachment, leading to an increased rate of retention (temporally decreasing breakthrough concentration), which is described by incorporation of a ripening term as shown in Figure 39 (Mays & Hunt, 2005).

6.2.3 Mechanistic Linking of Rate Coefficients to Pore- and Nanoscale Processes: Getting under the Hood of Rate Coefficients

The nanoscale colloid-surface repulsion and its impact on pore-scale processes is relevant to field-scale transport as indicated by field-scale experimental observations. For example, continuum-scale transport experiments indicate that minimum retention corresponds to the n-μ transition size range when surface properties are comparable (Gupta et al., 2009; Johnson et al., 2020a). Relevance is also indicated by the occurrence of non-exponential RPCs in field-scale experiments shown in Figure 39 and Figure 40 (Johnson et al., 2020a; Schijven & Hassanizadeh, 2000; Zhang et al., 2001b). For this reason, developing the ability to account for the impacts of nanoscale repulsion and inferred nanoscale surface heterogeneity will improve predictions of continuum-scale transport.

The goal of colloid filtration theory is to move beyond mere description of colloid transport observations via rate coefficients to prediction of rate coefficients via fundamental parameters. This will upscale the mechanistically simulated pore-scale collector efficiency (η) to predict the continuum-scale filtration rate coefficient (k_f). This topic is explored via a progression through the following topics:

1. defining clean-bed conditions (Section 6.2.3.1),
2. upscaling η to k_f under favorable conditions via compounded loss to each grain passed (Section 6.2.3.2),
3. upscaling η to k_f under unfavorable conditions via compounded loss within the near-surface fluid domain including the grain surface (Section 6.2.3.3),
4. assumptions to produce fast- and slow-attaching colloids from a population of identical individuals (Section 6.2.3.4),

98

5. a brief note of opportunities to mechanistically address temporal phenomena that arise under non-clean-bed conditions such as blocking and ripening (Section 6.2.3.5), and

6. simulating contrasting colloid transport behaviors in granular versus fractured media using mechanistically upscaled rate coefficients (Section 6.2.3.6).

6.2.3.1 Clean-Bed Conditions

Steady-state breakthrough in BTCs is not always temporally invariant. Instead, it can display temporal change such as increasing breakthrough concentrations with increased time of injection (Figure 39). This rise during an otherwise steady-state breakthrough is attributed to attached colloids *blocking* subsequent colloid attachment if colloid-colloid repulsion exceeds colloid-grain repulsion (Ko & Elimelech, 2000). Similarly, if colloid-grain repulsion exceeds colloid-colloid repulsion, then attached colloids may act as relatively favorable locations of colloid attachment, leading to *ripening* where breakthrough colloid concentrations decrease with increased time of injection (Tong et al., 2008).

Such temporal variation during what is otherwise observed as a steady-state breakthrough is associated with conditions under which colloid retention is high. An example is high injected colloid concentrations where retained colloid concentrations on grain surfaces are sufficiently high to impact the interaction with grain surfaces of mobile colloids in the near-surface fluid domain. Temporally constant steady-state breakthrough in colloid BTCs is associated with so-called clean-bed conditions where retained colloids do not significantly impact the interaction of mobile colloids with grain surfaces. The following discussion about simulation of continuum-scale colloid transport focuses on clean-bed conditions.

6.2.3.2 Upscaling Under Favorable Conditions: Compounded Loss to Grain Surfaces

Under favorable conditions, the upscaling of pore-scale η to the continuum-scale k_f is relatively simple, since one considers the porous medium as a series of, for example, Happel collectors to which colloids are delivered and become attached according to the mechanisms described in Section 5. The fraction of colloids that pass one collector $(1-\eta)$ enters the next collector, such that after passing through a number of collectors (N_c), the relative concentration (C/C_0) that emerges is $(1-\eta)^{N_c}$ (Figure 43 and Equation (92)). However, this upscaling assumes complete pore-scale mixing, such that colloids are distributed equivalently across the approach area upstream of each successive collector.

Upscaling – porous media as a series of collectors to mechanistically predict k_f
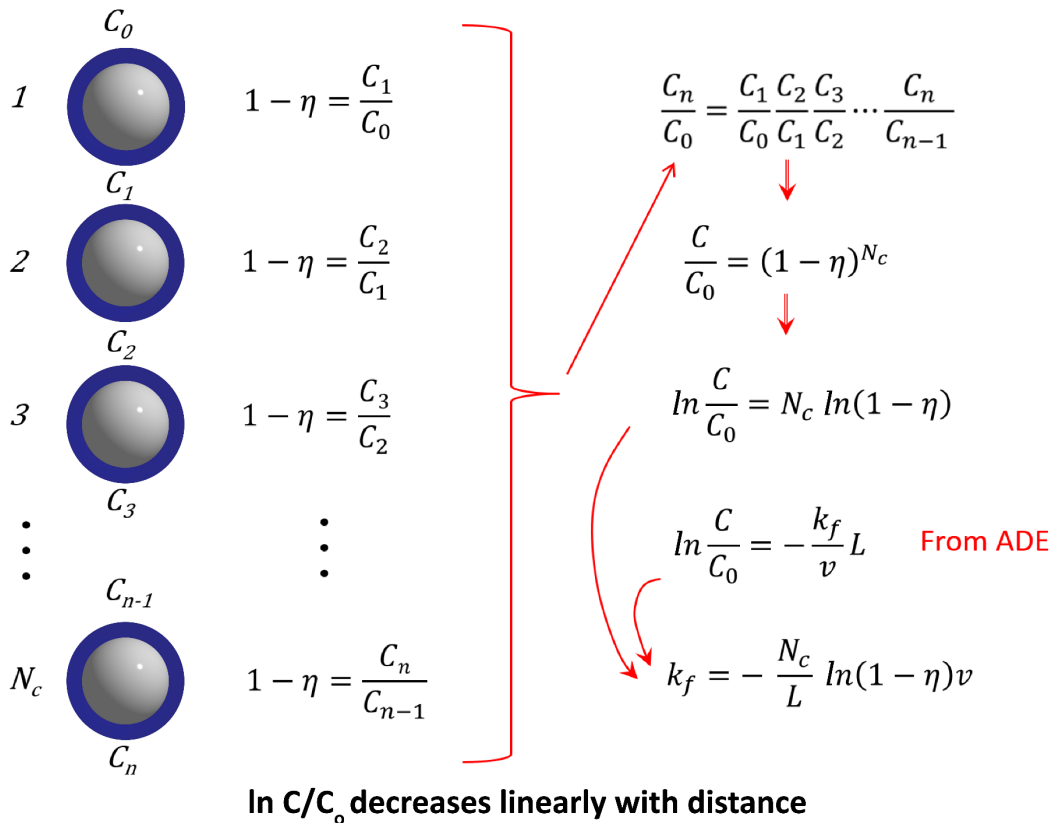
Figure 43 - Upscaling from pore-scale collector efficiencies (η) to continuum-scale rate coefficients (k_f) where ADE is the advection-dispersion equation.

$$\frac{C}{C_0} = (1 - \eta)^{N_c} \tag{92}$$

Taking the log of both sides of Equation (92) yields Equation (93).

$$\ln\frac{C}{C_0} = N_c \ln(1 - \eta) \tag{93}$$

Hence, upscaling of η interprets the exponential (log-linear) RCPs observed under favorable conditions as resulting from compounded loss of a fraction of the colloid population for each grain (collector) passed.

Equating this relationship to that derived from the advection-dispersion-filtration Equation (85) yields Equation (94).

$$\ln\frac{C}{C_0} = -\frac{k_f}{v}L = N_c \ln(1 - \eta) \tag{94}$$

Then the relationship of k_f and η is as defined in Equation (95).

$$k_f = -\frac{N_c}{L}\ln(1 - \eta)v \tag{95}$$

This upscaling relationship produces the continuum-scale k_f from mechanistically simulated pore-scale η. The number of collectors per unit length (N_c/L) is defined by the collector geometry (as in Johnson & Hilpert, 2013), which is shown by Equation (96) for the Happel collector. Expressions for N_c/L of other collectors are provided by Johnson and others (2007a) for simple and dense cubic packed collectors and by Ma and others (2009) for the hemisphere-in-cell collector.

$$N_c = \frac{3(1-\theta)^{\frac{1}{3}}}{4a_g} \tag{96}$$

Misconception: Greater retention near the source is evidence of non-exponential retention.

Greater retention near the source is observed for both exponential and non-exponential RCPs. As colloids move through a porous medium, a fraction (η) of the population is removed for each grain passed such that the ratio of the concentration exiting versus entering each collector is (1-η). The concentration exiting a series of collectors is the value of (1-η) raised to the power of the number of collectors passed (N_c) such that the concentration C at some distance downstream of the source C_o is $C = C_o(1-\eta)^{Nc}$.

Since Nc increases linearly with distance, the concentration decreases exponentially with distance due to compounded loss to each collector. So, the concentration decreases exponentially with increasing distance from the source. This theoretical expectation proves to be true under favorable conditions. Under unfavorable conditions, this relationship changes, and concentrations as a function of distance decrease non-exponentially. However, the concentrations near the source are still much greater than those downgradient. Since this profound change from favorable to unfavorable conditions is observed for biological and non-biological colloids, it is a fundamental process that can be explored in Parti-Suite using the xDLVO, Traj-Hap, and Upscale modules.

Upscaling of mechanistically predicted pore-scale η by this simple method yields reasonable predictions of observed continuum-scale under favorable conditions (Long & Hilpert, 2009; Tong & Johnson, 2006a). Modest (i.e., a factor of two to three) discrepancies that are observed likely result from collectors that do not represent with full accuracy the impacts of pore space topology in granular media (Johnson & Hilpert, 2013).

Given that $ln(1-\eta) \cong \eta$, for $\eta > \approx 0.5$, the relationship between k_f and η is approximately direct ($k_f = \eta N_c/L$). Hence, predicted k_f also shows a minimum value for colloids corresponding to the n-μ size (as occurs for η) at least under favorable conditions where η and upscaled k_f values quantify both delivery and attachment to surfaces. However, this expectation of least delivery/retention of colloid sizs corresponding to the n-μ size range is observed under unfavorable conditions in some pore-scale experiments (Ron et al., 2019b) and in some continuum-scale experiments (Gupta et al., 2009; Johnson et al., 2020a.

A video providing an overview of the capabilities of the Upscale Continuum module of Parti-Suite can be accessed by clicking on the white arrow in the middle of Figure 44, then on the "▶" in the next screen. The video provides the information needed to undertake the corresponding Exercise 8↴.
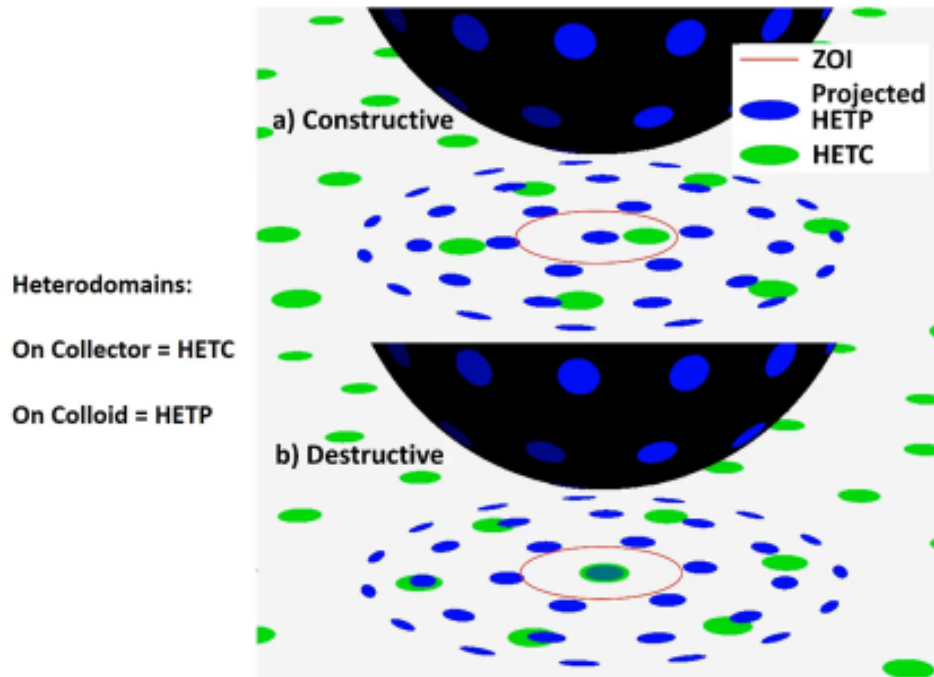
Figure 44 - A video providing an overview of the capabilities of the Upscale Continuum module of Parti-Suite can be accessed by clicking on the white arrow in the middle of the figure then on "▶" in the next screen or on YouTube▶.

A link to a video demonstrating how to use the Upscale Continuum module of Parti-Suite can be accessed in Figure 45 by clicking on the white arrow in the middle of the figure, then on the "▶" in the next screen. The video provides the information needed to undertake the corresponding Exercise 9↴.
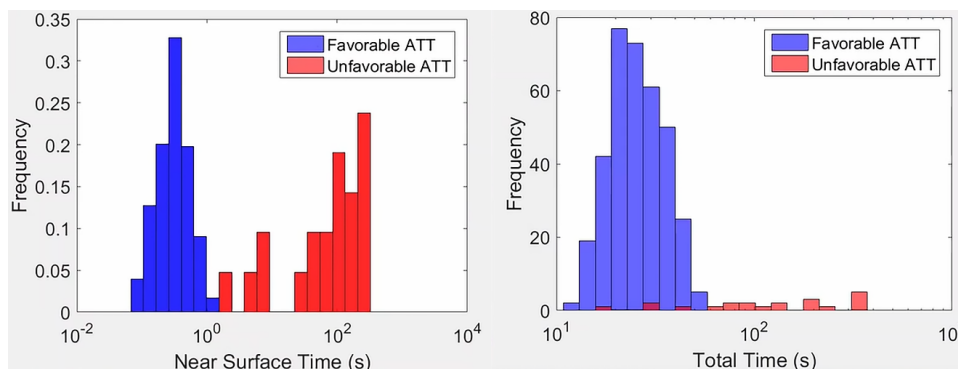
Figure 45 - A video demonstrating how to use the Upscale Continuum module in Parti-Suite can be accessed by clicking on this figure, then on "▶" in the next screen or on YouTube▶. ATT refers to attachment under favorable (blue) versus unfavorable with heterogeneity (red) conditions.

6.2.3.3 Upscaling Under Unfavorable Conditions: Compounded Loss to Grain Surface Plus Near-Surface Fluid Domain

Mechanistic prediction of rate coefficients k_f, k_r, and their variations required to describe BTCs and RCPs observed under unfavorable conditions is a longstanding challenge (Johnson et al., 2018). As described earlier, the attachment efficiency (α) has been used to quantify the discrepancy (ratio) of η values from favorable relative to unfavorable conditions. However, no relationship yet exists to account for the impacts on α of colloid size, fluid velocity, or other transport variables likely to impact α. More importantly, α (at least as defined conventionally as the ratio of η under unfavorable relative to favorable conditions) is simply a reduction of k_f, and so α cannot produce the near-surface slow-moving colloids under unfavorable conditions that are presumed to

a) produce the extended tailing of low colloid concentrations following initial elution under unfavorable conditions (Ginn, 2000; Johnson et al., 1995),

b) contribute to the continuum-scale release of colloids upon IS reduction under unfavorable conditions (Franchi & O'Melia, 2003; Hahn et al., 2004a; Pazmiño et al., 2014b; Rasmuson et al., 2019a; Tong et al., 2006a), and

c) produce the non-monotonic RCPs observed under unfavorable conditions (Johnson, 2020; Johnson et al., 2018; Li & Johnson, 2005).

Pore-scale mechanistic simulations with nanoscale heterogeneity produce near-surface slow-moving colloids and immobilized primary-minimum-associated colloids that may or may not detach in response to IS reduction depending on the degree of ZOI overlap with attractive heterodomains as shown in Figure 46 (Pazmiño et al., 2014a; Rasmuson et al., 2019a; Ron et al., 2019a, 2019ab; Trauscht et al., 2015). For these reasons, it seems that improved predictive capability will require mechanistic simulations incorporating nanoscale charge heterogeneity combined with a modified upscaling process that considers all outcomes in the near-surface fluid domain (slow motion, fast attachment, slow attachment, re-entrainment).
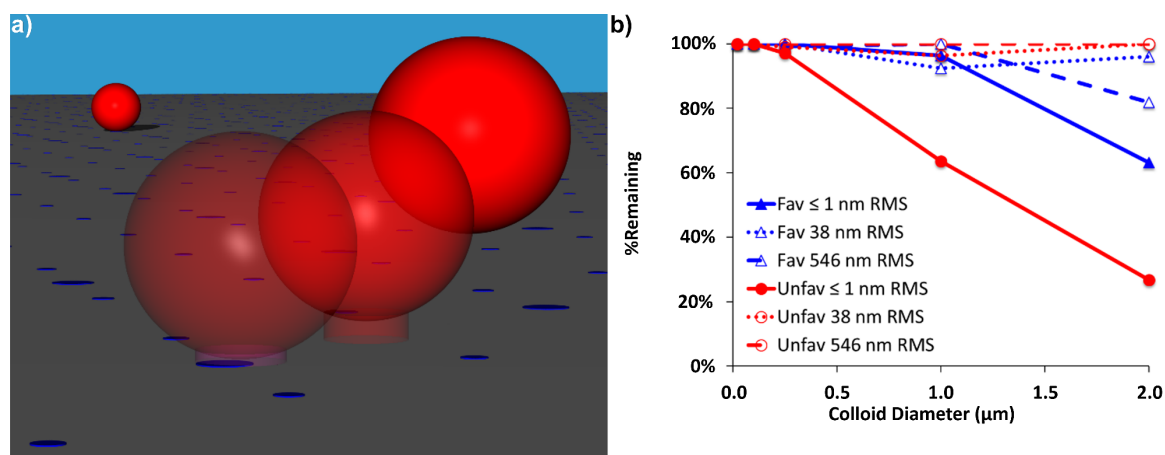
Figure 46 - Colloid re-entrainment after high flow perturbation. a) Schematic of colloid (red spheres with ZOI shown as a cylinder initially over a blue heterodomain) re-entrainment in response to increased fluid drag under unfavorable conditions. b) Percent remaining on various surfaces after high flow perturbation (0.15 ms^{-1}) for colloids loaded under the 1.7x10^{-3} ms^{-1} velocity condition (from Rasmuson et al., 2017).

To accomplish this objective, the control boundary used in upscaling η (i.e., the grain surface) is expanded to include the near-surface fluid domain where colloid-surface interactions become significant, approximately out to 200 *nm* separation distance from the grain surface (Johnson, 2020a; Johnson et al., 2018) as shown in Figure 47. Redefining the control boundary for upscaling to include the near-surface fluid domain redefines η as reflecting colloid delivery to the near-surface fluid domain, which is equivalent to attachment under favorable conditions but not under unfavorable conditions. Colloid delivery to the near-surface fluid domain under unfavorable conditions may result in several distinct outcomes such as

a) fast attachment,

b) slow attachment,

c) re-entrainment back to bulk fluid, or

d) retention in the near-surface fluid domain without attachment in a low velocity region such as the rear flow stagnation zone (RFSZ).

For each of these outcomes, we can define corresponding efficiencies α_1, α_2, α_{reent}, and α_{RFSZ}, respectively, to quantify the number of near-surface colloids culminating in each outcome relative to the total number of near-surface colloids (Figure 47), such that the product of η and these efficiencies provides the number of colloids culminating in each outcome relative to the number of colloids in the bulk fluid domain as expressed in Equations (97), (98), (99), and (100).

$$k_f = -\frac{N_c}{L} Ln(1 - \eta)v$$

Fast Attaching Fraction (α_1 of all colloids)

Implicit Near Surface Transport ($1-\alpha_1$ of all colloids)

$$k_{f2} = -\frac{N_c}{L} Ln\left(1 - \eta\left(\alpha_2 + \alpha_{RFSZ}\alpha_{trans-gg} + \alpha_{Reent}\alpha_{trans-bg}\right)\right)v_{ns}$$

Explicit Near Surface Transport ($1-\alpha_1$ of all colloids)

$$k_{ns} = -\frac{N_c}{L} Ln\left(1 - \eta\left(\alpha_2 + \alpha_{RFSZ}\alpha_{trans-gg} + \alpha_{Reent}\alpha_{trans-bg}\right)\right)v^*$$

$$k_{f2}^* = -\left(\frac{v_{ns}}{\pi \frac{d_c}{2}}\right)Ln(1 - \eta\alpha_2)$$
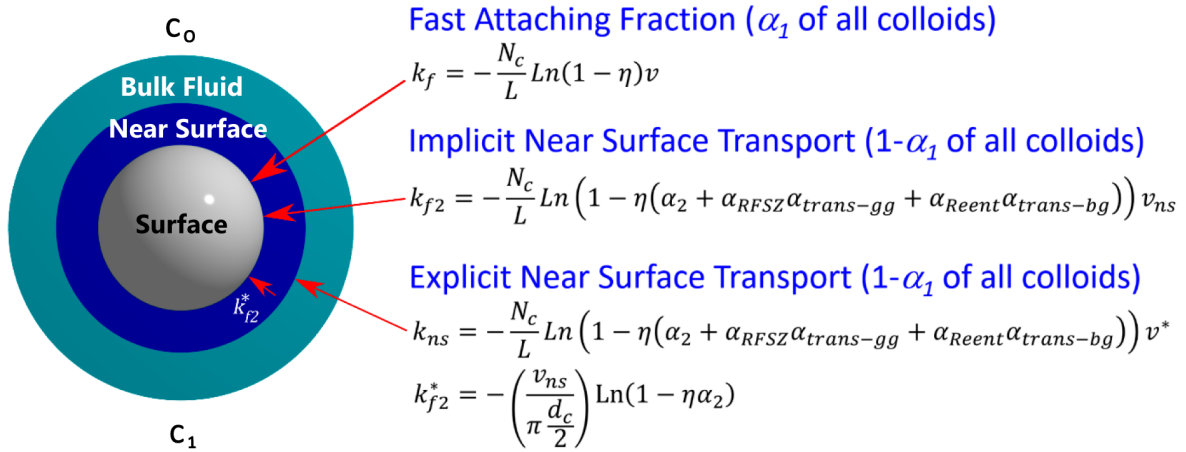
Figure 47 - Upscaling algorithm for unfavorable conditions (from Johnson, 2020).

$$\frac{\# \text{ fast attach}}{\# \text{ bulk fluid}} = \frac{\# \text{ near surface}}{\# \text{ bulk fluid}}\frac{\# \text{ fast attach}}{\# \text{ near surface}} = \eta\alpha_1 \tag{97}$$

$$\frac{\# \text{ slow attach}}{\# \text{ bulk fluid}} = \frac{\# \text{ near surface}}{\# \text{ bulk fluid}}\frac{\# \text{ slow attach}}{\# \text{ near surface}} = \eta\alpha_2 \tag{98}$$

$$\frac{\# \text{ reentrain}}{\# \text{ bulk fluid}} = \frac{\# \text{ near surface}}{\# \text{ bulk fluid}}\frac{\# \text{ reentrain}}{\# \text{ near surface}} = \eta\alpha_{reent} \tag{99}$$

$$\frac{\# \text{ RFSZ}}{\# \text{ bulk fluid}} = \frac{\# \text{ near surface}}{\# \text{ bulk fluid}}\frac{\# \text{ RFSZ}}{\# \text{ near surface}} = \eta\alpha_{RFSZ} \tag{100}$$

The values of η and all four of the above efficiencies (α_1, α_2, α_{reent}, and α_{RFSZ}) are predicted and reported in mechanistic pore-scale simulations incorporating nanoscale charge heterogeneity. The values of α_1 and α_2 are determined by the fraction of overlap among the simulated distributions of colloid residence time prior to attachment under unfavorable versus favorable conditions (Figure 48). If there is complete overlap of these residence time distributions, the unfavorable conditions are practically favorable. All colloids attach fast, $\alpha_1 \to 1$ and $\alpha_2 \to 0$, as can occur under high IS or other conditions that quash colloid-surface repulsion. If there is minimal overlap of these residence time distributions, then $\alpha_1 \to 0$ and $\alpha_2 \to 1$, as occurs under highly unfavorable conditions (Johnson et al., 2018; Johnson, 2020). The transition between these extremes is observed for experiments with varied colloid size (Figure 48), as well as IS (Johnson, 2020).
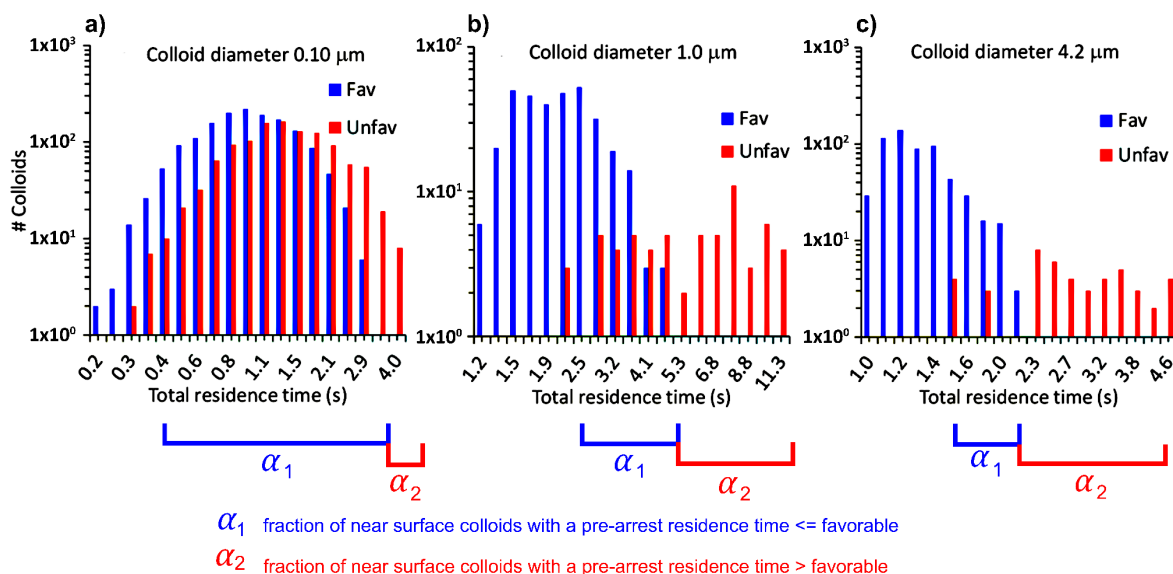
Figure 48 - Histograms of pore scale (Happel sphere-in-cell) simulated total residence times prior to attachment for the three, contrasting carboxylate-modified polystyrene latex colloids of three sizes in fine sand, a) 0.1 μm, b) 1.0 μm, and c) 4.2 μm (from Johnson, 2020).

Upscaling these efficiencies to produce continuum-scale rate coefficients follows the upscaling process for favorable conditions where attachment eliminated further transport, such that the fraction of the population undergoing further transport to the next collector was (1-η) (Figure 43). Under unfavorable conditions, fast and slow attachment each eliminate further transport. However, the fate of α_{RFSZ} colloids (those that move to the rear flow stagnation zone of the grain and remain without attachment in secondary minimum association with the surface) is undefined in mechanistic simulations, at least for those performed in a Happel collector (Johnson et al., 2018; Johnson, 2020). For this reason, we employ a *knob* ($\alpha_{trans\text{-}gg}$) to define the fraction of α_{RFSZ} colloids that at the continuum scale will move down-gradient in the near-surface fluid domain from grain to grain and also potentially undergo slow attachment. Hence, the fraction undergoing further transport in the bulk fluid past a single collector $(C/C_0)^1$ is given as in Equation (101) with the superscript of 1 indicating it is for the fraction passing a single collector.

$$\left(\frac{C}{C_0}\right)^1 = \left(1 - \eta\left(\alpha_1 + \alpha_2 + \alpha_{trans\text{-}gg}\alpha_{RFSZ}\right)\right) \tag{101}$$

We also define an independent knob ($\alpha_{trans-bg}$) for the fraction of re-entrained colloids that may reenter the near-surface fluid domain downstream of the collector. However, this second knob was added for the purpose of symmetry (Johnson, 2020); its significance to the simulations has, to date, been negligible and its utility remains undetermined. All this points to the fact that future pore network simulations will increasingly define such parameters and will render obsolete the knob approach in which increasing values of $\alpha_{trans-gg}$ are invoked to increase the near-surface colloid population at the continuum scale. To be complete by including down-gradient re-entry to the near-surface fluid

domain, the fraction undergoing further bulk fluid transport as the colloid passes by each collector beyond the single collector is shown in Equation (102).

$$\left(\frac{C}{C_0}\right)^1 = \left(1 - \eta\big(\alpha_1 + \alpha_2 + \alpha_{trans-gg}\alpha_{RFSZ} + \alpha_{trans-bg}\alpha_{reent}\big)\right) \tag{102}$$

Considering compounded loss through a series (N_c) of collectors yields Equation (103).

$$\frac{C}{C_0} = \left(1 - \eta\big(\alpha_1 + \alpha_2 + \alpha_{trans-gg}\alpha_{RFSZ} + \alpha_{trans-bg}\alpha_{reent}\big)\right)^{N_c} \tag{103}$$

Ongoing pore network experiments and simulations are needed to further parameterize these efficiencies. Improved approaches will arise from the colloid transport research community.

Equating Equation (103) with the advection-dispersion-filtration equation under steady-state conditions (as performed to produce Equation (95) under favorable conditions) yields the relationship expressed in Equation (104) between η and k_f under unfavorable conditions ($k_{f,unf}$).

$$k_{f,unf} = -v\frac{N_c}{L}\ln\left(1 - \eta\big(\alpha_1 + \alpha_2 + \alpha_{trans-gg}\alpha_{RFSZ} + \alpha_{trans-bg}\alpha_{reent}\big)\right) \tag{104}$$

The arrangement shown in Equation (104) highlights the two primary components of the rate coefficient where the vN_c/L term quantifies the number of collectors passed per unit time and the ln term quantifies the ln-transformed fraction of the population passing each collector. In plain language, these terms represent a frequency and a likelihood, respectively, of passing collectors.

Implementing this rate coefficient ($k_{f,unf}$) in the advection-dispersion-filtration equation produces a reduced steady-state breakthrough relative to favorable conditions. However, it does not produce the ubiquitously observed extended tailing of low colloid concentrations nor the non-exponential RCPs observed under unfavorable conditions.

6.2.3.4 Assumptions to Produce Fast- and Slow-Attaching Colloids from a Population of Identical Individuals

The hypothesis that fast-attaching colloids comprise a subset of the injected colloids, one that is effectively distinct from the slow-attaching subset, and that is not replenished during transport (Johnson, 2020; Johnson et al., 2018) is evaluated in this section. Although this standing hypothesis is unproved, it produces multi-exponential RCPs (Johnson, 2020; Johnson et al., 2018), and is raised on the basis that incomplete pore-scale fluid mixing (de Anna et al., 2013) combined with the colloid-surface repulsion that is imposed under unfavorable conditions, decreases the opportunity for fast attachment as the population moves down-gradient in granular media (Johnson, 2020; Johnson et al., 2018).

The mechanism by which fast attachment may be progressively diminished with increasing transport distance is reduced colloid delivery to FFSZ or other points of flow

impingement on surfaces resulting from the juxtaposition of incomplete mixing lamellae and repulsive barriers to attachment. This hypothesis is being investigated in ongoing pore network experiments.

The incomplete mixing/repulsion hypothesis leads to the following treatment of the mechanistically produced α_1 and α_2 subsets of the near-surface colloid population where the fast-attaching subset (α_1 fraction of the overall population) is governed by determined from η (favorable conditions); the slow-attaching subset (1-α_1 fraction of the overall population) is governed by k_{f2} as derived equivalently to $k_{f,unf}$ independent of the α_1 fraction of the overall population. In this treatment, Equations (105), (106), and (107) apply (Johnson, 2020).

$$\frac{\partial C}{\partial t} = -v\frac{\partial C}{\partial x} + D\frac{\partial^2 C}{\partial x^2} - \alpha_1 k_f C - (1-\alpha_1)k_{f2}C \tag{105}$$

$$\frac{\partial C_{sed}}{\partial t}\frac{\rho_b}{\theta} = \alpha_1 k_f C + (1-\alpha_1)k_{f2}C \tag{106}$$

$$k_{f2} = -v_{ns}\frac{N_c}{L}\ln\left(1 - \eta\left(\alpha_2 + \alpha_{trans-gg}\alpha_{RFSZ} + \alpha_{trans-bg}\alpha_{reent}\right)\right) \tag{107}$$

where:

v_{ns} = average near-surface fluid velocity, which can be reasonably approximated as 5 percent of the bulk pore water velocity in uniform granular media (Johnson, 2020; Johnson et al., 2018), (LT^{-1})

The rationale for using v_{ns} rather than v to define the rate at which colloids pass collectors in Equation (107) is that the slow attachment rate k_{f2} reflects near-surface translation of colloids across grain surfaces (significant near-surface residence times) prior to attachment. In contrast, the rate coefficient defining attachment for the α_1 subset of the colloid population reflects negligible time spent in the near-surface fluid domain prior to attachment (Johnson, 2020; Johnson et al., 2018). The equation for k_{f2} in the SI of Johnson (2020) incorrectly identified v rather than v_{ns} as the characteristic velocity.

The RCPs that emerge from the above treatment are multi-exponential (Figure 49) showing a fast-attaching fraction increasingly depleted with increasing distance of transport and a slow-attaching fraction that increasingly dominates the colloid population with increasing distance of transport. This approach does not produce extended tailing nor non-monotonic RCPs since it treats the near-surface fluid domain implicitly. That is, the impact of the near-surface fluid domain is implicit in the rate coefficients. Simulating the non-monotonic RCPs and extended tailing via explicit simulation of the near surface fluid domain is described subsequently.
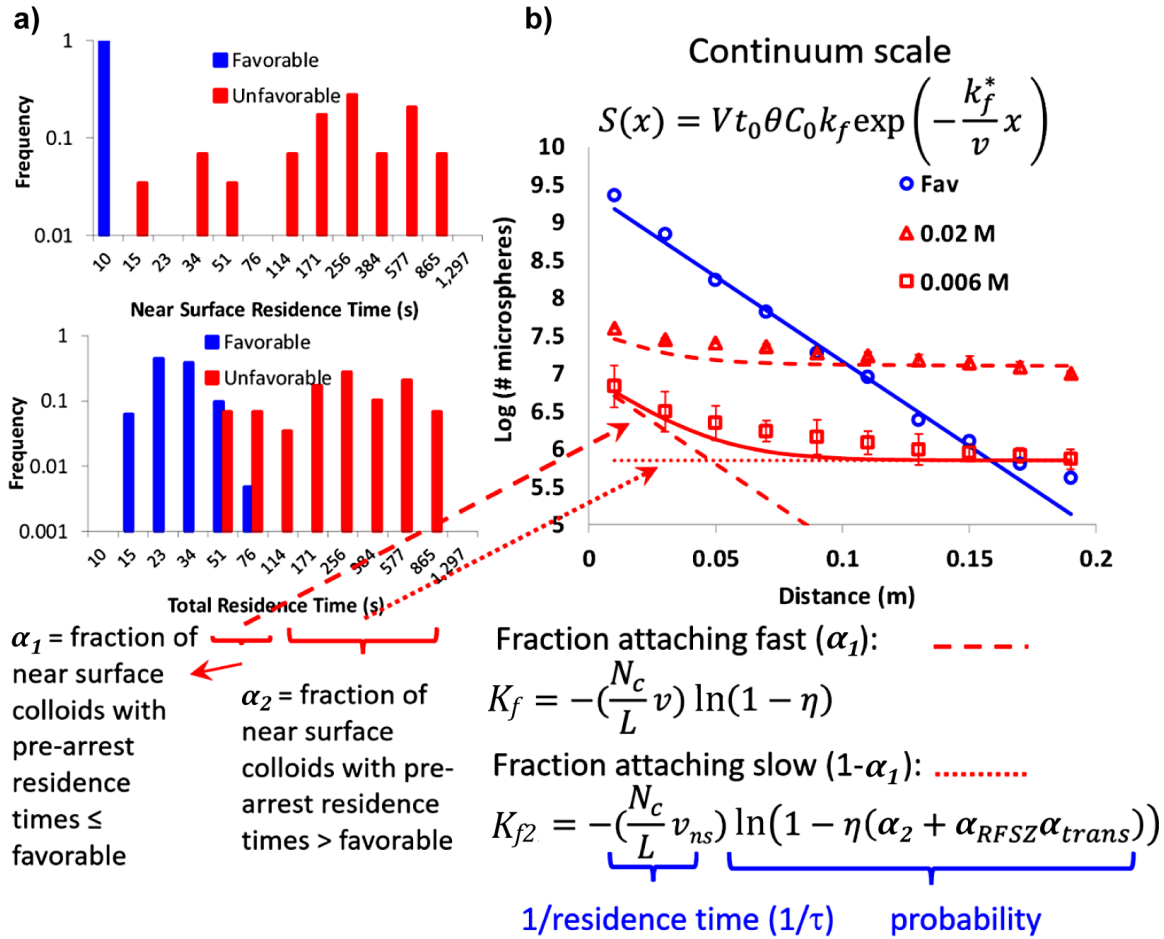
Figure 49 - a) Residence time distributions from pore-scale trajectory simulations under the conditions of Li and others (2004) for carboxylate-modified polystyrene colloids in glass beads at 6 mM NaCl. b) Predicted retention profiles using attachment rate coefficients predicted from residence time distribution as implemented in the expression for *S(x)* (retained # of colloids).

Explicit treatment of near-surface colloid transport is required to produce extended tailing in BTCs and non-monotonic RCPs (Johnson, 2020; Johnson & Hilpert, 2013; Johnson et al., 2018;). Whereas this same assertion and outcome has been produced by other equally useful methods (e.g., Hilpert et al., 2017; Hilpert & Johnson, 2018), the focus here is on a method that descends directly from the method described earlier and is available in Parti-Suite freeware.

Explicit near-surface transport of colloids requires breaking the slow attachment process into two steps as shown by Equations (108), (109), and (110):

1. entry to the near surface governed by k_{ns}, and
2. slow attachment of near-surface colloids governed by k_{f2}^*.

$$\frac{\partial C}{\partial t}\theta_b = -v\frac{\partial C}{\partial x}\theta_b + D\frac{\partial^2 C}{\partial x^2}\theta_b - \alpha_1 k_f C\theta_b - (1-\alpha_1)k_{ns}C\theta_b \qquad (108)$$

$$\frac{\partial C_{ns}}{\partial t}\theta_{ns} = -v_{ns}\frac{\partial C_{ns}}{\partial x}\theta_{ns} + (1-\alpha_1)k_{ns}C\theta_b - k_{f2}^*C_{ns}\theta_{ns} \qquad (109)$$

109

$$\frac{\partial C_{sed}}{\partial t}\rho_b = \alpha_1 k_f C\theta_b + k_{f2}^* C_{ns}\theta_{ns} \tag{110}$$

where:

θ_b	=	volumetric water content of bulk fluid in the REV (dimensionless)
θ_{ns}	=	volumetric water content of near-surface fluid in the REV (dimensionless)
rate coefficients	=	expressed by Equation (111) for entry into the near-surface fluid and Equation (112) for slow attachment of near-surface colloids (T⁻¹)

$$k_{ns} = -v^* \frac{N_c}{L} \ln\left(1 - \eta\left(\alpha_2 + \alpha_{trans-gg}\alpha_{RFSZ} + \alpha_{trans-bg}\alpha_{reent}\right)\right) \tag{111}$$

$$k_{f2}^* = -\left(\frac{v_{ns}}{\pi a_g}\right)\ln(1 - \eta\alpha_2) \tag{112}$$

where:

v^*	=	a characteristic velocity (ranging from v_{ns} to v) governing the residence time in the bulk fluid from which colloids potentially enter the near-surface fluid domain (Johnson, 2020) (LT⁻¹)

The frequency of passing collectors (residence time in near-surface fluid domain) for the slow-attaching colloids is set by the ratio of the v_{ns} to the grain arc length shown in Equation (112). In Figure S3 of Johnson (2020), k_{ns} is incorrectly labeled as K_{f2}.

In explicit simulations with $\alpha_{RFSZ} > 0$ and $\alpha_{trans-gg} > 0$, extended tailing is significant and the multi-exponential profiles that emerge in the absence of consideration of slow-moving near-surface colloids is overprinted by them to produce non-monotonic RCPs as shown in Figure 50 (Johnson, 2020; Johnson et al., 2018).

a)

b)

c)

$$k_f = -\left(\frac{N_c}{L}v\right)\ln(1-\eta)$$

$$k_{ns} = -\left(\frac{N_c}{L}v\right)\ln\left(1-\eta(\alpha_2 + \alpha_{RFSZ}\alpha_{trans})\right)$$

$$k_{f2}^* = -\frac{v_{ns}}{\pi a_c}\ln(1-\alpha_2)$$

d)
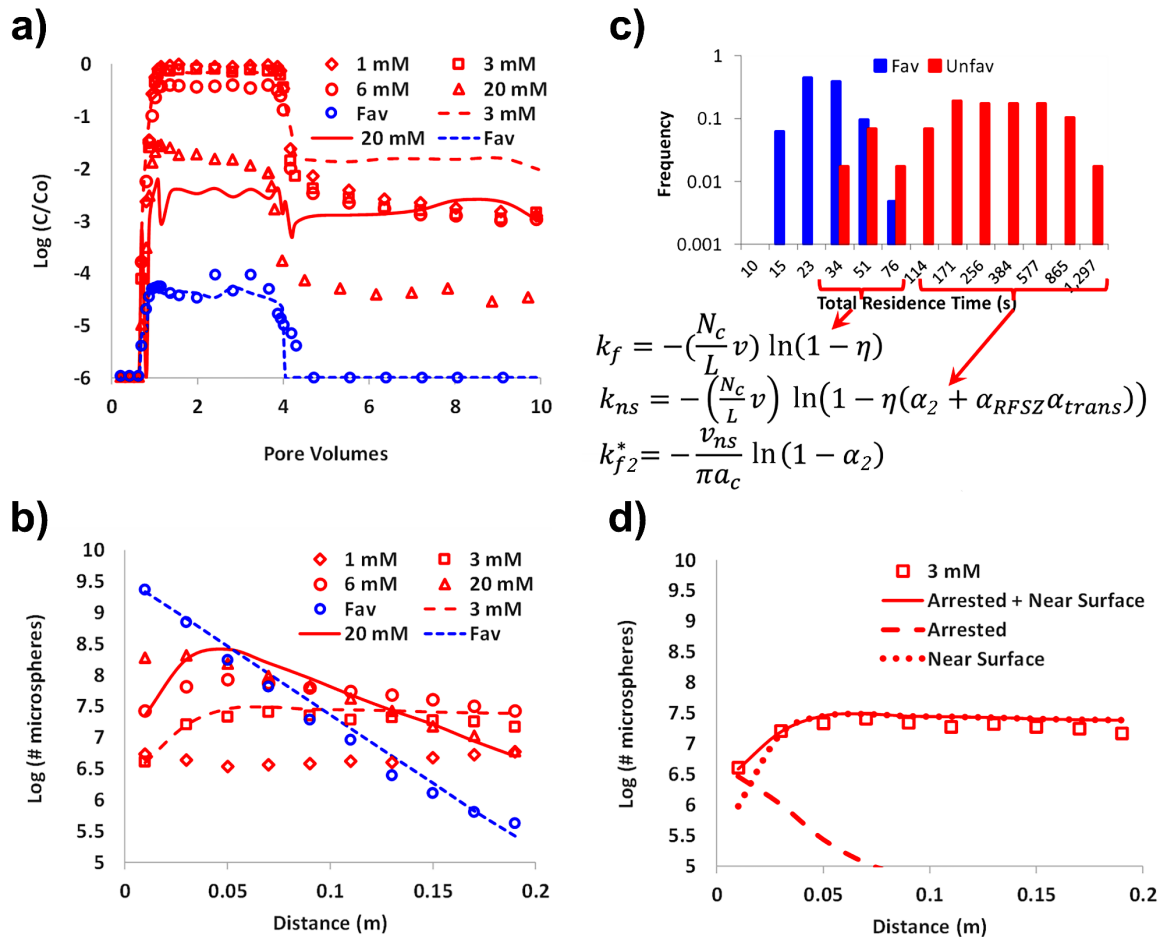
Figure 50 - a) Breakthrough-elution and b) retention profiles with experimental data (symbols) of Li & Johnson (2005); including two-layer simulations (solid and dashed lines for 6 and 3 mM, respectively). c) Histograms of total (bulk plus near-surface) colloid residence times prior to arrest. d) Contributions of arrested (dashed line) and near-surface colloids (dotted line) to 0.006 M retention profile.

Simulation of steady-state plateaus, extended tailing of BTCs, as well as both forms of non-exponential RCPs, from rate coefficients emergent from pore-scale mechanistic simulations with nanoscale heterogeneity is a significant step forward in colloid modeling. Although the sizes and spatial frequencies of nanoscale heterogeneity are empirical and not independently determined, this empiricism is performed at a deeper level than purely descriptive rate coefficients. This allows rate coefficients to emerge from the assumed nanoscale heterogeneity in addition to solution chemistry (e.g., IS) and physical (e.g., α_p, v) parameters as described earlier. We anticipate that future leveraging of such simulations with direct detection of surface heterogeneity by spectrometric, spectroscopic, and force measurement techniques will provide independent constraints on discrete representative nanoscale surface heterogeneity.

6.2.3.5 Opportunities to Mechanistically Address Temporal Phenomena Under Non-Clean-Bed Conditions: Blocking and Ripening

Incorporation of discrete representative nanoscale heterogeneity in mechanistic simulations can lead directly to a maximum attachment capacity (blocking) as well as

111

enhanced attachment to previously attached colloids (ripening). This is dependent on the repulsion associated with colloid-surface versus colloid-colloid interaction in mechanistic simulations. Inclusion of this capability in simulation codes has lagged because it requires that all processors working on trajectory simulations be "aware" of previously attached colloids and inter-processor communication is computationally expensive. This represents a future opportunity to extend mechanistic simulations to predict blocking and ripening (i.e., simulation beyond clean-bed conditions).

6.2.3.6 Contrasting Colloid Transport Behaviors in Granular Versus Fractured Media

An additional issue involves mechanistic simulation of preferential pathways in porous media. This book presents the use of Happel or other collectors to represent flow around grains wherein colloid delivery to the surface occurs primarily in zones of flow impingement (i.e., FFSZ). In contrast, pore-scale representation of transport in fractures is performed using parallel plate geometry (Rasmuson et al., 2019b) to examine systems where colloid delivery to surfaces via flow impingement is absent and instead delivery is dominated by diffusion and/or gravity (Figure 51). Rasmuson and others (2019b) used these contrasting models in Wisconsin to explain the greater detection frequency of pathogens in water wells located in fractured till and limestone relative to granular sand.
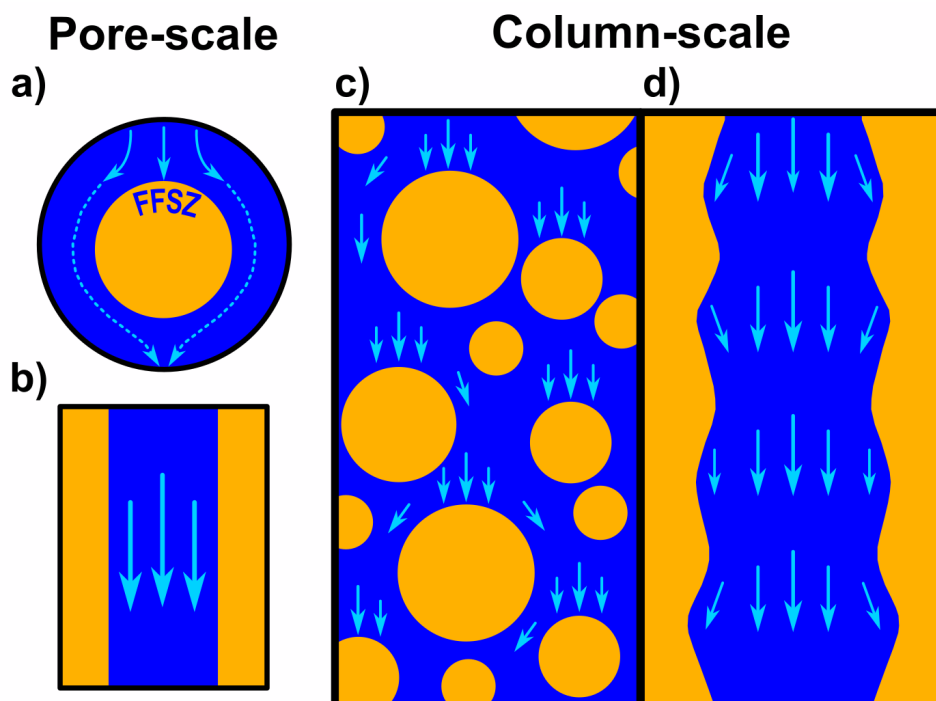
Figure 51 - Contrasting colloid transport simulation geometries at the pore scale in a) granular versus b) fractured media and at the column scale in c) granular versus d) fractured media (modified from Rasmuson et al., 2019b).

7 Wrap Up

This book provides a coherent multi-scale description of existing knowledge about colloid transport in groundwater within granular media. The treatment focuses on transport governed by the intersection of physics and chemistry at the nano, pore, and continuum scales.

At the nanoscale, the overall interactions between colloids and surfaces that emanate from VDW, EDL, Born, LAB, and steric types of interactions are examined. The profound impact of opposite versus like charges among colloids and surfaces is explored. Like-charged conditions generate a repulsive barrier to attachment of magnitude inversely related to solution IS.

At the pore scale, the following are described:

1. the profound contrast in colloid transport under conditions where a repulsive barrier is absent (favorable attachment conditions) versus present (unfavorable attachment conditions);

2. the integration of colloid-surface interaction forces with fluid drag, diffusion, and gravitational forces to simulate colloid trajectories in representations of porous media (collectors) for comparison with experimental data;

3. how simulations performed under unfavorable attachment conditions yield zero predicted attachment (except for those with very low repulsive barriers) unless nanoscale charge heterogeneity is incorporated into the simulations;

4. how incorporation of discrete representative nanoscale heterogeneity (DRNH) into simulations reproduce experimentally observed pore-scale colloid transport behaviors and trends in colloid attachment as a function of colloid size, among other parameters; and

5. the contrasting interactions of solutes versus colloids with surfaces, relating them to equilibrium versus irreversible interactions with surfaces.

At the continuum scale, it is shown that:

1. experimentally observed colloid breakthrough-elution concentration histories (BTCs) and profiles of retained colloids (RCPs) exhibit profound contrasts under favorable versus unfavorable attachment conditions;

2. equilibrium versus irreversible interactions in transport simulations lead to later versus lesser breakthrough, respectively;

3. interactions of solutes and colloids potentially impact the transport of both;

4. compounded loss of colloids to each grain passed produces an exponential decrease in the colloid concentration with increasing distance of transport, thereby creating a quantitative link between pore- and continuum-scale transport (upscaling);

5. simulated colloid trajectories produce distributions of colloid residence times in the near-surface fluid domain prior to attachment, and that fast- and slow-attaching subpopulations emerge among identical individuals in these simulations;

6. the process of upscaling under unfavorable conditions, which involves considering colloid retention is not only at the grain surface, but also within the surrounding near-surface fluid domain; and

7. simulating the fast-attaching colloid population as depleted rather than replenished due to incomplete pore-scale mixing produced experimentally observed non-exponential RCPs and extended tailing in BTCs under unfavorable conditions.

This book focuses on physical and chemical aspects of colloid transport, and does not address monitoring, protection, and other practical aspects of colloids in groundwater. Also, the biology at play in many colloid transport scenarios is not discussed herein. For example, changes in microbial surface properties that occur in response to metabolic processes (growth and starvation) impact transport (e.g., in microbial enhanced oil recovery, or bioaugmentation for contaminant remediation) are not considered in this book.

there is only cursory mention of the impacts of macroscale physical and chemical heterogeneity that impact field-scale transport in particular. Likewise, other complicating factors such as non-spherical colloids are not addressed, rather only the proverbial "spherical cow" is considered. Even so, the similarity of experimentally observed BTCs and RCPs among microspheres, microbes, clays, and engineered nanoparticles of widely contrasting shapes and composition indicates that the processes described here are relevant despite the incomplete treatment of other processes at play.

The focus in this book is on bridging scales to understand the role of nanoscale interactions in pore- and continuum-scale colloid transport. Toward that end, hypotheses that link these three scales and warrant further investigation are presented. Topics ripe for further investigation include direct detection of nanoscale heterogeneity and reconciliation with simulations, as well as the potential intersection of incomplete pore-scale mixing and colloid-surface repulsion in producing distinct transport behaviors among a population of identical individuals.

We encourage readers to make use of Parti-Suite freeware to explore the concepts presented here and to enhance its capabilities to address a broader array of concepts and applications.

8 Exercises

These exercises correspond to the descriptive and how-to videos for using Parti-Suite freeware to explore concepts described in the text.

Exercise 1

This exercise corresponds to Figure 1 of the text which links to a video describing an overview of Parti-Suite freeware.

a) How are the modules linked across scales?

b) Can the correlation equations module be used to predict colloid attachment for a broad range of conditions?

Exercise 2

Exercise 2 corresponds to Figure 14 of the text which provides a link to a video describing the xDLVO module of Parti-Suite freeware, including the impacts of roughness.

a) What is the primary parameter that determines whether a repulsive barrier will exist at separation distances beyond a primary minimum in the colloid-surface interaction profile?

b) What is the effect of increased roughness?

c) Can roughness create attraction?

d) What is the zone of interaction (ZOI) and how does heterodomain size affect the xDLVO profiles?

Exercise 3

This Exercise 3 corresponds to Figure 22 of the text that presents a video describing the GUI of the particle trajectory (Traj-Hap) module of Parti-Suite freeware.

Must I use the GUI to perform colloid trajectory simulations?

Exercise 4

This Exercise 4 corresponds to Figure 23 of the text which links to a video describing how to perform particle trajectory simulations under favorable attachment conditions in the Traj-Hap module of Parti-Suite freeware.

a) What are the main differences in the trajectories simulated for relatively large versus small colloids (e.g., 4 μm versus 0.4 μm diameters)?

b) Where do I learn more about the time step and other simulation controls for the trajectory simulations?

c) Are charge heterogeneity and roughness both treated explicitly in the trajectory simulations?

Click for Solution to Exercise 4⤵

Return to where text linked to Exercise 4⤴

Exercise 5

This exercise corresponds to Figure 25 of the text which links to a video describing how to obtain collector efficiencies from particle trajectory simulations in the Traj-Hap module of Parti-Suite freeware.

a) In determining whether the injection radius is sufficiently large to produce a valid collector efficiency, is it sufficient to examine the locations of attached and exited colloids in the plane normal to flow and determine whether there is a halo of exiting colloids surrounding the attached colloids?

b) What happens if the injection radius (R_{lim}) approaches the fluid shell radius?

Click for Solution to Exercise 5⤵

Return to where text linked to Exercise 5⤴

Exercise 6

This Exercise 6 corresponds to Figure 29 of the text which links to a video describing how to perform detachment due to perturbations in the Traj-Hap module of Parti-Suite freeware.

How are IS reduction and increased fluid velocity perturbations simulated in the Traj-Hap module?

Click for Solution to Exercise 6⤵

Return to where text linked to Exercise 6⤴

116

The GROUNDWATER PROJECT   ©The Author(s)   Free download from gw-project.org

Anyone may use and share gw-project.org links. Direct distribution of the book is strictly prohibited.

Exercise 7

This exercise corresponds to Figure 34 of the text which links to a video describing how to perform particle trajectory simulations under unfavorable attachment conditions in the Traj-Hap module of Parti-Suite freeware.

a) In the simulation, grain heterodomains appear in different locations inside the zone of influence (ZOI). Does this influence colloid attachment?

b) If the heterodomain occupies more than 50 percent of the ZOI, is attachment guaranteed?

Exercise 8

This exercise corresponds to Figure 44 of the text which links to a video describing the upscaling process from nano- to pore- to continuum-scale using concepts employed in Parti-Suite freeware.

a) Do the simulations in Parti-Suite under unfavorable attachment conditions incorporate nanoscale charge heterogeneity, even though there is little direct spectroscopic or spectrometric measurements constraining this inferred heterogeneity?

Exercise 9

This exercise corresponds to Figure 45 of the text which links to a video describing how to perform upscaling from nano- to pore- to continuum-scale using Parti-Suite freeware.

a) Are both the pore-scale and continuum-scale transport simulations Lagrangian, or is the latter Eulerian?

9 References

Albinger, O., Biesemeyer, B. K., Arnold, R. G., & Logan, B. E. (1994). Effect of bacterial heterogeneity on adhesion to uniform collectors by monoclonal populations. *FEMS Microbiology Letters, 24*(3), 321–326. https://doi.org/10.1111/j.1574-6968.1994.tb07303.x↗.

Ashraf, M. A., Shatirah, A., & Mohd, J. A. (2014). Cesium-137: Radio-chemistry, fate, and transport, remediation, and future concerns. *Critical Reviews in Environmental Science and Technology, 44*, 1740–1793. https://doi.org/10.1080/10643389.2013.790753↗.

Auld, H., MacIver, D., & Klaassen, J. (2004). Heavy rainfall and waterborne disease outbreaks: The Walkerton example. *Journal of Toxicology and Environmental Health, - Part A, 67*(20-22), 879–1887. https://doi.org/10.1080/15287390490493475↗.

Auset, M., & Keller, A. A. (2006). Pore-scale visualization of colloid straining and filtration in saturated porous media using micromodels. *Water Resources Research, 42*, 1–9. https://doi.org/10.1029/2005WR004639↗.

Babakhani, P. (2019). The impact of nanoparticle aggregation on their size exclusion during transport in porous media: One- and three-dimensional modelling investigations. *Scientific Reports, Report 14071, 9*(1), 1–12. https://doi.org/10.1038/s41598-019-50493-6↗.

Bai, R. B., & Tien, C. (1996). A new correlation for the initial filter coefficient under unfavorable surface interactions. *Journal of Colloid and Interface Science, 179*(2), 631–634. https://doi.org/10.1006/jcis.1996.0259↗.

Bai, R. B., & Tien, C. (1999). Particle deposition under unfavorable surface interactions. *Journal of Colloid and Interface Science, 218*(2), 488–499. https://doi.org/10.1006/jcis.1999.6424↗.

Bargozin, H., Hadadhania, R. A., Faraji, H., & Yousefzadeh, H. (2015). Effect of rough nanoparticle orientation on DLVO energy interaction. *Journal of Dispersion Science and Technology, 36*(6), 755–764. https://doi.org/10.1080/01932691.2014.921189↗.

Baygents, J. C., Glynn, J. R., Albinger, O., Biesemeyer, B. K., Ogden, K. L., & Arnold, R. G. (1998). Variation of surface charge density in monoclonal bacterial populations: Implications for transport through porous media. *Environmental Science & Technology, 32*(11), 1596–1603. https://doi.org/10.1021/es9707116↗.

Bedrikovetsky, P., Osipov, Y., Kuzmina, L., Malgaresi, G. (2019). Exact upscaling for transport of size-distributed colloids. *Water Resources Research, 55*(2), 1011–1039. https://doi.org/10.1029/2018WR024261↗.

Bendersky, M., & Davis, J. M. (2011). DLVO interaction of colloidal particles with topographically and chemically heterogeneous surfaces. *Journal of Colloid and Interface Science 353*(1), 87–97. https://doi.org/10.1016/j.jcis.2010.09.058↗.

Berge, N. D., & Ramsburg,, C. A. (2009). Oil-in-water emulsions for encapsulated delivery of reactive iron particles. *Environmental Science & Technology, 43*(13), 5060–5066. https://doi.org/10.1021/es900358p↗.

Bhattacharjee, S., Chun-Han, K., & Elimelech, M. (1998). DLVO interaction between rough surfaces. *Langmuir, 14*(12), 3365–3375. https://doi.org/10.1021/la971360b↗.

Bianco, C., Higuita, J. E., Tosco, T., Tiraferri, A., & Sethi, R. (2017). Controlled deposition of particles in porous media for effective aquifer nanoremediation. *Nature Scientific Reports, 71*, 12992. https://www.nature.com/articles/s41598-017-13423-y↗.

Bolster, C. H., Mills, A. L., Hornberger, G., & Herman, J. (2000). Effect of intra-population variability on the long-distance transport of bacteria. *Groundwater, 38*(3), 370–375. https://doi.org/10.1111/j.1745-6584.2000.tb00222.x↗.

Bolster, C. H., Mills, A. L., Hornberger, G. M., & Herman, J. S. (1999). Spatial distribution of deposited bacteria following miscible displacement experiments in intact cores. *Water Resources Research, 35*(6), 1797–1807. https://doi.org/10.1029/1999WR900031↗.

Borchardt, M. A., Bertz, P. D., Spencer, S. K., & Battigelli, D. A. (2003). Incidence of enteric viruses in groundwater from household wells in Wisconsin. *Applied and Environmental Microbiology Journal, 69*(2), 172–1180.
https://doi.org/10.1128/AEM.69.2.1172-1180.2003↗.

Bradbury, K. R., Borchardt, M. A., Gotkowitz, M., Spencer, S. K., Zhu, J., & Hunt, R. J. (2013). Source and transport of human enteric viruses in deep municipal water supply wells. *Environmental Science & Technology, 47*(9), 4096–4103.
https://doi.org/10.1021/es400509b↗.

Bradford, S., Bettahar, M., Simunek, J., & Genuchten, G. M. (2004). Straining and attachment of colloids in physically heterogeneous porous media. *Vadose Zone Journal, 3*(2), 384–394. https://doi.org/10.2136/vzj2004.0384↗.

Brenner, H. (1961).The slow motion of a sphere through a viscous fluid towards a plane surface. *Chemical Engineering Science, 16*(3–4), 242–251. https://doi.org/10.1016/0009-2509(61)80035-3↗.–

Brow, C., Tong, M., Johnson, W. P., & Ricka, J. (2005). Comparison of microsphere deposition in porous media versus simple shear systems. *Colloids & Surfaces A: Physicochemical and Engineering Aspects, 253*(1–3), 125–136.
https://doi.org/10.1016/j.colsurfa.2004.11.005↗.

Burganos, V.., Paraskeva, C. A., Christofides, P. D., & Payatakes., A. C. (1994). Motion and deposition of non-brownian particles in upflow collectors. *Separations Technology, 4*(1), 47–49. https://doi.org/10.1016/0956-9618(94)80005-7↗.

Burganos, V. N., Paraskeva, C., & Payatakes, A. (1992).Three-dimensional trajectory analysis and network simulation of deep bed filtration. *Journal of Colloid and Interface Science, 148*(1), 167–181. https://doi.org/10.1016/0021-9797(92)90125-6↗.

Busch, J., Meißner, T., Bleyl, Potthoff, A., Bleyl, S., Georgi, A., Mackenzie, K., Trabitzsch, R., Werban, U., & Oswald, S. E. (2015). A field investigation on transport of carbon-supported nanoscale zero-valent ion (NZVI) groundwater. *Journal of Contaminant Hydrology, 181*, 59–68. https://doi.org/10.1016/j.jconhyd.2015.03.009↗.

Butt, H. J., Cappella, B., & Kappl, M. (2005). Force measurements with the atomic force microscope: Technique, interpretation and applications. *Surface Science Reports*, *59*(1–6), 1–152. https://doi.org/10.1016/j.surfrep.2005.08.003↗.

Camesano, T. A., Unice, K. M., & Logan, B. E. (1999). Blocking and ripening of colloids in porous media and their implications for bacterial transport. *Colloids and Surfaces A: Physicochemical and Engineering Aspects, 160*(3), 291–308. https://doi.org/10.1016/S0927-7757(99)00156-9↗.

Cardenas, M. B. (2008).Three-dimensional vortices in single pores and their effects on transport. *Geophysical Research Letters, 35*(18), 1–14. https://doi.org/10.1029/2008GL035343↗.

Chandrasekhar, S. (1943). Stochastic problems in physics and astronomy. *Reviews of Modern Physics, 15*(1), 1–89. https://doi.org/10.1103/RevModPhys.15.1↗.

Chang, Y. I., Cheng, W. Y., & Chan, H. C. (2009). A proposed correlation equation for predicting filter coefficient under unfavorable deposition conditions. *Separations Technology, 65*(3), 248–250. https://doi.org/10.1016/j.seppur.2008.10.031↗.

Charmas, R., Zarzycki, P., Villiéras, F., Thomas, F., Prélot, B., & Piasecki, W. (2004). Influence of electrolyte ion adsorption on the derivative of potentiometric titration curve of oxide suspension - Theoretical analysis. *Colloids Surfaces: A Physicochemical Engineering Aspects, 244*(1–3), 9–17. https://doi.org/10.1016/j.colsurfa.2004.06.001↗.

Chatterjee, J., Pratap, S., & Abdulkareem, S. (2011). Dual-deposition rates in colloid filtration caused by coupled heterogeneities in a colloidal population. *Journal of Colloid and Interface Science, 356*(1), 362–368. https://doi.org/10.1016/j.jcis.2010.12.029↗.

Cheng, T., & Saiers, J. E. (2015). Effects of dissolved organic matter on the co-transport of mineral colloids and sorptive contaminants. *Journal of Contaminant Hydrology, Report 177–178C*(1), 148–157. https://doi.org/10.1016/j.jconhyd.2015.04.005↗.

Chiou, C. T., Malcolm, R. L., Brinton, T. I., & Kile, D. E. (1986). Water solubility enhancement of some organic pollutants and pesticides by dissolved humic and fulvic acids. *Water Environmental Science & Technology, 20*(5), 502-508. https://doi.10.1021/es00147a010↗.

Conboy, M. J., & Goss, M. (2000). Natural protection of groundwater against bacteria of fecal origin. *Journal of Contaminant Hydrology, 43*(1), 1–24. https://doi.org/10.1016/S0169-7722(99)00100-X↗.

Corapcioglu, Y. M., & Jiang, S. (1993). Colloid facilitated groundwater transport. *Water Resources Research*, *29*(7), 2215. https://doi.org/10.1029/93WR00404↗.

Cortis, A., Harter, T., Hou, L., Atwill, E. R., Packman, A. I., & Green, P. G. (2006). Transport of *Cryptosporidium parvum* in porous media: Long-term elution experiments and continuous time random walk filtration modeling. *Water Resources Research, 42*(12,), W12S13. https://doi.org/10.1029/2006WR004897↗.

Curriero, F. C., Patz, J. A., Rose, J. B., & Lele, S. (2001). The association between extreme precipitation and waterborne disease outbreaks in the United States, 1948–1994. *American Journal of Public Health, 91*(8), 1194–1199. https://doi.org/10.2105/ajph.91.8.1194↗.

Cushing, R. S., & Lawler, D. F. (1998) Depth filtration: Fundamental investigation through three-dimensional trajectory analysis. *Environmental Science & Technology, 32*(23), 3793–3801. https://doi.org/10.1021/es9707567↗.

Davis, J. A. (1982). Adsorption of natural dissolved organic matter at the oxide/water interface. *Geochimica et Cosmochimica Acta, 46*(11), 2381–2393. https://doi.org/10.1016/0016-7037(82)90209-5↗.

de Jonge H., Jacobsen, O. H., de Jonge, L. W., & Moldrup, P. (1998). Particle-facilitated transport of prochloraz in undisturbed sandy loam soil columns. *Journal of Environmental Quality, 27*(6), 1495–503. https://doi.org/10.2134/jeq1998.00472425002700060028x↗.

DeBorde, D. C., Woessner, W. W., Kiley, Q. T., & Ball, P. (1999). Rapid transport of viruses in a floodplain aquifer. *Water Research, 33*(10), 2229–2238. https://doi.org/10.1016/S0043-1354(98)00450-3↗.

Dentz, M., & Berkowitz, B. (2003). Transport behavior of a passive solute in continuous time random walks and multirate mass transfer. *Water Resources Research, 39*(5), SBH 1–20. https://doi.org/10.1029/2001WR001163↗.

Derjaguin, B., & Landau, L. (1941). Theory of the stability of strongly charged lyophobic sols and of the adhesion of strongly charged particles in solutions of electrolytes. *Progress in Surface Science, 43*(1–4), 30–59. https://doi.org/10.1016/0079-6816(93)90013-L↗.

Drelich, J., & Wang, Y. U. (2011). Charge heterogeneity of surfaces: Mapping and effects on surface forces. *Advances in Colloid and Interface Science, 165*(2), 91–101. https://doi.org/10.1016/j.cis.2010.12.009↗.

Duffadar, R. D., & Davis, J. M. (2007). Interaction of micrometer-scale particles with nanotextured surfaces in shear flow. *Journal of Colloid and Interface Science, 308*(1), 20–29. https://doi.org/10.1016/j.jcis.2006.12.068↗.

Duffadar, R. D., & Davis, J. M. (2008). Dynamic adhesion behavior of micrometer-scale particles flowing over patchy surfaces with nanoscale electrostatic heterogeneity. J*ournal of Colloid and Interface Science, 326*(1), 18–27. https://doi.org/10.1016/j.jcis.2008.07.004↗.

Duffadar, R., Kalasin, S., Davis, J. M., & Santore, M. M. (2008). The impact of nanoscale chemical features on micron-scale adhesion: Crossover from heterogeneity-dominated to mean-field behavior. *Journal of Colloid and Interface Science, 337*(2), 396–407. https://doi.org/10.1016/j.jcis.2009.05.046↗.

Dunphy Guzman, K. A., Finnegan, M. P., & Banfield, J. F. (2006). Influence of surface potential on aggregation and transport of titania nanoparticles. *Environmental Science & Technology, 40*(24), 7688–7693. https://doi.org/10.1021/es060847g.

Dykaar, B. B., & Kitanidis, P. K. (1996). Macrotransport of a biologically reacting solute through porous media. *Water Resources Research, 32*(2), 307–320. https://doi.org/10.1029/95WR03241.

Elimelech, M., & O'Melia, C. R. (1990). Kinetics of deposition of colloidal particles in porous media. *Environmental Science & Technology, 24*(10), 1528–1536. https://doi.org/10.1021/es00080a012.

Elimelech, M. (1992). Predicting collision efficiencies of colloidal particles in porous media. *Water Research, 26*(1), 1–8. https://doi.org/10.1016/0043-1354(92)90104-C.

Elimelech, M. (1994). Particle deposition on ideal collectors from dilute flowing suspensions: Mathematical formulation, numerical solution, and simulations. *Separations Technology, 4*(4), 186-212. https://doi.org/10.1016/0956-9618(94)80024-3.

Elimelech, M., Nagai, M., Ko, C. H., & Ryan, J. N. (2000). Relative insignificance of mineral grain zeta potential to colloid transport in geochemically heterogeneous porous media. *Environmental Science & Technology, 34*(11), 143–2148. https://doi.org/10.1021/es9910309.

Elimelech, M., Gregory, J., & Jia, X. (1995). *Particle deposition and aggregation: Measurement, modelling and simulation.* Elsevier. https://www.elsevier.com/books/particle-deposition-and-aggregation/elimelech/978-0-7506-0743-8.

Embrey, S. S., & Runkle, D. L. (2006). *Microbial quality of the nation's ground-water resources 1993–2004 (Scientific Investigations Report 2006-5290).* National Water-Quality Assessment Program Principal Aquifers, US Geological Survey. https://pubs.usgs.gov/sir/2006/5290/pdf/sir20065290.pdf.

Ermak, D. L., & McCammon, J. A. (1978). Brownian dynamics with hydrodynamic interactions. *The Journal of Chemical Physics, 69*(4), 1352–1360. https://doi.org/10.1063/1.436761.

Foppen, J. W., van Herwerden, M., & Schijven, J. (2007). Transport of *Escherichia coli* in saturated porous media: Dual mode deposition and intra-population heterogeneity, *Water Research, 41*(8), 1743–1753. https://doi.org/10.1016/j.watres.2006.12.041.

Franchi, A., & O'Melia, C. R. (2003). Effects of natural organic matter and solution chemistry on the deposition and reentrainment of colloids in porous media. *Environmental Science & Technology, 37*(6), 1122–1129. https://doi.org/10.1021/es015566h.

Ginn, T.R. (2000). On the distribution of multicomponent mixtures over generalized exposure time in subsurface flow and reactive transport: Theory and formulations for residence-time-dependent sorption/desorption with memory. *Water Resources Research, 36*(10), 2885–2893. https://doi.org/10.1029/2000WR900170.

Ginn, T. R. (2009). Generalization of the multirate basis for time-convolution to unequal forward and reverse rates and connection to reactions with memory. *Water Resources Research, 45*(12), 1122–1129. https//doi.org/10.1029/2009WR008320↗.

Goldman, A. J., Cox, R. G., & Brenner, H. (1967a). Slow viscous motion of a sphere parallel to a plane wall—I. Motion through a quiescent fluid. *Chemical Engineering Science, 22*(4), 637–651. https://doi.org/10.1016/0009-2509(67)80047-2↗.

Goldman, A. J., Cox, R. G., & Brenner, H. (1967b). Slow viscous motion of a sphere parallel to a plane wall—II. Couette flow. *Chemical Engineering Science, 22*(4), 653–660. https://doi.org/10.1016/0009-2509(67)80048-4↗.

Gomez-Eyles, J. L., Yupanqui, C., Beckingham, B., Riedel, G., Gilmour, C., & Ghosh, U. (2013). Evaluation of biochars and activated carbons for in situ remediation of sediments impacted with organics, mercury, and methylmercury. *Environmental Science & Technology, 47*(23), 13721–13729. https://doi.org/10.1021/es403712q↗.

Gondret, P., Lance, M., & Petit, L. (2002). Bouncing motion of spherical particles in fluids. *Physics of Fluids, 14*(2), 643–652. https://doi.org/10.1063/1.1427920↗.

Goren, S. L., & O'Neill, M. E. (1971). On the hydrodynamic resistance to a particle of a dilute suspension when in the neighborhood of a large obstacle. *Chemical Engineering Science, 26*(3), 325–338. https://doi.org/10.1016/0009-2509(71)83008-7↗.

Gregory, J. (1981). Approximate expressions for retarded van der Waals interaction. *Journal of Colloid and Interface Science, 83*(1), 138–145. https://doi.org/10.1016/0021-9797(81)90018-7↗.

Gupta, V., Johnson, W. P., Shafeian, P., Ryu, H., Alum, A., Abbaszadegan, M., Hubbs, S., & Rauch-Williams, T. (2009). Riverbank filtration: Comparison of pilot-scale transport with theory. *Environmental Science & Technology, 43*(3), 669–676. https://doi.org/10.1021/es8016396↗.

Haggerty, R., McKenna, S. A., & Meigs, L. C. (2000). On the late-time behavior of tracer test breakthrough curves. *Water Resources Research, 36*(12), 3467–3479. https://doi.org/10.1029/2000WR900214↗.

Hahn, M. W., Abadzic, D., & O'Melia, C. R. (2004). Aquasols: On the role of secondary minima. *Environmental Science & Technology, 38*(22), 5915–5924. https://doi.org/10.1021/es049746d↗.

Happel, J. (1958). Viscous flow in multiparticle systems: Slow motion of fluids relative to beds of spherical particles. *AIChE Journal, 4*(2), 197–201. https://doi.org/10.1002/aic.690040214↗.

Happel, J., & Brenner, H. (1983). *Mechanics of fluids and transport processes, Vol. 1. Low Reynolds number hydrodynamics with special applications to particulate media* (2nd ed., revised). Kluwer Boston. http://gidropraktikum.narod.ru/Happel-Brenner-eng.pdf↗.

Harter, T., Wagner, S., & Atwill, E. R. (2000). Colloid transport and filtration of *Cryptosporidium parvum* in sandy soils and aquifer sediments. *Environmental Science & Technology, 34*(1), 62–70. https://doi.org/10.1021/es990132w↗.

Harvey, R. W. (1997). Microorganisms as tracers in groundwater injection and recovery experiments: A review. *AFEMS Microbiology Reviews, 20*(3–4), 461–472. https://doi.org/10.1016/S0168-6445(97)00026-0↗.

Harvey, R. W., & Garabedlan, S. P. (1991). Use of colloid filtration theory in modeling movement of bacteria through a contaminated sandy aquifer. *Environmental Science and Technology, 25*(1), 178–185. http://doi.org/10.1021/es00013a021↗.

Harvey, R. W., Kinner, N. E., Bunn, A., MacDonald, D., & Metge, D. (1995).Transport behavior of groundwater protozoa and protozoan-sized microspheres in sandy aquifer sediments. *Applied and Environmental Microbiology, 61*(1), 209–217. https://doi.org/10.1128/aem.61.1.209-217.1995↗.

Hendry, M. J., Lawrence, J. R., & Maloszewski, P. (1997). The role of sorption in the transport of *Klebsiella oxytoca* through saturated silica sand. *Groundwater, 35*(4), 574–584. https://doi:org/10.1111/j.1745-6584.1997.tb00122.x↗.

Hilpert, M., Rasmuson, A., & Johnson, W. P. (2017). A binomial modeling approach for upscaling colloid transport under unfavorable conditions: Emergent prediction of extended tailing. *Water Resources Research, 53*(7), 5626–5644. https://doi.org/10.1002/2016WR020123↗.

Hilpert, M., & Johnson, W. P. (2018). A binomial modeling approach for upscaling colloid transport under unfavorable attachment conditions: Emergent prediction of nonmonotonic retention profiles. *Water Resources Research, 54*(1), 46–60. https://doi.org/10.1002/2017WR021454↗.

Hoek, E. M. V., Bhattacharjee, S., & Elimelech, M. (2003). Effect of membrane surface roughness on colloid–membrane DLVO interactions. *Langmuir, 19*(11), 4836–4847. https://doi.org/10.1021/la027083c↗.

Hoek, E. M. V., & Agarwal, G. K. (2006). Extended DLVO interactions between spherical particles and rough surfaces. *Journal of Colloid and Interface Science, 298*(1), 50–58. https://doi.org/10.1016/j.jcis.2005.12.031↗.

Hrudey, S. E., & Hrudey, E. J. (2004). *Safe drinking water – Lessons from recent outbreaks in affluent nations*. IWA Publishing. https://www.ncbi.nlm.nih.gov/pmc/articles/PMC6976236/↗.

Huang, X., Bhattacharjee, S., & Hoek, E. M. V. (2010). Is surface roughness a "scapegoat" or a primary factor when defining particle–substrate interactions? *Langmuir, 26*(4), 2528–2537. https://doi.org/10.1021/la9028113↗.

Hubbe, M. A. (1984). Theory of detachment of colloidal particles from flat surfaces exposed to flow. *Colloids and Surfaces, 12*, 151-178. https://doi.org/10.1016/0166-6622(84)80096-7↗.

Hunt, J. R., & Johnson, W. P. (2016). Pathogen transport in groundwater systems-Contrasts with traditional hydrogeological approaches. *Hydrogeology Journal, 46*(40), 551–560. https://doi.org/10.1007/s10040-016-1502-z↗.

Israelachvili, J. N. (2011). *Intermolecular and surface forces* (3rd ed.). Elsevier. https://www.elsevier.com/books/intermolecular-and-surface-forces/israelachvili/978-0-12-391927-4↗.

Jahan, S., Alias, Y. B., Bakar, A. F. B. A., & Yusoff, I. B. (2019). Transport and retention behavior of carbonaceous colloids in natural aqueous medium: Impact of water chemistry. *Chemosphere, 217*, 213–222. https://doi.org/10.1016/j.chemosphere.2018.11.015↗.

Jardine, P. M., McCarthy, J. F., & Weber, N. L. (1989). Mechanisms of dissolved organic carbon adsorption on soil. *Soil Science Society of America Journal, 53*(5), 1378–1385. .https://doi.org/10.2136/sssaj1989.03615995005300050013x↗.

Jaisi, D. P., & Elimelech, M. (2009). Single-walled carbon nanotubes exhibit limited transport in soil columns. *Environmental Science & Technology, 43*(24), 9161–9166. https://doi.org/10.1021/es901927y↗.

Jeffery, G. B. (1922). The motion of ellipsoidal particles immersed in a viscous fluid, *Proceedings of the Royal Society A: Mathematical, Physical and Engineering Sciences, 102*(715), 161–179. https://doi.org/10.1098/rspa.1922.0078↗.

Jin, Y., & Flury, M. (2002). Fate and transport of viruses in porous media. *Advances in Agronomy, 77*, 39–102. https://doi.org/10.1016/S0065-2113(02)77013-2↗.

Jin, C., Normani, S. D., & Emelko, M. B. (2015). Surface roughness impacts on granular media filtration at favorable deposition conditions: Experiments and modeling. *Environmental Science & Technology, 49*(13), 7879–7888. https//doi.org/10.1021/acs.est.5b01998↗.

Johnson, K. L., Kendall, K., & Roberts, A. D. (1971). Surface energy and the contact of elastic solids. *Proceedings of the Royal Society A: Mathematical, Physical and Engineering Sciences, 324*(1558), 301–313. https://royalsocietypublishing.org/doi/pdf/10.1098/rspa.1971.0141↗.

Johnson, P. R., Sun, N., & Elimelech, M. (1996). Colloid transport in geochemically heterogeneous porous media: Modeling and measurements. *Environmental Science & Technology, 30*(11), 3284–3293. https://doi.org/10.1021/es960053↗.

Johnson, R. L., Nurmi, J. T., O'Brien Johnson, G. S., Fan, D., O'Brien Johnson, R. T., Shi, Z., Salter-Blanc, A. J., Tratnyek, P. G., & Lowry, G. V. (2013). Field-scale transport and transformation of carboxymethylcellulose-stabilized nano zero-valent iron. *Environmental Science & Technology, 47*(3), 1573–1580. https://doi.org/10.1021/es304564q↗.

Johnson, W. P., & Amy, G. L. (1995). Facilitated transport and enhanced desorption of polycyclic aromatic hydrocarbons (PAH) by natural organic matter (NOM) in aquifer sediments. *Environmental Science and Technology, 29*(3), 807–817. https://doi.org/10.1021/es00003a032↗.

Johnson, W. P., Blue, K.A., Logan, B. E. & Arnold, R. G. (1995). Modeling bacterial detachment during transport through porous media as a residence-time-dependent process. *Water Resources Research*, 31(11), 2649–2658. https://doi.org/10.1029/95WR02311.

Johnson, W. P., & Logan, B. E. (1996). Enhanced transport of bacteria in porous media by sediment-phase and aqueous-phase natural organic matter. *Water Research*, 30(4), 923–931. https://doi.org/10.1016/0043-1354(95)00225-1.

Johnson, W. P., Cabral, K., Lion L. W., & Corapcioglu, Y. M. (1998). Reconciliation of expressions for the modified retardation factor and incorporation of non-linear contaminant sorption to the stationary phase. *Journal of Contaminant Hydrology*, 32(3–4), 247–266. https://agris.fao.org/agris-search/search.do?recordID=US201302934616.

Johnson, W. P. (2006). Comment on Pang et al., 2006, Filtration and transport of *Bacillus subtilis* spores and the F-RNA phage MS2 in a coarse alluvial gravel aquifer: Implications in the estimation of setback distances. *Journal of Contaminant Hydrology*, 86(1–2), 160–161. https://doi.org/10.1016/j.jconhyd.2006.02.005.

Johnson, W. P., Li, X., & Gozde, Y. (2007a). Colloid retention in porous media: Mechanistic confirmation of wedging and retention in zones of flow stagnation. *Environmental Science & Technology*, 41(4), 1279–1287. https://doi.org/10.1021/es061301x.

Johnson, W. P., Li, X., & Assemi, S. (2007b). Deposition and re-entrainment dynamics of microbes and non-biological colloids during non-perturbed transport in porous media in the presence of an energy barrier to deposition. *Advances in Water Resources*, 30(6–7), 1432–1454. https://doi.org/10.1016/j.advwatres.2006.05.020.

Johnson, W. P., Pazmiño, E., & Ma, H. (2010). Direct observations of colloid retention in granular media in the presence of energy barriers and pitfalls of inferring mechanisms from indirect observations. *Water Research*, 44(4), 1158–1169. https://doi.org/10.1016/j.watres.2009.12.014.

Johnson, W. P., Ma, H., & Pazmiño, E. (2011). Straining credibility: A general comment regarding common arguments used to infer straining as the mechanism of colloid retention in porous media. *Environmental Science & Technology*, 45(9), 3831-3832. https://doi.org/10.1021/es200868e.

Johnson, W. P., & Hilpert, M. (2013). Upscaling colloid transport and retention under unfavorable conditions. *Water Resources Research*, 49(9), 5328–5341. https://doi.org/10.1002/wrcr.20433.

Johnson, W. P., Rasmuson, A., Hilpert, M., & Pazmiño, E. (2018). Why variant colloid transport behaviors emerge among identical individuals in porous media when colloid-surface repulsion exists. *Environmental Science & Technology*, 52(13), 7230-7239. https://doi.org/10.1021/acs.est.8b00811.

Johnson, W. P., Anna, R., Erickson, B., VanNess, K., Ron, C., Bolster, D., & Peters, B. (2020). Anionic nanoparticle and microplastic non-exponential distributions from source scale

with grain size in environmental granular media. *Water Research, 182*(12), 1160. https://doi.org/10.1016/j.watres.2020.116012↗.

Johnson, W. P. (2020). Quantitative linking of nanoscale interactions to continuum-scale nanoparticle and microplastic transport in environmental granular media. *Environmental Science & Technology, 54*(13), 8032–8042. https://doi.org/10.1021/acs.est.0c01172↗.

Johnson, W. P., Pazmiño, E., Frederick, L., Ron, C., & Chica, A. (2020b).Contaminant removal and precious metal recovery by lateral channel filtration in mining impacted alluvial floodplains. *Frontiers in Water, 2*, 586698. https://doi.org/10.3389/frwa.2020.586698↗.

Johnson, W. P., Tong, M., & Li, X. (2007). On colloid retention in saturated porous media in the presence of energy barriers: The failure of α, and opportunities to predict η. *Water Resources Research, 43*(12), W821033. https://doi.org/10.1029/2006WR005770↗.

Johnson, W. P., Li, X., Tong, M., & Ma, H. (2009). Comment on "Transport and fate of bacteria in porous media: Coupled effects of chemical conditions and pore space geometry" by Saeed Torkzaban et al. *Water Resources Research, 45*(9), W09603. https://doi.org/10.1029/2008WR007389↗.

Johnson, W. P., Blue, K. A., Logan, B. E., & Arnold, R. G. (1995). Modeling bacterial detachment during transport through porous media as a residence-time-dependent process. *Water Resources Research, 31*(11), 2649–2658. https://doi.org/10.1029/95WR02311↗.

Kalasin, S., & Santore, M. M. (2008). Hydrodynamic crossover in dynamic microparticle adhesion on surfaces of controlled nanoscale heterogeneity. *Langmuir, 24*(9), 4435–4438. https://doi.org/10.1021/la8000202↗.

Kelly, W. R., Panno, S. V., Hackley, K. C., Martinsek, A. T., Krapac, I. G., Weibel, C. P., & Storment, E. C. (2009). Bacteria contamination of groundwater in a mixed land-use karst region. *Water Quality, Exposure and Health, 1*, 69–78. https://link.springer.com/article/10.1007/s12403-009-0006-7↗.

Kersting, A. B., Efurd, D. W., Finnegan, D. L., Rokop, D. J., Smith, D. K., & Thompson, J. L. (1999). Migration of plutonium in groundwater at the Nevada Test Site. *Nature, 397*, 56–59. https://doi.org/10.1038/16231↗.

Kim, M., & Zydney, L. (2004). Effect of electrostatic, hydrodynamic, and Brownian forces on particle trajectories and sieving in normal flow filtration. *Journal of Colloid and Interface Science, 269*(2), 425–431. https://doi.org/10.1016/j.jcis.2003.08.004↗.

Ko, C. H., & Elimelech, M. (2000). The shadow effect in colloid transport and deposition dynamics in granular porous media: Measurements and mechanisms. *Environmental Science and Technology, 34*(17), 3681–3689. https://doi.org/10.1021/es0009323↗.

Kuniansky, E. L., Taylor, C. J., Williams, J. H., & Paillet, F. (2022). *Introduction to karst aquifers*. The Groundwater Project. https://doi.org/10.21083/978-1-77470-040-2↗.

Lecoanet, H. F., Bottero, J. Y., & Wiesner, M. R. (2004). Laboratory assessment of the mobility of nanomaterials in porous media. *Environmental Science & Technology, 38*(19), 5164–5169. https://doi.org/10.1021/es0352303↗.

Li, K., & Ma, H. (2019). Rotation and retention dynamics of rod-shaped colloids with surface charge heterogeneity in sphere-in-cell porous media model. *Langmuir, 35*(16), 5471–5483. https://doi.org/10.1021/acs.langmuir.9b00748↗.

Li, T., Shen, C., Johnson, W. P., Ma, H., Jin, C., Zhang, C., Chu, X., Ma, K., & Xing, B. (2022). Important role of concave surfaces in deposition of colloids under favorable conditions as revealed by microscale visualization. *Environmental Science & Technology, 56*(7), 4121–4131. https://doi.org/10.1021/acs.est.1c07305↗.

Li, X., & Johnson, W. P. (2005). Non-monotonic variations in deposition rate coefficients of microspheres in porous media under unfavorable deposition conditions. *Environmental Science & Technology, 39*(6), 1658–1665. https://doi.org/10.1021/es048963b↗.

Li, X., Scheibe, T. D., & Johnson, W. P. (2004). Apparent decreases in colloid deposition rate coefficients with distance of transport under unfavorable deposition conditions: A general phenomenon. *Environmental Science & Technology, 38*(21), 5616–5625. https://doi.org/10.1021/es049154v↗.

Li, X., Lin, C. L., Miller, J. D., & Johnson, W. P. (2006a). Pore-scale observation of microsphere deposition at grain-grain contacts over assemblage-scale porous media domains using x-ray microtomography. *Environmental Science & Technology, 40*(12), 3762–3768. https://doi.org/10.1021/es0525004↗.

Li, X., Lin, C. L., Miller, J. D., & Johnson, W. P. (2006b). Role of grain to grain contacts on profiles of retained colloids in porous media in the presence of an energy barrier to deposition. *Environmental Science & Technology, 40*(12), 3769–3774. https://doi.org/10.1021/es052501w↗.

Li, X., Li, Z., & Zhang, D. (2010a). Role of low flow and backward flow zones on colloid transport in pore structures derived from real porous media. *Environmental Science & Technology, 44*(13), 4936–4942. https://doi.org/10.1021/es903647g↗.

Li, Z., Zhang, D., & Li, X. (2010b). Tracking colloid transport in porous media using discrete flow fields and sensitivity of simulated colloid deposition to space discretization. *Environmental Science & Technology, 44*(4), 1274–1280. https://doi.org/10.1021/es9027716↗.

Li, Z., Zhang, D., & Li, X. (2012). Tracking colloid transport in real pore structures: Comparisons with correlation equations and experimental observations. *Water Resources Research, 48*(5), 1–11. https://doi.org/10.1029/2012WR011847↗.

Liang, Y., Bradford, S. A., Simunek, J., Vereecken, H., & Klumpp, E. (2013). Sensitivity of the transport and retention of stabilized silver nanoparticles to physicochemical factors. *Water Research, 47*(7), 2572–2582. https://doi.org/10.1016/j.watres.2013.02.025↗.

Lin, D., Hu, L., Bradford, S. A., Zhang, X., & Lo, I. M. (2021). Pore-network modeling of colloid transport and retention considering surface deposition, hydrodynamic bridging, and straining. *Journal of Hydrology, 603*(Part B), 127020. https://doi.org/10.1016/j.jhydrol.2021.127020↗.

Lin, S., & Wiesner, M. R. (2012). Theoretical investigation on the steric interaction in colloidal deposition. *Langmuir, 28*(43), 15233–15245. https://doi.org/10.1021/la302201g↗.

Lindsey, B. D., Rasberry, J. S., & Zimmerman, T.M. (2002). *Microbiological quality of water from noncommunity supply wells in carbonate and crystalline aquifers of Pennsylvania (*Water-Resources Investigations Report 01-4286*).* US Geological Survey. https://pubs.er.usgs.gov/publication/wri014268↗.

Liu, Y., Yang, C. H., & Li, J. (2007). Influence of extracellular polymeric substances on *Pseudomonas aeruginosa* transport and deposition profiles in porous media. *Environmental Science & Technology, 41*(1), 198–205. https://doi.org/10.1021/es061731n↗.

Liu, Q., Lazouskaya, V., He, Q., & Jin, Y. (2010). Effect of particle shape on colloid retention and release in saturated porous media. *Journal of Environmental Quality, 39*(2), 500–508. https://doi.org/10.2134/jeq2009.0100↗.

Long, W., & Hilpert, M. (2009). A correlation for the collector efficiency of Brownian particles in clean-bed filtration in sphere packings by a Lattice-Boltzmann method. *Environmental Science & Technology, 43*(12), 4419–4424. https://doi.org/10.1021/es8024275↗.

Loveland, J. P., Bhattacharjee, S., Ryan, J. N., & Elimelech, M. (2003). Colloid transport in a geochemically heterogeneous porous medium: Aquifer tank experiment and modeling. *Journal of Contaminant Hydrology, 65*(3–4), 161–182. https://doi.org/10.1016/S0169-7722(02)00238-3↗.

Ma, H., Bolster, C.. Johnson, W. P., Li, K., Pazmiño, E., Camacho K. M., Anselmo, A. C., & Mitragotri, S. (2020). Coupled influences of particle shape, surface property and flow hydrodynamics on rod-shaped colloid transport in porous media. *Journal of Colloid and Interface Science, 577*, 471–480. https://doi.org/10.1016/j.jcis.2020.05.022↗.

Ma, H., Hradisky, M., & Johnson, W. P. (2013). Extending applicability of correlation equations to predict colloidal retention in porous media at low fluid velocity. *Environmental Science & Technology, 47*(5), 2272–2278. https://doi.org/10.1021/es304753r↗.

Ma, H., Pedel, J., Fife, P., & Johnson, W. P. (2009). Hemispheres-in-cell geometry to predict colloid deposition in porous media. *Environmental Science & Technology, 43*(22), 8573–8579. https://doi.org/10.1021/es901242b↗.

Ma, H., Hradisky, M., & Johnson, W. P. (2013). Response to comment on "Extending applicability of correlation equations to predict colloidal retention in porous media at low fluid velocity." *Environmental Science & Technology, 47*(14), 8080–8089. https://doi.org/10.1021/es4024942↗.

Ma, H., Pazmiño, E., & Johnson, W. P. (2011). Surface heterogeneity on hemispheres-in-cell model yields all experimentally-observed non-straining colloid retention mechanisms in porous media in the presence of energy barriers. *Langmuir, 27*(24), 14982–14994. https://doi.org/10.1021/la203587j↗.

MacKay, A. A., & Gschwend, P. M. (2001). Enhanced concentrations of PAHs in groundwater at a coal tar site. *Environmental Science & Technology, 35*(7), 1320–1328. https://doi.org/10.1021/es0014786↗.

Magee, B. R., Lion, L.W., & Lemley, A. T. (1991). Transport of dissolved organic macromolecules and their effect on the transport of phenanthrene in porous media. *Environmental Science & Technology, 25*(2), 323–331. https://doi.org/10.1021/es00014a017↗.

Martin, M. J., Logan, B. E., Johnson, W. P., Jewett, D. G., & Arnold, R. G. (1996). Scaling Bacterial Filtration Rates in Different Sized Porous Media. *Journal of Environmental Engineering, 122*, 407–415. https://doi.org/10.1061/(ASCE)0733-9372(1996)122:5(407)↗.

Masliyah, J., & Bhattacharjee, S. (2005). *Electrokinetic and colloid transport phenomena*. John Wiley and Sons. https://doi.org/10.1021083/9780471788829↗.

May, R., Akbariyeh, S., & Li, Y. (2012,). Pore-scale investigation of nanoparticle transport in saturated porous media using laser scanning cytometry. *Environmental Science & Technology, 46*(18), 9980–9986. https://doi.org/10.1021/es301749s↗.

Mays, D. C., & Hunt, J. R. (2005). Hydrodynamic aspects of particle clogging in porous media. *Environmental Science & Technology, 39*(2), 577–584. https://doi.org/10.1021/es049367k↗.

McCarthy, J. F., & Zachara, J. (1989). Subsurface transport of contaminants. *Environmental Science & Technology, 23*(5), 496–502. https://doi.org/10.1021/es00063a001↗.

McCaulou, D. R., Bales, R. C., & Arnold, R. G. (1995). Effect of temperature-controlled motility on transport of bacteria and microspheres through saturated sediment. *Water Resources Research, 31*p(2), 271–280. https://doi.org/10.1029/94WR02569↗.

McDowell-Boyer, L. M., Hunt, J. R., & Sitar, N. (1986). Particle transport through porous media. *Water Resources Research, 22*(13), 1901–1921. https://doi.org/10.1029/WR022i013p01901↗.

McKay, L. D., Gillham, R. W., & Cherry, J. A. (1993). Field experiments in a fractured clay till: 2. Solute and colloid transport. *Water Resources Research, 29*(12), 3879–3890. https://doi.org/10.1029/93WR02069↗.

McNaught, A. D., & Wilkinson, A. (1997). *Compendium of chemical terminology: International Union of Pure and Applied Chemists recommendations* (UPAC Gold Book, Version 3.0.1). Blackwell Scientific. https://doi.org/10.1351/goldbook↗.

Metwalli, E., Haines, D., Becker, O., Conzone, S., & Pantano, C. G. (2006). Surface characterizations of mono-, di-, and tri-aminosilane treated glass substrates. *Journal of Colloid and Interface Science, 298*(2), 825–831. https://doi.org/10.1016/j.jcis.2006.03.045↗.

Molnar, I. L., Johnson, W. P., Gerhard, J. I., Willson, C. S., & O'Carroll, D. M. (2015). Predicting colloid transport through saturated porous media: A critical review. *Water Resources Research, 51*(9), 6804–6845. https://doi.org/10.1002/2015WR017318.

Nelson, K. E., & Ginn, T. R. (2001). Theoretical investigation of bacterial chemotaxis in porous media. *Langmuir, 17*(18), 5636–5645. https://doi.org/10.1021/la010456+.

Nelson, K. E., & Ginn, T. R. (2005). Colloid filtration theory and the Happel sphere-in-cell model revisited with direct numerical simulation of colloids. *Langmuir, 21*(6), 2173–2184. https://doi.org/10.1021/la048404i.

Nelson, K. E., & Ginn, T. R. (2011). New collector efficiency equation for colloid filtration in both natural and engineered flow conditions. *Water Resources Research, 47*(5), 1–17. https://doi.org/10.1029/2010WR009587.

Neukum, C., Braun, A., & Azzam, R. (2014). Transport of stabilized engineered silver (Ag) nanoparticles through porous sandstones. *Journal of Contaminant Hydrology, 158*, 1–13. https://doi.org/10.1016/j.jconhyd.2013.12.002.

Novikov, A. P., Kalmykov, S. N., Utsunomiya, S., Ewing, R.C., Horreard, F., Merkulov, A., Clark, S. B., Tkachev, V. V., & Myasoedov, B. F. (2006). Colloid transport of plutonium in the far-field of the Mayak Production Association, Russia. *Science, 314*(5799), 638–641. https://doi.org/10.1126/science.1131307.

O'Connor, D. R. (2002). *Part one: A summary. Report of the Walkerton inquiry: The events of May 2000 and related issues*. Queen's Printer for Ontario. http://www.archives.gov.on.ca/en/e_records/walkerton/report1/pdf/WI_Summary.pdf.

Ogata, A., & Banks, R. B. (1961). *A solution of the differential equation of longitudinal dispersion in porous media in fluid movement in earth materials* (Professional Paper 411-A). US Geological Survey. https://oi.org/10.3133/pp411A.

O'Neill, M. N. (1968). A sphere in contact with a plane wall in a slow linear shear flow. *Chem. Eng. Sci., 23*(11), 1293–1298. https://ui.adsabs.harvard.edu/abs/1968ChEnS..23.1293O/abstract.

Ouyang, Y., Shinde, D., Mansell, R. S., & Harris, W. (1996). Colloid-enhanced transport of chemicals in subsurface environments: A review, *Critical Reviews in Environmental Science and Technology, 26*(2), 189–204. https://doi.org/10.1080/10643389609388490.

Packman, A. I., & MacKay, J. S. (2003). Interplay of stream-subsurface exchange, clay particle deposition, and streambed evolution. *Water Resources Research, 39*(4), 1097. https://doi.org/10.1029/2002WR001432.

Pang, L., Close, M., Goltz, M., Noonan, M., & Sinton, L. (2005). Filtration and transport of *Bacillus subtilis* spores and the F-RNA phage MS2 in a coarse alluvial gravel aquifer: Implications in the estimation of setback distances. *Journal of Contaminant Hydrology, 77*(3), 165–194. https://doi.org/10.1016/j.jconhyd.2004.12.006.

Paraskeva, C. A., Burganos, V. N., & Payatakes, A. C. (1991). Three-dimensional trajectory analysis of particle deposition in constricted tubes. *Chemical Engineering Communications, 108*(1), 23–48. https://doi.org/10.1080/00986449108910949↗.

Payatakes, A. C., Tien, C., & Turian, R. M. (1974a). Trajectory calculation of particle deposition in deep bed filtration: Part I. Model formulation. *AIChE Journal, 20*(5), 889–900. https://doi.org/10.1002/aic.690200509↗.

Payatakes, A. C., Rajagopalan, R., & Tien, C. (1974b). On the use of Happel's model for filtration studies. *Journal of Colloid and Interface Science, 49*(2), 321–325. https://doi.org/10.1016/0021-9797(74)90369-5↗.

Pazmiño, E. F., Ma, H., & Johnson, W. P. (2011). Applicability of colloid filtration theory in size-distributed, reduced porosity, granular media in the absence of energy barriers. *Environmental Science & Technology, 45*(24), 10401–10407. https://doi.org/10.1021/es202203m↗.

Pazmiño, E., Trauscht, J., Dame, B., & Johnson, W. P. (2014a). Power-law size-distributed heterogeneity explains colloid retention on soda-lime glass in the presence of energy barriers. *Langmuir, 30*(19), 5412–5421. https://doi.org/10.1021/la501006p↗.

Pazmiño, E., Trauscht, J., & Johnson, W. P. (2014b). Release of colloids from primary minimum contact under unfavorable conditions by perturbations in ionic strength and flow rate. *Environmental Science & Technology, 48*(16), 9227–9235. https://doi.org/10.1021/es502503y↗.

Porubcan, A. A., & Xu, S. (2011). Colloid straining within saturated heterogeneous porous media. *Water Research, 45*(4), 1796–1806. https://doi.org/10.1016/j.watres.2010.11.037↗.

Prélot, B., Villiéras, F., Pelletier, M., Gérard, G, Gaboriaud, F., Ehrhardt, J.-J., Perrone, J., Fedoroff, M., Jeanjean, J., Lefèvre, G., Mazerolles, L., Pastol, J.-L., Rouchaud J.-C., & Lindecker, C. (2003). Morphology and surface heterogeneities in synthetic goethites. *Journal of Colloid and Interface Science, 261*(2), 244–254. https://doi.org/10.1016/S0021-9797(03)00058-4↗.

Prieve, D. C., & Ruckenstein, E. (1974). Effect of London forces upon the rate of deposition of Brownian particles. *AIChE Journal, 20*(6), 1178–1187. https://doi.org/10.1002/aic.690200618↗.

Rajagopalan, R., & Tien, C. (1976). Trajectory analysis of deep-bed filtration with the sphere-in-cell porous media model. *AIChE Journal, 22*(3), 523– 533. https://doi.org/10.1002/aic.690220316↗.

Rakowska, M. I., Kupryianchyk, D., Harmsen, J., Grotenhuis, T., & Koelmans, A. A. (2012). In situ remediation of contaminated sediments using carbonaceous materials. *Environmental Toxicology and Chemistry, 31*(4), 693–704. https://doi.org/10.1002/etc.1763↗.

Rasmuson, A., Pazmiño, E., Assemi, S., & Johnson, W. P. (2017). The contribution of nanoscale roughness to heterogeneity: Closing the gap between unfavorable and

favorable colloid attachment conditions. *Environmental Science & Technology, 51*(4), 2151–2160. https://doi.org/10.1021/acs.est.6b05911↗.

Rasmuson, A., Erickson, B., Borchardt, M., Muldoon, M., & Johnson, W. P. (2019b). Pathogen prevalence in fractured versus granular aquifers and the role of forward flow stagnation zones on pore scale delivery to surfaces. *Environmental Science & Technology, 54*(1), 137–145. https://doi.org/10.1021/acs.est.9b03274↗.

Rasmuson, A., VanNess, K., Ron, C. A., & Johnson, W. P. (2019a). Hydrodynamic versus surface interaction impacts of roughness in closing the gap between favorable and unfavorable colloid transport conditions. *Environmental Science & Technology, 53*(5), 2450–2459. https://doi.org/10.1021/acs.est.8b06162↗.

Raychoudhury, T., Naja, G., & Ghoshal, S. (2020). Assessment of transport of two polyelectrolyte-stabilized zero-valent iron nanoparticles in porous media. *Journal of Contaminant Hydrology, 118*(3–4), 143–151. https://doi.org/10.1016/j.jconhyd.2010.09.005↗.

Ritschel, T., Lehmann, K., Brunzel, M., Vitz, J., Nischang, I., Schubert, U. S., & Totsche, K. U. (2021). Well-defined poly(ethylene glycol) polymers as non-conventional reactive tracers of colloidal transport in porous media. *Journal of Colloid and Interface Science, 584*, 592–601. https://doi.org/10.1016/j.jcis.2020.09.056↗.

Ron, C., & Johnson, W. P. (2020). Complimentary colloid and collector nanoscale heterogeneity explains microparticle retention under unfavorable conditions. *Environmental Science: Nano, 7*(12), 4010–4021. https://doi.org/10.1039/D0EN00815J↗.

Ron, C., VanNess, K., Rasmuson, A., & Johnson, W. P. (2019a). How nanoscale surface heterogeneity impacts transport of nano- to micro-particles on surfaces under unfavorable attachment conditions. *Environmental Science: Nano, 6*(6), 1921–1931. https://pubs.rsc.org/en/content/articlelanding/2019/en/c9en00306a↗.

Ron, C. A., Dong, M., Wooley, K. L., & Johnson, W. P. (2019b). Theory-guided targeted delivery of nano- and micro-particles in advective environmental porous media. *Environmental Science & Technology Letters, 6*(10), 617–623. https://doi.org/10.1021/acs.estlett.9b00474↗.

Ruckenstein, E., & Prieve, D. C. (1976). Adsorption and desorption of particles and their chromatographic separation. *AIChE Journal, 22*(2), 276–283. https://doi.org/10.1002/aic.690220209↗.

Russell, T. L., Yamahara, K. M., & Boehm, A. B. (2012). Mobilization and transport of naturally occurring enterococci in beach sands subject to transient infiltration of seawater. *Environmental Science & Technology, 46*(11), 5988–5996. https://doi.org/10.1021/es300408z↗.

Ryan, J. N., Elimelech, M., Ard, R. A., Harvey, R. W., & Johnson, P. R. (1999). Bacteriophage PRD1 and silica colloid transport and recovery in an iron oxide-coated sand aquifer. *Environmental Science & Technology, 33*(1), 63–73. https://doi.org/10.1021/es980350+↗.

Ryan, J. N., Illangasekare, T. H., Litaor, M. I., & Shannon, R. (1998). Particle and plutonium mobilization in macroporous soils during rainfall simulations. *Environmental Science & Technology, 32*(4), 476–482. https://doi.org/10.1021/es970339u.

Ryan, J. N., & Elimelech, M. (1996). Colloid mobilization and transport in groundwater. In M Elimelech & J. G. Henry (Eds.), *Colloids and surfaces A: Physicochemical and engineering aspects, 107*(95), 1–56. *A collection of papers presented at the Symposium on Colloid and Interfacial Phenomena in Aquatic Environments6 April 1995, Anaheim CA, USA.* https://doi.org/10.1016/0927-7757(95)03384-X.

Saiers, J. E., & Hornberger, G. M. (1996). The role of colloidal kaolinite in the transport of cesium through laboratory sand columns. *Water Resources Research, 32*(1), 33–41. https://doi.org/10.1029/95WR03096.

Salerno, M. B., Flamm, M., Logan, B. E., & Velegol, D. (2006). Transport of rodlike colloids through packed beds. *Environmental Science & Technology, 40*(20), 6336–6340. https://doi.org/10.1021/es0614565.

Scheibe, T. D., Hubbard, S. S., Onstott, T. C., & DeFlaun, M. F. (2011). Lessons learned from bacterial transport research at the South Oyster Site. *Groundwater, 49*(5), 745–763. https://doi.org/10.1111/j.1745-6584.2011.00831.x.

Schijven, J. F., & Šimůnek, J. (2002). Kinetic modeling of virus transport at the field scale. *Journal of Contaminant Hydrology, 55*(1–2), 113–135. https://doi.org/10.1016/S0169-7722(01)00188-7.

Schijven, J. F., & Hassanizadeh, S. M. (2000). Removal of viruses by soil passage: Overview of modeling, processes, and parameters. *Critical Reviews in Environmental Science and Technology, 30*(1), 49–127. https://doi.org/10.1080/10643380091184174.

Schijven, J. F., Hoogenboezem, W., Hassanizadeh, S. M., & Peters, J. H. (1999). Modeling removal of bacteriophages MS2 and PRD1 by dune recharge at Castricum, Netherlands. *Water Resources Research, 35*(4), 1101–1111. https://doi.org/10.1029/1998WR900108.

Scholl, M. A., &. Harvey, W. (1992). Laboratory investigations on the role of sediment surface and groundwater chemistry in transport of bacteria through a contaminated sandy aquifer. *Environmental Science & Technology, 26*(7), 1410–1417. https://doi.org/10.1021/es00031a020.

Schwarzenbach, R. P., Gschwend, P. M., & Imboden, D. M. (1993). *Environmental organic chemistry*. John Wiley and Sons. Environmental Organic Chemistry 1st ed. 1993.

Sen, T. K., & Khilar, K. C. (2006). Review on subsurface colloids and colloid-associated contaminant transport in saturated porous media. *Advances in Colloid and Interface Science, 119*(2–3), 71–96. https://doi.org/10.1016/j.cis.2005.09.001.

Sharma, M. M., Chamoun, H., Sarma, D. S. H. R., &. Schechter, R. S. (1992). Factors controlling the hydrodynamic detachment of particles from surfaces. *Journal of Colloid and Interface Science, 149*(1), 121–134. https://doi.org/10.1016/0021-9797(92)90398-6.

Shave, M.K., Kalasin, S., Ying, E., & Santore, M. M. (2018). Nanoscale functionalized particles with rotation-controlled capture in shear flow. *ACS Applied Materials & Interfaces, 44410*(34), 29058–29068. https://doi.org/10.1021/acsami.8b05328↗.

Shellenberger, K., & Logan, B. E. (2002). Effect of molecular scale roughness of glass beads on colloidal and bacterial deposition. *Environmental Science & Technology, 36*(2), 184–189. https:///doi.org/10.1021/es015515k↗.

Shen, C., Li, B., Huang, Y., & Jin, Y. (2007). Kinetics of coupled primary- and secondary-minimum deposition of colloids under unfavorable chemical conditions. *Environmental Science & Technology, 41*(20), 6976–6982. https://doi.org/10.1021/es070210c↗.

Shen, C., Huang, Y., Li, B., & Jin, Y. (2010). Predicting attachment efficiency of colloid deposition under unfavorable attachment conditions. *Water Resources Research, 46*(11), 1–12. https://doi.org/10.1029/2010WR009218↗.

Shen, C., Lazouskaya, V., Zhang, H., Li, B., Jin, Y, & Huang, Y. (2013). Influence of surface chemical heterogeneity on attachment and detachment of microparticles. *Colloids and Surfaces, 433*, 14–29. https://doi.org/10.1016/j.colsurfa.2013.04.048↗.

Shen, C., Bradford, S. A., Li, T., Li, B., & Huang, Y. (2018). Can nanoscale surface charge heterogeneity really explain colloid detachment from primary minima upon reduction of solution ionic strength? *Journal of Nanoparticle Research, 20*(6), 165–168. https://doi.org/10.1007/s11051-018-4265-8↗.

Simoni, S. F., Harms, H., Bosma, T. N. P., & Zehnder, A. J. B. (1998). Population heterogeneity affects transport of bacteria through sand columns at low flow rates. *Environmental Science & Technology, 32*(14), 2100–2105. https://doi.org/10.1021/es970936g↗.

Šimůnek, J., van Genuchten, M. Th., & Šejna, M. (2016). Recent developments and applications of the HYDRUS computer software packages. *Vadose Zone Journal, 15*(7), 1–25. https://doi.org/10.2136/vzj2016.04.0033↗.

Singha, K., Johnson, T. C., Day-Lewis, F. D., & Slater, L. D. (2022). *Electrical imaging for hydrogeology*. The Groundwater Project. https://gw-project.org/books/electrical-imaging-for-hydrogeology/↗.

Song, L., & Elimelech, M. (1994). Transient deposition of colloidal particles in heterogeneous porous media. *Journal of Colloid and Interface Science, 167*(2), 301–313. https://doi.org/10.1006/jcis.1994.1365↗.

Song, L., Johnson, P. R., & Elimelech, M. (1994). Kinetics of colloid deposition onto heterogeneously charged surfaces in porous media. *Environmental Science & Technology, 28*(6), 1164–1171. https://doi.org/10.1021/es00055a030↗.

Spielman, L. A. (1977). Particle capture from low-speed laminar flows. *Annual Review of Fluid Mechanics, 9*, 297–319. https://www.annualreviews.org/doi/10.1146/annurev.fl.09.010177.001501↗.

Spielman, L. A., & Fitzpatrick, J. A. (1972). Theory for particle collection under London and gravity forces. *Journal of Colloid and Interface Science, 42*(3), 607–623.

Spielman, L. A., & Goren, S. L. (1970). Capture of small particles by London forces from low-speed liquid flows. *Environmental Science &Technology, 4*, 135–140.

Sprague, L.A., Herman, J. S, Hornberger, G.M., & Mills, A. L. (2000). Atrazine adsorption and colloid-facilitated transport through the unsaturated zone. *Journal of Environmental Quality, 29*, 1632. https://doir.org/10.2134/jeq2000.00472425002900050034x↗.

Sund, N., Aquino, T., & Bolster, D. (2019). Effective models for transport in complex heterogeneous hydrologic systems. *Encyclopedia of Water: Science, Technology, and Society*, 1–19.

https://scholar.google.com/citations?view_op=view_citation&hl=en&user=3owpA8wAAAAJ&citation_for_view=3owpA8wAAAAJ:4DMP91E08xMC↗.

Swistock, B. R., Clemens, S., & Rummel, S. (2013). Water quality and management of private drinking water wells in Pennsylvania. *Journal of Environmental Health, 75*, 60–66. https://www.jstor.org/stable/26329557↗.

Taboada-Serrano, P., Vithayaveroj, V., Yiacoumi, S., & Tsouris, C. (2005). Surface charge heterogeneities measured by atomic force microscopy. *Environmental Science & Technology, 39*(17), 6352–6360. https://doi.org/10.1021/es050100a↗.

Taghavy, A., Pennell, K. D. & Abriola, L. M. (2015). Modeling coupled nanoparticle aggregation and transport in porous media: A Lagrangian approach. *Journal of Contaminant Hydrology, 172*, 48–60. https://doi.org/ 10.1016/j.jconhyd.2014.10.012 ↗.

Tipping, E., & Cooke, D. (1982). The effects of adsorbed humic substances on the surface charge of goethite (α:-FeOOH) in freshwaters. *Geochimica et Cosmochimica Acta, 46*(1), 75–80. https://doi.org/10.1016/0016-7037(82)90292-7↗.

Tong, M., Li, X., Brow, C. N., & Johnson, W. P. (2005). Detachment-influenced transport of an adhesion-deficient bacterial strain within water-reactive porous media. *Environmental Science & Technology, 39*(8), 2500–2508. https://doi.org/10.1021/es049013t↗.

Tong, M., & Johnson, W. P. (2006a). Excess colloid retention in porous media as a function of colloid size, fluid velocity, and grain angularity. *Environmental Science & Technology, 40*(24), 7725–7731. https://doi.org/10.1021/es061201r↗.

Tong, M., & Johnson, W. P. (2006b). Colloid population heterogeneity drives hyper-exponential deviation from classic filtration theory. *Environmental Science & Technology, 41*(2), 493–499. https://doi.org/10.1021/es061202j↗.

Tong, M., Ma, H., & Johnson, W. P. (2008). Funneling of flow into grain-to-grain contacts drives colloid-colloid aggregation in the presence of an energy barrier. *Environmental Science & Technology, 42*(8), 2826–2832. https://doi.org/10.1021/es071888v↗.

Torkzaban, S., Tazehkand, S. S., Walker, S. L., & Bradford, S. A. (2008). Transport and fate of bacteria in porous media: Coupled effects of chemical conditions and pore space geometry. *Water Resources Research, 44*(4), 1–12. https://doi.org/10.1029/2007WR006541↗.

Tosco, T., Petrangeli Papini, M., Cruz Viggi, C., & Sethi, R. (2014). Nanoscale zerovalent iron particles for groundwater remediation: A review. *Journal of Cleaner Production, 77*, 10–21. https://doi.org/10.1016/j.jclepro.2013.12.026↗.

Trauscht, J., Pazmiño, E., & Johnson, W. P. (2015). Prediction of nanoparticle and colloid attachment on unfavorable mineral surfaces using representative discrete heterogeneity. *Langmuir, 31*(34), 9366–9378. https:///doi.org/10.1021/acs.langmuir.5b02369↗.

Tufenkji, N., Miller, G. F., Ryan, J. N., Harvey, R. W., & Elimelech, M. (2004). Transport of *Cryptosporidium* oocysts in porous media: Role of straining and physicochemical filtration. *Environmental Science & Technology, 38*(22), 5932–5938. https://doi.org/10.1021/es049789u↗.

Tufenkji, N., & Elimelech. M. (2004). Deviation from the classical colloid filtration theory in the presence of repulsive DLVO interactions. *Langmuir, 20*(25), 10818–10828. https://doi.org/10.1021/la0486638↗.

Tufenkji, N., & Elimelech, M. (2005a). Spatial distributions of cryptosporidium oocysts in porous media: Evidence for dual mode deposition. *Environmental Science & Technology, 39*(10), 3620–3629. https://doi.org/10.1021/es048289y↗.

Tufenkji, N., & Elimelech, M. (2005b). Breakdown of colloid filtration theory: Role of the secondary energy minimum and surface charge heterogeneities. *Langmuir, 21*,(3), 841–852. https://doi.org/10.1021/la048102g↗.

Tufenkji, N., Dixon, D. R., Considine, R., & Drummond, C. J. (2006). Multi-scale *Cryptosporidium*/sand interactions in water treatment. *Water Research, 40*(18), 3315–3331. https://doi.org/10.1016/j.watres.2006.07.036↗.

Uhlenbeck, G. E., & Ornstein, L. S. (1930). On the theory of the Brownian motion. *Physical Review, 36*, 823–841. https://journals.aps.org/pr/abstract/10.1103/PhysRev.36.823↗.

Vaidyanathan, R., & Tien, C. (1989). Hydrosol deposition in granular beds-an experimental study. *Chemical Engineering Communications, 81*, 123–144. https://doi.org/10.1080/00986448908940534↗.

Van Oss, C. J. (1994). *Interfacial forces in aqueous media*. Taylor & Francis.

Van Oss, C. J. (2008). The extended DVO theory. *Interface Science and Technology, 16*, 31–48. https://doi.org/10.1016/S1573-4285(08)00203-2↗.

Van Oss, C. J. (2002). Use of the combined Lifshitz-van Der Waals and Lewis acid-base approaches in determining the apolar and polar contributions to surface and interfacial tensions and free energies. *Journal of Adhesion Science and Technology, 16*(6), 669–677. https://doi.org/10.1163/156856102760099870↗.

VanNess, K., Rasmuson, A., Ron, C. A., & Johnson, W. P. (2019). A unified theory for colloid transport: Predicting attachment and mobilization under favorable and unfavorable conditions. *Langmuir, 35*(27), 9061–9070. https://doi.org/10.1021/acs.langmuir.9b00911↗.

Verwey, E. J. W., & Overbeek, J. T. G. (1947). Theory of the stability of lyophobic colloids. *The Journal of Colloid Science, 10*(2), 224–225. https://doi.org/10.1016/0095-8522(55)90030-1↗.

Vinogradova, O. I., & Belyaev, A. V. (2011). Wetting, roughness and flow boundary conditions. *Journal of Physics: Condensed Matter, 23*(18), 18410. https://doi.org/10.1088/0953-8984/23/18/184104↗.

Wallender, E. K., Ailes, E. C., Yoder, J. S., Roberts, V. A., & Brunkard, J. M. (2013). Contributing factors to disease outbreaks associated with untreated groundwater. *Groundwater, 52*(6), 886–897. https://doi.org/10.1111/gwat.12121↗.

Wang, P., & Keller, A. A. (2009). Natural and engineered nano and colloidal transport: role of zeta potential in prediction of particle deposition. *Langmuir, 25*(12), 6856–6862. https://doi.org/10.1021/la900134f↗.

Wang, D., Ge, L., He, J., Zhang, W., Jaisi, D. P., & Zhou, D. (2014). Hyperexponential and nonmonotonic retention of polyvinylpyrrolidone-coated silver nanoparticles in an ultisol. *Journal of Contaminant Hydrology, 164*, 35–48. https://doi.org/10.1016/j.jconhyd.2014.05.007↗.

Woessner, W. W., & Poeter, E. P. (2020). *Hydrogeologic properties of earth materials and principles of groundwater flow*. The Groundwater Project. https://gw-project.org/books/hydrogeologic-properties-of-earth-materials-and-principles-of-groundwater-flow/↗

Won, J., Kim, T., Kang, M., Choe, Y., & Choi, H. (2021). Kaolinite and illite colloid transport in saturated porous media. *Colloids and Surfaces A: Physicochemical and Engineering Aspects, 626*(5), 127052. https://doi.org/10.1016/j.colsurfa.2021.127052↗.

Wood, J. A., & Rehmann, L. (2014). Geometric effects on non-DLVO forces: Relevance for nanosystems. *Langmuir, 30*(16), 4623–4632. https://doi.org/10.1021/la500664c↗.

Worthington, S. R. H., & Smart, C. C. (2017). Transient bacterial contamination of the dual-porosity aquifer at Walkerton, Ontario, Canada. *Hydrogeology Journal, 25*, 1003–1016. https://ui.adsabs.harvard.edu/abs/2017HydJ...25.1003W/abstract↗.

Wu, X., Lyua, X., Li, Z., Gao, B., Zeng, X., Wu, J., & Sun, Y. (2020). Transport of polystyrene nanoplastics in natural soils: Effect of soil properties, ionic strength and cation type. *Science of the Total Environment, 707*, 136065. https://doi.org/10.1016/j.scitotenv.2019.136065↗.

Yahiaoui, S., & Feuillebois, F. (2010). Lift on a sphere moving near a wall in a parabolic flow. *Journal of Fluid Mechanics, 662*, 447–474. https://doi.org/10.1017/S0022112010003307↗.

Yang, H., & Balhoff, M. T. (2017). Pore-network modeling of particle retention in porous media. *AIChE Journal, 63*(7), 3118–3131. https://doi.org/10.1002/aic.15593↗.

Yang, B., Lin, H., Bartlett, S. L., Houghton, E. M., Robertson, D. M., & Guo, L. (2021). Partitioning and transformation of organic and inorganic phosphorus among

dissolved, colloidal and particulate phases in a hypereutrophic freshwater estuary. *Water Research, 196*, 117025. https://doi.org/10.1016/j.watres.2021.117025.

Yang, J., Chen, M., Yang, H., Xu, N., Feng, G., Li, Z., Su, C., & Wang, D. (2020). Surface heterogeneity mediated transport of hydrochar nanoparticles in heterogeneous porous media. *Environmental Science and Pollution Research,27*, 32842–32855. https://doi.org/10.1007/s11356-020-09482-w.

Yang, W., Shang, J., Sharma, P., Li, B., Liuc, K., & Flury, M. (2019). Colloidal stability and aggregation kinetics of biochar colloids: Effects of pyrolysis temperature, cation type, and humic acid concentrations. *Science of the Total Environment, 658*, 1306–1315. https://doi.org/10.1016/j.scitotenv.2018.12.269.

Yang, Y., Siqueira, F. D., Vaz, A. S. L., You, Z., & Bedrikovetsky, P. (2016). Slow migration of detached fine particles over rock surface in porous media. *Journal of Natural Gas Science and Engineering, 59*, 1159–1173. https://doi.org/10.1016/j.jngse.2016.07.056.

Yao, K., Habibian, M. T., & O'Melia, C. R. (1971). Water and waste water filtration. Concepts and applications. *Environmental Science & Technology, 5*(11), 1105–1112. https://doi.org/10.1021/es60058a005.

Zhang, P., Johnson, W. P., Piana, M. J., Fuller, C. C., & Naftz, D. L (2001a). Potential artifacts in interpretation of differential breakthrough of colloids and dissolved tracers in the context of transport in a zero-valent iron permeable reactive barrier. *Groundwater, 39*(6), 831–840. https://doi.org/10.1111/j.1745-6584.2001.tb02471.x.

Zhang, P., Johnson, W. P., Scheibe, T. D., Choi, K., Dobbs, F. C., & Mailloux, B. J. (2001b). Extended tailing of bacteria following breakthrough at the Narrow Channel Focus Area, Oyster, Virginia. *Water Resources Research, 37*(11), 2687–2698. https://doi.org/10.1029/2000WR000151.

Zhao, F., & van Wachem, B. G. M. (2013). Direct numerical simulation of ellipsoidal particles in turbulent channel flow. *Acta Mechanica, 224*, 2331–2358. https://doi.org/10.1007/s00707-013-0921-3.

Zhuang, J., Tyner, J. S., & Perfect, E. (2009). Colloid transport and remobilization in porous media during infiltration and drainage. *Journal of Hydrology, 377*(1–2), 112—119. https://doi.org/10.1016/j.jhydrol.2009.08.011.

10 Boxes

Box 1 - Development of expressions for hydrodynamic retardation factors

Our treatment of hydrodynamic retardation follows that of Spielman and co-workers (1977) who rigorously incorporated hydrodynamic interactions between the colloid and collectors by developing solutions to the creeping flow equation. The creeping flow equation corresponds to Stokes disturbance flow created by the colloid in proximity to the collector, which is viewed as locally planar because the colloid is assumed to be much smaller than the collector.

The boundary conditions are no-slip on the colloid and collector surfaces, with the undisturbed flow field outside the local disturbance. The net force and torque on the particle are taken to be zero; that is, both fluid and particle inertia are neglected, which permits the external and hydrodynamic forces to balance. Neglect of fluid inertia is justified by the small Reynolds number of the disturbance flow, and neglect of colloid inertia is justified because the colloid is small relative to the hydrodynamic forces acting on it.

The method of solution used by Spielman and co-workers (1977) involved the resolution of component flows that provided the far field boundary conditions for calculating the disturbance flows for a sphere near a plane using the creeping flow equations. The net motion of the particle is obtained by superposition, which is permitted by the linearity of the creeping flow equations. The motion of a sphere perpendicular to a plane in an otherwise stationary fluid is described by the hydrodynamic correction factor f_1. The correction factor f_1 represents the ratio of the particle velocity under an applied force perpendicular to the collector to that which the particle would have in an unbounded fluid under the same force (Spielman, 1977; Spielman and Fitzpatrick, 1972).

The drag force exerted by fluid motion on a stationary sphere near a flat plate, where the undisturbed far-field flow is normal to the flat plane, is given by the hydrodynamic correction factor f_2. The correction factor represents the ratio of the force (purely normal to the surface) that a stationary particle would experience near the collector relative to the force it would experience if held stationary in an unbounded fluid moving uniformly with the undisturbed flow (Brenner, 1961; O'Neill, 1968; Spielman, 1977; Spielman and Fitzpatrick, 1972). Heuristic expressions for f_1 and f_2—as shown in Equations (49) and (50)—were developed to fit the relationships provided in the parenthetical citations provided in this Box.

Colloid motion tangential to the collector surface includes translational and rotational components that are determined by the gradient of the tangential fluid velocity with distance from the collector surface (fluid shear). The translational, rotational, and shear components of the forces and torques governing colloid motion tangential to the

collector surface have been well described (Goldman et al., 1967a; Goldman et al., 1967b; Spielman, 1977; Spielman and Fitzpatrick, 1972). However, the development of the hydrodynamic functions corresponding to these components is complicated and thus worthy of some attention.

Goldman and co-workers (1967a, 1967b) defined the translational, rotational, and shear components of the tangential drag (F_t^{tr}, F_t^r, and F_t^s, respectively) as shown in Equation (Box 1-1).

$$F_t^{tr} = F_t^{tr*} 6\pi\mu a_p u_t \qquad F_t^r = F_t^{r*} 6\pi\mu a_p^2 \Omega \qquad F_t^s = F_t^{s*} 6\pi\mu a_p hS \qquad \text{(Box 1-1)}$$

where:

Ω = rotational velocity of the colloid, typically in radians per second (T^{-1})

h = distance between the colloid center and the collector surface, i.e., $H + a_p$, (L)

S = tangential fluid velocity gradient with distance from the collector surface, i.e., fluid shear (LT^{-1})

asterisks (*) = indicate corresponding hydrodynamic retardation factors

Similarly, Goldman and co-workers (1967a, 1967b) defined the translational, rotational, and shear components of the tangential torques (F_t^{tr}, F_t^r, and F_t^s, respectively) as shown in Equation (Box 1-2).

$$T_y^{tr} = T_y^{tr*} 8\pi\mu a_p^2 u_t \qquad T_y^r = T_y^{r*} 8\pi\mu a_p^3 \Omega \qquad T_y^s = T_y^{s*} 4\pi\mu a_p^3 S \qquad \text{(Box 1-2)}$$

where the subscript y refers to the axis of rotation (orthogonal to t). Note that the virtual mass, gravity, and Brownian forces are assumed to yield zero torque. Expressions for the hydrodynamic correction factors are given in Goldman and others (1967a, 1967b) for separation distances ranging from 0 to ∞.

The tangential force subcomponents can be summed as shown in Equation (Box 1-3).

$$m_p \frac{du_{t_i}}{dt} = F_t^{VM} + F_t^G + F_t^B - F_t^{tr} + F_t^r - F_t^s \qquad \text{(Box 1-3)}$$

Likewise, the torque subcomponents are summed (for each of the three dimensions) assuming zero inertial torque as shown in Equation (Box 1-4).

$$0 = T_y^{tr} - T_y^r + T_y^s \qquad \text{(Box 1-4)}$$

The explicit expression balancing the tangential forces for a given dimension is shown in Equation (Box 1-5), where non-drag forces (excepting F_t^{VM}) are grouped such that $F_t^{GRP} = F_t^G + F_t^B$.

$$m_p \frac{du_t}{dt} + \frac{4}{3}\pi a_p^3 \frac{1}{2}\rho_f \frac{du_t}{dt} = F_t^{GRP} + F_t^{tr*}6\pi\mu a_p u_t + F_t^{r*}6\pi\mu a_p^2\Omega + F_t^{s*}6\pi\mu a_p hS \quad \text{(Box 1-5)}$$

All force terms are positive here since the individual correction terms carry sign. Specifically, F_t^{tr*} carries a negative charge (Goldman et al., 1967a). The torque balance (where T_y^{r*} carries negative sign) is shown in Equation (Box 1-6).

$$0 = T_y^{tr*}8\pi\mu a_p^2 u_t + T_y^{r*}8\pi\mu a_p^3\Omega + T_y^{s*}4\pi\mu a_p^3 S \quad \text{(Box 1-6)}$$

Re-arranging the torque balance yields Equation (Box 1-7).

$$\Omega = \frac{-\frac{1}{2}ST_y^{s*} - \frac{1}{a_p}u_t T_y^{tr*}}{T_y^{r*}} \quad \text{(Box 1-7)}$$

Inserting the rotational velocity into the force balance yields Equation (Box 1-8).

$$\left(m_p + \frac{2}{3}\pi a_p^3\rho_f\right)\frac{du_t}{dt}$$

$$= F_t^{GRP} + F_t^{tr*}6\pi\mu a_p u_t + F_t^{r*}6\pi\mu a_p^2\left[\frac{-\frac{1}{2}ST_y^{s*} - \frac{1}{a_p}u_t T_y^{tr*}}{T_y^{r*}}\right] \quad \text{(Box 1-8)}$$

$$+ F_t^{s*}6\pi\mu a_p hS$$

Combining terms yields Equations (Box 1-9) and (Box 1-10).

$$\left(m_p + \frac{2}{3}\pi a_p^3\rho_f\right)\frac{du_{t_i}}{dt} =$$

$$F_t^{GRP} + 6\pi\mu a_p hS\left[+F_t^{s*} - \frac{1}{2}\frac{a_p}{h}\frac{T_y^{s*}}{T_y^{r*}}F_t^{r*}\right]$$

$$+ 6\pi\mu a_p u_t\left[F_t^{tr*} - F_t^{r*}\frac{T_y^{tr*}}{T_y^{r*}}\right] \quad \text{(Box 1-9)}$$

$$\left[\frac{T_y^{r*}}{F_t^{tr*}T_y^{r*} - F_t^{r*}T_y^{tr*}}\right]\left(m_p + \frac{2}{3}\pi a_p^3\rho_f\right)\frac{du_{t_i}}{dt} =$$

$$\left[\frac{T_y^{r*}}{F_t^{tr*}T_y^{r*} - F_t^{r*}T_y^{tr*}}\right]F_t^{GRP} + 6\pi\mu a_p hS\left[\frac{\frac{1}{2}\frac{a_p}{h}F_t^{r*}T_y^{s*} - F_t^{s*}T_y^{r*}}{F_t^{r*}T_y^{tr*} - F_t^{tr*}T_y^{r*}}\right] + 6\pi\mu a_p u_t \quad \text{(Box 1-10)}$$

Under steady-state conditions ($du_t/dt = 0$), and in the absence of non-drag forces ($F_t^{GRP} = 0$), Equation (Box 1-11) is obtained.

$$\frac{u_t}{hS} = \frac{u_t}{v_t} = f_3 = \frac{\frac{1}{2}\frac{a_p}{h}F_t^{r*}T_y^{s*} - F_t^{s*}T_y^{r*}}{F_t^{tr*}T_y^{r*} - F_t^{r*}T_y^{tr*}} \quad \text{(Box 1-11)}$$

142

These results are equivalent to those of Goldman and co-workers (1967b). As stated by Spielman and Fitzpatrick (1972) and Spielman (1977), the correction factor f_3 represents the ratio of the velocity of the entrained particle tangential to the collector surface (u_t) to the tangential velocity of the undisturbed fluid (v_t) evaluated at the particle center position. Equation (Box 1-12) defines f_4. In this equation, as stated by Spielman and Fitzpatrick (1972), the correction factor f_4 accounts for hydrodynamic retardation effects on forces acting tangential to the collector surface.

$$f_4 = \frac{T_y^{r*}}{F_t^{r*} T_y^{tr*} - F_t^{tr*} T_y^{r*}} \qquad \text{(Box 1-12)}$$

The hydrodynamic retardation function (f_3) developed by Goldman and others (1967a, 1967b) yielded a discrepancy with experimental data at zero separation distance. However, as argued by Spielman and Goren (1970), the proposed cause of the discrepancy (cavitation) was demonstrated to be restricted to dimensionless separation distances (relative to colloid radius) less than 4×10^{-4}. For colloids of 20-µm radius, this results in separation distances of 8 nm or less. Since colloid-collector interactions at these separation distances (and below) are dominated by EDL and VDW interactions, cavitation is considered an inconsequential influence for colloids of radius 20 µm or less. Functions f_3 and f_4 were tabulated across the range of separation distances ranging from ∞ to 0 using the functions provided by Goldman and others (1967a, 1967b) to develop the heuristic expressions provided by Equations (51) and (52).

Box 2 - Derivation of colloid translational velocity from rolling on surface in response to arresting and mobilizing torques

The torques acting on the colloid include the three hydrodynamic torques due to translation (τ^{tr}), rotation (τ^r), and shear (τ^s), in addition to the adhesive torque (τ^{adh}). Summing these torques yields Equation (Box 2-1). Variables that were defined in other sections of this book are included in the Notation list of Section 12.

$$\tau^{tr} + \tau^r + \tau^s - \tau^{adh} = I\alpha \qquad \text{(Box 2-1)}$$

where:

I = moment of inertia about the axis of rotation (ML^2)

α = rotational acceleration (T^{-2})

Using the parallel axis theorem, the moment of inertia is given by Equation (Box 2-2).

$$I = \frac{7}{5}\left(m_p + VM\right)a_p^2 \qquad \text{(Box 2-2)}$$

Assuming purely translational motion along the surface, the rotational acceleration is given by Equation (Box 2-3).

$$\alpha = \frac{d\Omega}{dt} = \frac{1}{a_p - \delta}\frac{du_t}{dt} \qquad \text{(Box 2-3)}$$

where:

Ω = rotational velocity of the colloid (T^{-1})

u_t = translational velocity (LT^{-1})

δ = vertical deformation of the colloid (L), as shown in (Figure 27)

The adhesive torque is given by Equation (Box 2-4).

$$\tau^{adh} = F_{adh}a_{cont} \qquad \text{(Box 2-4)}$$

where:

F_{adh} = adhesive attractive force between the colloid and collector (MLT^{-2})

a_{cont} = contact area radius (L)

The hydrodynamic torques are calculated using the forces given by Goldman and others (1967) and an effective lever arm following the work of others (Hubbe, 1984; Sharma et al., 1992). The effective lever arm for the shear force is given by Equation (Box 2-5).

$$l_s = a_p + \frac{\tau_s}{F_s} = a_p + \frac{4\pi\mu a_p^3 S T_t^{s*}}{6\pi\mu a_p(h + a_p)SF_t^{s*}} = a_p + \frac{2}{3} \cdot \frac{a_p^2}{h + a_p} \cdot \frac{T_t^{s*}}{F_t^{s*}} \qquad \text{(Box 2-5)}$$

$$= a_p\left(1 + \frac{2}{3} \cdot \frac{a_p}{h + a_p} \cdot \frac{T_t^{s*}}{F_t^{s*}}\right)$$

As h approaches 0, l_s approaches 1.37, which is the value obtained by Hubbe (1984) and used by others (Ryan & Elimelech, 1996; Sharma et al., 1992; Shen et al., 2010).

Assuming no sliding occurs on the surface (i.e., $a_p\Omega = u_t$), then the translational and rotational torques and forces can be combined as shown in Equation (Box 2-6).

$$l_{tr+r} = a_p + \frac{\tau_{tr+r}}{F_{tr+r}} = a_p + \frac{8\pi\mu a_p^2(u_t T_t^{tr*} + a_p\Omega T_t^{r*})}{6\pi\mu a_p(u_t F_t^{tr*} + a_p\Omega F_t^{r*})} \qquad \text{(Box 2-6)}$$

$$= a_p + \frac{4a_p(T_t^{tr*} + T_t^{r*})}{3(F_t^{tr*} + F_t^{r*})} = a_p\left(1 + \frac{4(T_t^{tr*} + T_t^{r*})}{3(F_t^{tr*} + F_t^{r*})}\right)$$

Using the forces and lever arms defined above, the torque balance becomes Equation (Box 2-7).

$$6\pi\mu a_p^2 u_t\left(F_t^{tr*} + F_t^{r*} + \frac{4}{3}(T_t^{tr*} + T_t^{r*})\right) \qquad \text{(Box 2-7)}$$

$$+ 6\pi\mu a_p^2 v_t\left(F_t^{s*} + \frac{2}{3} \cdot \frac{a_p}{h + a_p} \cdot T_t^{s*}\right) - F_{adh}a_{cont}$$

$$= \frac{7}{5}(m_p + VM)\frac{a_p^2}{a_p - \delta}\frac{du_t}{dt}$$

Approximation of the time differential is given in Equation (Box 2-8).

$$1.4(m_p + VM)\frac{1}{a_p - \delta}\frac{u_t^\tau - u_t^{\tau-1}}{\Delta t} \qquad \text{(Box 2-8)}$$

$$= 6\pi\mu u_t^\tau\left(F_t^{tr*} + F_t^{r*} + \frac{4}{3}(T_t^{tr*} + T_t^{r*})\right)$$

$$+ 6\pi\mu v_t\left(F_t^{s*} + \frac{2}{3} \cdot \frac{a_p}{h + a_p} \cdot T_t^{s*}\right) - F_{adh}\frac{a_{cont}}{a_p^2}$$

Solving for u_t^τ yields Equation (Box 2-9).

$$u_t^\tau = \frac{1.4(m_p + VM)u_t^{\tau-1} + 6\pi\mu(a_p - \delta)v_t\Delta t\left(F_t^{s*} + \frac{2}{3} \cdot \frac{a_p}{h + a_p} \cdot T_t^{s*}\right) - F_{adh}\frac{a_{cont}(a_p - \delta)}{a_p^2}\Delta t}{1.4(m_p + VM) - 6\pi\mu(a_p - \delta)\Delta t\left(F_t^{tr*} + F_t^{r*} + \frac{4}{3}(T_t^{tr*} + T_t^{r*})\right)} \qquad \text{(Box 2-9)}$$

The dimensionless forces and torques are taken from Goldman and others (1967) and are given by Equations (Box 2-10) through (Box 2-15).

$$F_t^{tr*} = \frac{8}{15}\ln\left(\frac{h}{a_p}\right) - 0.9588 \qquad \text{(Box 2-10)}$$

$$T_y^{tr*} = -\frac{1}{10}\ln\left(\frac{h}{a_p}\right) - 0.1895 \qquad \text{(Box 2-11)}$$

$$F_t^{r*} = -\frac{2}{15}\ln\left(\frac{h}{a_p}\right) - 0.2526 \qquad \text{(Box 2-12)}$$

$$T_y^{r*} = \frac{2}{5}\ln\left(\frac{h}{a_p}\right) - 0.3817 \qquad \text{(Box 2-13)}$$

$$F_t^{s*} = 1.7005 \qquad \text{(Box 2-14)}$$

$$T_y^{s*} = 0.9440 \qquad \text{(Box 2-15)}$$

11 Exercise Solutions

Solution Exercise 1

a) The xDLVO module determines the nanoscale interaction forces that become part of the force/torque balance at the pore scale as performed by the Traj-Hap and related modules. The pore-scale colloid residence times prior to each outcome (attachment, remaining in near surface without attachment, re-entrainment, and exit) are then upscaled in Upscale Continuum to develop rate coefficients that are used for continuum-scale prediction of breakthrough-elution curves at multiple transport distances and profiles of retained colloids with distance from source.

b) The correlation equations were developed for favorable conditions of attachment only, i.e., there is not significant repulsion between colloid and grain surfaces. Each correlation equation was calibrated from trajectory simulations for a limited range of colloid sizes, IS, and fluid velocity (typically creeping flow).

Solution Exercise 2

a) The colloid and collector zeta potentials along with solution IS are the primary parameters that determine whether a repulsive barrier will exist at separations distances greater than the primary minimum in the colloid-surface interaction profile.

b) Increased roughness decreases magnitude of colloid-surface interaction due to decreased radius of curvature of interacting surfaces.

c) Yes, according to research that examined colloid interaction with "concavities" where colloids can form multiple zones of interaction (e.g., by Chongyang Shen and colleagues). This phenomenon is NOT incorporated into the xDLVO module of Parti-Suite where asperities are implicitly represented. It is incorporated in the AFM module of Parti-Suite where asperities are explicitly represented.

d) The ZOI is the effective area of interaction between the colloid and the grain surface. Because the xDLVO interactions decay rapidly with separation distance, only the "nose" of the colloid has significant effect in the electrostatic interactions with the grain surface. In the module, the effect of surface charge heterogeneity is demonstrated for a single heterodomain located on the grain (this is equivalent to the case where the heterodomain is located on the colloid) centered inside the ZOI. For unfavorable conditions, the larger the heterodomain relative to the ZOI, the less repulsive the overall interaction. Once the heterodomain occupies more than approximately one-half the ZOI, the interaction becomes favorable.

Solution Exercise 3

No. Fortran executables for colloid trajectory simulations within three different collector geometries are available on the Parti-Suite website. However, we recommend learning to use the trajectory simulations via the Traj-Hap module available as a Matlab executable. Traj-Hap provides GUI images that are excellent for learning to perform trajectory simulations. When using this module, the user can selectively deactivate output images to speed up simulations.

Solution Exercise 4

a) The large colloid has a smooth trajectory produced by the combined effect of fluid drag and gravitational settling. In contrast, the small colloid has more random motion in the trajectory because diffusion has a more noticeable effect. Note that the simulation of smaller colloids takes significantly more time to perform because the time step is scaled to colloid size to avoid potential numerical artifacts.

b) The User Manuals for the Parti-Suite modules are also provided on the Parti-Suite website, and we have tried to provide useful information there. However, you can always contact us with questions, our emails are easy to find based on our affiliations, and we appreciate questions and feedback.

c) Charge heterogeneity is treated explicitly. In contrast, roughness asperities are currently implicit in the trajectory modules (as in the xDLVO module) because it is challenging to account impacts of roughness asperities on the near-surface fluid velocity and the torque balance.

Solution Exercise 5

a) Yes, we believe so for most circumstances. Additional strategies such as plotting collector efficiency as a function of injection radius require greater effort. The halo strategy may not be sufficient, for example, for non-neutrally buoyant colloids in flow orthogonal to the gravitational field, where the fields of attaching and exiting colloids may not be symmetrical with respect to the flow axis.

b) In theory, injecting colloids across the whole Happel domain will provide the most representative collector efficiency for a given set of conditions. However, it is a good rule of thumb to have 15 to 20 percent of injected colloids attach under favorable conditions to guarantee a healthy halo of exiting colloids. To achieve this number with an injection radius equal to the fluid shell radius, the number of colloids required in the simulation may be prohibitively large (the simulation prohibitively computationally expensive). Limiting the injection radius resolves this issue because we know without the expense of simulation that colloids injected outside R_{lim} will never reach the grain surface.

Solution Exercise 6

The simulations requires an input file with data for previously attached colloids (flux files output from previous run). The colloid positions and simulation parameters are loaded from the flux data files and provide the conditions at which attachment occurred. To perform the perturbation simulation, the user changes the IS and/or fluid velocity (which may represent influx of rainwater into a groundwater system or flushing of a packed column filter) and hits the "run perturbation simulation" button. The perturbation simulation employs force and torque balance to determine whether colloid detachment occurs under the perturbation conditions.

<div align="right">

Return to Exercise 6↰

Return to where text linked to Exercise 6↰

</div>

Solution Exercise 7

a) The colloid-surface interaction depends on the fraction of ZOI occupied by heterodomains, not on the specific location of heterodomains within the ZOI. Because ZOI scales to colloid size, the radius of curvature of the ZOI is always small such that the colloid–heterodomain separation distance is practically equivalent regardless of where the heterodomain falls within the ZOI.

b) No. The colloid has to achieve sufficiently close separation distance to feel the impact of the heterodomain. This can be observed in the lower right panel of the Traj-Hap dashboard where the fraction of ZOI occupied by heterodomains varies as the colloid traverses the grain surface. As the colloid translates from, for example, the bulk fluid to the near-surface fluid, heterodomains move into and out of the ZOI. If the colloid is in the near-surface fluid when a heterodomain occupies approximately 50 percent or more of the ZOI, then the colloid can come into contact. Whether it attaches (arrests) then depends on the torque balance at the surface, as shown in the upper right panel of the dashboard.

<div align="right">

Return to Exercise 7↰

Return to where text linked to Exercise 7↰

</div>

Solution Exercise 8

Yes. While direct spectrometric/spectroscopic analysis can easily detect variations (heterogeneity), the significance of that heterogeneity to colloid transport can be determined through simulations such as those performed in Parti-Suite. This problem needs to be worked from both ends, that is, perform measurements to directly detect heterogeneity and perform simulations to understand the significance of detected heterogeneity.

Solution Exercise 9

They are both Lagrangian in that they consider transport from the perspective of the particle (Lagrangian) versus a control volume into and out of which colloids move (Eulerian). In the pore-scale trajectory simulations, a mechanistic force torque balance governs the trajectory and outcome (e.g., exit, attachment, etc.) for each colloid. In the continuum-scale transport simulations, the rate coefficients determined from upscaling the pore-scale information are converted to probabilities (via multiplying the rate coefficient by the time step). At any given time step the probability of an outcome such as attachment is determined by comparison to a random number, and if the latter is larger, the outcome occurs. Once each particle has undergone an outcome (e.g., attachment or exit) the population at any given distance or time is determined and reported as a concentration.

12 Notation List

$1 - \eta$ fraction of colloids that pass one collector (dimensionless)

α_1 fraction of the overall population (dimensionless)

$\alpha_1, \alpha_2, \alpha_{re\text{-}ent},$ α_{RFSZ} the number of near-surface colloids culminating in each outcome (fast and slow attachment, re-entrainment, retention without attachment in RFSZ) relative to the total number of near-surface colloids (dimensionless)

A_{132} Hamaker constant (ML^2T^{-2})

a_{asp} radius of asperities (L)

a_{cont} lever arm defined by deformation upon contact (L)

a_{eff} ratio of the product over the sum of the colloid (a_P) and grain (a_g) radii (L)

a_g collector radius (L)

α rotational acceleration (T^{-2})

a_p colloid radius (L)

a_{STE} steric hydration contact radius (L)

$a_{trans\text{-}bg}$ fraction of re-entrained colloids that may reenter the near-surface fluid domain downstream of the collector (dimensionless)

$a_{trans\text{-}gg}$ fraction of α_{RFSZ} colloids that, at the continuum scale, will move down-gradient in the near-surface fluid domain from grain to grain and also potentially undergo slow attachment (dimensionless)

$a_{ZOI\text{–}EDL}$ radius of the ZOI for EDL interaction (L)

$a_{ZOI\text{–}LAB}$ radius of the ZOI for LAB interaction (L)

C average concentration in water (ML^{-3})

C/C_0 concentration relative to source concentration (dimensionless)

$(C/C_0)^1$ fraction of concentration undergoing further transport in the bulk fluid past a single collector (dimensionless)

C_{coll} colloid concentration (ML^{-3})

c_i concentration of ion I in solution, typically in mol/m^3 (amount of substance L^{-3})

c_{sed} contaminant concentration in sediment (MM^{-3})

D_{bm} Stokes-Einstein bulk diffusion coefficient (L^2T^{-1})

ΔG energy of retarded *VDW* interactions for sphere-sphere geometry (ML^2T^{-2})

ΔG_{EDL} energy of electric double layer interactions (ML^2T^{-2})

ΔG_{NC} energy of non-contact colloid surface interactions (ML^2T^{-2})

ΔG_{STE} energy of steric/hydration interactions (ML^2T^{-2})

ΔG_{VDW} energy of Van der Waals interactions (ML^2T^{-2})

δ vertical deformation (L)

Δt discrete time step length (T)

D_h hydrodynamic dispersion coefficient (L^2T^{-1})

$\hat{e}_r$ radial unit vector (dimensionless)

$\hat{e}_\omega$ tangential unit vector (dimensionless)

E_i Young's modulus for material i ($ML^{-1}T^{-2}$)

ε permittivity of water (typically units of C^2/Jm in Parti-Suite) ($ML^{-3}T^4I^2$), I is charge

η collector efficiency, ratio of the number of colloids that intercept the collector to the number of colloids that approach the collector (dimensionless)

$\mathfrak{R}$ Gaussian-distributed random number (dimensionless)

F force (MLT^{-2})

$f_1f_2f_3f_4$ hydrodynamic correction factors (dimensionless)

$\overrightarrow{F_{AB}}$ force of retarded acid-base interactions for sphere–sphere geometry (MLT^{-2})

F_{adh} net adhesive force (MLT^{-2})

$\overrightarrow{F_{EDL}}(H)$ force of retarded electric double layer interactions for sphere–sphere geometry (MLT^{-2})

F_i fluid drag force (MLT^{-2})

F_B^n diffusion force (MLT^{-2})

F_D^n fluid drag force (MLT^{-2})

F_G^n normal component of gravity force (MLT^{-2})

F_L^n lift force (MLT^{-2})

F_{SP} sphere-plate geometric correction (dimensionless)

F_{SS} sphere-sphere geometric correction (dimensionless)

F_D^t tangential component of fluid drag force (MLT^{-2})

F_t^{tr} rotational component of tangential fluid drag force (MLT^{-2})

F_t^{tr*} hydrodynamic retardation factor for rotational component of tangential fluid drag force (dimensionless)

F_t^s shear component of tangential fluid drag force (MLT^{-2})

F_t^{s*} hydrodynamic retardation factor for shear component of tangential fluid drag force (dimensionless)

F_t^r translational component of tangential fluid drag force (MLT^{-2})

F_t^{r*} hydrodynamic retardation factor for translational component of tangential fluid drag force (dimensionless)

$\overrightarrow{F_{VDW}}$ force of retarded Van der Waals interactions for sphere–sphere geometry (MLT^{-2})

g acceleration of gravity 9.81 ms^{-2} (LT^{-2})

γ $(1-\theta)^{1/3}$ cube root of volumetric water content (dimensionless)

γ_0^{AB} Lewis acid-base energy at minimum separation distance, typically in J (ML^2T^{-2})

γ_0^{STE} steric energy at minimum separation distance, typically in J (ML^2T^{-2})

h Planck's constant (ML^2T^{-1})

H colloid-surface separation distance (L)

H' equivalent smooth colloid-surface separation distance (L)

h_0 minimum separation distance in contact (L)

H_{asp} asperity height (L)

I moment of inertia about the axis of rotation (ML^2)

i subscript fluid forces and torques due to either colloid translation, or rotation, or fluid shear (dimensionless)

J jamming limit for hemispheric asperities in the circular ZOI (dimensionless)

$\hat{\jmath}$ x-direction (dimensionless)

J_A advective flux $(ML^{-2}T^{-1})$

J_D dispersive flux $(ML^{-2}T^{-1})$

K combined elastic modulus of the colloid and collector $(ML^{-1}T^{-2})$

$\hat{k}$ y-direction (dimensionless)

k_{f2}^* rate coefficient for slow attachment of near-surface colloids (T^{-1})

K_1 $1/w$ (dimensionless)

K_2 $-(3+2\gamma^5)/w$ (dimensionless)

K_3 $(2+3\gamma^5)/w$ (dimensionless)

K_4 $-\gamma^5/w$ (dimensionless)

155

κ inverse Debye length (L^{-1})

k_B Boltzmann constant, 1.3806×10^{-23} J/K ($ML^2T^{-1}\Theta^{-1}$)

$K_{col\text{-}sed}$ equilibrium constant for interactions between colloid and sediment (L^3M^{-1})

K_d equilibrium constant for distribution of solute between sediment and solution (L^3M^{-1})

k_f first-order rate coefficient used to represent irreversible filtration at the continuum scale (T^{-1})

$k_{f,unf}$ first-order rate coefficient under unfavorable conditions (T^{-1})

k_{ns} rate coefficient for entry into near-surface fluid (T^{-1})

$K_{sed\text{-}col}$ equilibrium constant for sediment and colloid interactions (L^3M^{-1})

$K_{sol\text{-}col}$ equilibrium constant for solute and colloid interactions (L^3M^{-1})

$K_{sol\text{-}sed}$ equilibrium constant for solute and sediment interactions (L^3M^{-1})

l lever arm (L)

λ_{AB} Lewis acid-base decay distance (L)

λ_{AB} Lewis acid-base decay distance (L)

λ_{STE} steric decay distance (L)

λ_{VDW} characteristic VDW wavelength (L)

m mass (M)

m^* colloid virtual mass, the inertia added to a system because an accelerating or decelerating body must deflect some volume of surrounding fluid as it moves through it (M)

M_c^* mass of solute in REV associated with the phase by which it is normalized to produce either C in water or C_{sed} on sediment (M)

M_{sed} mass of sediment in REV (M)

m_p colloid mass (M)

μ fluid viscosity $(ML^{-1}T^{-1})$

n refractive index (dimensionless)

N_A Avogadro's number $(6.02\times10^{+23}/mol)$

N_A in Table 2, attraction number, attractive versus mobilizing interactions (dimensionless)

N_{asp} number of asperities in the ZOI (dimensionless)

N_c number of collectors (dimensionless)

N_c/L number of collectors per unit length (dimensionless)

N_G gravity number, settling versus mobilizing interactions (dimensionless)

N_{Gi} inverse gravity number (dimensionless)

N_{IO} solution ionic strength (IS), typically mol/m^3 (amount-of-substance L^{-3})

N_{Lo} London number, attractive versus mobilizing interactions (dimensionless)

N_{Pe} ratio of advective to diffusive transport (dimensionless)

N_R aspect ratio of fluid shell radius to grain radius in the Happel unit cell (dimensionless)

v_i Poisson's ratio for material i (dimensionless)

N_{vdw} Van der Waals number, attractive versus thermal interactions (dimensionless)

ω tangential coordinate in radians (dimensionless)

Ω rotational velocity (T^{-1})

q elementary charge (I)

r radial coordinate (L)

R retardation factor (dimensionless)

r^* normalized radial coordinate r/a_g (dimensionless)

R^* modified retardation factor (dimensionless)

r_B Happel fluid shell radius (L)

REV Cartesian representative elementary volume (dimensionless)

ρ_b dry bulk density of soil (ML^{-3}, or when units are linked to phase: M_{sed}/L^3_{REV})

ρ_f fluid density (ML^{-3}, or when units are linked to phase: M_w/L^3_w)

ρ_p colloid density (ML^{-3})

r_{lever} roughness-based lever arm (L)

S tangential fluid velocity gradient with distance from the collector surface (T^{-1})

subscripts 1,2,3   colloid, grain, and fluid, respectively (dimensionless)

superscripts +/-   electron acceptor/donor properties (dimensionless)

superscripts LW   surface energy superscripts LW indicates Lifshitz-van der Waals properties (dimensionless)

T temperature (Θ)

t time (T)

T torque (ML^{2}T^{-2})

τ_i fluid torque with subscript indicating due to translation, rotation, or fluid shear (ML^{2}T^{-2})

θ volumetric water content (dimensionless, or when units linked to phase: L^3_w/L^3_{REV})

θ_b volumetric water content of bulk fluid in REV (dimensionless)

θ_{ns} volumetric water content of near-surface fluid in REV (dimensionless)

σ_c Born collision diameter

T^r_t rotational component of tangential torque (ML^{2}T^{-2})

T_t^{r*} hydrodynamic correction factor for rotational component of tangential torque (dimensionless)

T_t^s shear component of tangential torque (ML^2T^{-2})

T_t^{s*} hydrodynamic correction factor for shear component of tangential torque (dimensionless)

T_t^{tr} translational component of tangential torque (ML^2T^{-2})

T_t^{tr*} hydrodynamic correction factor for translational component of tangential torque (dimensionless)

u terminal velocity (LT^{-1})

u_t translational velocity (LT^{-1})

v average pore fluid velocity (LT^{-1})

v^* characteristic velocity (LT^{-1})

v_e main electronic absorption frequency, typically s^{-1} (T^{-1})

v_{ns} average near-surface fluid velocity (LT^{-1})

V_{sup} superficial (approach) velocity (LT^{-1})

w $2-3\gamma+3\gamma^5-2\gamma^6$ (dimensionless)

W work of adhesion (ML^2T^{-2})

z valence of the electrolyte (dimensionless)

$\zeta_1 \, and \, \zeta_2$ colloid and collector potential respectively, typically in volts ($ML^2T^{-3}I^{-1}$)

13 About the Authors

Dr. Bill Johnson is a Professor in the Department of Geology and Geophysics at the University of Utah. His research group examines fate and transport of contaminants in water ranging from particles and pathogens, to trace elements such as mercury and selenium, and organic compounds. His work spans field to laboratory settings as well as development and application of experimental and numerical simulation techniques. Dr. Johnson's research includes developing theory for predicting nano- and micro-particle transport in porous media, trace element cycling in the Great Salt Lake, and gold mining impacts on rivers in southern Ecuador.

Dr. Eddy Pazmiño, worked as a chemical engineer in small mining operations in the rainforest and high Andes in southern Ecuador. After this experience, he decided to pursue an academic career as an environmental scientist. As a graduate student, he collaborated in field efforts aimed to characterize the extent of mining contamination in multiple Ecuadorian river basins (2010). After finishing his doctorate at the University of Utah in 2015, he returned to Ecuador as a faculty member at Escuela Politécnica Nacional, Quito. He maintains an active collaboration with the University of Utah in developing field-scale biofiltration systems for mitigation of mining contamination and improvement of gold recovery for artisanal miners. As part of this collaboration, he has co-developed novel computational software to facilitate the learning and use of colloid transport theories focused on environmental and engineering applications. Since 2018, he has been a member of the expert working group for the review of annexes of the Basel Convention representing Ecuador.

Please consider signing up for the GW-Project mailing list to stay informed about new book releases, events, and ways to participate in the GW-Project. When you sign up for our email list it helps us build a global groundwater community. Sign up↗.